Hide and seek

Radial-Velocity Searches For Planets Around Active Stars

by

Raphaëlle D. Haywood

University of
St Andrews

Accepted for the degree of Doctor of Philosophy in Astrophysics

3 September 2015

Declaration

I, Raphaëlle D. Haywood, hereby certify that this thesis, which is approximately 33,000 words in length, has been written by me, that it is the record of work carried out by me and that it has not been submitted in any previous application for a higher degree.

Date Signature of candidate

I was admitted as a research student in September 2011 and as a candidate for the degree of PhD in September 2015; the higher study for which this is a record was carried out in the University of St Andrews between 2011 and 2015.

Date Signature of candidate

I hereby certify that the candidate has fulfilled the conditions of the Resolution and Regulations appropriate for the degree of PhD in the University of St Andrews and that the candidate is qualified to submit this thesis in application for that degree.

Date Signature of supervisor

Copyright Agreement

In submitting this thesis to the University of St Andrews we understand that we are giving permission for it to be made available for use in accordance with the regulations of the University Library for the time being in force, subject to any copyright vested in the work not being affected thereby. We also understand that the title and the abstract will be published, and that a copy of the work may be made and supplied to any bona fide library or research worker, that my thesis will be electronically accessible for personal or research use unless exempt by award of an embargo as requested below, and that the library has the right to migrate my thesis into new electronic forms as required to ensure continued access to the thesis. We have obtained any third-party copyright permissions that may be required in order to allow such access and migration, or have requested the appropriate embargo below.

The following is an agreed request by candidate and supervisor regarding the electronic publication of this thesis: Access to Printed copy and electronic publication of thesis through the University of St Andrews.

Date Signature of candidate

Date Signature of supervisor

Collaboration Statement

This thesis is the result of my own work carried out at the University of St Andrews between September 2011 and March 2015. Parts of the work presented in this thesis have been published in refereed scientific journals. In all cases the text in the Chapters has been written entirely by me. All Figures, unless explicitly stated in the text have been produced by me.

- Chapters 2 and 3 are based on: "Planets and Stellar Activity: Hide and Seek in the CoRoT-7 system", R. D. Haywood, A. Collier Cameron, D. Queloz, S.C.C. Barros, M. Deleuil, R. Fares, M. Gillon, A.F. Lanza, C. Lovis, C. Moutou, F. Pepe, D. Pollacco, A. Santerne, D. Ségransan and Y. C. Unruh, 2014, Monthly Notices of the Royal Astronomy: 443, 2517. I developed the code to produce the results in this work and wrote the manuscript. A. Collier Cameron provided scientific advice. A. Collier Cameron, D. Queloz, M. Deleuil, M. Gillon, A.F. Lanza, C. Lovis, C. Moutou, F. Pepe, D. Pollacco, D. Ségransan and Y. C. Unruh initiated the project. All co-authors provided comments on the final manuscript.

- The discussion of the Kepler-10 system in Chapter 3 is based on: "The Kepler-10 Planetary System Revisited by HARPS-N: A Hot Rocky World and a Solid Neptune-Mass Planet", X. Dumusque, A. S. Bonomo, R. D. Haywood, L. Malavolta, D. Ségransan, L. A. Buchhave, A.C. Cameron, D. W. Latham, E. Molinari, F. Pepe, S. Udry, D. Charbonneau, R. Cosentino, C. D. Dressing, P. Figueira, A. F. M. Fiorenzano, S. Gettel, A. Harutyunyan, K. Horne, M. Lopez-Morales, C. Lovis, M. Mayor, G. Micela, F. Motalebi, V. Nascimbeni, D. Phillips, G. Piotto, D. Pollacco, D. Queloz, K. Rice, D. Sasselov, A. Sozzetti, A. Szentgyorgyi, C. A. Watson, 2014, Astrophysics Journal, 789, 154. I developed the code to produce the Monte Carlo Markov Chain analysis on radial-velocity observations with priors from the photometry. A. S. Bonomo produced the combined analysis of the radial velocities and the photometry. X. Dumusque initiated the project and wrote the final manuscript; however, this Chapter presents results additional to those published, and the text presented was written by me for this thesis.

- The discussion of the Kepler-78 system in Chapter 3 is based on: "Measuring the Mass of Kepler-78b using a Gaussian Process Model", S.K. Grunblatt, A.W. Howard & R.D. Haywood, 2015, ApJ, 808, 127. S. K. Grunblatt developed the code to produce the results presented in this paper. A. W. Howard initiated the project. I provided substantial scientific advice and comments to the manuscript. S. K. Grunblatt wrote the final manuscript; however, this Chapter presents results additional to those published, and the text presented was written by me for this thesis.

- Chapter 4 is based on: "The Sun as a planet-host star: Proxies from SDO images for HARPS radial-velocity variations", R. D. Haywood, A. Collier Cameron, Y. C. Unruh, C. Lovis, A. F. Lanza, J. F. Llama, M. Deleuil, R. Fares, M. Gillon, C. Moutou, F. Pepe, D. Pollacco, D. Queloz, and D. Ségransan, submitted for publication to Monthly Notices of the Royal Astronomy. I developed the code to produce the results in this work and wrote the manuscript. J.F. Llama modelled the limb-darkening in the SDO/HMI intensity images. A. Collier Cameron, Y.C. Unruh and C. Lovis provided scientific advice. All co-authors provided comments on the final manuscript.

Abstract

The detection of low-mass extra-solar planets through radial-velocity searches is currently limited by the intrinsic magnetic activity of the host stars. The correlated noise that arises from their natural radial-velocity variability can easily mimic or conceal the orbital signals of super-Earth and Earth-mass extra-solar planets. I developed an intuitive and robust data analysis framework in which the activity-induced variations are modelled with a Gaussian process that has the frequency structure of the photometric variations of the star, thus allowing me to determine precise and reliable planetary masses.

I applied this technique to three recently discovered planetary systems: CoRoT-7, Kepler-78 and Kepler-10. I determined the masses of the transiting super-Earth CoRoT-7b and the small Neptune CoRoT-7c to be $4.73 \pm 0.95\,\mathrm{M}_\oplus$ and $13.56 \pm 1.08\,\mathrm{M}_\oplus$, respectively. The density of CoRoT-7b is 6.61 ± 1.72 g.cm^{-3}, which is compatible with a rocky composition. I carried out Bayesian model selection to assess the nature of a previously identified signal at 9 days, and found that it is best interpreted as stellar activity. Despite the high levels of activity of its host star, I determined the mass of the Earth-sized planet Kepler-78b to be 1.76 ± 0.18 $\mathrm{M}_\oplus$. With a density of $6.2^{+1.8}_{-1.4}$ g.cm^{-3}, it is also a rocky planet. I found the masses of Kepler-10b and Kepler-10c to be 3.31 ± 0.32 $\mathrm{M}_\oplus$ and 16.25 ± 3.66 $\mathrm{M}_\oplus$, respectively. Their densities, of $6.4^{+1.1}_{-0.7}$ g.cm^{-3} and 8.1 ± 1.8 g.cm^{-3}, imply that they are both of rocky composition – even the 2 Earth-radius planet Kepler-10c!

In parallel, I deepened our understanding of the physical origin of stellar radial-velocity variability through the study of the Sun, which is the only star whose surface can be imaged at high resolution. I found that the full-disc magnetic flux is an excellent proxy for activity-induced radial-velocity variations; this result may become key to breaking the activity barrier in coming years.

I also found that in the case of CoRoT-7, the suppression of convective blueshift leads to radial-velocity variations with an RMS of 1.82 m.s^{-1}, while the modulation induced by the presence of dark spots on the rotating stellar disc has an RMS of 0.46 m.s^{-1}. For the Sun, I found these contributions to be 2.22 m.s^{-1} and 0.14 m.s^{-1}, respectively. These results suggest that for slowly rotating stars, the suppression of convective blueshift is the dominant contributor to the activity-modulated radial-velocity signal, rather than the rotational Doppler shift of the flux blocked by starspots.

Acknowledgements

First, I would like to thank my supervisor Andrew for his unwavering support throughout my PhD. I enjoyed our numerous debug sessions, which you always made time for despite your Head of School duties. Your boundless enthusiasm has made research more fun than I would have ever imagined! Thank you also for sending me on all those conferences and observing trips – I have discovered much more than exoplanets in the past three years!

I am also very grateful to my first ever journal referee, Suzanne Aigrain, who introduced me to the power of Gaussian processes – a cornerstone in my thesis work.

I am indebted to everyone in my office, particularly Will, Laura, Milena, and especially Claire, for listening to my incessant rants, both happy and angry, and for cheering me up when I needed it. For this I should also thank the postdocs in the office next door, and the astronomy group as a whole. I hope the Monday cake tradition and the long coffee breaks continue!

I am grateful to Joe and Will for all their Fortran-related help, to Annelies for answering my random science questions and for post-telecon rants, and to Guillaume for providing me extremely useful advice for my postdoc applications.

Joe, thank you for the many evenings spent at your house back in my first year, and for the fun we had at conferences together – there will be more soon! Jack, thank you for the endless hours we spent talking about everything and nothing, sometimes stretching far into the night, or sitting on a tree over a river. Rim, I miss our late lunches at Pizza Express, your crazy talk (your serious talk too) and all our laughs about silly things! Now that I am done with this thesis I really ought to visit you in Sicily.

João, you kept me sane during the final months of writing-up. You stood by me even in the times when I was as intolerable as only my brother James knows – I am sure he will tell you that is quite an achievement. Also, you proofread pretty much the entirety of this thesis. Thank you!

Finally, I wish to give an enormous thank you to my family, who has always encouraged and supported me. None of this would have been possible without the very frequent phone conversations with my Dad, and his constant stream of advice and encouragement. I am grateful for the regular Sunday phone calls to my grandma, and the comforting (and sometimes hilarious) chats with my sisters Adèle and Lucie, and my brothers James and Germain. I am also very much indebted to Anne-Sophie for her support. I look forward to another great family holiday together!

A mon père,
modèle de force, courage,
patience et détermination

Contents

Introduction
The hunt for extra-solar planets

> "In future, children won't perceive the stars as mere twinkling points of light: they'll learn that each is a 'Sun', orbited by planets fully as interesting as those in our Solar system."
>
> Sir Martin Rees, 2003

Since the dawn of civilisation we have looked up to the stars, wondering whether other worlds exist and what they might look like. In the last few decades, developments in instrumentation and observation techniques have led to revolutionary discoveries: we now know that planets revolving around other stars than our Sun exist, and better still, they appear to be very common.

Early searches In the 1940s, a few independent exoplanet discovery claims were made (Strand, 1943; Reuyl & Holmberg, 1943), based on perturbations in the astrometric motions of their host stars. There was also a flurry of interest in astrometric detection in the late 1960s, when van de Kamp (1969) claimed the detection of two planets orbiting Barnard's star. Although these findings were soon proved wrong, they sparked new appeal in the astronomy community at the time. The idea that we might be able to detect the radial motion of a star induced by the gravitational tug of orbiting planets was proposed by Struve (1952), and several radial-velocity (RV) monitoring surveys were initiated, including those of Campbell & Walker (1985), Latham et al. (1989) and Marcy & Butler (1994). This technique has proved very successful at detecting and confirming exoplanets since then, and has yielded some of the most exciting results in this new field of astronomy.

Wolszczan & Frail (1992) reported on the first detection of two Earth-mass planets orbiting a pulsar, based on variations in the timing of its pulses. In 1995, Mayor & Queloz (1995) announced the discovery of 51 Peg b, the first planet-mass companion of a Sun-like star. It was found through RV observations taken with the ELODIE spectrograph (Baranne et al., 1996), mounted on the 1.93-metre telescope at the Observatoire de Haute-Provence (France). 51 Peg b has half the mass of Jupiter, but orbits its host star once every 4 days: it is much closer to its star than Mercury, which orbits the Sun every 88 days.

An army of planet-hunting spectrographs was formed including SOPHIE, to replace ELODIE on the 1.93m (Perruchot et al., 2008) and HARPS (High Accuracy Radial-Velocity Planet Searcher, Mayor et al. (2003)), commissioned in 2003 on the 3.6m telescope at La Silla, Chile. The first planet-hunting spectrographs, including ELODIE, HIRES, mounted on Keck I at Mauna Kea observatory, Hawaii (Vogt

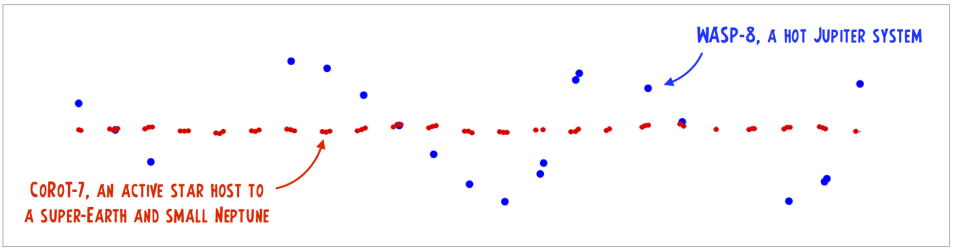

Figure 1: Yesterday's discoveries and today's challenges: RV variations of WASP-8, host to a hot-Jupiter in an 8-day orbit recorded with CORALIE and HARPS (Queloz et al., 2010) *(blue)*, and HARPS RV variations of CoRoT-7, an active star host to a super-Earth in an 0.85-day orbit and a small Neptune at 3.65 days (Haywood et al., 2014) *(red)*. The horizontal and vertical scales are the same for both RV curves.

et al., 1994), and CORALIE, mounted on the Euler telescope at La Silla, Chile (Queloz et al., 2000) had an RV precision of about 15 $\mathrm{m.s}^{-1}$ (see Perryman (2011), p.24. for a complete list of planet-hunting spectrographs). Over the years, improved calibration techniques (see Mayor et al. (2014); Pepe et al. (2014a) and references therein) have pushed the RV sensitivity down by an order of magnitude. HARPS is able to detect RV signals with amplitudes as low as 1 $\mathrm{m.s}^{-1}$ (Queloz et al., 2001b), and has paved the way towards the discovery of Neptune- and super-Earth-mass planets through new blind RV planet surveys (see Figure 1).

From RV monitoring to planet detection The radial velocity of a star is defined as "the component of its motion along the line of sight of the observer" (Murdin, 2002). The presence of a planet exerts a gravitational pull on the star that causes it to wobble by tiny amounts around their common centre of mass, as shown in Figure 2a. The light we receive from the star is slightly blueshifted or redshifted as the star gets pulled towards or away from us (Figure 2b).

As it reaches the observer, light with a wavelength λ_{obs} has undergone a relativistic Doppler shift relative to when it was initially emitted by the star as λ_{rest} (the wavelength of a spectral line in a rest frame). Each line is thus shifted by an amount:

$$\Delta\lambda = \lambda_{\mathrm{obs}} - \lambda_{\mathrm{rest}}. \tag{1}$$

It is possible to show that the radial component of the velocity of the star is proportional to this wavelength shift:

$$v_{\mathrm{radial}} \approx \frac{\Delta\lambda}{\lambda_{\mathrm{rest}}} c, \tag{2}$$

where c is the speed of light (refer to Perryman (2011), p.16 and references therein for the full derivation of this equation).

Monitoring the RV of a star in time allows us to detect any variations induced by the orbit of a planet. A few examples of existing and hypothetical planets and their expected RV semi-amplitudes are listed in Table 1.

The mass m of the planet can be derived from the semi-amplitude K and period P

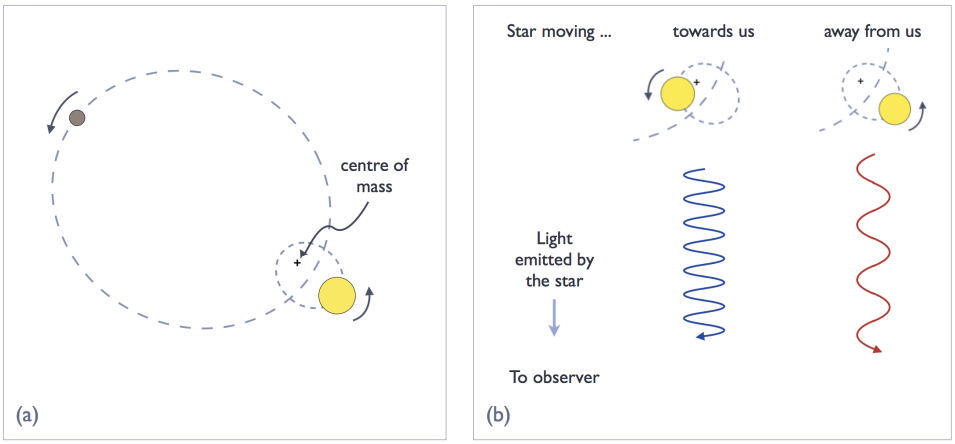

Figure 2: The radial-velocity method: as a planet orbits its host star, the star wobbles around their common centre of mass (panel (a)). As a result, the starlight is Doppler shifted (panel (b)).

of the signal, if we know the stellar mass $M_\star$. The mass function $f(m)$ is given by:

$$f(m) = \frac{m^3 \sin i}{(M_\star + m)^2} = \frac{K^3 P}{2\pi G} (1 - e^2)^{3/2}, \tag{3}$$

where i is the planet's orbital inclination and G is the gravitational constant (the full derivation of this equation can be found in Perryman (2011) or Hilditch (2001)).

Ground-based photometric surveys The surprising discovery of 51 Peg b was soon followed by others, through photometric surveys such as the Hungarian Automated Telescope Network, operational since 2001 (HATNet, Bakos et al. (2004)), and the Wide-Angle Search for Planets initiated in 2004 (WASP, Pollacco et al. (2006); Cameron et al. (2009)). These arrays of small robotic telescopes monitor the brightness variations of hundreds of thousands of stars at a time, looking for tiny, periodic dips of less than 1% in the star's light, which may be caused by a planet crossing the disc of its host star. Together, WASP and HATNet have found over 200 transiting planets as of March 2015.

One of the most common ways to detect extra-solar planets is to look for the periodic dimming of the host star as a planet passes in front of it relative to the observer, as illustrated in Figure 3. Transit events are very unlikely as they require the observer, planet and host star to be very well aligned. If the radius of the star and the orbital eccentricity are known, then the radius of the planet can be inferred (see Seager & Mallen Ornelas (2003)). If our planetary system contains one or more transiting planets we can assume i approximately equal to 90°. This is usually a reasonable assumption for all the planets in a compact system since over 85% of observed compact planetary systems containing transiting super-Earths and Neptunes are thought to be coplanar within 3° (Lissauer et al., 2011b).

Combining transit and RV observations together yields a complete set of planetary and orbital parameters. The bulk density of the planet can then be inferred from its mass and radius, allowing us to take a first guess at its structure and composition.

Planet mass	**Distance to star**	**Orbital period**	**K**
Jupiter (317 $M_\oplus$)	5 AU	5 years	12 m.s^{-1}
Jupiter	1 AU	1 year	28 m.s^{-1}
Neptune (17 $M_\oplus$)	0.1 AU	36 days	5 m.s^{-1}
Super-Earth (5 $M_\oplus$)	0.1 AU	36 days	1.4 m.s^{-1}
Earth	1 AU	1 year	0.09 m.s^{-1}

Table 1: Approximate RV semi-amplitudes expected from some of the planets of our solar system at a range of distances (values obtained from the Wikipedia page "Doppler spectroscopy", in March 2015).

The space revolution After the turn of the century, several photometric satellites were launched into space to look for transits of small super-Earth- and Earth-size planets without the disruptive twinkling induced by the Earth's atmosphere. The European CoRoT[1] satellite (Baglin & Team, 1998; Auvergne et al., 2009), launched at the end of 2006 was the first space mission dedicated, in part, to the detection of exoplanets. It discovered 32 validated planets to date (see a recent review by Hatzes (2014)), most of them giant gas planets, but also several small rocky planets, including CoRoT-7b, the first transiting rocky planet ever discovered (Léger et al., 2009).

In addition to finding transiting exoplanets, the CoRoT satellite, together with the Canadian space mission MOST[2] (Matthews et al., 2000) launched in 2003 and the *Kepler* mission (launched in 2009) sparked huge advances in the field of asteroseismology. Sun-like stars constantly pulsate due to the numerous acoustic oscillations bouncing within their interiors; by monitoring the amplitude and frequency structure of the flickering induced by these oscillations, we can probe stellar interiors and characterise stars with unprecedented accuracy and precision (see Campante (2015), Chaplin et al. (2014) and Kjeldsen et al. (2010) among others). In particular, asteroseismology provides very accurate and precise measurements of radii and masses of stars, which are essential to characterise extra-solar planets (see Campante (2015) and references therein).

In addition to these missions, the Gaia spacecraft was launched at the end of 2013 by ESA. It will measure fundamental parameters (including distance, radius and effective temperature) of about 1 billion stars, which amounts to 1% of the stars in our Galaxy (Lindegren, 2009). It is expected to detect 5000 transiting exoplanets via photometric monitoring as well as a further 2000 exoplanets via astrometric measurements, which should allow it to detect every Jupiter-mass planet with orbital periods between 1.5 and 9 years (de Bruijne, 2012; Sozzetti, 2011).

The *Kepler* space mission funded by NASA (Borucki et al., 2011; Koch et al., 2010) prompted an explosion in exoplanet discoveries: as of March 2015, over 1000 planets have been confirmed, and another 4200 candidates are awaiting further investigation. Because of their sheer number and that many of them are too faint for ground-based telescopes, *Kepler* candidates cannot all be confirmed via RV follow-up observations

[1] COnvection, ROtation et Transits planétaires
[2] Microvariability and Oscillations of STars

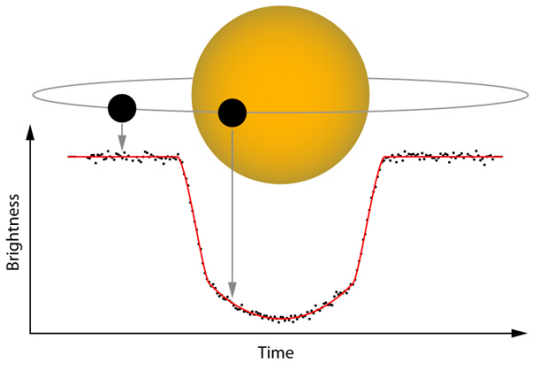

Figure 3: Transit of WASP-10b: the planet casts its shadow upon the stellar disc when it passes in front of it, thereby reducing the total brightness observed. Image credit: John Johnson.

or transit timing variations induced by gravitational interactions between planets in multiple systems. Instead, a large number of candidates are now elevated to planet status via statistical validation (Rowe et al., 2014; Lissauer et al., 2014b; Torres et al., 2011). In this procedure, the likelihood of a planet nature is weighted against other possible phenomena such as a grazing eclipsing stellar binary, blend with a background binary system, instrumental effects, etc.

Among its most notable discoveries, *Kepler*'s first Earth-size rocky planet was Kepler-10b (Batalha et al., 2011a); a rocky Neptune-mass companion Kepler-10c was confirmed soon after (Fressin et al., 2011). I determine the masses of both planets using HARPS-N RV data in Chapter 3. The first system characterised via transit timing variations was Kepler-9, a system of two giants (Holman et al., 2010); see also Kepler-36, a curious system because its two transiting planets have very different densities (Carter et al., 2012). Kepler-11 was found to host 6 small transiting planets, 5 of which have orbital periods between 10 and 47 days (Lissauer et al., 2011a, 2013); this was the first of many multiple compact systems. *Kepler* also found several circumbinary planets, including Kepler-16b (Doyle et al., 2011), Kepler-47b and c (Orosz et al., 2012b) and the Neptune-size Kepler-38b (Orosz et al., 2012a). The first planet discovered with the same radius and mass as the Earth was Kepler-78b (Sanchis-Ojeda et al., 2013); with an orbital period of just 8.5 hours, it is sure to be a hellish world! I re-determine its mass using HARPS-N and HIRES observations in Chapter 3. Kepler-186f, was the first validated Earth-size planet to lie in the habitable zone of an M dwarf, where liquid water can be sustained (it is believed to be a key element for the emergence and survival of carbon-based life) (Quintana et al., 2014). The *Kepler* mission uncovered a great diversity of planets, which are giving us a unique insight on planet occurence rates (see recent statistical studies by Howard et al. (2010), Mayor et al. (2011), Fressin et al. (2013), Petigura et al. (2013) and others) and shaping our theories of planet formation (see Lissauer et al. (2014a) and references therein).

The initial aim of the *Kepler* mission was to find and characterise "Earth twins", i.e. rocky planets orbiting Sun-like stars in the habitable zone. Achieving this goal has been more difficult than anticipated, however, mainly because the intrinsic photometric variability of stars due to oscillations, granulation, spots, flares, etc. had been underestimated. Since the failure of two of its reaction wheels in May 2013, *Kepler* has been recycled into K2, which points to fields near the ecliptic

plane for about 80 days at a time (Haas et al., 2014). Its photometric performance is still excellent, and it is already discovering transiting planets (Barclay, 2014).

RV follow-up of *Kepler* candidates and future instruments In order to confirm the brightest and most exciting *Kepler* candidates, a replica of HARPS for the Northern hemisphere was designed as the *Kepler* field is not visible from the South. HARPS-N is mounted on the 3.57m Telescopio Nazionale Galileo (TNG) at La Palma, Spain (Pepe, 2010; Cosentino et al., 2012). It has now been in operation for three years and routinely achieves a precision better than 1 m.s^{-1}. HARPS-N has already enabled the characterisation of several *Kepler* systems, including Kepler-78 (Pepe et al., 2013), Kepler-10 (Dumusque et al., 2014), two close-in giant planet hosts KOI-200 and 889 (Hébrard et al., 2014) and a close-in super-Earth host Kepler-93 (Dressing et al., 2015).

Several other high-precision spectrographs are currently being commissioned (see Pepe et al. (2014a) and references therein). *Minerva* (Hogstrom et al., 2013) is due to start operations this year and will contribute to the follow-up of transiting planets found by K2 and TESS, the Transiting Exoplanet Survey Satellite (Ricker et al., 2015), to be launched in 2017. In the same year, CHEOPS (CHaracterising ExOPlanets Satellite, (Fortier et al., 2014)) will be sent out to determine the radii of planets found in current RV surveys and for more precise photometric follow-up of targets identified by K2 and TESS.

A new generation of near-infrared spectrographs is also emerging, with CARMENES (Quirrenbach et al., 2013), which is expected to begin work this year, and SPiROU (Delfosse et al., 2013), scheduled for 2017. These spectrographs will be ideally suited to look for planets in the habitable zones of M dwarfs, which are more luminous in the infrared than in the visible. The effects of stellar activity, which are a major obstacle in RV searches, are less marked in this region of the spectrum.

The ESPRESSO spectrograph, to be mounted on the 8-m VLT at Paranal Observatory, Chile in 2016 is expected to achieve a precision of 0.1 m.s^{-1} (Pepe et al., 2014b). PLATO (Rauer et al., 2014), a photometry mission planned for launch in 2024, is a wide-field instrument like WASP, which will enable the discovery of Earth-radius planets in the habitable zones of their host stars. It will target bright stars, enabling much more precise determination of the planetary masses – if we can overcome the challenges imposed by stellar activity (see later paragraph). PLATO will perform asteroseismology on the host stars, enabling accurate determination of stellar parameters and ages. It will also allow us to explore the architecture of planetary systems as a whole, which will provide unique insights on planet formation.

High-precision RV measurements The key to measuring the RV of a star with high precision is to obtain a spectrum with as many lines as possible. High-resolution spectrographs are fitted with a grating, which splits the light into many wavelength orders, with the same resolution at all wavelengths; each order is then cross-dispersed

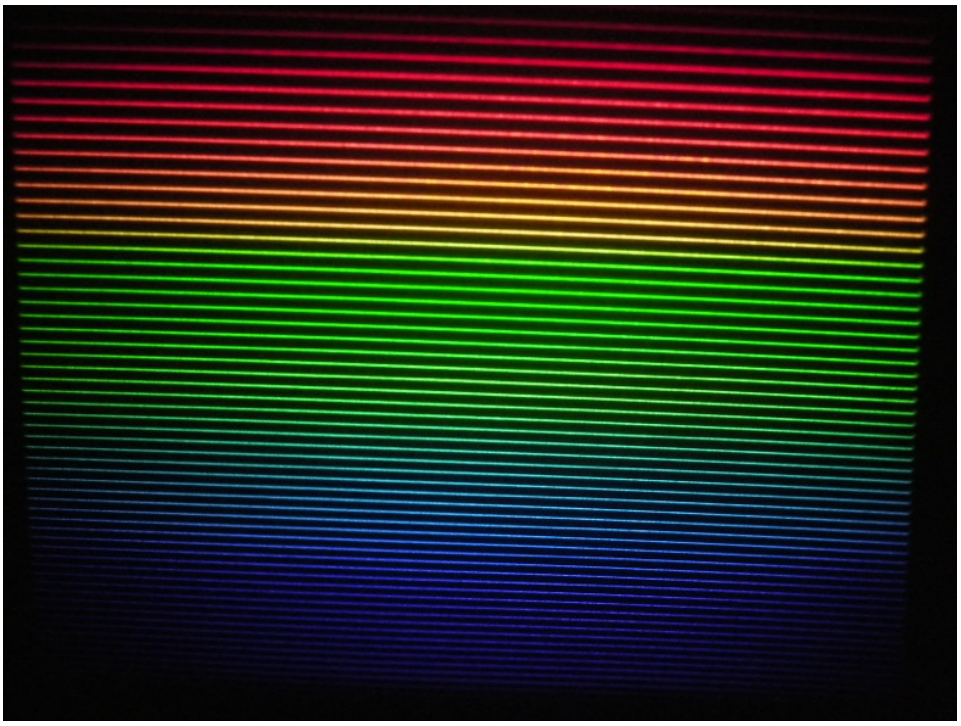

Figure 4: (Pre-) first light spectrum obtained by HARPS-N. The horizontal bands are the wavelength orders split by a grating, each of which is then split by a grism. This setup produces thousands of spectral lines, from which a precise RV measurement can be extracted. Picture captured by Francesco Pepe with a DSLR camera.

by a grism in order to separate the different spectral orders spatially. The resultant spectrum is projected onto a high quality square CCD unit, as pictured in Figure 4. Such a spectrum contains thousands of absorption spectral lines. We can create "line masks" of the strongest lines expected in the spectrum of a given star (eg. F, G, K) based on wavelength atlases of line positions measured in laboratory experiments, and assuming the profile of the lines (eg, Gaussian). We cross-correlate our observed spectrum with a line mask in order to determine the wavelength shift and mean shape of each line. From this procedure, we can create a "mean" line known as the cross-correlation function (CCF). It is centred at λ_{obs} and its shape is a combination of all the lines in the spectrum; the more lines we have, the better defined the CCF. The cross-correlation technique is commonly used in spectroscopic data reduction pipelines (eg. for HARPS and HARPS-N, see Baranne et al. (1996) and Lovis & Pepe (2007)).

HARPS-N is a twin of HARPS, its most notable differences being that it is fed by an octagonal fibre, which scrambles the light more effectively. It also uses a Thorium-Argon lamp for the wavelength calibration, but experiments are being carried out with a laser comb which is currently being used to map the locations of the individual pixels on the CCD, to combat systematic errors caused by irregular pixel sizes. The RV uncertainty due to photon noise on HARPS and HARPS-N measurements can be reduced down to 0.5 m.s^{-1} with appropriate exposure times. The level of instrumental noise, arising mostly from wavelength calibration, is now of the order of a fraction of a m.s^{-1} (Mayor & Udry, 2008; Dumusque et al., 2010).

Further descriptions of telescope and spectrograph setups as well as wavelength

calibration methods (iodine cell, Thorium-Argon lamp, laser frequency comb), along with references for further information are given by Perryman (2011), pp.16-21.

This thesis: towards breaking the stellar activity barrier We have now reached a level of precision where the most significant source of noise comes from the star itself. Observations have shown that activity-induced RV variations are of the order of 0.5 $m.s^{-1}$ for a quiet dwarf star (Makarov et al., 2009); they can reach tens of $m.s^{-1}$ in active stars, and in some cases up to 50 $m.s^{-1}$ (Saar & Donahue, 1997). In comparison, a super-Earth orbiting a Sun-like star at 0.1 AU induces a signal with an amplitude of just 1.4 $m.s^{-1}$. A habitable Earth-mass planet has an RV signature of under 10 $cm.s^{-1}$ (see Table 1). Activity-induced signals can therefore conceal and even mimic planetary orbits in RV surveys, and this has resulted in several false detections (Queloz et al. (2001a); Bonfils et al. (2007); Huélamo et al. (2008); Boisse et al. (2009, 2011); Gregory (2011); Haywood et al. (2014); Santos et al. (2014); Robertson et al. (2014) and others). I review the magnetic activity processes and features responsible for RV variability in Chapter 1.

To this day, various activity decorrelation methods have been tested (including the methods of Queloz et al. (2009); Hatzes et al. (2011); Aigrain et al. (2012); Haywood et al. (2014)) but no simple and all-inclusive recipe has yet been proposed. During my thesis, I developed a new analysis technique to account for activity-induced signals in RV searches using Gaussian processes. I present my method in Chapter 2, and apply it to RV observations of CoRoT-7, Kepler-78 and Kepler-10 in Chapter 3.

Understanding the effects of stellar activity on RV observations is crucial to develop the next generation of more sophisticated activity models, and further improve our ability to detect and characterise low-mass planets. In Chapter 4, I explore the physical origin of stellar RV variability and identify a new activity proxy through the study of the Sun. It is the only star whose surface can be directly resolved at high resolution, and therefore constitutes an excellent test case.

1

Stellar activity as a source of radial-velocity variability

The key to breaking the activity barrier in exoplanet detections lies in our understanding of the physical origin and temporal structure of stellar RV variability. This Chapter provides a review of the manifestations of magnetic activity, their impact on photometric and spectroscopic observations, and the analysis techniques that have been developed in recent years to account for activity-induced RV signals. I also present the target selection criteria I proposed to pick "magnetically manageable" stars for HARPS-N RV follow-up.

The signatures of magnetic activity span a wide range of spatial and temporal scales. We tend to naturally think of things in terms of their physical sizes. But when it comes to looking at stars, we see them as minuscule point-like objects in the night sky, and it is impossible to observe their surfaces with high resolution (except for the Sun). We can thus only gather limited information about spatial structures on the stellar surfaces.

The time-dependent nature of observations allows us to watch the surfaces of stars change and evolve over time and thus form a detailed picture of the various time scales at play. The temporal structure of the signals we observe can tell us a lot about the stars they originate from. In the first part of this Chapter, I will present each stellar activity timescale, starting from acoustic oscillations that evolve within minutes, up to magnetic cycles that last decades.

1.1 Magnetic activity and its manifestations

Before we look at the temporal and spatial diversity of magnetic activity signatures, however, let us catch a glimpse at how magnetic fields are produced within stars. It has long been found that a dynamo process operates within the stellar interior (Babcock (1961); Parker (1963), see Tobias (2002) and references therein). Over recent years, helioseismic studies and sophisticated numerical models have taught us much about the Sun's internal dynamics, although much debate remains (see review by Charbonneau (2010)). Current theories of solar dynamo processes are detailed in Choudhuri (2007).

The Sun, like all stars, generates energy in its core through the process of nuclear fusion. This energy is carried outwards in the form of radiation through the radiative zone, where photons undergo a random walk which takes about 10 million years (Lockwood, 2005). The radiative zone constitutes the majority of the Sun's interior. Above it lies a convective zone which takes up around 30% of the interior (in radius). In less massive stars, the radiative layer is thinner or may not be present at all – for stars with masses less than 0.35 $M_\odot$ (corresponding to early M spectral type), convection is the dominant mechanism for energy transport throughout the star (Hansen & Kawaler, 1994; Chabrier & Baraffe, 1997). Hot fluid cells are driven upwards due to buoyancy forces. The cells cool when they reach the stellar surface and eventually sink back, and so on.

In Sun-like stars, the radiative and convective layers are separated from each other by a thin layer called the tachocline (Spiegel & Zahn, 1992; Miesch, 2005). In this region, strong radial shearing forces arise due to the transition between the uniformly rotating radiative zone and the differentially rotating convection zone. It is now generally accepted that this shear is the source of the stellar magnetic dynamo, which is responsible for stellar activity (Tobias, 2002). Fully convective stars, in which there is no tachocline, have a different type of dynamo which can result in both basic magnetic field topologies (Morin et al., 2008) or very complex ones (Chabrier & Küker, 2006). Fully radiative stars have very weak and unordered fields, if any, and it is unclear how they are created (see Walder et al. (2012) and references therein). A small subset, however, such as the chemically peculiar A stars, have very strong magnetic fields, but these appear to be fossil fields rather than dynamo-generated. Their configurations do not change with time (see Aurière et al. (2014) and references therein).

Light escapes from stars in the bottom layer of the stellar atmosphere: the photosphere. Above the photosphere lies the chromosphere, which is surrounded by the corona, which extends out into space through the solar wind. The photosphere is commonly regarded as the stellar surface and is peppered with granulation, spots and faculae: these are some of the signatures of stellar magnetic activity.

Useful textbooks and reviews on the topics covered in this Chapter include Rutten & Schrijver (1994) – proceedings of *Solar Surface Magnetism*[1], Schrijver & Zwaan (2000) – a book on solar and stellar magnetic activity, Hall (2008) – a review on chromospheric activity, and Reiners (2012) – a review on observations of magnetic fields in Sun-like stars. A great place to find general reviews and articles on solar and

[1]NATO Advanced Research Workshop, held in the Netherlands in 1993.

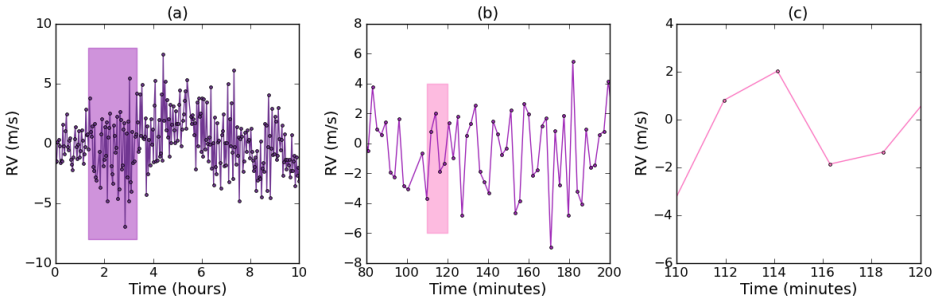

Figure 1.1: RV observations of the bright star μ Arae (also known as HD 160691, $V = 5.1$ mag), monitored at high-cadence (100-s exposures with 31-s of dead time in between) as part of an 8-night HARPS run in June 2004 (ESO program 073.D-0578, Bouchy et al. (2005)). Panel (a) shows observations made over one night. Panel (b) is a zoom-in over a 2 hour period, and panel (c) is a zoom-in over 10 minutes. Panel (a) clearly shows the 2-h granulation signal, while panels (b) and (c) highlight the p-modes.

stellar activity is the *Living Reviews in Solar Physics*[2]. For more general information on stellar interiors and atmospheres, two classic textbooks are Novotny (1971) and Gray (1992). I also provide more specific references throughout this Chapter.

1.1.1 Minutes: oscillations

Stars breathe. Their internal pressure constantly fluctuates by tiny amounts; this creates acoustic waves going through the star's interior, which result in the formation of ripples on the stellar surface. These waves were first observed on the Sun by Leighton et al. (1962); later on, Bedding et al. (2001) reported on the first clear detection of similar oscillations in a star other than the Sun, α Cen A. These oscillations, commonly known as p-modes, repeat on timescales of about 5 to 15 minutes and produce RV oscillations with an amplitude of a few m.s^{-1}.

To illustrate this, I retrieved RV observations of the bright Sun-like star μ Arae, taken at a 2-minute cadence over an 8-night run for an asteroseismic study (Bouchy et al., 2005). The RV variations recorded on one of the nights are plotted in Figure 1.1. The p-mode oscillations are clearly visible, particularly in panel (c), which shows a close-up on an oscillation with a period of about 8 minutes. We can confirm the presence of this signal by looking at the Lomb-Scargle periodogram (Lomb (1976); Scargle (1982); Zechmeister & Kürster (2009); see Section 1.3.2.1) of the dataset, displayed in Figure 1.2. We also see other peaks at 5 and 11 minutes, which arise from p-mode oscillations that have a slightly different frequency.

We can average out the RV effects of these short frequency oscillations simply by making sure our observations are at least 10 minutes long (Dumusque et al., 2010). It is common practice with HARPS and HARPS-N to make 15-minute observations in order to cancel their effect.

[2]Published by the Max-Planck-Institut für Sonnensystemforschung, Germany. Available online at: http://solarphysics.livingreviews.org/.

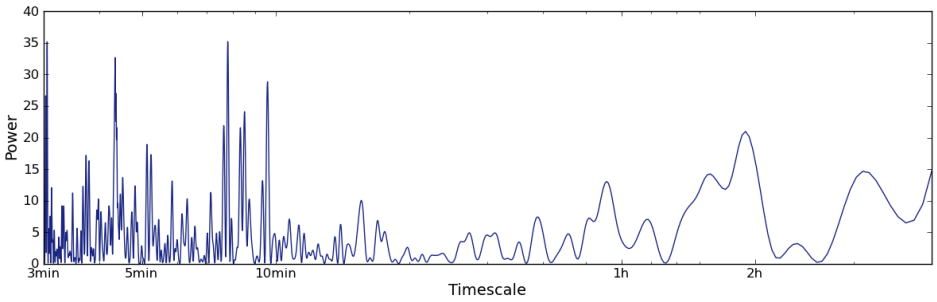

Figure 1.2: Lomb-Scargle periododgram of the RVs of μ Arae plotted in Figure 1.1. The strong peaks close to 4 and 8 minutes are caused by the p-modes, while the peak at about 2 hours is due to granulation motions.

1.1.2 Minutes: flares and coronal mass ejections

The magnetic energy stored in active regions and their surroundings can lead to sudden releases in the form of large eruptions known as flares or coronal mass ejections (see Hathaway (2010) and references therein). These events lead to sudden and sharp increases of brightness, and have been observed on other Sun-like stars in *Kepler* lightcurves (see Walkowicz et al. (2011) and others).

These dramatic events are rare in the sort of low-activity stars suitable for planetary RV searches, and easily identified in RV observations as they will generate spikes of several tens of m.s^{-1} in the mean RV variations of a star, and show strong signatures in the Hα emission profile (Reiners, 2009).

1.1.3 Minutes to hours: granulation

A small patch of the Sun's surface is pictured in Figure 1.3, revealing the bright and dark granulation structures in impressive detail. This pattern originates from the convective motions taking place below the surface: hot fluid cells rise up to the surface, forming large and bright patches, which sink once they have cooled and become dense enough for gravity to pull them back down.

Granules have a diameter of a few hundred kilometres, and a lifetime of the order of about 8 minutes (Bahng & Schwarzschild, 1961; Hall, 2008). There also exist larger structures called mesogranules; these have lifetimes of 30-40 minutes (Roudier et al., 1998). The largest convective cells, known as supergranules, have sizes of order 40-50 Mm and remain on the stellar surface for about a day (Del Moro et al., 2004).

This short frequency bustling leads to variations in brightness, which we can now easily probe on Sun-like stars thanks to high precision, short cadence *Kepler* photometry (Gilliland et al., 2011).

The vertical motions of convection produce RV variations of the order of around 2 km.s^{-1}. Since there are about 1 million granules on the visible hemisphere of the Sun at any time, the global RV variations can be thought of as arising from fluctuations in the number of granules present. The fluctuations obey Poisson statistics, so they are on the order of the square root of the number of granules, reducing the observed RV flicker on the granulation timescale from 2 km.s^{-1} down to 2 m.s^{-1} (Lindegren & Dravins, 2003). The first evidence of the such RV variations were observed by

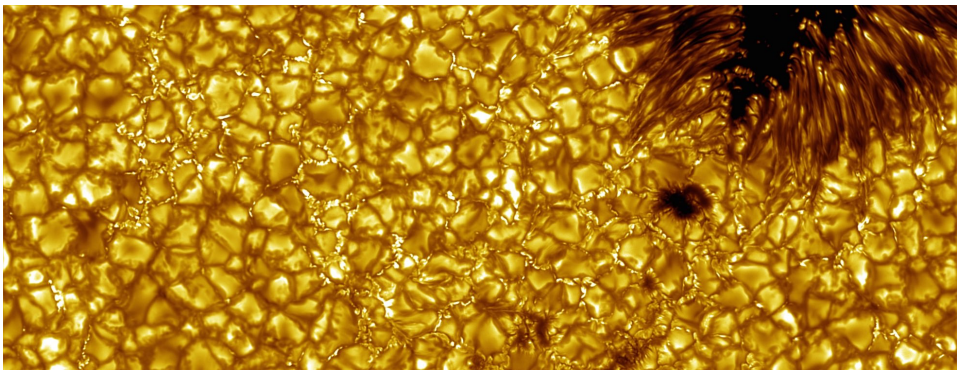

Figure 1.3: Granulation on the solar surface, observed at high resolution with the Swedish 1-m telescope, at La Palma. A sunspot is visible in the top-right corner – its dark centre, known as the umbra, is surrounded by a lighter region known as the penumbra. Convection cells are visible on the photosphere surrounding the spot. Image credit: Vasco Henriques, http://www.isf.astro.su.se/gallery/images/2010/ (link valid as of March 2015).

Labonte et al. (1981) and Kuhn (1983) on the Sun. Several years later, Kjeldsen et al. (1999) reported on the first clear evidence of periodic fluctuations due to granulation in a star other than the Sun, α Cen A.

We can go back to the RV observations of μ Arae, shown in Figure 1.1 to identify its granulation signature. In panels (a) and (b), we can see variations over a longer timescale than that of the p-mode ocscillations. An inspection of the periodogram in Figure 1.2 reveals peaks close 1 and 2 hours, which can be attributed to granulation (although in this particular case, these peaks may be aliases of a longer 8-h cycle that can be seen in plots of the full 8 nights of data, presented in Bouchy et al. (2005)).

As for p-modes, adapting our observing strategy to mitigate their effect on RV measurements also works for granulation. Taking several RV measurements on each night observed (generally 2 to 3 measurements) spaced by about 2 hours significantly reduces the RV effects of granulation (Dumusque et al., 2010).

1.1.4 Days and longer: Gravitational redshift

Photons escaping from the photosphere are slowed down by the strong gravitational potential of the star; the photons become redshifted, causing the centres of the spectral lines to shift. In the case of the Sun, this results in a shift in RV of order 600 m.s^{-1} (Lindegren & Dravins, 2003). The magnitude of this shift depends on the stellar radius, and Cegla et al. (2012) calculated that a change of 0.01% in the radius of the Sun would induce a shift of about 6 cm.s^{-1} in RV This is enough to mimic or mask the orbital reflex motion of the Earth in our solar system if the radius fluctuations are taking place on a long enough timescale. Cegla et al. (2012) found that fluctuations occuring over 10 days or longer became significant. This means that we do not have to worry about the effect of p-modes; however, changes in the graulation pattern on the stellar surface and the Wilson depression of starspots (see Solanki (2003) and references therein) can potentially produce radius fluctuations that would yield small, but significant RV variations (see Cegla et al. (2012) and

references therein). Variable gravitational redshift is not a major source of activity-induced RV variations, however.

1.1.5 Stellar rotation period: spots, faculae and plage regions

Stellar surface features such as spots and networks of faculae induce photometric and spectroscopic variations that are modulated by the rotation period of the star. These signals pose a serious challenge to the detection of exoplanets. Various decorrelation methods have been developed (see Section 1.2), but no simple and all-inclusive recipe has yet been found.

1.1.5.1 Sunspots and starspots

Sunspots are seen as dark areas on the surface of the Sun (see top right corner of Figure 1.3). Hale (1908) was the first to notice Zeeman splitting of lines produced in these dark regions and deduced that sunspots are regions of strong magnetic fields. They are indeed areas where magnetic flux loops emerge from the solar surface (Solanki, 2002), as illustrated in Figure 1.7; the magnetic fields inhibit part of the outgoing convective heat flux, resulting in areas of reduced brightness and temperature. The spots usually appear as pairs of opposite magnetic polarity. For a detailed review of the general properties of sunspots, refer to Solanki (2003).

Observations of similar dark and magnetic structures on the surfaces of other stars have led to the concept of stellar spots. Starspots are defined as "an environment in which magneto-convective interaction significantly suppresses convective energy transport over an area large enough that a structure forms that is cool and dark relative to the surrounding photosphere" (Schrijver, 2002). They are similar to sunspots in many aspects; the most notable difference is that starspots can attain huge sizes and can exist near the poles of their stars (Strassmeier, 2009). In the next few paragraphs, I briefly describe the main properties of sunspots and starspots. Many of the papers cited below are part of the Proceedings of the First Potsdam Thinkshop on Sunspots and Starspots (Strassmeier et al., 2002). I also learned much on starspots from reviews by Berdyugina (2005) and Strassmeier (2009). Thomas & Weiss (2008) is a comprehensive book on starspots and sunspots. These are all excellent sources of information to find out more about the physical properties of sunspots and starspots.

Sunspots have temperatures ranging from 600 to 1800 K less than the surrounding photosphere, and starspots have similar temperature differences ranging from 500 to 2000 K (Schrijver, 2002). Since spots have lower temperatures than the rest of the stellar surface, they appear darker. We can determine their magnetic field strength and the magnetic filling factor over the whole stellar surface via Zeeman splitting of spectral lines, using high-resolution spectra; we are not yet able, however, to disentangle these two quantities (Saar (1991); see Reiners (2012) and references therein).

As spots grow and decay, they induce variations in photometry that are modulated by the star's rotation (see some example lightcurves in Figure 1.13). As a star rotates, one half of the disc is moving towards us, while the other half is moving away; as a result, the flux emitted by the approaching half is blueshifted, while the receding

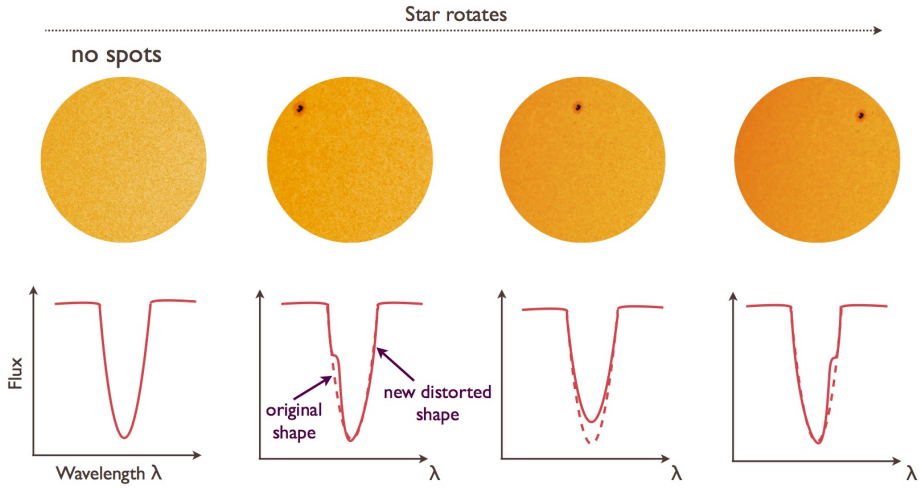

Figure 1.4: Diagram illustrating how flux blocked by starspots on the rotating stellar disc induces asymmetries in the spectral lines, leading to variations in RV.

half is redshifted. If the stellar surface presents no features, the Doppler shifts from both sides cancel each other out and the spectral line profile is undisturbed, as pictured in the left diagram of Figure 1.4. A starspot coming in and out of view as the star rotates, as shown in the subsequent diagrams of Figure 1.4, blocks some of the flux of the star, inducing an imbalance between the redshifted and blueshifted halves of the star. This produces an asymmetry in the shape of the total line profile, thus shifting its centroid by a small amount. These perturbations to the line profile translate into RV variations of the order of $1\,\mathrm{m.s^{-1}}$ for sunspots (Lagrange et al., 2011; Makarov et al., 2009); starspot-induced RV variations can be much greater for more active, more rapidly rotating stars.

We can monitor these line-profile distortions to track the evolution of spots. This technique, commonly known as *Doppler imaging*, was first applied to the rapidly-rotating star HR 1099 by Vogt & Penrod (1983) to reconstruct a stellar surface brightness map. It was later applied to the rapidly-rotating K dwarf AB Doradus, by Donati & Collier Cameron (1997) to map the stellar magnetic flux distrbution. The procedure is illustrated in Figure 1.5, with HARPS cross-correlations functions (CCFs) of sunlight scattered from the bright asteroid Vesta (I present a detailed analysis of these observations in Chapter 4). The CCFs obtained from each observation are first stacked on top of one another to obtain a time series of line profiles, as shown in panel (a); I then compute the mean line profile shown in panel (b); finally, I subtract this mean profile from each CCF of the time series, in order to reveal asymmetries in the line profiles, as shown in panel (c). These distortions are produced by sunspot groups drifting across the solar disc. Using this technique, we can deduce the latitude of the spot groups and therefore construct maps of the stellar surface. The Doppler imaging technique works best on (fast-rotating) stars with long-lived spot groups that will remain on the stellar disc for several rotations.

Sunspots have sizes ranging from 1,500 to 20,000 km, and even the largest spots will only cover a small fraction of the solar surface ($< 1\%$). The average sunspot coverage on the Sun is typically between 0.0001-0.1%, depending on the phase of the

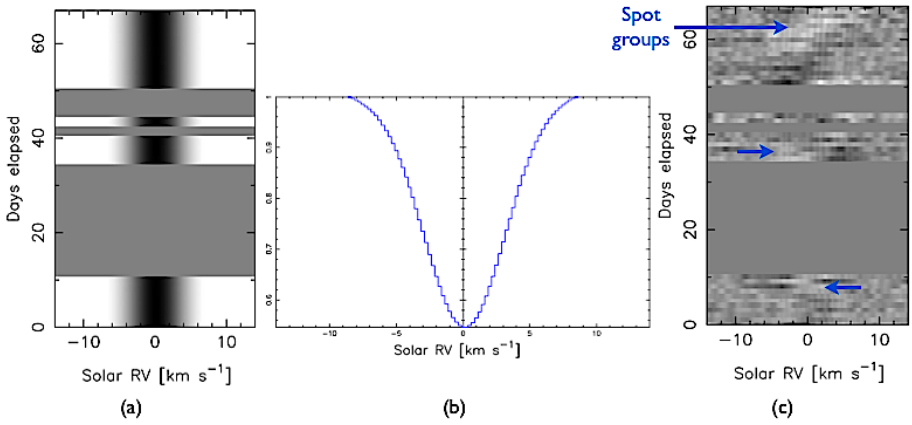

Figure 1.5: Doppler-imaging the Sun! in three simple steps: (a) make a time series of the CCFs; (b) compute the mean line profile; (c) subtract the mean line profile from the time series to reveal line-profile distortions caused by sunspots and groups of faculae trailing across the solar disc.

solar cycle (Strassmeier, 2009). It is trickier to determine the sizes of starspots are we cannot resolve their surfaces at high resolution. The amplitude of photometric variations depends on the size of a spot, or group of spots present at a given longitude, but it also depends on the contrast in brightness of the spot group, which itself depends on the temperature contrast. This is a complex issue, and many studies have been carried out to disentangle these two quantities using Doppler imaging (Catalano et al. (2002) and references therein). Doppler imaging uncovered starspots of all sizes ranging from 0.1% up to 22% of the stellar surface (Strassmeier, 2009). There have also been observations of huge polar spots on some stars (see Schrijver (2002), Strassmeier (2009) and references therein).

Sunspots as well as small starspots live from a few days up to several weeks (Schrijver, 2002; Allen, 1973; Hussain, 2002). In general, the lifetime of a spot is proportional to its size (Berdyugina, 2005); spots decay by diffusing out into the surrounding photosphere, so spots with a relatively larger area-to-perimeter ratio should take more time to disappear (Solanki, 2003; Petrovay & van Driel-Gesztelyi, 1997; Robinson & Boice, 1982). This has been confirmed observationally via *Kepler* data (see Helen Giles, MSci project at University of St Andrews, results to be published).

On the Sun, sunspots are always found between the latitudes of $\pm 35°$; they migrate closer to the equator as the solar cycle progresses (see Section 1.1.6). A similar behaviour is seen on other stars, although spots can also be found at much higher latitudes. Sunspots preferentially appear at so-called active longitudes, where increased magnetic activity in a localised region causes spots to manifest repeatedly in the same region (Berdyugina & Usoskin, 2003). Active longitudes have also been observed on other stars (Olah et al. (1989), Lanza et al. (2009) and others). They rotate in phase with the stellar rotation (modulo differential rotation), and could explain a persistent coherent starspot signal. Ivanov & Kharshiladze (2013) found that prominent solar active longitudes can survive for up to 20 solar rotations.

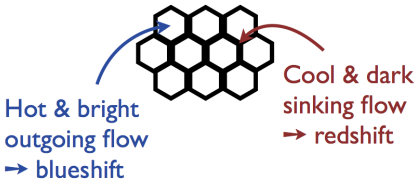

Figure 1.6: Schematic representation of convection cells on the stellar surface.

1.1.5.2 Faculae and plage

Faculae are small bright pores on the stellar photosphere and are associated with strong magnetic fields (Spruit, 1976). On the Sun, they are around 100 K hotter than the rest of the photosphere (Thomas & Weiss, 2008). They are found in the intergranular lanes, and surround spots – spots are always surrounded by faculae and plage. Faculae, however, can exist on their own and are grouped together into large networks. Because they are shaped as thin flux tubes with bright walls, they are best seen near the stellar limb. Faculae have lifetimes of a couple of hours (Hirayama, 1978), but groups of faculae can remain on the stellar surface for several weeks and will last for several stellar cycles. Faculae always appear before spots and will also outlive them. As we will see in Section 1.1.6, old and slowly-rotating Sun-like stars are dominated by faculae over starspots.

Plage regions are bright areas of the chromosphere made up of small bright points known as flocculi (see Zirin (1966) and references therein). Flocculi, or facular bright points (Soltau, 1993) are surrounded by thin and dark upward moving jets known as spicules (Roberts, 1945; Zirin, 1966). Similarly to faculae, flocculi (and spicules) have short lifetimes of 15 to 30 minutes and appear brighter close to the limb (although as we get too close to the edge they become obscured by the tall spicules).

Chromospheric plage regions map closely to faculae and spots in the underlying photosphere. Plages and faculae tend to be located near sunspots, although their relationship is not yet understood (Hall, 2008; Schrijver, 2002). Athay (1974)[3] provides further in-depth discussions on the nature of plage regions and possible relations between photospheric and chromospheric active regions (see Bumba & Ambroz (1974) in particular).

Emission lines such as Ca II H&K, Hα and the Ca II triplet lines form at the level of the chromosphere, and are good indicators of plage regions (Mallik, 1996; Cincunegui et al., 2007). Activity indicators based on the Ca II H&K lines are discussed further in Section 1.2.1.1.

The photometric effect of faculae is negligible as they are not significantly brighter than the quiet photosphere and they are evenly spread on the stellar disc; they do, however, induce a strong signature in spectroscopic observations. The strong magnetic fields present in faculae and spots act to inhibit the convection process taking place at the stellar surface. Let us think back on granulation, and take a closer look at its spatial structure. Granules can be approximated as bright hexagonal cells; they are surrounded by dark intergranular lanes, as illustrated in Figure 1.6. The

[3]Chromospheric fine structure: proceedings from IAU Symposium no. 56 held at Surfer's Paradise, Qld., Australia, 3-7 September 1973.

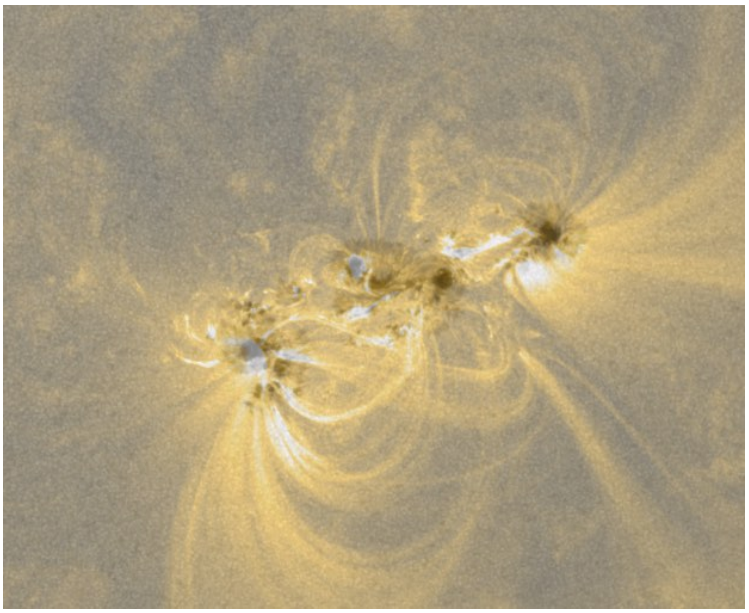

Figure 1.7: This image was created by combining a background SDO/HMI white light image, showing sunspots on the solar photosphere, and a transparent coronal wavelength SDO/AIA image, which reveals the magnetic field structure in the upper solar atmosphere. Credit: Fraser Watson.

material in the intergranular lanes is cooler and therefore more compact than the hot fluid of the granules, which means that over the whole stellar disc, we see a larger proportion of hot, uprising fluid over cool, sinking material (Gray, 1989). This results in a net blueshift, with a magnitude of about 200 m.s^{-1} on the Sun (see Meunier et al. (2010) and references therein). The presence of networks of faculae suppresses part of this blueshift[4]. As they evolve, active regions can lead to RV variations of up to 8-10 m.s^{-1} for the Sun (Meunier et al., 2010), as well as the active Sun-like star CoRoT-7 (Haywood et al. (2014), see Chapter 3). Suppression of convective blueshift is thought to play a dominant role in activity-induced RV variations on Sun-like stars, particularly in the case of faculae/plage, which are thought to cover a much larger fraction of the stellar surface than spots.

1.1.5.3 Other possible sources of surface velocity fields

As I have shown in this Chapter so far, the stellar photosphere and chromosphere are bustling with all kinds of constantly evolving and moving features such as granulation, spots, networks of faculae and plage regions. There are other phenomena that may induce RV variations, such as ~ 50 m.s^{-1} horizontal inflows towards active regions recently found on the Sun (Gizon, Duvall & Larsen (2001); Gizon, Birch & Spruit (2010)). Such photospheric velocity fields may affect the RV curve (particularly when located towards the limb, as they are horizontal flows) even if they have no detectable photometric signature.

[4]Starspots also act to suppress convection, but they contribute little flux and therefore do not play a significant role in this process (see Dumusque et al. (2014) and references therein.

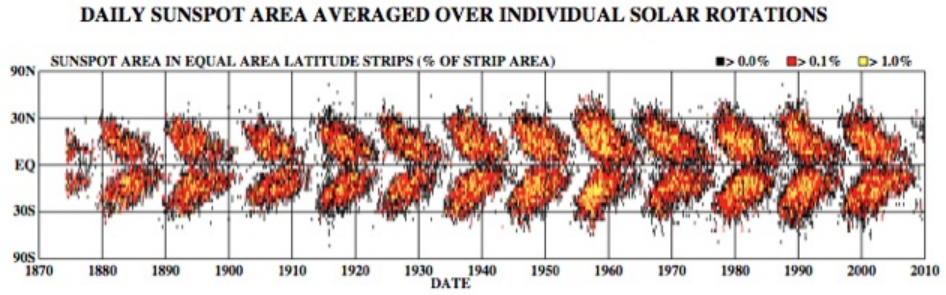

Figure 1.8: The butterfly diagram, showing sunspot area as a function of latitude and time. Image from Hathaway (2010).

1.1.6 Decades: magnetic cycles

The Sun has an activity cycle of 11 years (Schwabe, 1844; Hathaway, 2010). Progression into the cycle towards higher activity is observed as an increase in the number of sunspots, faculae, plages and is also accompanied by a more frequent occurence of violent events such as prominences and coronal mass ejections (see Hathaway (2010) for a detailed review). At minimum activity, sunspots are located at latitudes of 30-35°. As the cycle advances, they are found closer and closer to the equator. This results in a pattern known as the "butterfly diagram" (Maunder, 1904), shown in Figure 1.8.

In 1966, Dr Olin Wilson founded the HK Project, a survey of 1296 Sun-like stars within 50 pc of our Sun that was undertaken in an effort to characterise their activity levels and see whether other stars also displayed activity cycles similar to the Sun's (Wilson, 1968). Observations were made with the Coudé scanner attached to the 100-inch telescope at the Mount Wilson observatory. The fluxes in the Ca II H and K lines were measured, as it was already known for the Sun that the flux in these lines is correlated with the number of sunspots, i.e. an indicator of activity (Leighton (1959), Sheeley (1967) – see Section 1.2.1.1). Wilson (1978) presented results on 91 stars after the first 11 years of observations, showing the first evidence for cyclic stellar variability.

In 1977, an improved photoelectric spectrometer was built by Dr Arthur Vaughan and placed on the 60-inch telescope, also on Mount Wilson (Vaughan et al., 1978). The activity index S was developed by Vaughan et al. (1978) in order to quantify levels of activity; I will define it further in Section 1.2.1.1. Values of the S-index (or the $\log R'_{\rm HK}$, also see Section 1.2.1.1) for over a thousand stars were calculated and reported in Duncan et al. (1991), Baliunas et al. (1995), Henry et al. (1996), and Lockwood et al. (1997).

Baliunas et al. (1998) noticed that the majority of stars surveyed showed periodic variations with cycles of at least 7 years, and some lasting more than 30 years. A quarter of the stars displayed variability but with no apparent periodicity, while the remaining 15% seemed to show no activity at all. The survey ran until 2003, and to this date remains the most extensive survey on stellar activity and variability. A similar and complementary project at Lowell Observatory (Arizona, USA) with the Solar-Stellar Spectrograph was initiated in 1994 (Hall et al., 2007) to record activity in Sun-like stars, and has made more than 20,000 observations since.

In parallel, it was found that as Sun-like stars get older, they rotate more slowly and their magnetic activity levels decline (Wilson (1963), Kraft (1967), Skumanich (1972), Noyes et al. (1984)). This means that young stars tend to rotate faster and be more active, and old stars like the Sun rotate more slowly and have lower activity levels.

Further studies on the variability of Sun-like stars by Radick et al. (1998) and Lockwood et al. (2007), based on the Mount Wilson and Lowell stellar samples, revealed the existence of distinct types of variability patterns. In young stars, photometric variations tend to be anti-correlated with chromospheric variations ($\log R'_{\rm HK}$), which indicates that their surfaces are dominated by spots during phases of high activity levels. In the case of older, slowly-rotating stars such as the Sun, photometric variations are positively correlated with chromospheric variations. This means that their surfaces are dominated by faculae rather than spots. The dividing line between these two types of variability was found to be at $\log R'_{\rm HK} = -4.7$. The Sun, with $\log R'_{\rm HK} = -4.96$ lies just below this limit and its surface is thus faculae-dominated.

The long-term, continuous observations obtained over the last decades have given us an invaluable insight into the time-variant activity patterns of stars other than our Sun. We are still left to wonder, however, about the spatial evolution of stellar activity over these long timescales. For example, do starspots migrate accross the surface in the same way that sunspots do? Sanchis-Ojeda et al. (2011) and Sanchis-Ojeda & Winn (2011) showed that it is possible to deduce the latitude of starspots occulted by planetary transits. Llama et al. (2012) successfully recovered spot locations from transit occultations in the continuous, high-precision photometry provided by the *Kepler* satellite over its 3.5-year lifetime. They carried out simulations of magnetic cycles for a range of cycle durations and found that it is possible to track the migration of spots on active stars with short activity cycles; with a longer dataset, they would be able to characterise spot-belts on Sun-like stars. A couple of simulated "butterfly diagrams" with different activity levels are shown in Figure 1.9.

Stellar magnetic cycles can produce significant RV variations, in some cases of up to 25 m.s^{-1} (Lovis et al., 2011). So far, we have been searching mostly for short-period planets ($P < 50$ days). A few large RV programs with HARPS and HIRES have been running for 5-10 years (including Lovis et al. (2011); Marcy et al. (2014)). They are only just beginning to catch glimpses of magnetic cycles in RV observations. In their recent detection of an Earth-mass planet with a 3-day orbit around α Centauri B, from the analysis of over 3 years of data, Dumusque et al. (2012) found that the long-term activity-induced RV variations followed the variations in $\log R'_{\rm HK}$. They were therefore able to model the RV variations assuming a linear relationship with $\log R'_{\rm HK}$. This may not work as well if the planet's orbital period is comparable to the magnetic cycle, however, and as we begin to look for Jupiters and Saturns with orbital periods comparable to magnetic activity cycle durations, this will become a growing concern.

1.1.7 Timescales: summary

The surface of a star is constantly bustling with magnetic activity, which leads to a plethora of RV perturbations. On the shortest timescales (oscillations, granulation), we can average out most of the effects on RV by adapting our observing strategy. On

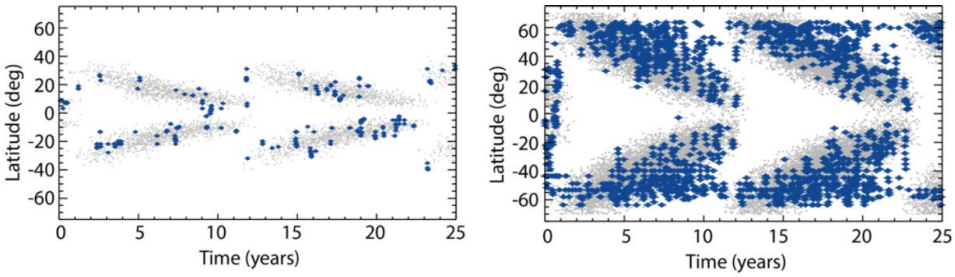

Figure 1.9: Simulated "butterfly diagrams" for stars with an 11-year activity cycle like the Sun, with low and high activity levels, respectively. The blue dots show spots that have been recovered through bumps in the transit lightcurve, while the small grey dots represent the input butterfly pattern, for reference. These plots were made by Dr Joe Llama, based on work from Llama et al. (2012).

timescales of the order of decades, assuming a linear relationship between long-term activity RV variations and $\log R'_{\rm HK}$ variations will work as a first approximation, although as we begin to look for long-period planets we are going to require more effective methods and proxies.

The most complex activity-induced RV variations, which cause the most trouble in today's RV exoplanet surveys arise from processes taking place on the stellar rotation timescale. Strongly magnetised photospheric features such as starspots and networks of faculae (as well as chromospheric plage regions) inhibit convective motions occuring just below the stellar surface, thus suppressing part of the blueshift naturally resulting from granulation. This effect can lead to variations in RV of up to 10 m.s^{-1} (Meunier et al., 2010; Haywood et al., 2014). In addition, starspots coming in and out of view as the star rotates induce an imbalance between the redshifted and blueshifted halves of the star which translates into an RV modulation of the order of 1 m.s^{-1} (Lagrange et al., 2011; Makarov et al., 2009). There may even be other processes at play which induce significant RV variations (Haywood et al., 2014), such as horizontal flows toward active regions (Gizon et al., 2001, 2010) or other unknown processes, whose impact on RV variations will require further investigation.

Identifying informative and reliable proxies for activity-driven RV variations has become crucial for exoplanet detection and characterisation. In the next Section, I outline the various proxies and activity decorrelation techniques that have been developed for RV planet searches so far.

1.2 Existing treatments for activity-induced RV variations

This Section provides a detailed summary of the analysis techniques developed to identify planetary signals in the presence of stellar activity. The methods of harmonic decomposition, pre-whitening and nightly offsets were initially developed to determine the mass of transiting super-Earth CoRoT-7b, so if you wish to place them in a more "historical" context, you can read the introduction on CoRoT-7 in Chapter 3, Section 3.1.1 in parallel.

1.2.1 Spectroscopic activity indicators

The following indicators, derived from the same stellar spectra used to measure the stellar RV, are affected by stellar activity only, so any variations present in RV observations but not seen in these indicators may point to a planetary signal.

1.2.1.1 Activity indicators based on Ca II H & K line fluxes

The S-index was first used by Vaughan et al. (1978). In his review on stellar chromospheric activity, Hall (2008) defines it as "a dimensionless ratio of the emission in the line cores [of Ca II H & K] to that in two nearby continuum bandpasses on either side of the H and K lines". The S-index can therefore be expressed as:

$$S = \alpha \frac{\Psi_H + \Psi_K}{\Psi_V + \Psi_R}, \tag{1.1}$$

where Ψ_H and Ψ_K refer to the fluxes in the cores of the H and K lines respectively, and Ψ_V and Ψ_R refer to the fluxes in the bands on the violet and red sides of the H and K lines. The term α is a normalisation factor. The amount of flux measured in the reference passes, however, depends on spectral type so the S index cannot be used to compare stars of different colours. The S-index also varies when applied to measurements taken with different instruments, since the level of transmission of the bandpasses depends intrinsically on the intrumentation used. Middelkoop (1982) was the first to apply a correction term to the S-index in order to overcome its color dependence.

The $R^{'}_{HK}$ index was introduced by Noyes et al. (1984) in an effort to propose an activity index independent on spectral type and intrument design. Hall (2008) defines it as "the fraction of a star's bolometric luminosity radiated as chromospheric H and K emission". This is expressed in mathematical terms as (Martínez-Arnáiz et al., 2010):

$$R^{'}_{HK} = \frac{\Psi^{'}_H + \Psi^{'}_K}{\sigma T^4_{\rm eff}}, \tag{1.2}$$

where σ denotes the Stefan-Boltzmann constant and $T_{\rm eff}$ is the effective temperature of the star. The primes on the fluxes Ψ are to show that the chromospheric contribution of the reference star has been subtracted. Note that there Ψ' values in this context are also in the form of fluxes measured at the stellar surface, rather than those received by the observer, to be consistent with the use of $\sigma T^4_{\rm eff}$. The $R^{'}_{HK}$ index is widely used, usually in logarithmic units.

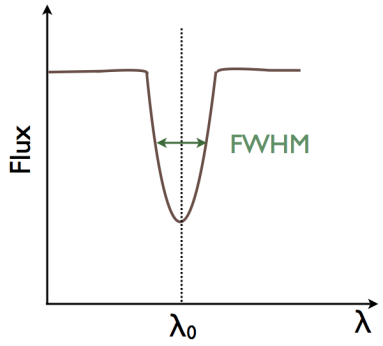

Figure 1.10: The full width at half-maximum of the cross-correlation function.

1.2.1.2 Indicators derived from the cross-correlation function

As I described in the previous Chapter, in order to measure the RV of a star all the lines of a spectrum are combined together to produce a mean line profile known as the cross-correlation function (CCF). Its shape reflects the shape of all the lines in the spectrum, which are affected by physical processes taking place in the stellar atmosphere, where these lines form. Here I present two measures of the shape of the CCF, that have been used in previous studies to identify activity-induced signals in RV data.

Full width at half-maximum (FWHM) The full width at half-maximum of the CCF, or FWHM is shown in Figure 1.10. The FWHM is determined by the stellar rotation rate, i.e. the $v \sin i$ of the star (Desort et al., 2007). Since younger, fast rotating stars tend to be more active, it ensues that the FWHM gives a general indication of the levels of magnetic activity of a star. The FWHM also incorporates the intrinsic width of the line due to thermal and turbulent motions in the stellar photosphere.

The FWHM changes as a spot of facular region crosses the stellar disc, in order to conserve the area enclosed by the line profile (see Figure 1.4). RV perturbations arising from the flux blocked by starspots on a rotating star are therefore correlated with variations in the FWHM. This indicator has been used by a number of studies, including Queloz et al. (2009), Hatzes et al. (2010) and Lanza et al. (2010) in the case of CoRoT-7 (see Chapter 3, Section 3.1.1) to identify activity-related signals.

Bisector of the cross-correlation function (BIS) A more sophisticated measure is the bisector of the CCF (see Figure 1.11). It is defined as a measure of the general asymmetry of the lines of a spectrum (Voigt, 1956), and was first used for exoplanet detection by Queloz et al. (2001a). A more rigorous definition of the bisector, given by Perryman (2011) is: "the locus of median points midway between equal intensities on either side of a spectral line, thereby dividing it into two halves of equal equivalent width". For a line profile with a perfect Gaussian shape, this would be a straight vertical line going through the middle of the line profile (dotted lines in Figure 1.11c). However, the net blueshift produced by granulation on the stellar surface (explained back in Section 1.1.5.2) results in a bisector curved towards the top (see Figure 1.11c). The granulation pattern is made of dark regions surrounding bright granules (panel (a); see Section 1.1.3). The bright upflowing granules produce the blueshifted line profile shown in yellow in panel (b), while the

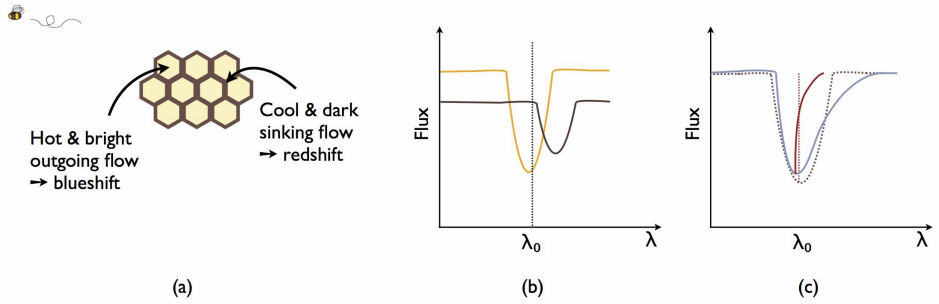

Figure 1.11: How the shape of the line bisector is affected by surface granulation. Panel (a): Schematic representation of granulation pattern. Panel (b): Line profiles resulting from light emitted by the bright granular regions (top, yellow line) and dark intergranular regions (bottom, brown line). Panel (c): Effective line profile (blue), with its "C"-shaped line bisector (red); the undisturbed profile and its bisector are drawn in dotted lines. This figure was inspired from a similar figure in Dravins et al. (1981).

dark sinking intergranular flow leads to the redshifted line with a lower intensity, shown in brown on panel (b). The total line profile is the sum of these two profiles, as pictured in blue in panel (c). It is asymmetric, and its bisector (full red line) is curved at the top. Active regions that reduce this net blueshift will thus produce small distortions in the bisector. Many quantities have been defined in relation to the bisector, such as the bisector velocity span (Toner & Gray, 1988), the curvature of the line bisector (Hatzes, 1996), and the bisector inverse slope (Queloz et al., 2001a); see Figueira et al. (2013) and references therein for more detail.

Desort et al. (2007) found that the FWHM, the BIS and photometric variations do not give enough information for slowly rotating, Sun-like stars (low $v \sin i$) to disentangle stellar activity signatures from the orbits of super-Earth-mass planets (see also Chapter 4, Section **??**).

1.2.2 Nightly offsets method

This technique is very effective for short-period planets observed 2 to 3 times each night. It was successfully applied to the CoRoT-7 and Kepler-78 systems (Hatzes et al. (2010, 2011); Pepe et al. (2013); see Chapter 3).

Activity-related signals change on relatively long timescales (of the order of $P_{\rm rot}$), whereas the planet's orbital period will be of a few hours (up to 1-2 days). In such a case, it is reasonable to assume that, on a given night, the rotation-modulated stellar activity contribution to the RV signal is roughly constant, and all the variations occuring over the span of a few hours are caused by the orbital reflex motion of the planet. This will work well for stars with low granulation "flicker" (see Section 1.3.2.3 which introduces the F8 statistic, a good measure of this noise source).

We can fit a linear function of the form:

$$m_i = A\cos(\omega t_i) + B\sin(\omega t_i) + C_j, \tag{1.3}$$

where A and B give the amplitude and phase of the RV signal, and there is an offset C_j for each night which represents the offset produced by the slowly varying activity modulation. The best-fit parameters can be determined via an optimal scaling procedure as follows. First, C_j is calculated for each night by taking the

variance-weighted average of the data y_i in each single night:

$$\hat{C}_j = \frac{\sum_{i=1}^{n_j} y_{ij}\, w_{ij}}{\sum_{i=1}^{n_j} w_{ij}}. \tag{1.4}$$

The subscript j refers to each night and goes from 1 to the total number of nights, whereas the subscript i refers to each individual data point in each night and goes up to the number of points in each night (n_j). w_i are the inverse variance weights defined as:

$$w_i = \frac{1}{\sigma_i^2}, \tag{1.5}$$

where σ_i is the error associated with the data y_i.

The constant parameters A and B are found by performing the following summations over the whole dataset:

$$\hat{A} = \frac{\sum_{ij} \left[\, y_{ij} - \hat{C}_j - \hat{B}\sin(\omega t_{ij}) \,\right] \cos(\omega t_{ij})\, w_{ij}}{\sum_{ij} \cos^2(\omega t_{ij})\, w_{ij}}, \tag{1.6}$$

and

$$\hat{B} = \frac{\sum_{ij} \left[\, y_{ij} - \hat{C}_j - \hat{A}\cos(\omega t_{ij}) \,\right] \sin(\omega t_{ij})\, w_{ij}}{\sum_{ij} \sin^2(\omega t_{ij})\, w_{ij}}. \tag{1.7}$$

An iteration is then carried out until A and B both converge. For further detail on iterative optimal scaling, the reader may refer to Collier Cameron et al. (2006) or Keith Horne's *Ways of Our Errors*[5].

1.2.3 Harmonic decomposition

As shown by Jeffers et al. (2009), any starspot configuration can be modelled by a series of harmonics of $P_{\rm rot}$ containing only the first three or four Fourier terms[6]. Subtracting this model from the data will help reveal signals that do not originate from the star's activity. Harmonic decomposition is based on three parameters: the stellar rotation period, the number of harmonics and the coherence time. The rotation period can be determined via Lomb-Scargle or autocorrelation techniques, which I describe later in Sections 1.3.2.1 and 1.3.2.2.

Harmonic decomposition can be implemented by fitting a Fourier series of the form:

$$m_i = m_0 + \sum_{k=1}^{l} \left[C_k \cos(k\,\omega t_i) + S_k \sin(k\,\omega t_i) \right], \tag{1.8}$$

where the number of desired harmonics is given by l and m_0 is a constant. The best fit can be determined via an iterative optimal scaling procedure akin to that presented in Section 1.2.2.

[5] Unpublished as of August 2015 but available online at: http://star-www.st-and.ac.uk/ kdh1/ada/woe/woe.pdf.

[6] As a side note, this also means that we cannot reconstruct a map of the stellar surface solely based on its photometric variations!

In this case, the inverse variance weights are given by:

$$w_i = \frac{\mathcal{G}(t - t_i)}{\sigma_i^2}, \tag{1.9}$$

where $\mathcal{G}$ is a Gaussian function defined as:

$$\mathcal{G}(t - t_i) = \exp\left[-\frac{1}{2}\Big(\frac{t - t_i}{\tau}\Big)^2 \right]. \tag{1.10}$$

τ is the coherence time. It governs the time interval over which each data point at time t_i retains its importance. τ is normally chosen to be slightly less than the rotation period of the star, so that it is short enough to filter out the slow varying signals (due to activity – starspots usually have lifetimes of about one rotation period or longer), but not so much that it will destroy short period signals.

This technique was applied to CoRoT-7 using the first three harmonics (Queloz et al., 2009; Hatzes et al., 2010), and up to the first six harmonics (Ferraz-Mello et al., 2011). It was found that the activity signal can be reproduced nearly perfectly using only the first three (Queloz et al., 2009), since for higher harmonics the amplitude of the signal becomes negligible.

1.2.4 Pre-whitening

A Fourier analysis is carried out to find the strongest period in the signal, and a sinusoidal fit with this period is subtracted from the data. We repeat this until the noise level is reached. This is a quick way to uncover the strongest periods present in the signal and to compose a periodogram. It is analogous to the CLEAN method derived by Högbom (1974) and Roberts et al. (1987). See also Queloz et al. (2009); Hatzes et al. (2010).

1.2.5 The *FF'* method

Aigrain et al. (2012) found that RV variations induced by starspots are well reproduced by a model consisting of the product of the photometric flux F and its first time derivative F'. It is assumed that the spots are small and limb-darkening is ignored. Spots influence the stellar RV by suppressing the photospheric surface brightness at the local rotational Doppler shift of the spot. Also, in areas of high magnetic field such as faculae, which on the Sun are often associated with spot groups, the convective flow is inhibited, leading to an attenuation of the convective blueshift (see Section 1.1.5.2). This effect is thought to be the dominant contribution to the total RV signal in the Sun (Meunier, Desort and Lagrange 2010).

As shown in Figure 1.12, the RV perturbation $\Delta RV_{\rm rot}$ to the star's RV incurred by the presence of spots on the rotating photosphere varies with both the flux deficit of the spot (F) and the line-of-sight velocity; F varies with foreshortening, so it has a cos phase, while the line-of-sight velocity varies with a sin phase (so it is proportional to F'). As derived in Aigrain et al. (2012), the RV perturbation due to a spot crossing the disc can be expressed as follows:

$$\Delta RV_{\rm rot}(t) = -\frac{\dot{\Psi}(t)}{\Psi_0}\left[1 - \frac{\Psi(t)}{\Psi_0}\right]\frac{R_\star}{f}, \tag{1.11}$$

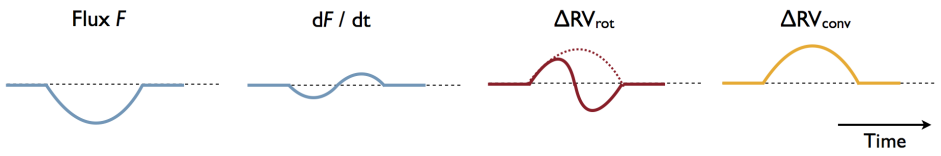

Figure 1.12: The *FF'* method for a spot crossing the stellar disc. The RV variations induced by flux blocking ($\Delta RV_{\rm rot}$) and suppression of the convective blueshift ($\Delta RV_{\rm conv}$) are proportional to $F\,{\rm d}F/{\rm d}t$ and F^2, respectively.

where $\Psi(t)$ is the observed stellar flux, Ψ_0 is the stellar flux for a non-spotted photosphere and $\dot{\Psi}(t)$ is the first time derivative of $\Psi(t)$. $R_\star$ is the stellar radius. The parameter f represents the drop in flux produced by a spot at the centre of the stellar disc, and can be approximated as:

$$f \approx \frac{\Psi_0 - \Phi_{\rm min}}{\Psi_0}, \tag{1.12}$$

where $\Phi_{\rm min}$ is the minimum observed flux, i.e. the stellar flux at maximum spot visibility.

The effect of the suppression of convective blueshift on the star's RV produced by starspots and magnetised areas surrounding them, written as $\Delta RV_{\rm conv}$, is shown in Figure 1.12. $\Delta RV_{\rm conv}$ varies with foreshortening and the angle between the convective velocity vector and the line of sight. Both vary with the flux, so $\Delta RV_{\rm conv}$ depends on F^2:

$$\Delta RV_{\rm conv}(t) = \left[1 - \frac{\Psi(t)}{\Psi_0}\right]^2 \frac{\delta V_{\rm c}\,\kappa}{f}, \tag{1.13}$$

where $\delta V_{\rm c}$ is the difference between the convective blueshift in the unspotted photosphere and that within the magnetised area, and κ is the ratio of this area to the spot surface (Aigrain et al., 2012). The two RV basis functions are pictured in Figure 1.12.

This method does not depend on the period of rotation of the star, nor does it rely on complicated spot models. Aigrain et al. (2012) report on tests on HD 189733 that show it successfully reproduces previous results based on more complex models (Lanza et al., 2011). They also tested it on 600 *Kepler* targets and obtained promising results, given that the *FF'* method is very easy and quick to implement and could thus be applied to large datasets.

The *FF'* method is likely to provide an incomplete representation of activity-induced RV variations, however (Haywood et al. (2014) – see Chapter 3, Section 3.1). The *FF'* method does not consider the broad-band photometric effect of faculae that are not physically associated with starspots; Aigrain et al. (2012) assume that their effect on $\Delta RV_{\rm rot}$ is quite small as they tend to have low photometric contrast. Indeed, according to Lockwood et al. (2007), faculae become less important (relative to spots) in stars more active than the Sun (see Section 1.1.6). Faculae do, however, have a significant impact on the suppression of convective blueshift (Meunier et al., 2010); indeed we find that this effect dominates the total RV contribution induced by stellar activity (see Section 3.1.5.7). There are other phenomena that the *FF'* method does not account for, such as ~ 50 ms^{-1} inflows towards active regions recently found on the Sun (Gizon et al. (2001, 2010) – see Section 1.1.5.3). Such

photospheric velocity fields may affect the RV curve even if they have no detectable photometric signature. In addition, some longitudinal spot distributions have almost no photometric signature, so the *FF'* method would not account for them.

1.2.6 Existing methods: summary

The planet masses determined via all these methods should all agree, though the RMS scatter in the residuals may differ depending on how good the assumptions are. This reflects the fact that planet mass determinations are intimately tied to the methods that we use to model activity-induced RV variations. It is therefore crucial that we design effective decorrelation techniques (see Chapter 3) and better proxies for activity signals (see Chapter 4). In the meantime, we can minimise the problem by selecting stars that are less likely to show activity-induced RV variations; this is the focus of the next Section of this Chapter.

1.3 RV target selection based on photometric variability

Since we do not yet know how to fully and reliably model all activity-induced RV variations, it is essential that we carefully pick stars for RV follow-up. Otherwise we may unknowingly choose a star with a rotation period that matches the orbital period of the planet, for example, and end up wasting huge amounts of telescope time for an imprecise, potentially even inaccurate planet mass determination.

Stars that have been observed by the high-precision photometry CoRoT and *Kepler* missions are ideally suited for potential RV follow-up, as we can learn a lot about their magnetic behaviour from their lightcurves.

The following question springs to mind: how do we define a magnetically "manageable" star for RV follow-up? This not only depends on the amplitude and frequency structure of activity variability; it is also tied with the mass and orbital period of the planet, and the decorrelation methods that we have developed to date.

For example, it is relatively easy to determine the mass of a super-Earth with a very short orbital period (typically less than 1 day), even if the host star is very active; the orbital and stellar rotation periods will be so different that we can take several observations per night and assume that all the variations produced within each night are solely due to the planet's orbital motion (see Section 1.2.2).

As a member of the Target Selection Tiger Team of the HARPS-N GTO collaboration, I was led to define magnetic manageability criteria to help us identify suitable *Kepler* candidates for HARPS-N RV follow-up (summer season of 2014).

1.3.1 Preliminary target selection criteria

Before subjecting *Kepler* candidates to activity-related triage, a preliminary selection (from a pool of 600 available targets) was done by other members of the HARPS-N team. It includes the following criteria:

1. Target brightness: the majority of *Kepler* stars are too faint for ground-based RV follow up. This criterion was embedded in an estimation of the RV precision that would be achieved with the HARPS-N instrument. In this particular aspect, HARPS-N is a twin of HARPS, so we can use a relatively simple formula determined by Bonfils et al. (2013). As a rule of thumb, stars should have a magnitude less than $V \approx 13$ mag.

2. Time required for a (3- or) 6-sigma detection: this can be calculated from the expected RV semi-amplitude of the planet candidate, which can itself be derived by assuming a bulk density (either a fixed value eg. $\rho = 3$ g.cm^{-3}, or a radius-dependent value determined from mass-radius relations such as those derived by Weiss & Marcy (2014)).

3. Number of planet candidates in the system; scientific interest related to each individual candidate (what is the scientific goal of this study: are we trying to populate the mass-radius diagram at a given radius/mass range? Are we trying to find other rocky mini-Neptunes like Kepler-10c?).

4. Observability: depending on how many months/years our survey is likely to last, determine the longest orbital periods it is reasonable to consider.

5. Asteroseismology information: this should be available if the target has been observed at short-cadence by *Kepler* or CoRoT. It will provide robust stellar parameters, which are essential to obtain a precise planet mass determination.

6. Previous follow-up: check the literature to see if this system has already been followed-up, and if this is the case, to assess whether additional RV measurements would be useful (eg., to determine the mass to a better precision, or to look for additional companions).

1.3.2 Generalised Lomb-Scargle periodograms & autocorrelation functions

118 *Kepler* candidates survived these cuts. In order to identify activity selection criteria for these candidates, I computed Lomb-Scargle periodograms and autocorrelation functions (Lomb, 1976; Scargle, 1982; Edelson & Krolik, 1988; Zechmeister & Kürster, 2009) for the *Kepler* lightcurves of each star. I concatenated the lightcurves all the quarters together by dividing by the inverse variance weighted mean flux level for each quarter. This procedure is approximate but works well, as confirmed by visual inspection of a few lightcurves (see Figure 1.13).

In the next two Sections, I outline the concepts and main equations of the Lomb-Scargle periodogram and autocorrelation techniques.

1.3.2.1 Generalised Lomb-Scargle periodogram

A natural first step as a planet hunter is to make a periodogram of the data, to get a first feel for what is in it. Most activity-induced signals will show some quasi-periodicity with a recurrence timescale related to the stellar rotation period, $P_{\rm rot}$ and/or its harmonics. The rotation of the star modulates both the lightcurve and RV curve.

The following method is based on the techniques proposed by Lomb (1976), Scargle (1982) and Zechmeister & Kürster (2009). We can fit a sinusoid to our dataset:

$$m_i = A\cos(\omega t_i) + B\sin(\omega t_i) + C, \tag{1.14}$$

where A and B are the amplitudes of the signal, C is an offset from zero, m_i is the fit to the photometric or RV data y_i at time t_i and $\omega = \frac{2\pi}{P_{\rm rot}}$ is the angular frequency associated with $P_{\rm rot}$.

The parameters A, B and C are calculated using iterative optimal scaling (also known as weighted least squares):

$$\hat{A} = \frac{\sum_i \left[\, y_i - \hat{C} - \hat{B}\sin(\omega t_i) \,\right]\cos(\omega t_i)\, w_i}{\sum_i \cos^2(\omega t_i)\, w_i}, \tag{1.15}$$

$$\hat{B} = \frac{\sum_i \left[\, y_i - \hat{C} - \hat{A}\cos(\omega t_i) \,\right]\sin(\omega t_i)\, w_i}{\sum_i \sin^2(\omega t_i)\, w_i}, \tag{1.16}$$

and

$$\hat{C} = \frac{\sum_i \left[y_i - \hat{B}\sin(\omega t_i) - \hat{A}\cos(\omega t_i) \right] w_i}{\sum_i w_i}. \tag{1.17}$$

The inverse-variance weights, w_i are defined in Equation 1.5. The three parameters are summed over all data. The operation is repeated until a convergence threshold is met, for example when the change in each parameter is less than a given fraction of their associated uncertainty.

The right frequency is found by optimising the chi square (χ^2) on a grid of frequencies. The χ^2 is defined as:

$$\chi^2 = \sum_i \left[(y_i - m_i)^2 \, w_i \right]. \tag{1.18}$$

The range of frequencies to be searched starts at the sidelobe frequency ($d\omega$) up to the Nyquist frequency ($\omega_{\rm nyq}$) at intervals given by the sidelobe frequency of the dataset. These two quantities are given by:

$$d\omega = \frac{2\pi}{t_{\rm tot}} \tag{1.19}$$

and

$$\omega_{\rm nyq} = \frac{n\pi}{t_{\rm tot}}, \tag{1.20}$$

where n is the number of points in the dataset, and $t_{\rm tot}$ is the total span of the observations. Care should be taken to have both frequencies in the same units (rad.s^{-1} or deg.sec^{-1}).

Zechmeister & Kürster (2009) provide slightly different equations that are very easy to implement and quick to compute. We can also calculate false alarm probability levels for each signal. They are are a measure of how likely it is for a signal with a given power to be caused purely by noise. Refer to Cumming (2004) and Collier Cameron et al. (2009) for a recipe on how to implement them.

1.3.2.2 Autocorrelation function

Another way to determine the stellar rotation period is to compute the autocorrelation function of the data (Edelson & Krolik, 1988). This technique provides us with much more than just the period of the main signals in the data; an autocorrelation function is a star's activity identity card. The autocorrelation function conveys the same information as the Lomb-Scargle periodogram: with one glance at it we can tell the rotation period, whether the star has spots, how long they live for, how fast they decay, if there are many active regions, etc. The concept is the following: we take two copies of our dataset and shift them against each other by a small time interval τ at each step. The discrete autocorrelation of a dataset y (observation times t, uncertainties σ) is equal to (Edelson & Krolik, 1988):

$$k_{i,j} = \frac{(y_i - \hat{y})\,(y_j - \hat{y})}{\sqrt{\sigma_i^2 \, \sigma_j^2}}, \tag{1.21}$$

where $\hat{y}$ is the inverse-variance weighted average of the dataset, defined as:

$$\hat{y} = \frac{\sum_{i=1}^{n} y_i/\sigma_i^2}{\sum_{i=1}^{n} 1/\sigma_i^2}. \tag{1.22}$$

The autocorrelation function can be normalised to 1 by dividing by its maximum. Each pair of points i, j is associated with the time lag:

$$\Delta t_{i,j} = t_j - t_i. \tag{1.23}$$

For best results, the coherence length τ should be at least a few times longer than the spacing of the data, so that the autocorrelation looks smooth, but short-period signals longer than τ are still resolved.

For faster computation, only the positive (or negative) side of the autocorrelation function can be calculated and then simply mirrored onto the opposite side for plotting. The main recurrence timescale (in our case, the stellar rotation period) is the time lag of the centre of the first sidelobe of the autocorrelation function. A parabola can be fitted to this sidelobe in order to determine a more precise value, for example via iterative optimal scaling[7].

1.3.2.3 Application to *Kepler* lightcurves

Although I did implement my own versions of these techniques, for this target selection work I used Andrew Collier Cameron's code for discrete correlation functions & periodograms (dcfpgm.f), which I adapted for my own purposes. Figure 1.13 shows lightcurves, Lomb-Scargle periodograms and autocorrelation functions for three example stars, with a short description of what we can learn about the behaviour of each star based on this information. In addition, I retrieved the following information:

- Two measures of the stellar rotation period – taken to be the strongest periodic signal identified in the Lomb-Scargle periodogram, and the time lag between the two main peaks of the autocorrelation function.
- The root mean scatter (RMS) of the *Kepler* lightcurves, obtained after removing points lying more than 5-sigma beyond average in order to remove any transits.
- The mean photometric error, $\sigma_{\rm av}$, defined as the mean relative error in the *Kepler* photometry.
- The ratio between the amplitude of the main peak of the autocorrelation function (at zero time-lag) and the next highest peak: it tells us about the lifespans of active regions on the stellar surface.
- The F_8 statistic defined by Bastien et al. (2013), in units of parts per thousand (ppt). It corresponds to the RMS of the lightcurve over an 8-hour timescale.

[7] See Advanced Data Analysis course by Keith Horne online at http://star-www.st-and.ac.uk/ kdh1/ada/ada.html (link valid as of March 2015). The method of optimal scaling is explained in his notes from Lecture 5. His draft textbook *"The Ways of Our Errors"* is a gold mine to the astronomer looking for optimal data analysis methods.

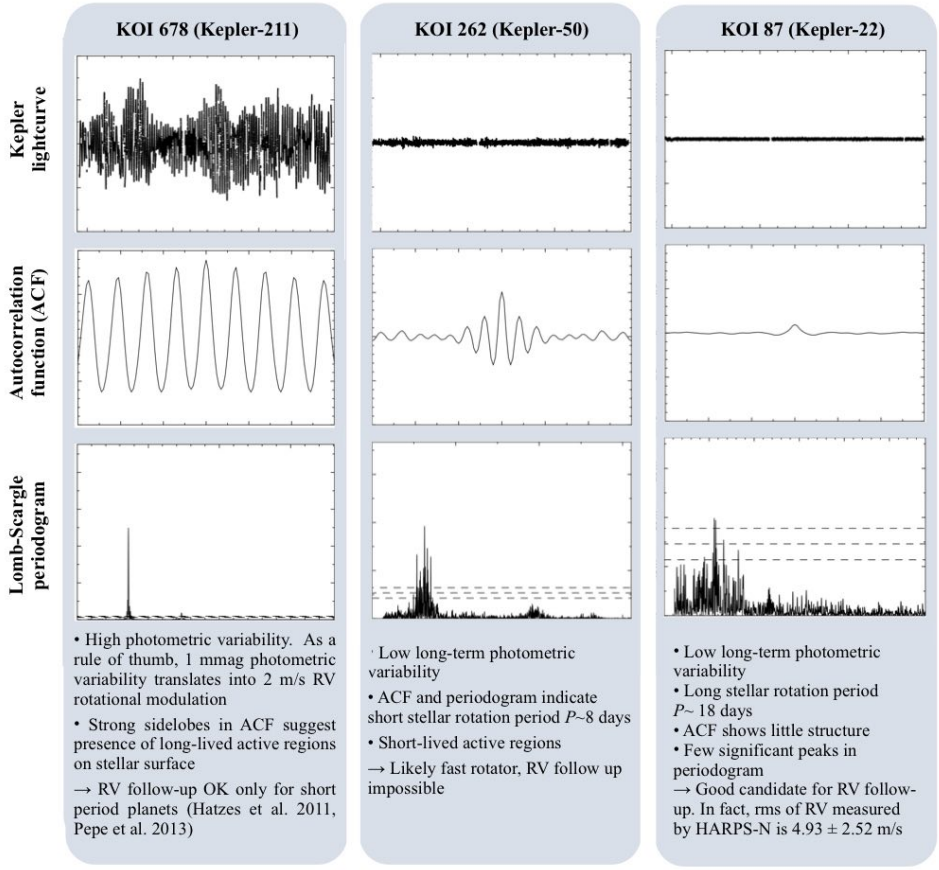

Figure 1.13: Revealing the temporal behaviour of *Kepler* main sequence stars, through autocorrelation (time lag vs. power) and Lomb-Scargle periodogram (frequency vs. power) analyses of high-precision *Kepler* photometry, spanning all quarters of data. Note that all three lightcurve plots are on the same scale, ranging from -3 to +3 mmag. The plots were made using Andrew Collier Cameron's *dcfpgm.f* code.

It is computed by taking the RMS scatter in the photometry residuals after applying a boxcar filter of width 8 hours. This scatter is caused by granulation and is known as the "8-hour flicker". Faint stars will naturally display more variability in F_8, which we correct for by applying the relation used by Bastien et al. (2013), based on the *Kepler* magnitude $V_{\rm kepler}$ of the star (available in the *Kepler* input catalogue):

$$\log_{10} F_8 = -0.03910 - 0.67187 V_{\rm kepler} + 0.06839 V_{\rm kepler}^2 - 0.001755 V_{\rm kepler}^3 \tag{1.24}$$

- log g: I deduced this value from the F_8 statistic, using the relationship established by Bastien et al. (2013):

$$\log_{10} g = 1.15136 - 3.59637 \log_{10}(F_8) - 1.40002 \log_{10}(F_8)^2 - 0.22993 \log_{10}(F_8)^3 \tag{1.25}$$

It is useful to check the value of the log g as it gives an indication of whether the star is on the main sequence or if it is a giant or sub-giant star. Giants

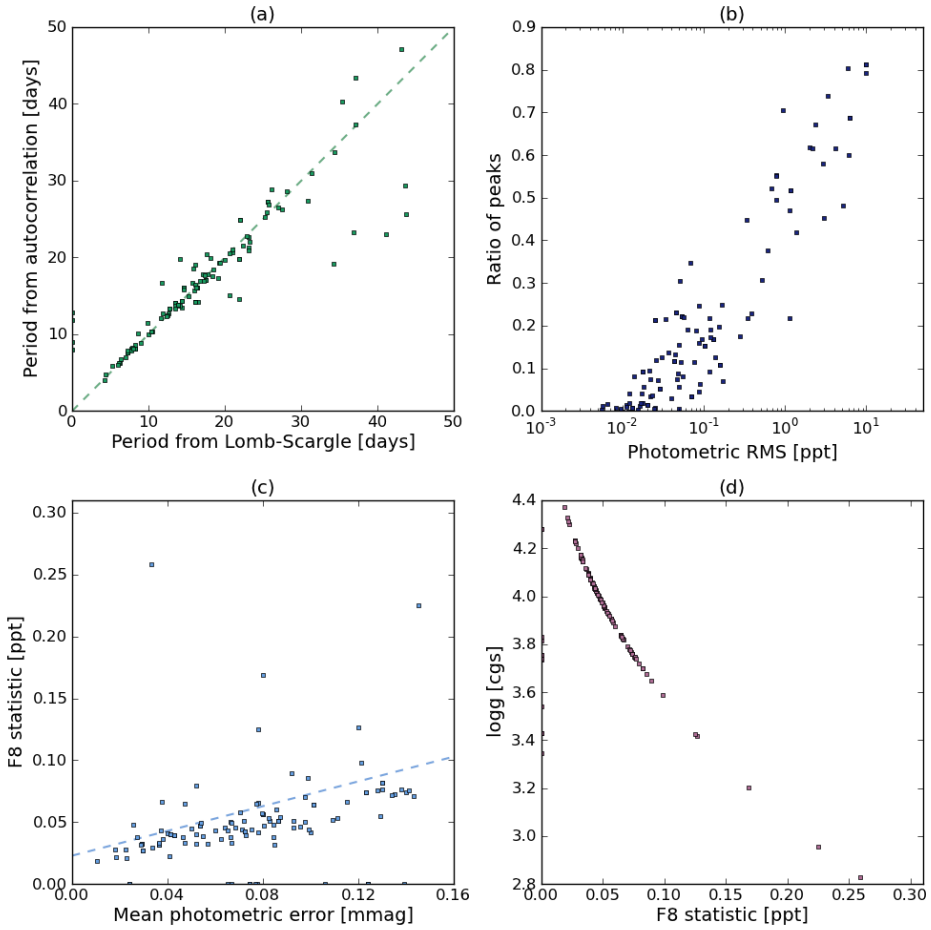

Figure 1.14: Photometric variability characteristics of our stars as a sample. Panel (a): periods obtained through both methods plotted against one another; panel (b): Main-peak-to-first-sidelobe of autocorrelation function ratio, as a function of photometric RMS; panel (c): F_8 statistic plotted vs. mean photometric error, $\sigma_{\rm av}$; panel (d): log g values derived from the F_8 statistic. (The stars with zero Lomb-Scargle period or zero F_8 statistic are errors arising from the code, and further investigation would be required to solve this.)

and sub-giants have lower surface gravity, bigger atmospheric scale heights, and hence fewer granules. The uncertainty in the number of granules on the stellar surface at any time is proportional to the square root of the number of granules (see Section 1.1.3), so the fractional uncertainty, and hence the noise (quantified in the F_8 statistic), goes up when there are fewer granules (Lindegren & Dravins, 2003).

The plots in Figure 1.14 illustrate the general behaviour of all 118 stars as a sample.

Stellar rotation periods The rotation periods obtained via both methods are plotted against each other in panel (a) of Figure 1.14. They are in good agreement overall. In a few cases, especially at long periods, the period identified via Lomb-Scargle is twice as long as that of the autocorrelation. Period halving is a common problem at times when there are active regions on opposing hemispheres of the star. In such cases the autocorrelation sidelobes often alternate in amplitude, making

it easier to identify the true period. I decided to use the stellar rotation period obtained from the autocorrelation method.

Care should be taken, however, mainly for two reasons:

- The majority of the stars in our sample show very little photometric variations; many stars display photometric RMS of order 0.1 or even 0.01 parts per thousand (ppt), as seen in panel (b) in Figure 1.14. This means that it can be difficult to measure the rotation period reliably, even through the autocorrelation method which will exhibit weak sidelobe amplitudes.
- The lightcurves were reduced with *Kepler*'s PDC-MAP pipepline (Stumpe et al., 2012), which is a decorrelation method designed to remove patterns of instrumental origin that are common to all stars in a given field of view of the *Kepler* CCD. It should not suppress signals of astrophysical origin, particularly variations due to the star's rotation and activity on short timescales. However, the *Kepler* Data Release 21 Notes caution that the PDC-MAP lightcurves should not be used to look for periodic signals longer than 20 days, as the pipeline erases long-term trends. On the other hand, McQuillan et al. (2014) and others have shown that it is possible to obtain reliable stellar rotational periods for a large number of *Kepler* stars.

Active region lifetimes The plot in panel (b) of Figure 1.14 shows that there is a correlation between the amplitude of the star's photometric variations (RMS of the lightcurve) and the lifespan of active regions, which indicates that large active regions live longer. Starspots are thought to decay through diffusion, which takes place around the edge of the spots: larger spots, which have a smaller perimeter-to-area ratio will thus take longer to diffuse away (see references in Section 1.1.5.1).

1.3.3 Selection criteria for "magnetically manageable" stars

I settled on the following selection criteria:

1. Eliminate stars with a rotation period of less than 10 days, as we do not want to do RV follow-up on fast rotators (the cross-correlation profile would be very broad and yield a poorly-constrained RV measurement).
2. Require the RMS of the lightcurve to be less than 0.001 mag. This seemed like a reasonable threshold beyond which the star is showing a lot of modulation from starspots coming in and out of view.
3. In order to eliminate stars with anomalously high levels of granulation noise, I require:
$$\frac{(F_8 - 0.023)}{1000\sigma_{\rm av}} < 0.5. \tag{1.26}$$
The value 0.023 mag corresponds to the flicker "floor" seen in panel (c) of Figure 1.14; an F_8 value below this limit indicates that the star is faint enough for the photon noise to dominate photometric variations induced by granulation. A high F_8 value makes it harder to average out the RV variations caused by granulation, even if we make a couple of observations separated by two hours. Indeed, most *Kepler* targets are so faint that we need to make 1800-second (30 minutes) exposures, and we therefore cannot really afford to take two per

night.

4. Rotational and orbital timescales: it is more difficult to disentangle the orbit of a planet if its orbital period is close to the stellar rotation $P_{\rm rot}$ or its first harmonics. I discarded cases where the orbital period is within 2 days of $P_{\rm rot}$, $P_{\rm rot}/2$, and $P_{\rm rot}/3$. I chose an interval of 2 days to be on the safe side since the stellar periods may not be very accurate.

5. It is also a problem if the orbital and stellar rotation timescales are too similar. I discarded cases where the rotation period was less than twice the orbital period.

6. However, if the timescales are *very* dissimilar, we can consider more active stars, i.e. a larger RMS. For these systems we can apply the nightly offset method detailed in Section 1.2.2. I therefore included targets for which the stellar rotational period is at least 10 times longer than the planet's orbital period, even if the photometric RMS was greater than 0.001 mag.

7. Distinguishing main sequence stars from giants: I require all viable candidates to have a log g greater than 3.5. This cutoff value is somewhat arbitrary, and it would be interesting to delve further into this to refine this criterion. The F_8 and log g are shown plotted against each other in panel (d) of Figure 1.14.

1.4 Concluding note: from photometric to radial-velocity variations

The next step would be to combine some of these indicators to predict the amplitude of activity-induced RV variations we might expect. The *FF'* method of Aigrain et al. (2012) (explained in Section 1.2.5) gives a recipe for doing exactly this. It does not fully account for the effect of faculae on the suppression of convective blueshift, or effects that have no photometric signature, however, so it is likely to largely underestimate the amplitude of activity-induced RV variations (see my work on CoRoT-7 in Chapter 3 and Haywood et al. (2014)).

Based on RV data for CoRoT-7, Kepler-10 and Kepler-78 (see Chapter 3), as well as the findings of Aigrain et al. (2012), we can infer a simple rule of thumb: 1 mmag of photometric RMS results in 2 m.s^{-1} of activity-induced RV variations. Of course, the amplitudes are not the whole story; Bastien et al. (2014) found that the Fourier components of the lightcurve provide important clues about the complexity of the activity-induced RV variations. In this perspective, decoding the temporal structure of a star's lightcurve is a natural step towards understanding stellar RV variability.

The frequency structure of stellar signals reflects the character and personality of a star. We can use it to build a model for activity-induced RV variations, as I will show in the next Chapter.

2

A toolkit to detect planets around active stars*

In this Chapter, I present a recipe to detect exoplanet orbits in RV observations in the presence of noise arising from stellar activity. I start by introducing Gaussian processes, which are a powerful and elegant way to model correlated noise. I will start from the very basics of Gaussian distributions, leading up to how I incorporate them in my model to account for stellar activity signals. I then present the model that I use to fit RV observations, and describe the Monte Carlo Markov Chain procedure that I apply to determine the best-fitting parameters of this model. Finally, I present the Bayesian model selection technique of Chib & Jeliazkov (2001) that I have implemented to estimate the most likely number of planets present in the system and therefore choose the most appropriate model.

*This Chapter uses material from, and is based on, Haywood et al., 2014, MNRAS, 443, 2517.

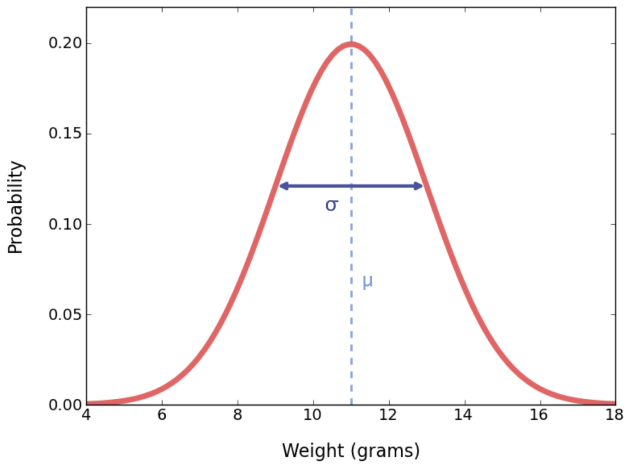

Figure 2.1: 1-dimensional Gaussian distribution, with mean μ and standard deviation σ.

2.1 Gaussian Processes

The first Sections (up to Section 2.1.1.5) of this introduction to Gaussian processes are based on a lecture given by Prof. David MacKay, from the Engineering Department at the University of Cambridge[2]. I am very thankful to him as it was only by watching his video that I finally understood what Gaussian processes really are! I thoroughly recommend watching it.

2.1.1 Definition

In statistical terms, a Gaussian process (GP) is defined as an n-dimensional random process, such that the joint probability distribution drawn from this process is a Gaussian distribution in n dimensions (Rasmussen & Williams, 2006). Let us first look at a 1-dimensional Gaussian distribution.

2.1.1.1 1-dimensional Gaussian distribution

Any random process can be described by a probability distribution function. In the natural world, many processes follow a probability distribution function that is well described by a Gaussian "bell" shape (shown in Figure 2.1). Imagine that we are on a field trip to measure the weights of blue tit birds. Before we catch a bird, we won't know exactly how much it weighs, but we can still take a pretty good guess because we know that the average weight of a tit is about 11 grams and that most blue tits weigh between 9 and 13 grams. Mathematically, we can write the probability P of measuring the blue tit's weight, y, as:

$$P(y) = \frac{1}{\sigma\sqrt{2\pi}} \exp^{-\frac{1}{2}\left(\frac{y-\mu}{\sigma}\right)^2}. \tag{2.1}$$

This is a Gaussian distribution centered at μ (=11 grams), with a standard deviation σ (= 2 grams). Since we have not weighed the blue tit yet, this is a *prior* distribution.

[2]This lecture is posted online at http://videolectures.net/gpip06_mackay_gpb/ (link correct as of March 2015).

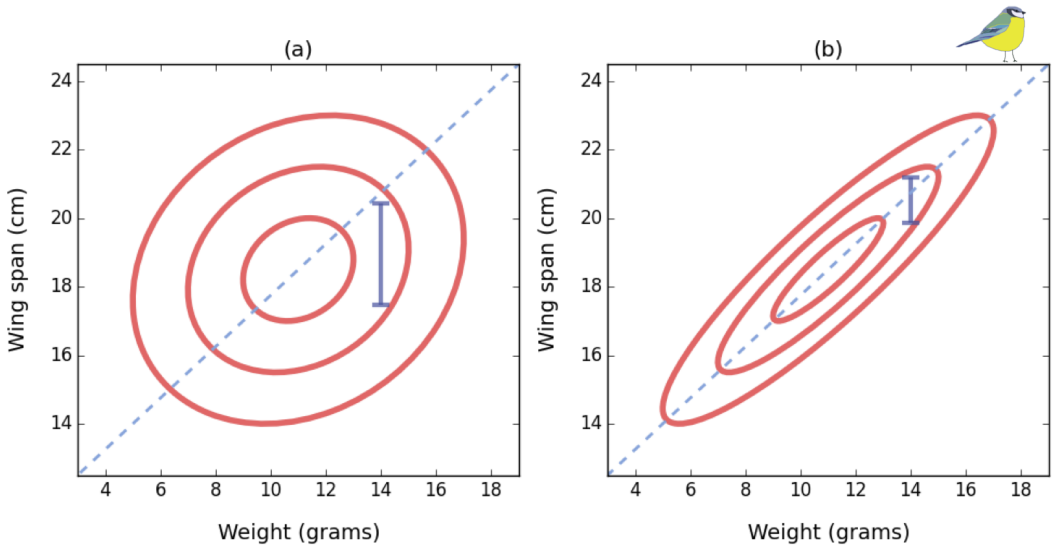

Figure 2.2: 2-dimensional Gaussian distributions, for two weakly (panel a) and strongly (panel b) correlated variables, with 1, 2 and 3-σ contours drawn in red (Note: the error bars are not drawn to scale with respect to the bivariate distributions.)

μ is the weight we are *most likely* to measure. Weighing birds, i.e. collecting data, will transform our prior beliefs into a posterior distribution.

2.1.1.2 2-dimensional Gaussian distribution

Let's now imagine that we are also measuring the wing span of our blue tits. We expect it to be between 17 and 20 cm and to follow a bell-shaped distribution. We are now considering two variables, y_1 (weight) and y_2 (wing span). These two characteristics are intimately linked to each other, as bigger blue tits will weigh more and have a larger wing span: y_1 and y_2 are correlated with each other. This means that if we know the value of one, we will be able to take a better guess at the value of the other. Statistically, their probability distributions are joint together and form a 2-dimensional Gaussian distribution (which you can imagine as a hat shape). We can picture it as in Figure 2.2.

The shape of the contours depends on how correlated the two variables are with each other; for example, they are weakly correlated in Figure 2.2 (a), while they are strongly correlated in Figure 2.2 (b). The quantitative relationship between these two variables (eg. $y_2 = 2y_1$ or $y_2 = y_1 + 5$) is not (yet) relevant. We shall leave this information encoded in a matrix $\mathbf{K}$, which we treat as a "black box" for the time being.

In addition to wondering how precisely we can guess the wing span of a blue tit before we catch it, we can now ask: how much more precise will our guess of the wing span be after we have weighed it? Before we weigh the blue tit and thus measure y_1, the wing span y_2 will have a wide range of probable values. After we have measured y_1, the likely possibilities for y_2 narrow down to the range shown by the blue error bars in Figure 2.2. If we now wish to predict y_2, knowing y_1, the values of y_2 will follow a Gaussian distribution centered at point μ_2. Note that if we had measured y_1 to be any other value, the most likely value of y_2, that is μ_2,

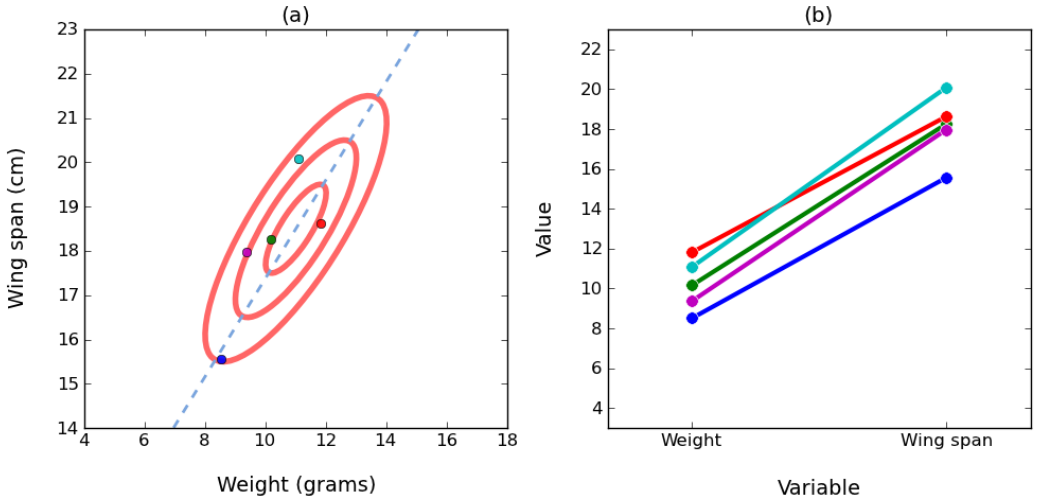

Figure 2.3: The same 2-dimensional Gaussian distribution, displayed in the traditional (panel a) and new (panel b) representation.

would always fall on the straight line drawn on the plot. In other words, μ_2 is a linear function of y_1[3].

As can be seen in Figure 2.2 (b), in which the correlation between the two variables is stronger, the standard deviation of the distribution of y_2 after we have measured y_1 (which is now a *posterior* distribution) is much smaller than in the case of a weak correlation between the two parameters.

2.1.1.3 New representation

In addition to the weight and wing span, we could measure as many features of our blue tits as we like, but plotting the joint distribution between more than 2 variables as in Figure 2.2 would become tedious. Figure 2.3 illustrates how we can represent the same 2-dimensional Gaussian distribution of Figure 2.2 in a different, simplified view. Imagine that we have now caught five birds (in statistical terms, we have drawn 5 samples from the joint prior distribution of the two variables "wing span" and "weight"). In the traditional view shown in panel (a), the set of measurements for each bird is marked with a dot; in the new representation in panel (b), it is represented by a line. In this new visualisation, the distributions of each variable y_1 and y_2 can be imagined standing vertically out of the page, centered at points μ_1 and μ_2.

2.1.1.4 n-dimensional Gaussian distribution

In this new representation, picturing a Gaussian distribution with more than two dimensions becomes possible. An example of a joint 6-dimensional distribution is shown in Figure 2.4. In panel (a), we draw several samples from the prior distribution; each of the coloured lines represents one sample, and tells us the value of each of the 6 variables. If we measure the value of one variable, such as in panel (b), this narrows the posterior distribution of the other variables, and so on. This

[3]Remember this for later; it provides insight on the form of Equation 2.16.

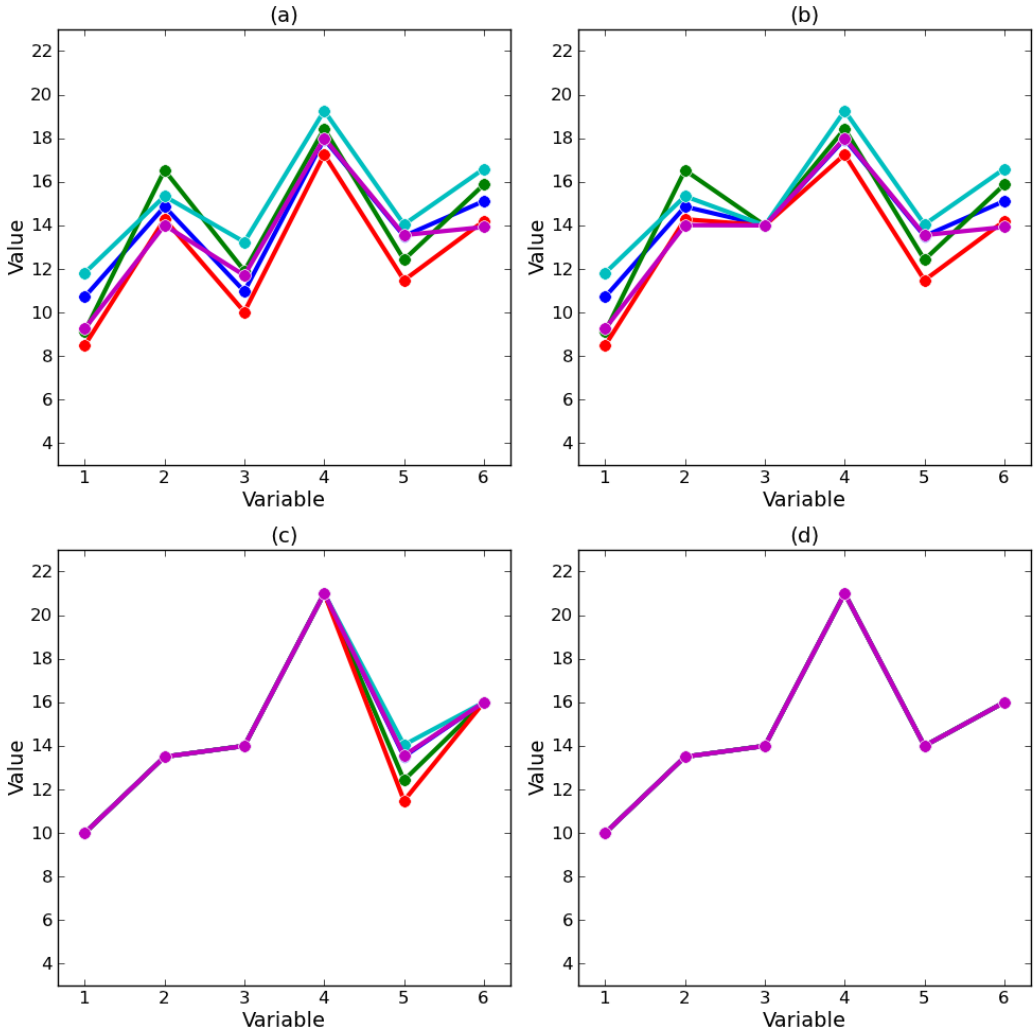

Figure 2.4: A 6-dimensional Gaussian distribution. (a) we draw 5 samples from the *prior* distribution – no measurements have been made yet; (b) we measure variable 3; (c) we measure all the variables except variable 5; (d) all the variables have been measured.

only happens because the variables are all correlated with each other, and therefore depend on each other.

Each time we measure one of the variables of the process we are considering, we are making a cut through the n dimensional probability distribution space: this cut therefore has $n-1$ dimensions. This is analogous to taking a cut through a 3-dimensional sphere, and obtaining a 2-dimensional disc. If we measure all the values of all the variables but one, we are left with a 1-dimensional Gaussian distribution which tells us about the behaviour of this last, unknown variable (panel (c)).

The nature of the correlation between y_i and y_j determines how little or how much the posterior distribution of y_j changes once we have measured y_i, and vice versa. Also, this correlation doesn't have to be the same between two other variables, say y_i and y_k. The correlation between each pair of variables of the process plays a key role in determining the process.

2.1.1.5 A Gaussian process

Let's go back to Figure 2.4, and use our imagination once more. If we just changed the labels on the axes, say the horizontal axis became "time", and the vertical axis became "flux", or "radial velocity" – the line in the plot suddenly looks like a fit to a set of observations! Yes, we can use a multi-dimensional Gaussian distribution to fit a dataset.

A Gaussian process is a non-parametric approach to fitting data. It is a Bayesian method. In the frequentist statistics approach, we start with a theory that we take for granted and we ask ourselves: *what is the probability that we will measure a given value?* We decide on the form of the model before we even start considering our observations, by specifying a parametric model, for example a sine function. Of course, such a model can, to some extent, be tailored to fit the observations; in the case of a sine function, we can determine the period, phase and amplitude that will provide the most optimal fit. The final model, however, will always be a sine curve and this may be a limitation in itself.

In the Bayesian world, we start with a dataset and use it to test our theory: *what is the likelihood that this model is correct?* Our model is non-parametric, which means that we do not impose the form of the model before we consider the observations; instead, we let the observations themselves determine the shape of the model. The only prior assumption that we make is about the way in which the data are correlated. We are making fewer prior assumptions and this gives us more freedom than having a model with a pre-determined shape.

We shall now ask: how do we define the correlations between points of a physical process? This is where the entity $\mathbf{K}$, which I briefly mentioned back in the 2-dimensional case, comes into play!

2.1.2 Covariance matrix K

For a dataset with n observations, $\mathbf{K}$ is an $n \times n$ matrix, which we refer to as the *covariance matrix*. Each element $\mathbf{K}_{i,j}$ gives the covariance between two dimensions y_i and y_j: this is a measure of how much these two variables change together.

There are two options possible:

- The two variables are independent; if one changes, the other one does not. They are not correlated with each other. This is known as "white" noise.
- The two variables are dependent on each other; changing one will affect the other, because there is a correlation between them. This is commonly referred to as "red" noise.

2.1.2.1 Independent data (white noise)

Figure 2.5 a represents the covariance matrix of a set of 4 data points y_i, all independent from each other. Down the diagonal, we have $i = j$, so the entries correspond to the covariance of each point with itself; this is simply their variance, σ. In general, σ incorporates uncertainties induced by instrument systematics, weather conditions, etc. – it is just the error bar of the data. Because we are considering a case in which

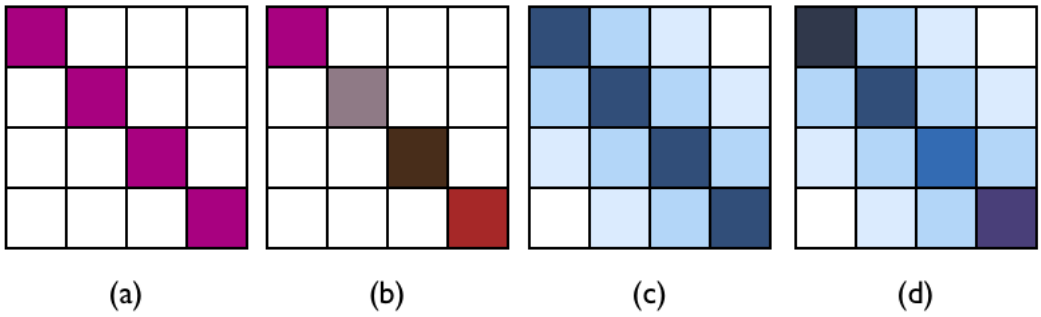

Figure 2.5: Covariance matrix corresponding to: (a) white noise with a constant variance, (b) white noise with varying variance, (c) red noise and constant variance, (d) red noise and variable variance.

the observations are uncorrelated, all the non-diagonal elements are zero.

We can allow the variance to be different for each data point (σ_i), in which case the covariance matrix looks like in Figure 2.5 b.

Assuming a Gaussian distribution, the probability distribution P of a data point y_i can be written as:

$$P\left(y_i\right) = \frac{1}{\sigma_i \sqrt{2\pi}} \cdot \exp\left[-\frac{\left(y_i - \mu_i\right)^2}{2\sigma_i^2}\right]. \tag{2.2}$$

The joint probability distribution of all data points is:

$$P\left(\underline{y}\right) = \prod_{i=1}^{n} P\left(y_i\right), \tag{2.3}$$

and is referred to as the likelihood $\mathcal{L}$. Expanding this expression, we obtain:

$$\mathcal{L} = \left(\frac{1}{2\pi}\right)^{n/2} \cdot \left(\prod_{i=1}^{n} \frac{1}{\sigma_i}\right) \cdot \exp\left[-\sum_{i=1}^{n} \frac{\left(y_i - \mu_i\right)^2}{2\sigma_i^2}\right]. \tag{2.4}$$

We see that the sum in the exponential term corresponds to the chi-squared value (χ^2) of the data, so we have:

$$\mathcal{L} = \left(\frac{1}{2\pi}\right)^{n/2} \cdot \left(\prod_{i=1}^{n} \frac{1}{\sigma_i}\right) \cdot \exp\left(-\frac{\chi^2}{2}\right). \tag{2.5}$$

We obtain the best fit parameters by maximising this function, i.e. by minimising the χ^2.

2.1.2.2 Correlated data (red noise)

We now consider data that are correlated with each other. The corresponding matrix is shown in Figure 2.5 c. The diagonal elements still represent the variance of the data, but some of the non-diagonal elements are now non-zero. The probability distribution function (i.e. the likelihood) is:

$$P\left(\underline{y}|\mathbf{K}\right) = \left(\frac{1}{2\pi}\right)^{n/2} \cdot \frac{1}{\sqrt{\det \mathbf{K}}} \cdot \exp\left[-\frac{1}{2}\left(\underline{y} - \underline{\mu}\right)^T \mathbf{K^{-1}} \left(\underline{y} - \underline{\mu}\right)\right], \tag{2.6}$$

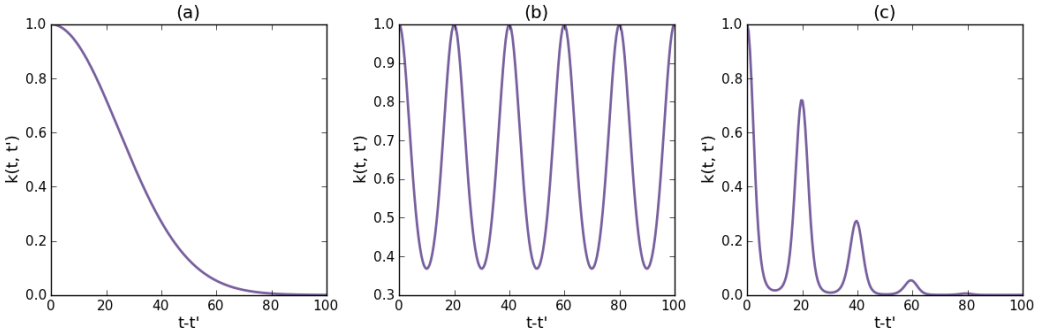

Figure 2.6: Different types of covariance functions: (a) square exponential, (b) periodic, and (c) quasi-periodic. The hyperparemeters are: $\theta_1 = 1$, $\theta_2 = 35$, $\theta_3 = 20$, $\theta_4 = 0.5$.

where $\det \mathbf{K}$ is the determinant of $\mathbf{K}$. This is just a generalised expression of Equation 2.4. In the case of white noise, the covariance matrix is equal to:

$$\mathbf{K} = \underline{\sigma}^2 \mathbf{I}, \tag{2.7}$$

where $\mathbf{I}$ is an $n \times n$ identity matrix. This reduces to a 1-dimensional array of size n, and hence leads to a simplified formulation of the likelihood that is proportional to the χ^2. The χ^2 can therefore only be used in the special case where the noise in our data is completely white.

Otherwise, we must use the generalised expression for $\mathcal{L}$:

$$\mathcal{L} = \left(\frac{1}{2\pi}\right)^{n/2} \cdot \frac{1}{\sqrt{\det \mathbf{K}}} \cdot \exp\left[-\frac{1}{2}\,(\underline{y} - \underline{\mu})^T\, \mathbf{K^{-1}} (\underline{y} - \underline{\mu})\right], \tag{2.8}$$

where the 2π term is a normalisation constant and the determinant of $\mathbf{K}$ acts as a penalty term for more complex models (Occam's razor).

We usually compute $\ln \mathcal{L}$:

$$\ln \mathcal{L} = -\frac{n}{2} \ln(2\pi) - \frac{1}{2} \ln(\det \mathbf{K}) - \frac{1}{2}\,(\underline{y} - \underline{\mu})^T\, \mathbf{K^{-1}} (\underline{y} - \underline{\mu}). \tag{2.9}$$

2.1.3 Covariance function $k(t, t')$

Each element of the covariance matrix $\mathbf{K}$ is determined by a covariance function $k(t, t')$:

$$\mathbf{K}_{i,j} = k(t, t'), \tag{2.10}$$

where t and t' are associated with data points i and j.

Here are a few commonly used functions:

1. White noise:

$$k_1(t, t') = \theta_1^2 \cdot \delta_{t,t'}. \tag{2.11}$$

   The term $\delta_{t,t'}$ is a Dirac delta function scaled according to the magnitude θ_1 of the white noise (usually given by σ_i). This is the simplest kind of covariance function. It leads to a diagonal matrix $\mathbf{K}$ and is almost always used, in combination with a more complex function.

2. Square exponential (Figure 2.6 a):

$$k_2(t,t') = \theta_1^2 \cdot \exp\left[-\frac{(t-t')^2}{\theta_2^2}\right]. \tag{2.12}$$

The hyperparameter θ_1 gives the maximum amplitude of the covariance between two points. The amplitude of the correlation falls exponentially over a (time)scale θ_2. This is the classic case in which we assume that points close to each other are more dependent on each other.

3. Periodic oscillation (Figure 2.6 b):

$$k_3(t,t') = \theta_1^2 \cdot \exp\left[-\sin^2\left(\frac{\pi(t-t')}{\theta_3}\right)\right]. \tag{2.13}$$

This kernel is ideal for a truly periodic, coherent signal, with a recurrence timescale θ_3.

4. Quasi-periodic oscillation (Figure 2.6 c):

$$k_4(t,t') = \theta_1^2 \cdot \exp\left[-\frac{(t-t')^2}{\theta_2^2} - \frac{\sin^2\left(\frac{\pi(t-t')}{\theta_3}\right)}{\theta_4^2}\right]. \tag{2.14}$$

This kernel, of maximum amplitude θ_1, combines a square exponential term with a periodic variation at a fixed period θ_3. The quasi-periodicity evolves over a timescale θ_2. The hyperparameter θ_4 determines the amount of high frequency structure of the fit. The relative importance of the decay and periodicity terms in the exponential is dictated by the relative sizes of θ_2 and θ_4.

The parameters θ_j of the covariance function are known as the *hyperparameters* of the Gaussian process. In the classical statistics world, we fit data by determining the optimal values of the parameters of our (parametric) model, for example the period, phase and amplitude of a sine function; we find the best parameters in "data space". In the Bayesian world, when we are fitting data with a (non-parametric) (Gaussian) process, we find the optimal values of the hyperparameters of the covariance function; we determine the best parameters in "correlation space", or "covariance space". Doing so will give us much more freedom – we shall find out more as we go along!

The form of the covariance function is the main prior assumption we will make (the other priors being those imposed on the hyperparameters), so we need to think carefully about our choice – this is the subject of Sections 2.1.4 and 2.1.5. We can also use Bayesian model selection tools to compare models with different covariance functions, in order to decide which one provides the best fit to the data, but is still the simplest function possible. For more detail on model selection, see Section 2.3.

2.1.4 Temporal structure & covariance

The shape of the covariance function is tightly linked to the temporal structure of the physical phenomenon that we are modelling. The perfect covariance function would

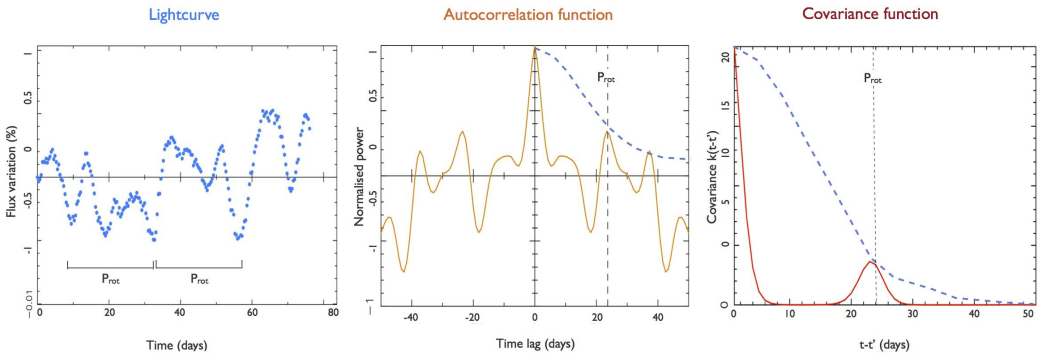

Figure 2.7: *From left to right:* the CoRoT-7 2012 lightcurve, its autocorrelation and the quasi-periodic covariance function used to fit the lightcurve.

look very similar to the autocorrelation function of the data[4]. This is illustrated in Figure 2.7 for a star's lightcurve. The lightcurve displays strong variations due to starspots drifting across the stellar disc as the star rotates. Some starspots remain from one rotation to the next, making it easy identify the rotation period even in the lightcurve itself. The autocorrelation of the lightcurve shows a clear peak at the rotation period – it is not as strong as the peak at zero time lag, reflecting the evolution of spots over time. The autocorrelation does show some additional structure, but to a first approximation, it is well represented by a quasi-periodic covariance function (see Case 4 in Section 2.1.3).

This intrinsic property of the covariance function sets the physical justification for using Gaussian processes to model activity-induced RV signals.

2.1.5 Gaussian processes for stellar activity signals

> "[...] the 'jitter' formalism is limited, because it treats the activity signal as an independent, identically distributed Gaussian noise process."
>
> S. Aigrain, F. Pont and S. Zucker (2012)

Time dependent photometric and spectroscopic observations of stars tell us that activity-driven variations are not random or stochastic in nature. They follow a pattern, modulated by the star's rotation, which evolves according to the growth and decay of magnetically active regions on the stellar surface. The RV variations of a star are a tangled mess of activity and planetary signals, but in photometry, the activity and planetary signals are very distinct, and planet transits can easily be removed from the activity variations. As I have shown in Chapter 1, each star has its own unique behaviour. This temporal "character" is encoded in the periodogram or autocorrelation function of the star's lightcurve.

Due to their ability to memorise patterns of a given frequency structure, Gaussian processes are an ideal tool to model activity-induced variations. A quasi-periodic

[4]They cannot be completely identical since the covariance functions used with Gaussian processes are always positive definite, whereas the autocorrelation function oscillates about zero. They are very similar though (see Figure 2.7), and it would be interesting to find out how they are related.

Parameter	Symbol	Prior
Amplitude	θ_1	Modified Jeffreys ($\sigma_{\rm data}$)
Evolution timescale	θ_2	Jeffreys
Recurrence timescale	θ_3	Gaussian ($P_{\rm rot}, \sigma_{P_{\rm rot}}$) or Jeffreys (if $P_{\rm rot}$ not known)
Relative importance of evolution vs. periodicity	θ_4	Uniform [0,1]

Table 2.1: Prior probability densities and ranges of the hyperparameters optimised via an MCMC procedure. The knee of the modified Jeffreys prior is given in brackets. In the case of a Gaussian distribution, the terms within brackets represent the mean $\bar{x}$ and standard deviation σ. The terms within square brackets stand for the lower and upper limit of the specified distribution; if no interval is given, no limits are placed.

covariance function is an appropriate choice in this context. The evolution timescale corresponds to the average lifetime of starspots on the stellar photosphere, and the recurrence timescale is the stellar rotation period. We want the covariance funtion to go to zero for up to half of the stellar rotation cycle (assuming that the stellar rotation axis is inclined to 90° of the line of sight, which is the case for most transiting systems), to reflect the fact that we do not know what is happening to the surface features when they are facing away from us. Panel (c) of Figure 2.6 shows clearly that the optimisation algorithm has selected a value of θ_4 that reduces the value of the covariance function to zero for roughly half of the stellar rotation cycle.

We can determine the hyperparameters of the covariance function using the star's off-transit lightcurve, since it shares the frequency structure of the star's magnetic activity. This is based on the assumption that the frequency structure of the covariance function representing the stellar activity should be the same for both the lightcurve and the RV curve. The Gaussian process fitting procedure is described in the following Sections.

2.1.6 Determining the hyperparameters θ_j

We can make rough guesses for the hyperparameters using our a priori knowledge of the phenomenon we are modelling, and this will provide a reasonable fit in most cases. However, it is best to let the data decide for themselves, so ideally we should use an optimisation method. In statistical jargon, determining the best hyperparameters to use is a procedure known as *training* the GP. I use a Monte Carlo Markov Chain (MCMC) in order to marginalise over all the hyperparameters – see a detailed description of this procedure in Section 2.2. The priors and ranges I normally apply to the hyperparameters are detailed in Table 2.1. We maximise the likelihood of Equation 2.9 with respect to the hyperparameters.

Computationally, the matrix inversion required in this step means that this process is of order n^3. This means that it can get very slow for large datasets, and we may wish to consider binning the dataset we will be training the GP on (especially if it is a short cadence lightcurve!). In my code, I invoke a Cholesky decomposition (Press et al., 1986), which makes this equation very easy to implement. I explain how to fill the covariance matrix in the following Section.

2.1.7 Constructing the covariance matrix K

Once we have determined the covariance function and its hyperparameters, we can construct a covariance matrix for a dataset containing both red and white noise, according to Equation 2.10. In my model, I use a quasi-periodic covariance function (Case 4 of Section 2.1.3), with some additional white noise given by the error bars of the data:

$$k(t,t') = \theta_1^2 \cdot \exp\left[-\frac{(t-t')^2}{\theta_2^2} - \frac{\sin^2\left(\frac{\pi(t-t')}{\theta_3}\right)}{\theta_4^2}\right] + \sigma_i^2 \cdot \delta_{tt'}. \tag{2.15}$$

For each observation at time t, we calculate its distance in time to all the other observations of the dataset. In this way we can build a matrix whose values tell us about the degree of correlation between each point at time t and all other points at times t'.

2.1.8 Fitting existing data & making predictions

Gaussian processes are a machine learning tool: the covariance function is the "memory" of the GP, which learns from the data itself. The more data we have, the better we can determine the hyperparameters (see Section 2.1.6); by doing this, we are *conditioning* the GP. In turn, having better determined hyperparameters leads to a more probable fit to the data.

In this perspective, the covariance function not only allows us to determine the optimal fit to our observations; it also provides a means of interpolating the fit for times at which we do not have observations. In this case, we are asking how likely it is to measure a given value at a given time. If we make an observation at time t_i, what is the range of possibilities at time t_j?

We already know the covariance matrix $\mathbf{K}$ of the n existing data points $\underline{y} = (y_1, y_2, ..., y_n)$, as it is governed by the covariance function that we have already chosen and whose hyperparameters we have already determined. It has a size $n \times n$. These are the *training* points of the GP.

We define the covariance matrix $\mathbf{K_{pp}}$ for the m *test points* at times $\underline{t}_p = (t_{p1}, t_{p2}, ..., t_{pm})$ at which we want to predict the data. This matrix is populated with the same covariance function, and has dimensions $m \times m$.

The covariance matrix $\mathbf{K_p}$ of the *cross-terms* has to be evaluated too, as it will be used to calculate the errors on $\underline{y}_p$. It has dimensions $m \times n$.

The predicted data $\underline{y}_p$ are given by the mean of the predictive distribution, which is calculated as follows:

$$\underline{y}_p = \mathbf{K_p}.\mathbf{K}^{-1} \cdot \underline{y}. \tag{2.16}$$

If we are simply determining a fit to our data (i.e. we are not "predicting" data at new observation times), then $m = n$ so $\mathbf{K_p}$ is of size $n \times n$, and $\mathbf{K}_{\rm pp} = \mathbf{K}$. Note that $\underline{y}_p$ is indeed a linear function of $\underline{y}$!

The errors associated with $\underline{y}_p$ are found by calculating the covariance of the predictive distribution, and then taking the square root of the diagonal elements of this

matrix:

$$\underline{\sigma}_{y_p} = \sqrt{\mathrm{diag}[\mathbf{K_{pp}} - \mathbf{K_p}.\mathbf{K}^{-1} \cdot \mathbf{K_p}^T]} \tag{2.17}$$

We can interpret this last equation as taking the covariance matrix of the predicted times and "removing" the parts where the predicted times and measured times overlap: at these points, there is less uncertainty so the error is smaller.

Computational trick If you have already determined your hyperparameters, speed up your code by predicting your GP for one point at a time only; this way, $\mathbf{K_p}$ becomes a 1-dimensional vector, and $\mathbf{K_{pp}}$ reduces down to a scalar. Now you only need to solve one linear equation instead of doing a full Cholesky decomposition, which can save a lot of CPU time! Create a little subroutine that does this and simply call it m times.

2.1.9 A word of caution

It is good to remember that samples from the predictive distribution don't behave like the mean of the predictive distribution: the error bars $\underline{\sigma}_{y_p}$ are just as important as the predicted data $\underline{y}_p$ themselves. The choice of covariance function is crucial – it is important to first think about the physical phenomena or instrumental sources responsible for the noise in the data, and to choose covariance functions that are appropriate for each source. At the end of the day, Gaussian processes are just like any other model: you get nothing more out than what you put in!

2.1.10 Useful References

Here is a list of references I have compiled over recent months, with help from others and which I hope you will in turn find useful.

- The following are milestone papers that have brought Gaussian processes to the field of exoplanets:
  - Gibson et al. (2011) and Czekala et al. (2014) introduced GPs to transmission spectroscopy for the study of planetary atmospheres;
  - Foreman-Mackey et al. (2015), Crossfield et al. (2015), Foreman-Mackey et al. (2014), Ambikasaran et al. (2014), Aigrain et al. (2015) and Barclay et al. (2015) harnessed the power of machine learning to detrend *Kepler* and *K2* lightcurves;
  - Baluev (2013), Haywood et al. (2014) and Grunblatt et al. (2015) applied GPs to RV studies;
  - Roberts et al. (2012) is not a paper specific to exoplanets but it provides a very clear introduction to GPs.

  The use of GPs in our field is growing fast; this is only a small selection of papers and is in no way exhaustive.
- C. E. Rasmussen & C. K. I. Williams, *Gaussian Processes for Machine Learning*, the MIT Press, 2006, ISBN 026218253X., 2006 Massachusetts Institute of Technology (online: www.GaussianProcess.org/gpml). This is the classic

reference in which you will find all the equations and statistical jargon.

- If you wish to develop your GP intuition, here is a fantastic lecture on the nature of Gaussian processes by Prof. David MacKay, from the Engineering Department at the University of Cambridge. The first Sections of this introduction to Gaussian processes are based on his lecture. I thoroughly recommend watching it! http://videolectures.net/gpip06_mackay_gpb/
- João Faria, from the Institute of Astrophysics and Space Sciences in Porto, has written a Fortran implementation of GPs, integrated in a platform for the analysis of RV data. The code is available at github.com/j-faria/OPEN.
- Daniel Foreman-Mackey at the department of Astronomy in New York University has written a lot of useful code in Python and C++, and has made it publicly available at: http://dan.iel.fm/research/.
- Finally, Dr Suzanne Aigrain and her group have given many talks and posters about GPs, and some of their slides can be found online.

2.2 Monte Carlo Markov Chain (MCMC)

In this part of the Chapter, I describe my RV model and outline the MCMC fitting procedure that I apply to determine the best fit parameters and their uncertainties.

2.2.1 Modelling planets

The orbit of each planet is assumed Keplerian. I model them as follows:

$$\Delta RV_{\rm k}(t_i) = K_k\big[\cos(\nu_k(t_i, t_{peri_k}, P_k) + \omega_k) + e_k\cos(\omega_k)\big]. \tag{2.18}$$

The period of the orbit of planet k is given by P_k, and its semi-amplitude is K_k. $\nu_k(t_i, t_{peri_k})$ is the true anomaly[5] of planet k at time t_i, and t_{peri_k} is the time of periastron. Because it is difficult to constrain the argument of periastron for planets in low-eccentricity orbits, we introduce two parameters C_k and S_k (Ford, 2006). They are related to the eccentricity e_k of the planet's orbit and the argument of periastron ω_k as follows:

$$C_k = \sqrt{e_k}\,.\cos(\omega_k), \tag{2.19}$$

$$S_k = \sqrt{e_k}\,.\sin(\omega_k). \tag{2.20}$$

The use of the square root imposes a uniform prior on e_k, reducing the bias towards high eccentricities typically seen when defining C_k and S_k as $e_k\cos(\omega_k)$ and $e_k\sin(\omega_k)$ (see Section 2.2.4 for more detail on priors).

The eccentricity is defined as:

$$e_k = S_k^2 + C_k^2, \tag{2.21}$$

and the argument of periastron is:

$$\omega_k = \tan^{-1}(S_k/C_k). \tag{2.22}$$

2.2.2 Modelling stellar activity

My activity model is based on a Gaussian process trained on the off-transit variations in the star's lightcurve, with the quasi-periodic covariance function presented in Sections 2.1.3 and 2.1.5.

In my analysis of the CoRoT-7 system, which was observed simultaneously with CoRoT and HARPS in 2012 (see Chapter 3), I was able to apply the *FF'* method of Aigrain et al. (2012) to model the suppression of convective blueshift and the flux blocked by starspots on the rotating stellar disc (see Chapter 1). I then used another Gaussian process with the same covariance properties to account for other activity-induced signals, such as photospheric inflows towards active regions or limb-brightened facular emission that is not spatially associated with starspots (Haywood et al., 2014).

For the vast majority of stars, however, we cannot obtain contemporaneous high precision photometric and spectroscopic observations – it is either too expensive or

[5]The true anomaly is "the angle between the direction of periastron and the current position of the planet measured from the barycentric focus of the ellipse" (Perryman, 2011).

impractical in terms of telescope time, or space-based, high precision photometry is not available for the system considered. In these cases I use a Gaussian process on its own to account for all activity-induced RV signals (see my analyses of the Kepler-10 and Kepler-78 systems in Chapter 3).

2.2.2.1 Evaluating the *FF'* activity basis functions

In order to calculate the *FF'* activity basis functions $\Delta RV_{\rm rot}(t)$ and $\Delta RV_{\rm conv}(t)$, the flux F at the time of each RV point has to be interpolated from the stellar lightcurve. I do this by training a Gaussian process on the lightcurve, which then allows me to predict the flux at each time of RV observation. I also interpolate the stellar flux at times $t + \Delta t$ and $t - \Delta t$, in order to compute the first time derivative of the flux:

$$F'(t) = \frac{F(t + \Delta t) - F(t - \Delta t)}{2\,\Delta t}. \tag{2.23}$$

This allows me to compute $\Delta RV_{\rm rot}(t)$ and $\Delta RV_{\rm conv}(t)$.

2.2.2.2 An additional activity basis function

I account for activity-related signals (not modelled by the *FF'* terms, if I am also applying this method) by introducing an activity basis function that takes the form of a GP. As I already discussed in Section 2.1.5, I implicitely assume that this GP has the same quasi-periodic covariance properties as the lightcurve. The basic concept is summarised in the diagram in Figure 2.8. The amplitude of the GP, θ_1 is a free parameter in my total RV model (see Section 2.2.3). The other hyperparameters, θ_2, θ_3 and θ_4 are equal to the respective hyperparameters obtained when training a GP on the lightcurve. As the stellar activity mostly generates low-frequency signals, I refer to this activity term as $\Delta RV_{\rm rumble}$.

2.2.2.3 Activity model

The total RV perturbation $\Delta RV_{\rm activity}$ induced by stellar activity is then:

$$\Delta RV_{\rm activity} = A\Delta RV_{\rm rot} + B\Delta RV_{\rm conv} + \Delta RV_{\rm rumble}, \tag{2.24}$$

where A and B are scaling factors, and the amplitude of $\Delta RV_{\rm rumble}$ is controlled by the hyperparameter θ_1 of Equation 2.14.

2.2.3 Total RV model

My final model consists of the three basis functions for the stellar activity as well as a Keplerian for each one of n_{pl} planets:

$$\begin{aligned} \Delta RV_{\rm tot}(t_i) &= RV_0 + \Delta RV_{\rm activity}(t_i, A, B, \Psi_0, \theta_1) \\ &+ \sum_{k=1}^{n_{pl}} K_k \big[\cos(\nu_k(t_i, t_{peri_k}, P_k) + \omega_k) + e_k \cos(\omega_k)\big], \end{aligned} \tag{2.25}$$

where RV_0 is a constant offset.

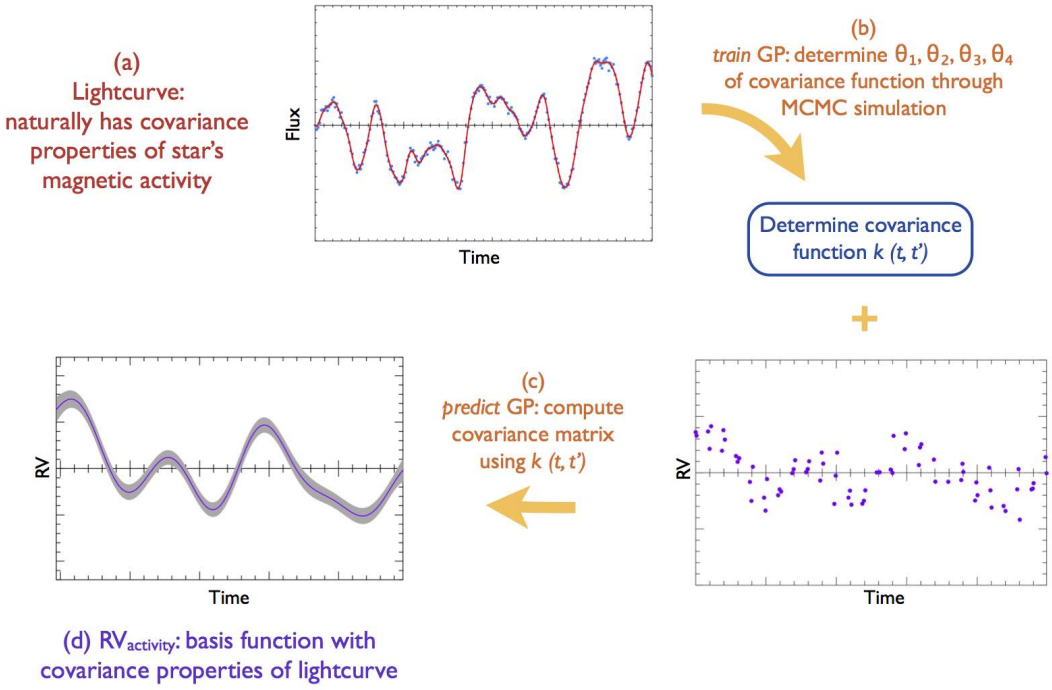

Figure 2.8: Diagram outlining the 4-step procedure to follow in order to absorb potential activity-related red noise RV residuals using a Gaussian process that has the covariance properties of the lightcurve.

2.2.4 Choice of priors

The priors I adopt for each parameter are given in Table 2.2. A Jeffreys prior for a parameter x has the form (Gregory, P. C., 2007):

$$P(x|\mathcal{M}) = \frac{1}{x \ln(\frac{x_{\max}}{x_{\min}})}, \tag{2.26}$$

where $x_{\min}$ and $x_{\max}$ are the lower and upper bounds of the parameter space that we choose to explore. For example, we apply this prior to parameters that represent timescales (eg. the planet orbital periods) because they follow a logarithmic scale; one year always seems longer to a child than to an adult because it represents a much larger fraction of their total life. In order to sample in an unbiased way, we must sample more sparsely at long timescales than at short timescales.

A modified Jeffreys prior is given by:

$$P(x|\mathcal{M}) = \frac{1}{x + x_0} \frac{1}{x \ln(\frac{x_{\max}}{x_{\min}})}, \tag{2.27}$$

where x_0 is the knee of the modified prior. This prior acts as a uniform prior when $K << \sigma_{RV}$, and as a Jeffreys prior for $K >> \sigma_{RV}$. I choose the knee of the modified Jeffreys prior for the semi-amplitudes of the planets to be the mean estimated error of the RV observations, σ_{RV}. This ensures that the semi-amplitudes do not get overestimated in the case of a non-detection. I adopt the same modified Jeffreys prior for the amplitudes A and B of the *FF'* basis functions and the amplitude of the GP (θ_1). θ_1 is naturally constrained to remain low through the calculation of $\mathcal{L}$

Symbol	Parameter	Prior
Systemic RV offset	RV_0	Uniform
Amplitude of GP	θ_1	Modified Jeffreys (σ_{RV})
Amplitude of $\Delta RV_{\rm rot}$	A	Modified Jeffreys (σ_{RV})
Amplitude of $\Delta RV_{\rm conv}$	B	Modified Jeffreys (σ_{RV})
Unspotted flux level	Ψ_0	Uniform [$\Psi_{\rm max}$, no upper limit]
Orbital period of non-transiting planet	$P_{\rm transiting}$	Gaussian ($P_{\rm transit}, \sigma_{P_{\rm transit}}$)
Transit ephemeris of non-transiting planet	$t_{0\rm transiting}$	Gaussian ($t_{\rm transit}, \sigma_{t_{\rm transit}}$)
Orbital period of transiting planet	$P_{k\neq\rm transiting}$	Jeffreys
Transit ephemeris of transiting planet	$t_{0k\neq\rm transiting}$	Uniform
Planet RV amplitude	K_k	Modified Jeffreys (σ_{RV})
Planetary eccentricity (if transiting)	$e_{\rm transiting}$	Square root $[0, 1 - \frac{R_\star}{a_b}]$
Planetary eccentricity (if not transiting)	$e_{k\neq\rm transiting}$	Square root $[0, 1 - \frac{a_{k-1}}{a_k}(1 + e_{k-1})]$
Argument of periastron	ω_k	Uniform $[0, 2\pi]$

Table 2.2: Prior probability densities and ranges of the parameters modelled in the MCMC procedure. The knee of the modified Jeffreys prior is given in brackets. In the case of a Gaussian distribution, the terms within brackets represent the mean $\bar{x}$ and standard deviation σ. The terms within square brackets stand for the lower and upper limit of the specified distribution; if no interval is given, no limits are placed.

(see the next Section). I constrain the orbital eccentricity of the innermost planet so that the planet's orbit remains above the stellar surface. I also impose a simple dynamical stability criterion on the outer planets by ensuring their eccentricities are such that the orbit of each planet does not cross that of its inner neighbour. I force the epochs of inferior conjunction of the outer non-transiting planets (corresponding to mid-transit for a 90° orbit) to occur close to the inverse variance-weighted mean date of the RV observations in order to ensure orthogonality with the orbital periods.

2.2.5 Fitting procedure

The procedure is illustrated in the flow chart of Figure 2.9. At every step of the chain, parameters A, B, Ψ_0, θ_1, RV_0, and the orbital elements of all planets are allowed to take a random jump in parameter space. The size of the step is equal to the size of the error bars of the parameters; at the start of the MCMC, these are mostly a guess, but the error bars (and therefore the step sizes) will be re-evaluated during the scaling phase, in order to ensure that the MCMC is taking steps of appropriate size. The hyperparameters θ_2, θ_3 and θ_4 are kept fixed as they are better constrained by the lightcurve than the RVs.

Likelihood The *FF'* activity basis functions (if used), together with the planet Keplerians and RV_0 are computed based on the present value of the parameters and subtracted from the data, in order to obtain the residuals r. The GP of the activity "rumble" term is then fitted to these residuals in order to absorb any signals with a frequency structure that matches that of the stellar activity. The likelihood $\mathcal{L}$ of the RV residuals is calculated at each step according to the following equation:

$$\ln \mathcal{L} = -\frac{n}{2}\ln(2\pi) - \frac{1}{2}\ln(\det \mathbf{K}) - \frac{1}{2}\,\underline{r}^T . \mathbf{K}^{-1} . \underline{r}, \tag{2.28}$$

which is very similar to Equation 2.9.

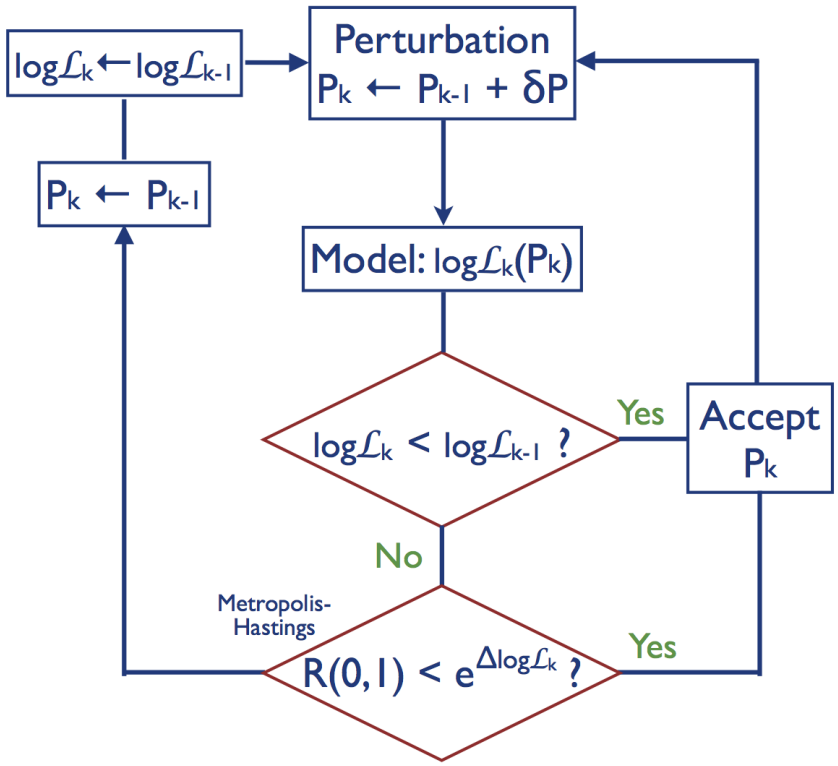

Figure 2.9: The thought process of an MCMC simulation at each step.

Step acceptance or rejection The value of the likelihood is compared with that at the previous step: if the likelihood is higher, it means that this set of parameters provides a better fit than the previous set. The step is then accepted or rejected, the decision being made via the Metropolis-Hastings algorithm (Metropolis et al., 1953). It allows some steps to be accepted when they yield a slightly poorer fit, in order to prevent the chain from becoming trapped in a local $\mathcal{L}$ maximum and instead explore the full parameter landscape. Ideally, the acceptance rate should be around 0.25; this ensures efficient and complete exploration of the parameter space (Ford, 2006).

Burn-in phase and choice of parameter starting points If the planets in the system are not transiting and therefore do not know the orbital period and epoch, I usually make a generalised Lomb-Scargle periodogram (Zechmeister & Kürster (2009); Lomb (1976); Scargle (1982); see Section 1.3.2.1) to identify the strongest signals present in the dataset. The period, phase and approximate amplitude of these signals can then be used as starting points for the MCMC run. If the starting parameter values are wildly off from their true value, the MCMC simulation gets lost in obscure areas of parameter space and never converges (or takes a very long time to do so). An MCMC simulation should only be used in the aim of refining the optimal parameters of a model, and to estimate their error bars in a rigorous way; it is not intended for a first glimpse of what signals might be hiding in a dataset. In most cases, however, as long as some thought has been given to the choice of starting points, it will not affect the outcome of the chains. The initial burn-in phase is complete once $\mathcal{L}$ becomes smaller than the median of all previous $\mathcal{L}$ (Knutson et al., 2008).

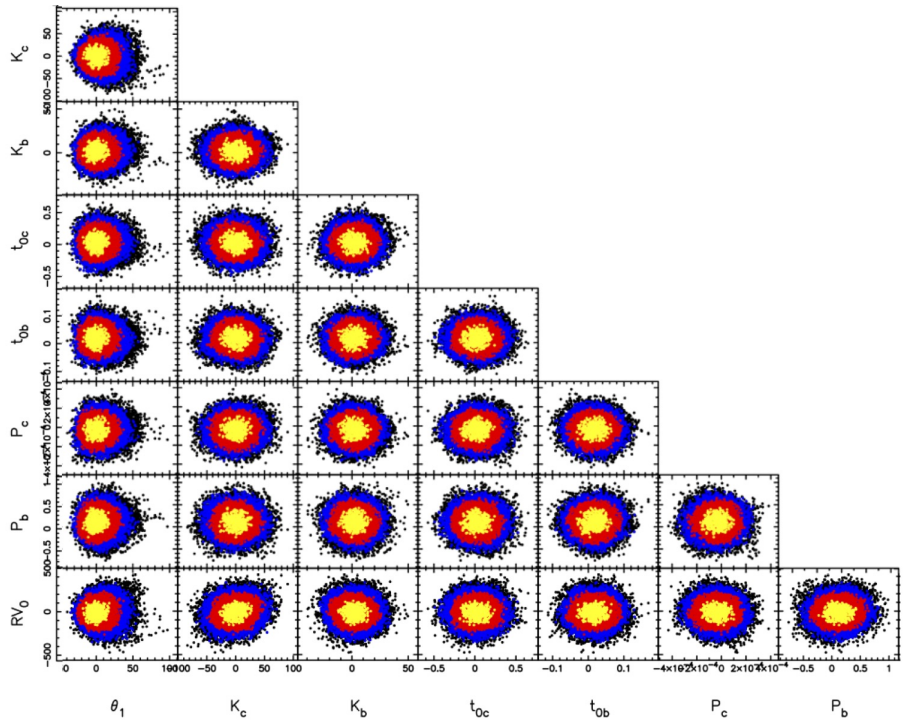

Figure 2.10: Phase plots for an MCMC simulation on the Kepler-10 data, with the model described in Section 3.3 (next Chapter). Points in yellow, red and blue are within the 1, 2 and 3-σ confidence regions, respectively. The scale of each axis corresponds to the departure of each parameter from its value at maximum likelihood. All are expressed in percent.

Scaling phase After the burn-in phase, the MCMC goes through another set of steps, over which the standard deviations of all the parameters are then calculated. This phase allows the step sizes to be adjusted and should result in an optimum acceptance rate for the exploration phase.

Exploration phase and chain convergence The chain goes through a final set of steps in order to fully explore the parameter landscape in the vicinity of the maximum of $\mathcal{L}$. This last phase provides the joint posterior probability distribution of all parameters of the model. I check the good convergence of my code by applying the Gelman-Rubin criterion (Gelman et al., 2004; Ford, 2006), which must be smaller than 1.1 to ensure that the chain has reached a stationary state. The best fit parameters are determined by taking the mean of the parameter chains over this phase, and their error bars can be obtained by calculating the standard deviations.

2.2.6 Care instructions

It is important to look after your MCMC simulation to make sure it is in good health. Checking the acceptance rate is one way to assess whether the chains are behaving reasonably. If it is too low, the chains will move very slowly and will look like "slug trails"; if it is too high, they will not be able to close in on the likelihood maximum, and they will look like an excited bouncy bean. The parameter chains can be plotted as a function of step number. Another useful diagnostic is to plot them against each other; such correlation plots for a healthy MCMC chain are shown in Figure 3.8. The plots allow you to see whether any parameters are correlated with

each other, which can considerably reduce the efficiency of an MCMC simulation. It is best practice to orthogonalise all your parameters before running the simulations.

2.3 Model selection with Bayesian inference

> "In general, nature is more complicated than our model and known noise terms."
> P. C. Gregory (2007)

I run MCMC chains for several different models and select the best one according to the principles of Bayesian inference.

2.3.1 Bayes' factor

Given a dataset $\mathbf{y}$, consider two models $\mathcal{M}_i$ and $\mathcal{M}_j$. In order to determine which one is the simplest but still gives the best fit to the data, we can compare the two models by estimating their posterior odds ratio:

$$\frac{P(\mathcal{M}_i|\mathbf{y})}{P(\mathcal{M}_j|\mathbf{y})} = \frac{Pr(\mathcal{M}_i)}{Pr(\mathcal{M}_j)} \cdot \frac{m(\mathbf{y}|\mathcal{M}_i)}{m(\mathbf{y}|\mathcal{M}_j)}, \tag{2.29}$$

where the first factor on the right side of the equation is the prior odds ratio. For the planetary systems I usually explore, all models that are tested have the same prior information, so this ratio is just 1. This leaves us with the second part of the right side of the equation. It is the ratio of the marginal likelihoods m of each model, and is known as Bayes' factor.

The marginal likelihood m of a dataset $\mathbf{y}$ given a model $\mathcal{M}_i$ with a set of parameters θ_i can be written as:

$$m(\mathbf{y}|\mathcal{M}_i) = \int f(\mathbf{y}|\mathcal{M}_i, \theta_i)\, \pi_i(\theta_i|\mathcal{M}_i)\, d\theta_i, \tag{2.30}$$

where $f(\mathbf{y}|\mathcal{M}_i, \theta_i)$ is the likelihood function $\mathcal{L}$. The term $\pi_i(\theta_i|\mathcal{M}_i)$ accounts for the prior distribution of the parameters and can be incorporated as a penalty to $\mathcal{L}$. According to Chib & Jeliazkov (2001), it is possible to write:

$$m(\mathbf{y}|\mathcal{M}_i) = \frac{f(\mathbf{y}|\mathcal{M}_i, \theta_i)\, \pi(\theta_i|\mathcal{M}_i)}{\pi(\theta_i|\mathbf{y}, \mathcal{M}_i)}. \tag{2.31}$$

The denominator $\pi(\theta_i|\mathbf{y}, \mathcal{M}_i)$ is the posterior ordinate, which we estimate using the posterior distributions of the parameters resulting from MCMC chains.

2.3.2 Posterior ordinate

According to Chib & Jeliazkov (2001), the posterior ordinate $\hat{\pi}(\theta_i|\mathbf{y})$ can be evaluated by comparing the mean transition probability for a series of M jumps from any given θ_i *to* a reference θ_*, to the mean acceptance value for a series of J transitions *from* θ_*. This can be written as:

$$\hat{\pi}(\theta_*|\mathbf{y}) = \frac{M^{-1} \sum_{i=1}^{M} \alpha(\theta_i, \theta_*|\mathbf{y}) \cdot q(\theta_i, \theta_*|\mathbf{y})}{J^{-1} \sum_{j=1}^{J} \alpha(\theta_*, \theta_j|\mathbf{y})}, \tag{2.32}$$

where $\alpha(\theta_i, \theta_*|\mathbf{y})$ is the acceptance probability of the chain from one parameter set θ_i to another set θ_*. The proposal density $q(\theta_i, \theta_*|\mathbf{y})$ from one step θ_i to another θ_* is equal to:

$$q(\theta_i, \theta_*|\mathbf{y}) = \exp\Big[-\sum_{k=1}^{K}\Big(\frac{\theta_i - \theta_*}{\sigma_{\theta_i}}\Big)^2/2\Big]. \tag{2.33}$$

The summation inside the exponential term is carried out over all K parameters of the model, in other words over each parameter contained within a set θ.

If we choose θ_* to be the best parameter set of the whole MCMC chain, then the acceptance probability $\alpha(\theta_i, \theta_*|\mathbf{y})$ is 1, and Equation 2.32 is much simplified.

2.3.3 Marginal likelihood

I obtain $\mathcal{L}_{ML}$ by subtracting the posterior ordinate from the maximum likelihood value of the whole MCMC chain:

$$\log \mathcal{L}_{ML} = \log \mathcal{L}_{best} - \log \hat{\pi}. \tag{2.34}$$

When the number of model parameters becomes very large, the summation on the numerator of Equation 2.32 is dominated by a relatively small fraction of points in the Markov chain that happen to lie close to the maximum likelihood value. A large number of trials is therefore needed to arrive at a reliable estimate of $\hat{\pi}$. I estimate the uncertainty in the posterior ordinate by running the chains several times and determining the variance empirically.

Once $\mathcal{L}_{ML}$ is known we can compute Bayes' factor for a pair of models. The posterior ordinate acts to penalise models that have too many parameters. Jeffreys (1961) found that the evidence in favour of a model is decisive if Bayes' factor exceeds 150, strong if it is in the range of 150-20, positive for 20-3 and not worth considering if lower than 3.

Concluding note

Now that we have a recipe to detect planets around active stars, we can go look for them! In the next Chapter, I present my analysis of the CoRoT-7, Kepler-78 and Kepler-10 systems.

3

Application to observations of planet-hosting stars*

In this Chapter, I present the work I have done towards characterising three planetary systems: CoRoT-7, Kepler-78 and Kepler-10. CoRoT-7 is an active star host to a small hot Neptune and the first Earth-size exoplanet ever discovered. Kepler-78 is an active star orbited by an extremely close-in hot, Earth-mass planet. Kepler-10 is old and quiet, and harbours two transiting planets – one a super-Earth, the other a rocky world the size of Neptune whose discovery challenges our theories of planet formation. All three of these systems were first discovered via the transit method, by the CoRoT and *Kepler* space missions. They were followed up with HARPS, HARPS-N and HIRES in order to obtain a precise mass determination of the planets present in these systems.

*This Chapter uses material from, and is based on, Haywood et al., 2014, MNRAS, 443, 2517 and my own contributions to Dumusque et al., 2014, ApJ, 789, 154, and Grunblatt, Howard & Haywood, 2015, ApJ, 808, 127

CoRoT-7b: the first transiting super-Earth with a measured radius! Selection of online press releases.

3.1 CoRoT-7

Since the discovery of the super-Earth CoRoT-7b, several investigations have yielded different results for the number and masses of planets present in the system, mainly owing to the star's high level of activity. This system has a long history, which I present in the next Section, before I report on my own analysis in the following Sections.

3.1.1 History of the system

In July 2009, Léger et al. (2009) announced the discovery of a transiting planet CoRoT-7b, the first Super-Earth with a measured radius found by the CoRoT space mission. At the time, it had the smallest exoplanetary radius ever measured, $R_{\rm b} = 1.68 \pm 0.09 R_{\oplus}$. CoRoT-7 is relatively bright (V = 11.7) but has fairly high activity levels, meaning that for a long time the number of planets detected around it and their precise physical parameters remained in debate.

Following this discovery, a 4-month intensive HARPS campaign was launched in order to measure the mass of CoRoT-7b. The results of this run are reported in Queloz et al. (2009). They expected the RV variations to be heavily affected by stellar activity, given the large modulations in the CoRoT photometry. The star's lightcurve (2008-2009 CoRoT run) shows modulations due to starspots of up to 2%, which tells us that CoRoT-7 is more active than the Sun, whose greatest

recorded variations in irradiance are of 0.34% (Kopp & Lean, 2011). Indeed, a few simultaneous photometric measurements from the Euler Swiss telescope confirmed that CoRoT-7 was very spotted throughout the HARPS run. In order to remove the activity-induced RV variations from the data, Queloz et al. (2009) applied a prewhitening procedure followed by a harmonic decomposition (see Section 1.2.3). For the prewhitening, the period of the stellar rotation signal was identified by means of a Fourier analysis, and a sine fit with this period was subtracted from the data. This operation was applied to the residuals to remove the next strongest signal, and so on until the noise level was reached. All the signals detected with this method were determined to be associated with harmonics of the stellar rotation period, except two signals at 0.85 and 3.69 days. The RV signal at 0.85 days was found to be consistent with the CoRoT transit ephemeris, thus confirming the planetary nature of CoRoT-7b. Its mass was determined to be 4.8 ± 0.8 $M_\oplus$. In order to assess the nature of the signal at 3.69 days, Queloz et al. (2009) used a harmonic decomposition to create a high pass filter: the RV data were fitted with a Fourier series comprising the first three harmonics of the stellar rotation period, within a time window sliding along the data. The length of this window (coherence time) was chosen to be 20 days, so that any signals varying over a longer timescale were filtered out – starspots typically have lifetimes of about a month (Schrijver (2002), Hussain (2002), see Chapter 1). The harmonically filtered data were found to contain a strong periodic signal at 3.69 days, which was attributed to the orbit of CoRoT-7c, another super-Earth with a mass of 8.4 ± 0.9 $M_\oplus$.

A few months later, Bruntt et al. (2010) re-measured the stellar radius with improved stellar analysis techniques, which led to a slightly smaller planetary radius for CoRoT-7b than initially found, of $1.58 \pm 0.10 R_\oplus$.

A separate investigation was later carried out by Lanza et al. (2010). The stellar induced RV variations were synthesized based on a fit to the CoRoT lightcurve, which was computed according to a maximum entropy spot model (Lanza et al., 2009, 2011). The existence of the two planets was then confirmed by demonstrating that the activity-induced RV variations did not contain any spurious signals at the orbital periods of the two planets, with an estimated false alarm probability of less than 10^{-4}.

In another analysis, Hatzes et al. (2010) applied a prewhitening procedure to the full width at half-maximum (FWHM), bisector span and Ca II H&K line emission derived from the HARPS spectra and cross-correlation analyses. These quantities vary according to activity only, and are independent of planetary orbital motions (see Section 1.2.1.1). No significant signals were found in any of these indicators at the periods of 0.85 and 3.69 days. Furthermore, they investigated the nature of a signal found in the RV data at 9.02 days. It had been previously detected by Queloz et al. (2009) but had been attributed to a "two frequency beating mode" resulting from an amplitude modulation of a signal at a period of 61 days. This is close to twice the stellar rotation period so it was deemed to be activity related. Hatzes et al. found no trace of a signal at 9.02 days in any of the activity indicators. They thus suggested this RV signal could be attributed to a third planetary companion with a mass of 16.7 ± 0.42 $M_\oplus$. They also confirmed the presence of CoRoT-7b and CoRoT-7c, but found different masses than calculated by Queloz et al. (2009). This was inevitable since the derived masses of planets are intimately connected with the

methods used to mitigate the effects of stellar activity on the RV data.

Hatzes et al. (2010, 2011) developed a very simple method to remove stellar activity-induced RV variations, to obtain a more accurate mass for CoRoT-7b. The method relied on making several well-separated observations on each night, which was the case for about half of the HARPS data. Under the assumption that the variations due to activity and other planets were negligible during the span of the observations on each night, it was possible to fit a Keplerian orbit assuming that the velocity zero-point differs from night to night but remained constant within each night (see Section 1.2.2). Hatzes et al. (2010) report a mass of CoRoT-7b of 6.9 ± 1.4 $M_\oplus$ and the second analysis (Hatzes et al., 2011) yields a mass of 7.42 ± 1.21 $M_\oplus$, which is consistent.

Pont, Aigrain and Zucker (2010) carried out an analysis based on a maximum entropy spot model (similar to Lanza et al. (2010)) which made use of many small spots as opposed to few large spots. The model was constrained using FWHM and bisector information. A careful examination of the residuals of the activity and planet models led to the authors to add an additional noise term in order to account for possible systematics beyond the formal RV uncertainties. Pont et al. (2010) argued that CoRoT-7b was detected in the RV data with much less confidence than in previous analyses, and reported a mass of 2.3 ± 1.8 $M_\oplus$ detected at a 1.2σ level. Furthermore, they argued that the RV data were not numerous enough and lacked the quality required to look for convincing evidence of additional companions.

Boisse et al. (2011) applied their SOAP tool (Boisse, Bonfils and Santos 2012) to the CoRoT-7 system. This program simulates spots on the surface of a rotating star and then uses this model to compute the activity-induced RV variations of the star. With this technique, they obtained mass estimates for CoRoT-7b and CoRoT-7c. They judge that their errors are underestimated and suggest adding a noise term of 1.5 $m.s^{-1}$ to account for activity-driven RV variations. Their mass estimate for CoRoT-7b was in agreement with the value reported by Queloz et al. (2009) but they found a slightly higher value for the mass of CoRoT-7c.

Ferraz-Mello et al. (2011) constructed their own version of the high-pass filter employed by Queloz et al. (2009) in order to test the validity of this method and estimated masses for CoRoT-7b and 7c. They compared it to the method used by Hatzes et al. (2010, 2011) and to a pure Fourier analysis. They concluded the method was robust, and obtained revised masses of 8.0 ± 1.2 $M_\oplus$ for CoRoT-7b and 13.6 ± 1.4 $M_\oplus$ for CoRoT-7c, but made no mention of CoRoT-7d.

The analysis by Lanza et al. (2010), which makes use of the CoRoT lightcurve (Léger et al., 2009) to model the activity-induced RV variations, and those by Pont et al. (2010) and Boisse et al. (2011), which rely on the tight correlation between the FWHM and the simultaneous Euler photometry (Queloz et al., 2009), could be much improved with simultaneous photometric and RV data (see Lanza et al., in prep.). The spot activity on CoRoT-7 changes very rapidly and it is therefore not possible to deduce the form of the activity-driven RV variations from photometry taken up to a year before the RV data.

In the next Section, I introduce the new simultaneous photometric and RV observations obtained in 2012 January with the CoRoT satellite and HARPS spectrograph.

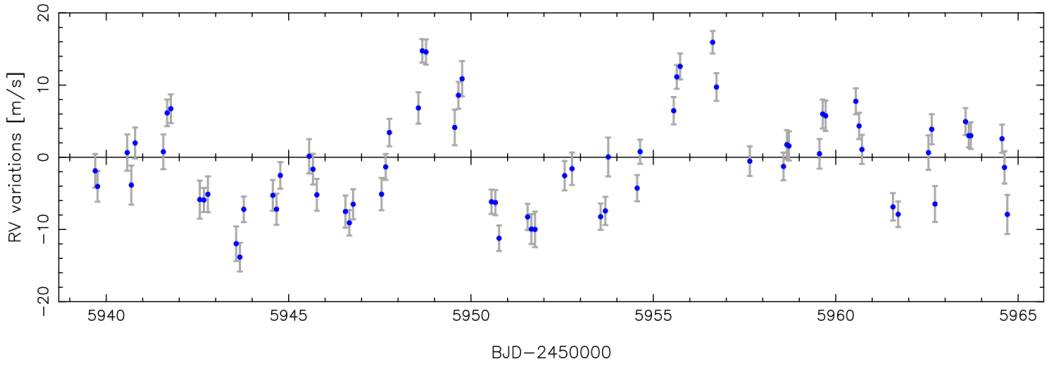

Figure 3.1: RV observations of CoRoT-7, made in January 2012 with HARPS.

I implement my model in Section 3.1.4, and discuss the outcomes in Section 3.1.5.

3.1.2 Observations

3.1.2.1 HARPS spectroscopy

Radial velocities The CoRoT-7 system was observed with the HARPS instrument on the ESO 3.6 m telescope at La Silla, Chile for 26 consecutive clear nights from 2012 January 12 to February 6, with multiple well-separated measurements on each night. The 2012 RV data, shown in Figure 3.1, were reprocessed in the same way as the 2008-2009 data (Queloz et al., 2009) using the HARPS data analysis pipeline. The cross-correlation was performed using a K5 spectral mask. The data are available in Table A1 of the Appendix. The median, minimum and maximum signal-to-noise ratio of the HARPS spectra at central wavelength 556.50 nm are 44.8, 33.8 and 56.2, respectively. The RV variations during the second run, shown in Figure 3.1 have a smaller amplitude than during the first HARPS campaign, implying that the star has become less active than it was in 2008-2009.

Time series of trailed spectra I grouped the reprocessed cross-correlation functions (CCFs) into nightly averages, and subtracted the mean CCF (calculated over the full run) in order to obtain the residual perturbations to each line profile. I then stacked each of these residuals on top of one another as a function of time. The resultant trail of spectra is shown in Figure 3.2. The bright trails are produced by starspots or groups of faculae drifting across the surface as the star rotates.

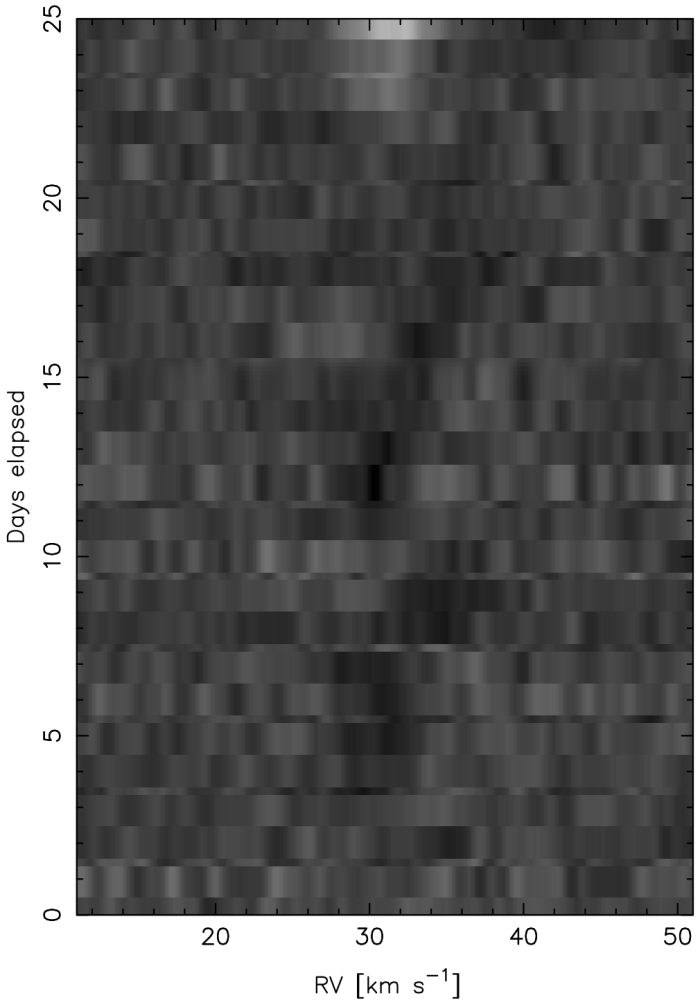

Figure 3.2: Trailed CCFs: the average line profile is subtracted from the individual profiles, which are then stacked vertically as a function of time. The two vertical dark lines represent gaps between groups of magnetically active regions crossing the stellar disc as the star rotates.The small variations along the horizontal scale within individual line profiles arise from the uniqueness of each pixel on the CCD.

CoRoT-7	
Spectral type	G9V
Mass	$0.913 \pm 0.017\, M_{\odot}$
Radius	$0.820 \pm 0.019\, R_{\odot}$
Age	1.32 ± 0.76 Gyr
CoRoT-7b	
Orbital period	$0.85359165 \pm 5.6 \times 10^{-7}$ day
Transit ephemeris	$2454398.07694 \pm 6.7 \times 10^{-4}$HJD
Transit duration	1.42 ± 0.15 h
Orbital inclination	$80.78^{+0.51}_{-0.23}$ deg
Radius	$1.585 \pm 0.064\, \mathrm{R}_{\oplus}$

Table 3.1: Transit and star information based on both CoRoT runs (results from Barros et al. (2014)).

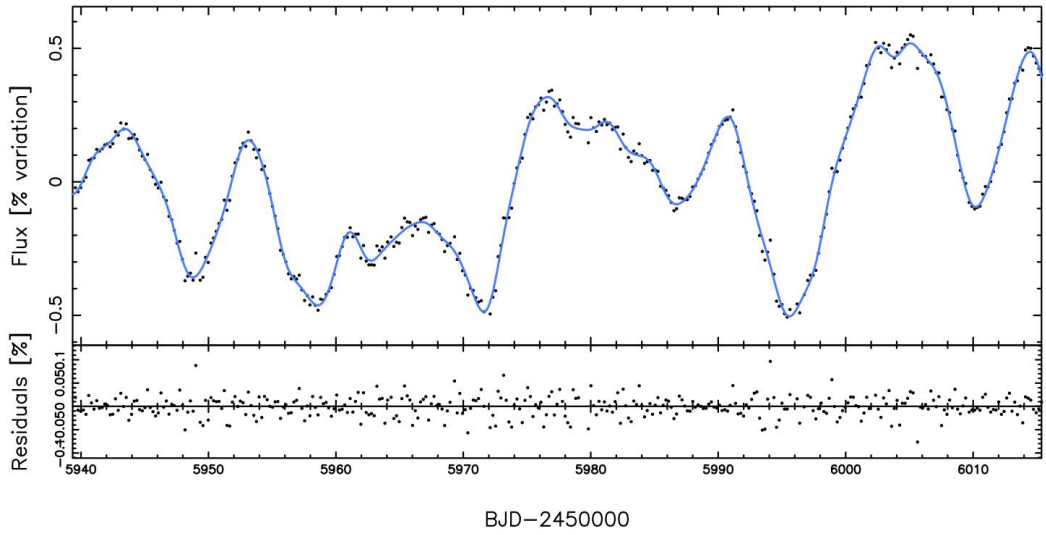

Figure 3.3: *Upper panel:* CoRoT-7 lightcurve over the span of the 2012 RV run, with my photometric fit at each RV observation overplotted as the blue curve. *Lower panel:* Residuals of the fit.

3.1.2.2 CoRoT photometry

CoRoT-7 was observed with the CoRoT satellite (Auvergne et al., 2009) from 2012 January 10 to March 29. Figure 3.3 shows the part of the lightcurve which overlaps with the 2012 HARPS run. Measurements were taken in CoRoT's high cadence mode (every 32 seconds). The data were reduced with the CoRoT imagette pipeline with an optimised photometric mask in order to maximise the signal-to-noise ratio of the lightcurve. Further details on the data reduction are given by Barros et al. (2014), who present a combined analysis of both CoRoT datasets. They derive the revised orbital period and epoch of first transit shown in Table 3.1. These values will be used as prior information in my MCMC simulations (see Section 3.1.4). I binned the data in blocks of 0.07 day, which corresponds to 6176 s and is close to the orbital period of the satellite of 6184 s (Auvergne et al., 2009) in order to average the effects of all sources of systematic errors related to the orbital motion of CoRoT.

3.1.3 Preliminary periodogram analysis

In order to determine an appropriate set of parameters as a starting point for my MCMC analysis, I made a periodogram of the 2012 RV data, shown in Figure 3.4 (see Section 1.3.2.1). The stellar rotation period and its harmonics are marked by the red lines (solid and dashed, respectively). Because the orbital period of CoRoT-7b is close to 1 day, its peak in the periodogram is hidden amongst the aliases produced by the two strong peaks at 3.69 and 8.58 days. The peak at 3.69 days matches the period for CoRoT-7c of Queloz et al. (2009). We see another strong peak at a period of 8.58 days, which is close to the period found by Lanza (in prep.) of 8.29 days for the candidate planet signal CoRoT-7d, and about half a day shorter than that determined by Hatzes (in prep.) based on the same dataset. The periodogram shows that this peak is very broad and spans the whole 8-9 days range. Several stellar rotation harmonics are also present within this range, so at this stage I cannot conclude on the nature of this signal (this is discussed further in

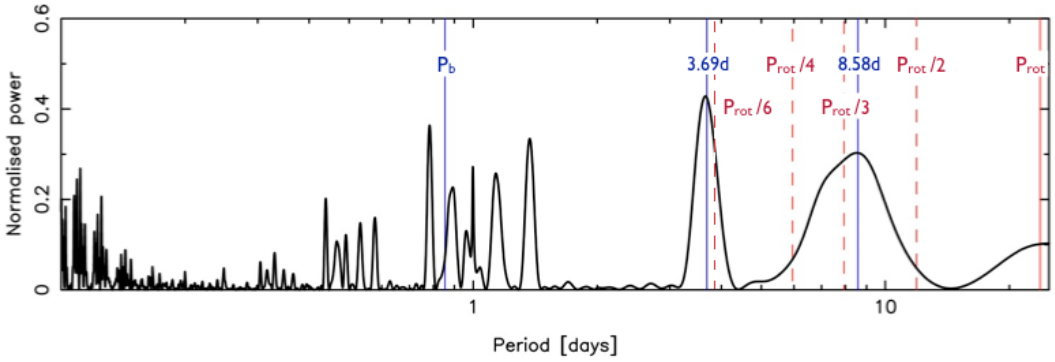

Figure 3.4: Generalised Lomb-Scargle periodogram of the 2012 RV dataset. The stellar rotation fundamental, $P_{\rm rot}$, and harmonics are represented with solid and dashed lines, respectively. Also shown are the orbital period of CoRoT-7b derived from the transit analysis of Barros et al. (2014), $P_{\rm b}$, and the periods of the two strong peaks at 3.69 and 8.58 days.

Section 3.1.5.3).

3.1.4 MCMC analysis

3.1.4.1 RV model

The planet orbits are modelled as Keplerians, while the activity model is based on a Gaussian process with a quasi-periodic covariance function trained on the off-transit variations in the star's lightcurve (see next Section). I then use this Gaussian process in two ways:

(a) I model the suppression of convective blueshift and the flux blocked by starspots on a rotating star, via the *FF'* method of Aigrain et al. (2012). This method is explained in detail in Section 1.2.5 of Chapter 1.

(b) I use another Gaussian process with the same covariance properties to account for other activity-induced signals, such as photospheric inflows towards active regions or limb-brightened facular emission that is not spatially associated with starspots (Haywood et al. (2014), see Section 1.1.5.3).

The total RV model has the form:

$$\begin{aligned}\Delta RV_{\rm tot}(t_i) = RV_0 + A\Delta RV_{\rm rot} + B\Delta RV_{\rm conv} + \Delta RV_{\rm rumble} \\ + \sum_{k=1}^{n_{pl}} K_k\big[\cos(\nu_k(t_i, t_{peri_k}, P_k) + \omega_k) + e_k\cos(\omega_k)\big],\end{aligned} \tag{3.1}$$

where all the symbols have their usual meaning (refer to Section 2.2.3). The stellar radius $R_\star$, which is needed to calculate the $\Delta RV_{\rm rot}$ basis function of the *FF'* method, is set to the value determined by Barros et al. (2014), given in Table 3.1. The second *FF'* basis function, $\Delta RV_{\rm conv}$, depends on the difference between the convective blueshift in the unspotted photosphere and that within the magnetised area ($\delta V_{\rm c}$) and the ratio of this area to the spot surface (κ). We do not know their values in the case of CoRoT-7 so they will be absorbed into the scaling constant B.

3.1.4.2 Gaussian process

I interpolated the flux from the CoRoT lightcurve at the time of each RV point using a Gaussian process with a quasi-periodic covariance function:

$$k\,(t,t') = \eta_1^2\,.\,\exp\Big(-\frac{(t-t')^2}{2\eta_2^2} - \frac{2\sin^2(\frac{\pi(t-t')}{\eta_3})}{\eta_4^2}\Big). \tag{3.2}$$

It is the same as Equation 2.14 that I introduced in the previous Chapter. The shape of this covariance function reflects the quasi-periodic nature of the CoRoT lightcurve, as evolving active regions come in and out of view.

The hyperparameters are determined via the MCMC simulation described in Section 2.1.6.

1. Amplitude of the Gaussian process, η_1;
2. Timescale for growth and decay of active regions, η_2: I found it to be $\eta_2 = 20.6 \pm 2.5$ days. This implies that the active regions on the stellar surface evolve on timescales similar to the stellar rotation period;
3. Stellar rotation period, η_3: I computed the discrete autocorrelation function (Edelson & Krolik, 1988) of the lightcurve (it is displayed in the second panel of Figure 2.7 in the previous Chapter). I find $P_{\rm rot} = 23.81 \pm 0.03$ days, which is consistent with the estimate of Léger et al. (2009) of about 23 days. I applied this value as a Gaussian prior in the MCMC simulation I ran to determine the other hyperparameters;
4. Finally, η_4 determines how smooth the fit is.

The fit is shown in the top panel of Figure 3.3. The residuals of the fit shown in the bottom panel show no correlated noise and have an RMS scatter of 0.02 %. The parameters of the RV model are then fitted via the MCMC procedure that I presented in Section 2.2 of the previous Chapter.

3.1.5 Results and discussion

3.1.5.1 Justification for the use of a Gaussian process in addition to the *FF'* method

Initially, I used the *FF'* basis functions on their own to account for activity-induced signals in the RVs. However, it quickly became apparent that an additional term is needed to account for all slowly-varying signals. I find that an RV model including a Gaussian process with a quasi-periodic covariance structure is the only model that yields uncorrelated, flat residuals. Regardless of the number of planets modelled, without the inclusion of this Gaussian process the residuals always display correlated behaviour. Figure 3.5 shows the residuals remaining after fitting the orbits of CoRoT-7b, CoRoT-7c and a third Keplerian, and the two basis functions of the *FF'* model. We see that even the addition of a third Keplerian does not absorb these variations, which appear to be quasi-periodic. Also, I note that a Gaussian process with a less complex, square exponential covariance function does not fully account for correlated residuals in either a 2- or 3-planet model. A comparison between a model with 2 planet orbits, the *FF'* basis functions and a Gaussian process that

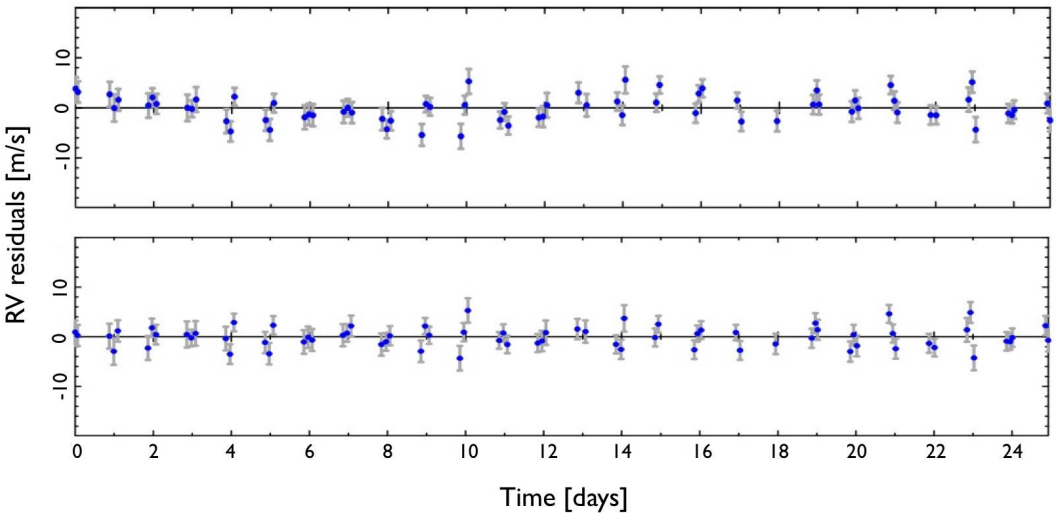

Figure 3.5: *Top:* RV residuals remaining after fitting a 3-planet + *FF'* activity functions model. They contain quasi-periodic variations, and show the need to use a red noise "absorber" such as a Gaussian process. *Bottom:* RV residuals after including a Gaussian process with a quasi-periodic covariance function in our RV model. The RMS of the residuals, now uncorrelated, is 1.96 m.s^{-1} which is at the level of the error bars of the data.

has square exponential or quasi-periodic covariance properties yields a Bayes factor of 3.10^6 in favour of the latter. This implies that the active regions on the stellar surface do remain, in part, from one rotation to the next.

3.1.5.2 Identifying the best model using Bayesian model selection

I ran MCMC simulations for models with 0 (activity only), 1, and 2 planets. I estimated the marginal likelihood of each model from the MCMC samples using the method of Chib & Jeliazkov (2001), which I described in Section 2.3. The log marginal likelihoods are listed in the second to last row of Table 3.2. I also tested a 3-planet model, which I discuss in the next Section.

The 2-planet model is preferred over the activity-only and 1-planet model (see the first three columns in Table 3.2). I also found that a 2-planet model with free orbital eccentricities is preferred over a model with forced circular orbits by a Bayes' factor of 5.10^3 (see Section 2.3). The model with forced circular orbits is penalised mostly because of the non-zero eccentricity of CoRoT-7c. Indeed, keeping e_b fixed to zero while letting e_c free yields a Bayes' factor of 270 (over a model with both orbits circular), while the Bayes' factor between models with e_b fixed or free (e_c free in both cases) is only 36. A model with no planets, consisting solely of the *FF'* basis functions and a quasi-periodic Gaussian process (Model 0) is severely penalised; this attests that models with the covariance properties of the stellar activity do not absorb the signals of planets b and c.

3.1.5.3 CoRoT-7d or stellar activity?

I investigated the outputs of 3-planet models in order to look for the 9-day signal present in the 2009 RV data (Queloz et al., 2009; Hatzes et al., 2010), whose origin has been strongly debated (cf. Section 3.1.1 and references therein).

	Model 0	Model 1	Model 2	Model 2b
Stellar activity				
A [m.s^{-1}]	-0.36 ± 0.20	-0.35 ± 0.21	0.06 ± 0.13	0.06 ± 0.12
B [m.s^{-1}]	0.84 ± 1.07	-0.35 ± 1.30	0.64 ± 0.28	0.49 ± 0.35
$\Psi_0/\Psi_{\max}$	1.014 ± 0.013	1.014 ± 0.012	1.014 ± 0.012	1.014 ± 0.013
θ_1 [m.s^{-1}]	75 ± 19	86 ± 20	7 ± 2	8 ± 2
CoRoT-7b				
P [days]		0.85359165(6)	0.85359165(5)	0.85359163(6)
t_0 [BJD - 2450000]		4398.0769(7)	4398.0769(8)	4398.0769(8)
$t_{\rm peri}$ [BJD - 2450000]		4398.10(7)	4398.21(9)	4398.863(1)
K [m.s^{-1}]		3.95 ± 0.71	3.42 ± 0.66	3.10 ± 0.68
e		0.17 ± 0.09	0.12 ± 0.07	0 (fixed)
ω [°]		105 ± 61	160 ± 140	0 (fixed)
m [M$_\oplus$]		5.37 ± 1.02	4.73 ± 0.95	4.45 ± 0.98
ρ [g.cm^{-3}]		7.51 ± 1.43	6.61 ± 1.33	6.21 ± 1.37
a [AU]		0.017(1)	0.017(1)	0.017(1)
CoRoT-7c				
P [days]			3.70 ± 0.02	3.68 ± 0.02
t_0 [BJD - 2450000]			5953.54(7)	5953.59(5)
$t_{\rm peri}$ [BJD - 2450000]			5953.3(3)	5952.67(6)
K [m.s^{-1}]			6.01 ± 0.47	5.95 ± 0.48
e			0.12 ± 0.06	0 (fixed)
m [M$_\oplus$]			13.56 ± 1.08	13.65 ± 1.10
a [AU]			0.045(1)	0.045(2)
$n_{\rm obs}$	71	71	71	71
$n_{\rm params}$	5	10	15	11
$\log \mathcal{L}_{\max}$	-237.6 ± 0.3	-223.6 ± 0.5	-188.0 ± 0.2	-196.28 ± 0.04
$\hat{\pi}$	0 ± 1	2 ± 1	2 ± 1	2.2 ± 0.8
$\log \mathcal{L}_{\rm ML}$	-237 ± 1	-225 ± 1	-190.1 ± 0.7	-198.5 ± 0.8
Bayes' factor: $B_{k,2}$	4×10^{-21}	6×10^{-16}	-	2×10^{-4}
BIC	496.5	489.8	439.9	439.4

Table 3.2: Outcome of a selection of models: Model 0: stellar activity only, modelled by the *FF'* basis functions and a Gaussian process with a quasi-periodic covariance function; Model 1: activity and 1 planet; Model 2: activity and 2 planets; Model 2b: activity and 2 planets with eccentricities fixed to 0. The numbers in brackets represent the uncertainty in the last digit of the value. Also given are the number of observations used ($n_{\rm obs}$), the number of parameters in each model ($n_{\rm params}$), the maximum likelihood ($\log \mathcal{L}_{\max}$), the posterior ordinate ($\hat{\pi}$), the marginal likelihood ($\log \mathcal{L}_{\rm ML}$) and the Bayesian Information Criterion (BIC) for each model. In the last row, each model is compared to Model 2 using Bayes' factor.

First, I fitted a model comprising three Keplerians, the *FF'* basis functions and an additional Gaussian process with a quasi-periodic covariance function. I recover the orbits of the two inner planets but do not detect another signal with any significance. The residuals are uncorrelated and at the level of the error bars. I then constrained the orbital period of the third planet with a Gaussian prior centred around the period recently reported by Tuomi et al. (2014) at $P_{\rm d} = 8.8999 \pm 0.0082$ days, and imposed a Gaussian prior centred at 2455949.97 ± 0.44 BJD on the predicted time of transit (which corresponds to the phase I determined based on the orbital period of

Tuomi et al. (2014)). I recover a signal which corresponds to a planet mass of 13 ± 5 $M_\oplus$ and is in agreement with the mass proposed by Tuomi et al. (2014). However, the log marginal likelihood of this model is -192.5 ± 0.7; this is lower than the log marginal likehood of the 2-planet model (Model 2, $\log\mathcal{L}_{ML} = -190.1 \pm 0.7$), which suggests that the addition of an extra Keplerian orbit at 9 days is not justified in view of the improvement to the fit.

Since this orbital period is very close to the second harmonic of the stellar rotation, it is plausible that the Gaussian process could be absorbing some or all of the signal produced by a planet's orbit at this period. In order to test whether this is the case, I took the residuals of Model 2 and injected a synthetic sinusoid with the orbital parameters of planet d reported by Tuomi et al. (2014). I fitted this fake dataset with a model consisting of a Gaussian process (with the same quasi-periodic covariance function as before), a Keplerian and a constant offset. I find that the planet signal is completely absorbed by the Keplerian model, within uncertainties – the amplitude injected was 5.16 ± 1.84 m.s^{-1}, while that recovered is 4.97 ± 0.35 m.s^{-1}. This experiment attests that the likelihood of the model (see Equation 2.28) acts to keep the amplitude of the Gaussian process as small as possible, in order to compensate for its high degree of flexibility, and allow other parts of the model to fit the data if they are less complex than the Gaussian process. I therefore conclude that if there were a completely coherent signal close to 9 days, it would be left out by the Gaussian process and be absorbed by the third Keplerian of the 3-planet model.

This signal therefore cannot be fully coherent over the span of the observations. Indeed, we see in the periodogram of the RV data in Figure 3.4 that the peak at this period is broad. I note that despite the lower activity levels of the star in the 2012 dataset, the 9-day period is less well determined in this dataset than in the 2008-2009 one. This peak is also broader than we would expect for a fully coherent signal at a period close to 9 days with the observational sampling of the 2012 dataset. This is likely to be caused by variations in the phase and amplitude of the signal over the span of the 2012 data.

Based on the 2012 RV dataset, I do not have enough evidence to confirm the presence of CoRoT-7d as its orbital period of 9 days is very close to the second harmonic of the stellar rotation. Furthermore, the period measured for the 2009 dataset by Hatzes et al. (2010) $P_\mathrm{d} = 9.021 \pm 0.019$ days is not precise enough to allow me to determine whether the signals from the two seasons are in phase, as was done in the case of α Centauri Bb by Dumusque et al. (2012). The cycle count of orbits elapsed between the two datasets is: $n = 1160/9.021 = 128.6$ orbits. The uncertainty is $n\,\sigma_{P_\mathrm{d}}/P_\mathrm{d} = n\,(0.019/9.021) = 0.27$ orbits. Although this 1-sigma uncertainty is less than one orbit, it is big enough to make it impossible to test whether the signal is still coherent. The most likely explanation, given the existing data, is that the 8-9 day signal seen in the periodogram of Figure 3.4 is a harmonic of the stellar rotation.

3.1.5.4 Best RV model: 2 planets & stellar activity

Figure 3.6 shows each component of the total RV model plotted over the duration of the RV campaign. We see that the suppression of convective blueshift by active regions surrounding starspots has a much greater impact on RV than flux blocked

by starspots; I discuss this further in Section 3.1.5.7.

Figure 3.7 shows Lomb-Scargle periodograms of the CoRoT 2012 lightcurve and the HARPS 2012 RV data. Panel (a) shows the periodogram of the full CoRoT 2012 lightcurve, while panel (b) represents the periodogram of the Gaussian process fit to the lightcurve sampled at the times of the HARPS 2012 RV observations. Both periodograms reveal a stronger peak at $P_{\rm rot}/2$ than at $P_{\rm rot}$, which indicates the presence of two major active regions on opposite hemispheres of the star. This is in agreement with the variations in the lightcurve in Figure 3.3. Given that suppression of convective blueshift appears to be the dominant signal, we would expect a similar frequency structure to be present in the periodogram of the RV curve (panel (c)). Indeed, we see that the stellar rotation harmonics bracket the 6 to 10 day peak in the periodogram, which has significantly greater power than the fundamental 23-day rotation signal. In panel (d), I remove the two *FF'* basis functions. I then subtract the Gaussian process (panel (e)). We see that the Gaussian process absorbs most of the power present in the 6-10 day range. In panel (f), I have also subtracted the orbit of planet c. This removes the peaks at $P_{\rm c}$ and its 1-day alias at ~ 1.37 days. The peak due to CoRoT-7b now stands out along with its 1-day alias at $P = 1/(1 - 1/P_{\rm b}) \sim 5.82$ days and harmonics $P_{\rm b}/2$ and $P_{\rm b}/3$. Finally, I subtract the orbit of planet b, which leaves us with the periodogram of the residuals. We see that no strong signals remain except at the 1- and 2-day aliases arising from the window function of the ground-based HARPS observations.

The posterior joint probability distributions of each pair of parameters for the 2-planet (free eccentricities) model are shown in Figure 3.8. There are no strong correlations between any of the parameters. The K amplitudes of planets b and c are found to be unaffected by the number of planets, choice of eccentric or circular orbits, or choice of activity model (all, some or none of $\Delta RV_{\rm activity}$), even when I leave $P_{\rm c}$ unconstrained. The residuals, with an RMS scatter of 1.96 m.s^{-1}, are at the level of the error bars of the data and show no correlated behaviour, as seen in the bottom panel of Figure 3.5.

3.1.5.5 CoRoT-7b

The orbital parameters of CoRoT-7b are listed in the third column of Table 3.2. The orbital eccentricity of 0.12 ± 0.07 is detected with a low significance and is compatible with the transit parameters determined by Barros et al. (2014).

As I mentioned in Section 3.1.5.2, the mass of CoRoT-7b is not affected by the choice of model, which attests to the robustness of this result. My mass of 4.73 ± 0.95 M$_\oplus$ is compatible, within uncertainties, with the results found by Queloz et al. (2009), Boisse et al. (2011) and Tuomi et al. (2014). It is within 2-sigma of the masses found by Pont et al. (2010), Hatzes et al. (2011) and Ferraz-Mello et al. (2011).

3.1.5.6 CoRoT-7c

I make a robust detection of CoRoT-7c at an orbital period of 3.70 ± 0.02 days, which is in agreement with previous works that considered planet c. I estimate its mass to be 13.56± 1.08 M$_\oplus$ (see Table 3.2). This is in agreement with that given by Boisse et al. (2011) and Ferraz-Mello et al. (2011). It is just over 2-sigma lower than the mass found by Hatzes et al. (2010), and over 3-sigma greater than the

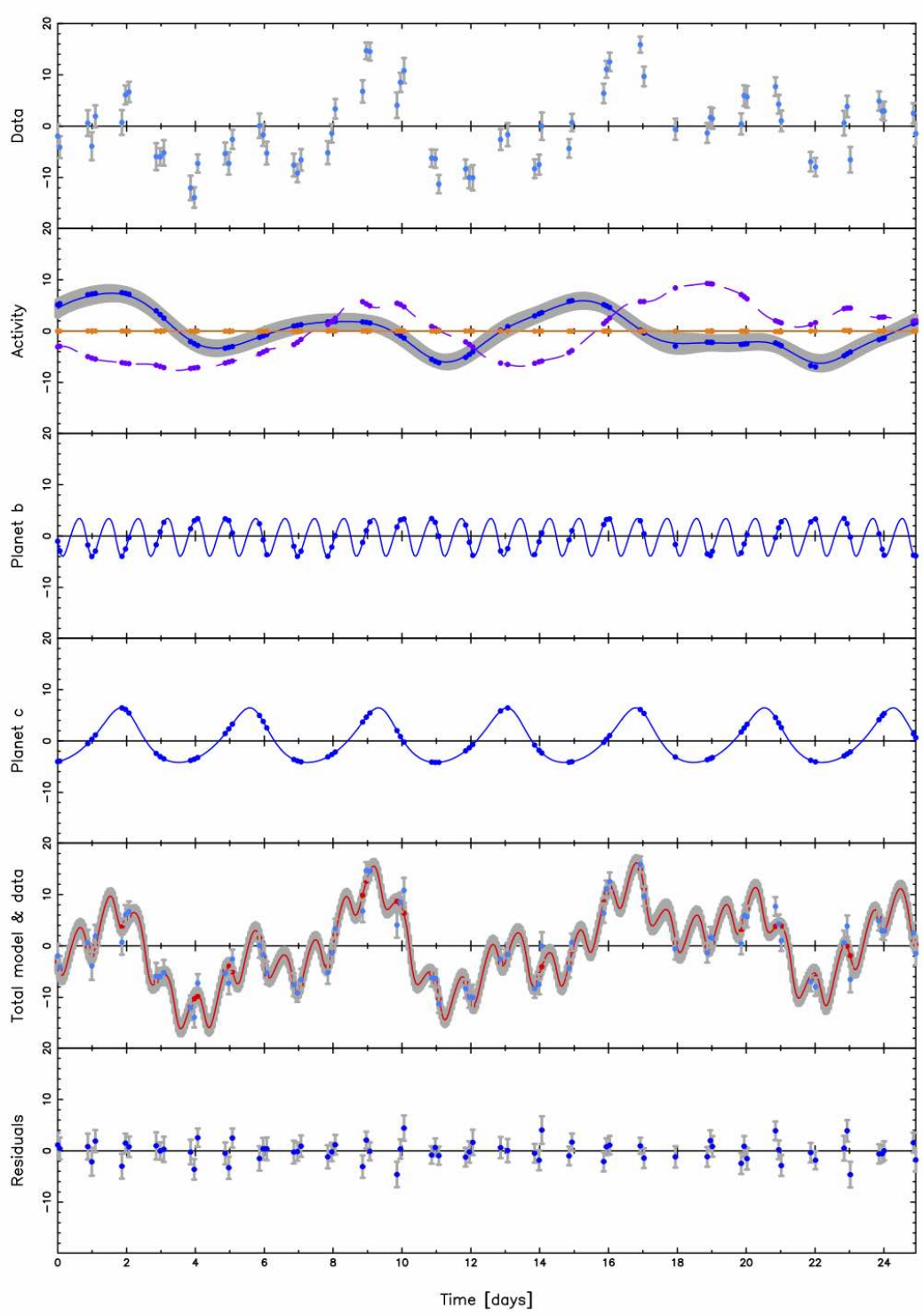

Figure 3.6: Time series of the various parts of the total RV model for Model 2, after subtracting the star's systemic velocity RV_0. All RVs are in m.s^{-1}. Panel (b): $A\Delta RV_{\rm rot}$ (orange full line), $B\Delta RV_{\rm conv}$ (purple dashed line) and $\Delta RV_{\rm rumble}$ (blue full line with grey error band). Panel (e): the total model (red), which is the sum of activity and planet RVs, is overlaid on top of the data (blue points). Subtracting the model from the data yields the residuals plotted in panel (f).

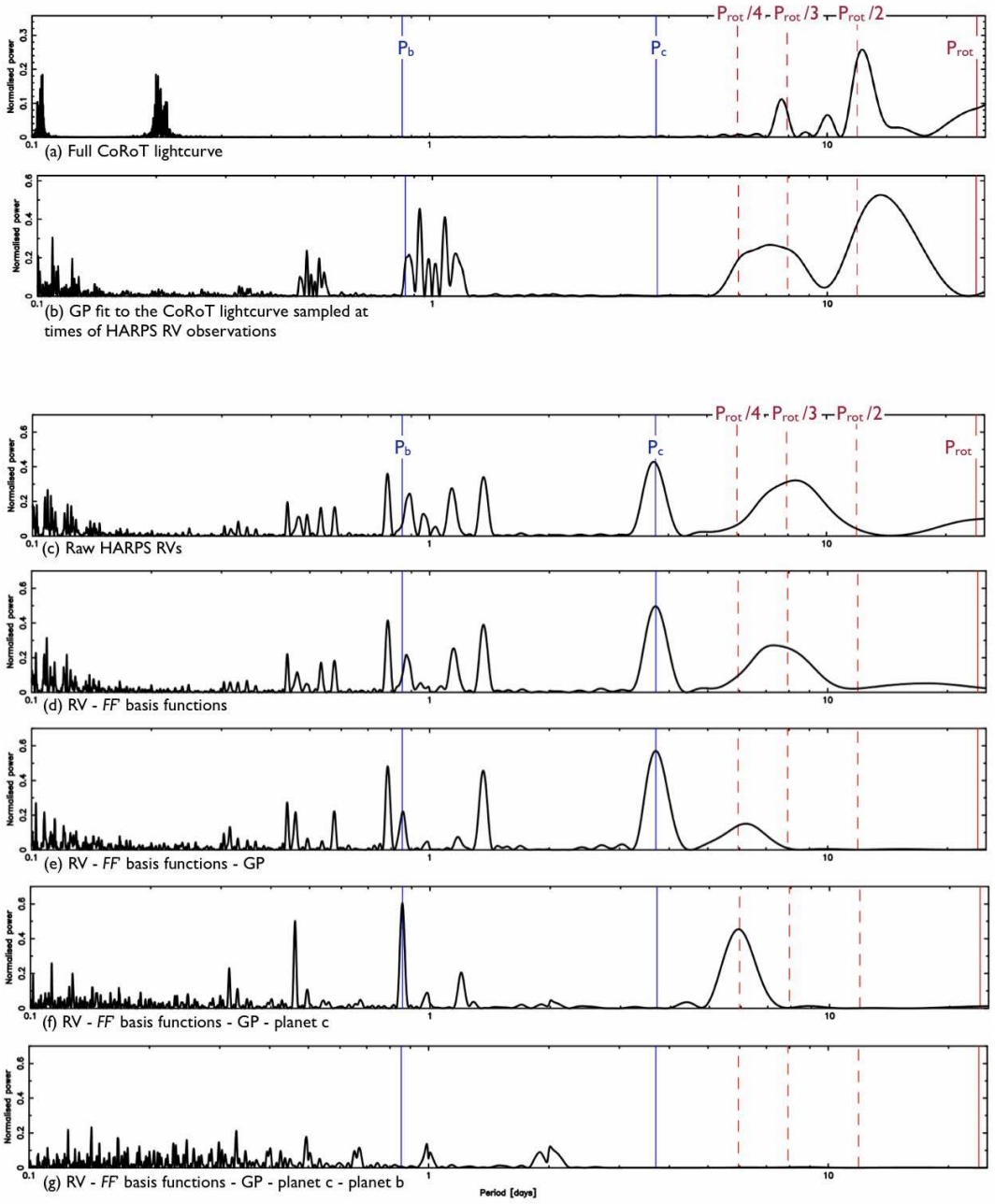

Figure 3.7: Lomb-Scargle periodograms of: (a) the full 2012 CoRoT lightcurve; (b) the Gaussian process fit to the 2012 CoRoT lightcurve sampled at the times of RV observations; (c) the raw 2012 HARPS RV observations; (d) the RV data, from which I subtracted the *FF'* basis functions; (e) same as (d), with the Gaussian process also removed; (f) same as (e), with the signal of planet c removed; (g) same as (f), with planet b removed.

mass calculated by Queloz et al. (2009). It suggests that the harmonic filtering technique employed by Queloz et al. (2009) suppresses the amplitude of the signal at this period. This may be due to the fact that P_c is close to the fifth harmonic of the stellar rotation, $P_{rot}/6 \sim 3.9$ days (see Figure 3.4), but Queloz et al. (2009) only model RV variations using the first two harmonics, thus leaving P_c and $P_{rot}/6$ entangled. Ferraz-Mello et al. (2011), who performed a similar analysis to that

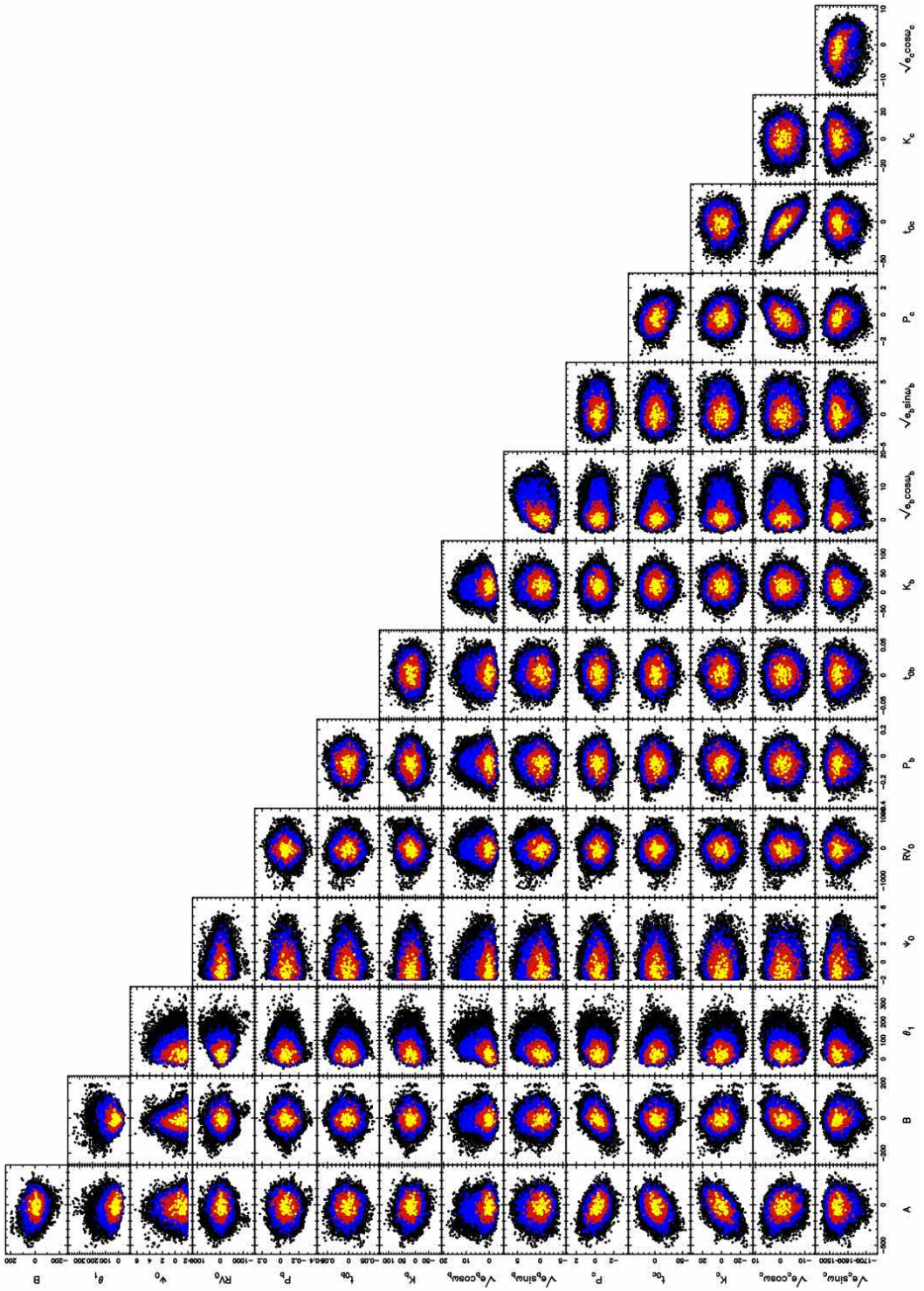

Figure 3.8: Phase plots for the MCMC chain of Model 2 for all parameters A, B, θ_1, Ψ_0, RV_0, P_b, $t_{0\mathrm{b}}$, K_b, $\sqrt{e}_\mathrm{b}\sin\omega_\mathrm{b}$, $\sqrt{e}_\mathrm{b}\cos\omega_\mathrm{b}$, P_c, $t_{0\mathrm{c}}$, K_c, $\sqrt{e}_\mathrm{c}\sin\omega_\mathrm{c}$, and $\sqrt{e}_\mathrm{c}\cos\omega_\mathrm{c}$. Points in yellow, red and blue are within the 1, 2 and 3-σ confidence regions, respectively. The scale of each axis corresponds to the departure of each parameter from its value at maximum likelihood. All are expressed in percent except for P_b, $t_{0\mathrm{b}}$ and $t_{0\mathrm{c}}$ which are expressed as one part per million. The distributions of Ψ_0 display a sharp cutoff at its minimum allowed value, which corresponds to the maximum observed flux value Ψ_max.

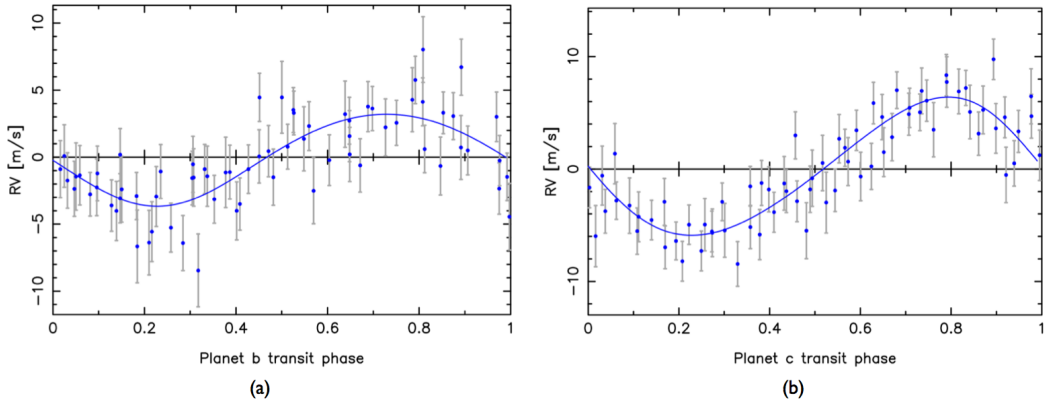

Figure 3.9: *Panel a:* Phase plot of the orbit of CoRoT-7b for Model 2, with the contribution of the activity and CoRoT-7c subtracted. *Panel b:* Phase plot of the orbit of CoRoT-7c for Model 2, with the contribution of the activity and CoRoT-7b subtracted.

of Queloz et al. (2009), mention that the proximity of P_c to $P_{rot}/6$ may lead to underestimating the RV amplitude of CoRoT-7c by up to 0.5 m.s^{-1} due to beating between these two frequencies.

I estimated the minimum orbital inclination this planet has to have in order to be transiting. Its radius R_c can be approximated using the formula given by Lissauer et al. (2011b):

$$R_c = \left(\frac{M_c}{M_\oplus}\right)^{1/2.06} R_\oplus, \tag{3.3}$$

where $M_\oplus$ and $R_\oplus$ are the mass and radius of the Earth. Using the mass for CoRoT-7c given in the third column of Table 3.2, I find $R_c = 3.54\ R_\oplus$. With this radius, CoRoT-7c would have to have a minimum orbital inclination of 83.7° in order to be passing in front of the stellar disc with respect to the observer.

CoRoT-7b's orbital axis is inclined at 79.0° to the line of sight (preliminary result of Barros et al. (2014)). According to Lissauer et al. (2011b), over 85% of observed compact planetary systems containing transiting super-Earths and Neptunes are coplanar within 3°. Planet c is therefore not very likely to transit. Indeed, no transits of this planet are detected in any of the CoRoT runs. Any planets further out from the star with a similar radius or smaller are even less likely to transit.

3.1.5.7 The magnetic activity of CoRoT-7

In Model 2, the RMS scatter of the total activity model is 4.86 m.s^{-1} (see Figure 3.6 b). For moderately active host stars such as CoRoT-7, the activity contribution largely dominates the reflex motion induced by a closely orbiting super-Earth.

The RMS scatter of ΔRV_{rot} and ΔRV_{conv} are 0.46 m.s^{-1} and 1.82 m.s^{-1}, respectively. The smaller impact of the surface brightness inhomogeneities on the RV variations could be due to the small $v \sin i$ of the star (Bruntt et al., 2010), because the amplitude of these variations scales approximately with $v \sin i$ (Desort et al., 2007). This suggests that for slowly rotating stars such as CoRoT-7, the suppression of convective blueshift is the dominant contributor to the activity-modulated RV signal, rather than the rotational Doppler shift of the flux blocked by starspots. This corroborates the findings of Meunier et al. (2010) and Lagrange et al. (2010),

who showed that the suppression of convective blueshift is the dominant source of activity-induced RV variations on the Sun, which is also a slowly rotating star (see discussions back in Chapter 1).

I use a Gaussian process to absorb correlated residuals due to other physical phenomena occurring on timescales of order of the stellar rotation period. In the case of CoRoT-7, these combined signatures have an RMS of 3.95 $\mathrm{m.s^{-1}}$, suggesting that there are other processes than those modelled by the *FF'* method at play.

3.1.6 Summary

The CoRoT-7 system was re-observed in 2012 with the CoRoT satellite and the HARPS spectrograph simultaneously. These observations allowed me to apply the *FF'* method of Aigrain et al. (2012) to model the RV variations produced by the magnetic activity of CoRoT-7. If I only use the *FF'* method to model the activity, I find correlated noise in the RV residuals which cannot be accounted for by a set of Keplerian planetary signals. This indicates that some activity-related noise is still present. Indeed, as previously mentioned in Section 1.2.5 in Chapter 1, the *FF'* method does not account for all phenomena such as the effect of limb-brightened facular emission on the cross-correlation function profile, photospheric inflows towards active regions, or faculae that are not spatially associated with starspot groups. Furthermore, some longitudinal spot distributions have almost no photometric signature (see Section 1.1.5.3). To model this low-frequency stellar signal, I use a Gaussian process with a quasi-periodic covariance function that has the same frequency structure as the lightcurve (see Chapter 2).

I run an MCMC simulation and use Bayesian model selection to determine the number of planets in this system and estimate their masses. I find that the transiting super-Earth CoRoT-7b has a mass of $4.73 \pm 0.95\,\mathrm{M_\oplus}$. Using the planet radius estimated by Bruntt et al. (2010), CoRoT-7b has a density of $(6.61 \pm 1.72)(R_\mathrm{p}/1.58\ \mathrm{R_\oplus})^{-3}\ \mathrm{g.cm^{-3}}$, which is compatible with a rocky composition. I confirm the presence of CoRoT-7c, which has a mass of $13.56 \pm 1.08\,\mathrm{M_\oplus}$. My findings agree with the analyses made by Barros et al. (2014), Hatzes et al. (in prep.), Lanza et al. (in prep.) and Tuomi et al. (2014).

I search for evidence of an additional planetary companion at a period of 9 days, as proposed by Hatzes et al. (2010) following an analysis of the 2008-2009 RV dataset. While the Lomb-Scargle periodogram of the 2012 RVs displays a strong peak in the 6-10 days range, I find that this signal is more likely to be associated with the second harmonic of the stellar rotation at ~ 7.9 days.

In CoRoT-7, the RV modulation induced by stellar activity dominates the total RV signal despite the close-in orbit of (at least) one super-Earth and one sub-Neptune-mass planet. Understanding the effects of stellar activity on RV observations is therefore crucial to improve our ability to detect low-mass planets and obtain a precise measure of their mass.

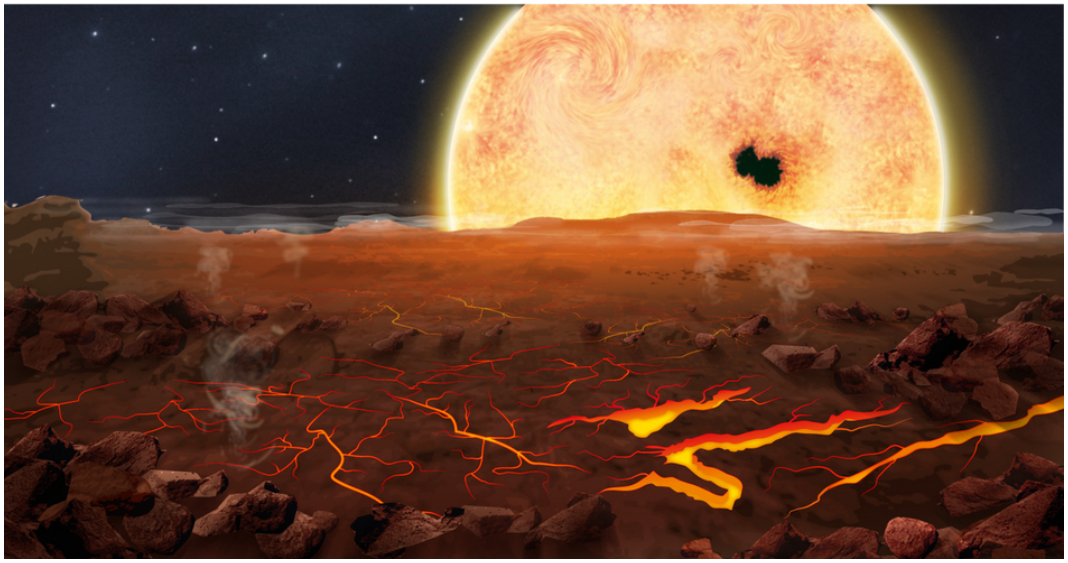

Artist impression of Kepler-78b: "an infernal Earth".
Credit: Jasiek Krzysztofiak, Nature.

3.2 Kepler-78

Kepler-78 is a very active star, and would have never been selected for an RV campaign were it not for the discovery of an Earth-size planet crossing its disc every 8.5 hours. It was found around the time at which I finished writing my MCMC code with Gaussian processes, so I decided to give it a go. It turns out that a Gaussian process trained on the lightcurve is very effective at modelling activity-driven RV variations for this kind of system.

3.2.1 History of the system

In 2013, Sanchis-Ojeda et al. (2013) reported on the discovery of a transiting short period Earth-size planet around Kepler-78. At the time, this was one of the first planets found with an orbital period of less than 1 day, and it was one of the smallest planets ever discovered. The main characteristics of the star and the transit parameters of Kepler-78b found by Sanchis-Ojeda et al. (2013) are detailed in Table 3.3.

Shortly after this announcement, the star was observed intensively with HARPS-N and HIRES in order to measure the mass of the planet. This was made tricky due to the high levels of activity of the host star. Its full *Kepler* lightcurve, shown in Figure 3.11 displays peak-to-peak variations of about 10 mmag. By my rule of thumb (acquired from my experience with CoRoT-7, Kepler-10 and results by Aigrain et al. (2012) – see Chapter 1), this translates into activity-induced variations of about 20 $m.s^{-1}$ peak to peak, and indeed this is what we see in the HIRES and HARPS-N RV observations (see Figure 3.10).

Pepe et al. (2013) reported on the HARPS-N observations. In order to determine the mass of the planet, they applied the nightly offsets method of Hatzes et al. (2011), originally developed to measure the mass of CoRoT-7b (see Sections 1.2.2 and 3.1.1). This technique relies on the stellar activity timescales (the stellar rotation period of about 12 days and its main harmonics) being much longer than the planet orbital

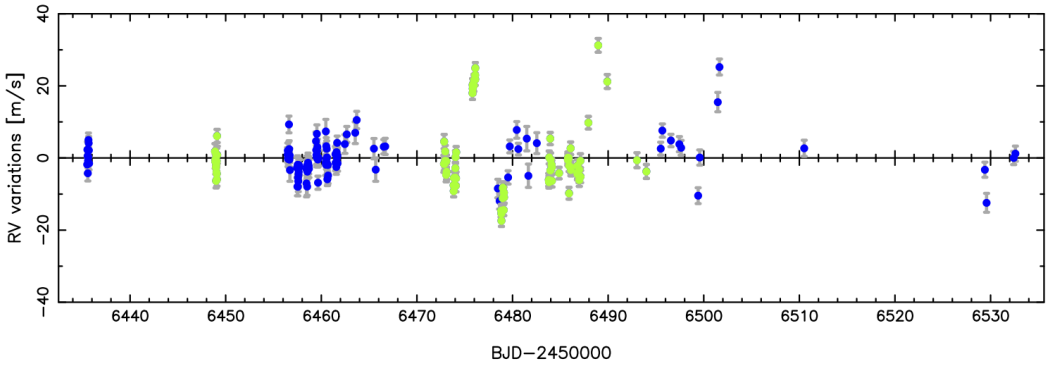

Figure 3.10: Kepler-78 RV observations by HARPS (blue points) and HIRES (green points).

period (about 8.5 hours). Over the span of a single night, all the variations in RV can be attributed to the planet's motion. It is therefore possible to treat the stellar activity signal as a nightly constant. Using this technique, Pepe et al. (2013) recover a semi-amplitude for Kepler-78b $K_\mathrm{b} = 1.96 \pm 0.32$ m.s^{-1}.

Howard et al. (2013) present the analysis of the HIRES RV data. They model the activity-induced RV variations as a sum of Fourier components with periods equal to the stellar rotation period and its first two harmonics (they show that the power at higher harmonics is negligible). This worked well since the activity signals are strongly modulated by the stellar rotation. With this technique, the semi-amplitude obtained for Kepler-78b is $K_\mathrm{b} = 1.66 \pm 0.40$ m.s^{-1}. The semi-amplitudes obtained through both analyses of the two independent datasets are in good agreement.

Following the analyses by Pepe et al. (2013) and Howard et al. (2013), Grunblatt, Howard & Haywood (2015) took a step further and combined the two RV datasets together in order to make a more precise mass determination. The model for activity-induced RV variations is based on a Gaussian process with a quasi-periodic covariance function, trained on the lightcurve in order to extract its frequency structure. We tested a variety of models, including quasi-periodic and square exponential covariance functions, additional white noise parameters and combinations thereof. The two spectrographs have a different wavelength coverage, and the active regions leading to RV variations may produce different amplitudes at different wavelengths, so we also tried modelling the activity signals with a separate Gaussian process for each RV dataset. We compared models in a qualitative way rather than doing a full Bayesian model selection analysis, which we deemed unnecessary at the time. We found that modelling the activity-driven RV variations as two separate Gaussian processes with separate η_1 but the same η_2, η_3 and η_4 hyperparameters, with the addition of two separate white noise terms provided the best fit. The results of this analysis are given in the second column of Table 3.4. We determine the planet mass to a 6.5-sigma precision, an improvement of 2.5-sigma over the value of Howard et al. (2013). Our mass value is in agreement with those of Pepe et al. (2013) and Howard et al. (2013).

The analysis I present here is much simpler: I only use a single Gaussian process for both datasets, with no additional white noise parameter. I will show that both analyses are in agreement. A Gaussian process on its own is effective at modelling activity-induced RV variations reliably, even for a star as active as Kepler-78.

Kepler-78	
Mass	$0.81 \pm 0.05\, M_\odot$
Radius	$0.74^{+0.10}_{-0.08}\, R_\odot$
Age	750 ± 150 Gyr
Projected rotation, $v \sin i$	2.4 ± 0.5 km.s^{-1}
Kepler-78b	
Orbital period	$0.35500744 \pm 0.00000006$ day
Mid-transit time	$2454953.95995 \pm 0.00015$ BJD
Orbital inclination	79^{+9}_{-14} deg
Radius	$1.16^{+0.19}_{-0.14}$ R$_\oplus$
Mass	$1.86^{+0.38}_{-0.25}$ M$_\oplus$

Table 3.3: Stellar parameters and transit parameters of Kepler-78b (from Sanchis-Ojeda et al. (2013)), adopted in my analysis. They derived the star's age based on its rotation period and mass, using the formula found by Schlaufman (2010) (this age is compatible with the star's projected rotation). The mass of Kepler-78b is that determined by Pepe et al. (2013).

3.2.2 Observations

3.2.2.1 Spectroscopy

The HARPS-N RV campaign spans 2013 May 23-August 28, with 112 observations. I discarded one observation at 24556435.724 BJD as its very low signal-to-noise ratio clearly indicates that it was taken during bad weather. The HIRES campaign, from 2013 June 05 to July 20 overlaps this period, and contains 84 observations. The RVs are shown in Figure 3.10. The data from both campaigns can be found in Tables A5 and A3 of the Appendix.

3.2.2.2 Photometry

Kepler-78 was observed by the *Kepler* satellite at long cadence. Figure 3.11 shows the lightcurve (transits removed) of all quarters concatenated together.

3.2.3 MCMC analysis

3.2.3.1 RV model

The orbit of Kepler-78b is modelled as a Keplerian signal. I model the stellar activity RV variations in both RV datasets using a single Gaussian process with a quasi-periodic covariance function trained on the off-transit lightcurve. My final model is as follows:

$$\begin{aligned}\Delta RV_{\rm tot}(t_i) = RV_{0,\rm Keck} + RV_{0,\rm HARPN} + \Delta RV_{\rm rumble}(t_i, \theta_1) \\ + \cos(\nu_{\rm b}(t_i, t_{\rm peri_b}, P_{\rm b}) + \omega_{\rm b}) + e_{\rm b}\cos(\omega_{\rm b})\big],\end{aligned} \tag{3.4}$$

where $RV_{0\rm Keck}$ and $RV_{0\rm HARPN}$ are constant offsets for each of the datasets. The period of the orbit of Kepler-78 is given by $P_{\rm b}$, and its semi-amplitude is $K_{\rm b}$. $\nu_{\rm b}(t_i, t_{\rm peri_b})$ is the true anomaly of the planet at time t_i, and $t_{\rm peri_b}$ is the time of periastron. I fix the eccentricity to zero, since with an orbital period of 8.5 hours it is reasonable to assume that the planet will be tidally locked to its star.

The period and phase of the planet's orbit are given Gaussian priors centred at the values determined though the photometric analysis of Sanchis-Ojeda et al. (2013), and with a sigma equal to the corresponding error bars of the photometry results.

I determine the parameters of my RV model following my usual MCMC procedure that I described in the previous Chapter.

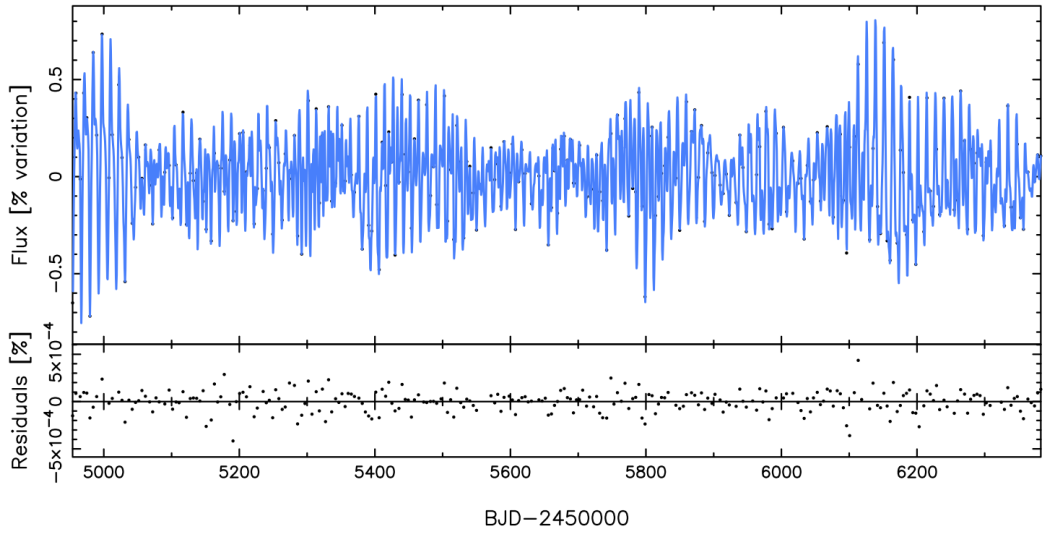

Figure 3.11: Kepler-78 binned lightcurve, fitted with a Gaussian process (quasi-periodic covariance function).

3.2.3.2 Gaussian process

I choose a quasi-periodic covariance function of the form:

$$k\,(t,t') = \eta_1^2\,.\,\exp\Big(-\frac{(t-t')^2}{2\eta_2^2} - \frac{2\sin^2(\frac{\pi(t-t')}{\eta_3})}{\eta_4^2}\Big). \tag{3.5}$$

In order to determine the best values of the hyperparameters η, I train the Gaussian process on half the lightcurve, sampled at every 100th point. The resultant lightcurve had 268 points, thus allowing me to compute the covariance matrix (of size 268×268) in reasonable time. The sampling corresponds to one point roughly every 2 days, which gives about 6 points per rotation period. Selecting only half the lightcurve still provides me with plenty of rotation cycles in order to estimate the evolution timescale of active regions.

I assume Jeffreys priors for the two timescales η_2 (active-region evolution) and η_3 (rotation period). I also constrain the smoothing factor η_4 to remain between 0 and 1 in order to prevent it from interfering with the evolution timescale. For example, high frequency variations could be accounted for with either a very high value of η_4 or a very small η_2. Constraining η_4 helps avoid this "degeneracy". The best hyperparameter values, determined through the MCMC procedure described in Section 2.1.6, are as follows:

1. Amplitude $\eta_1 = 0.0024 \pm 0.0001$ flux units. I subtracted the average value of the flux and then divided by this same value so that the numbers were between 0 and 1;

2. Evolution timescale $\eta_2 = 17\pm1$ days. It is longer than the recurrence timescale, which is consistent with the long-lived spots we can see from the autocorrelation function of the lightcurve, shown in Figure 3.12;

3. Recurrence timescale $\eta_3 = 12.74 \pm 0.06$ days. This rotation period is in agreement with the value $P_{\rm rot} = 12.71$ days that I get from an autocorrelation analysis, and $P_{\rm rot} = 12.5 \pm 1$ days found by Sanchis-Ojeda et al. (2013);

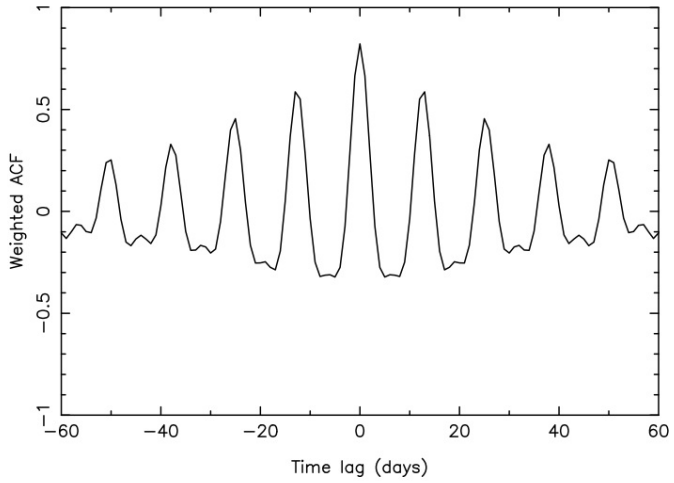

Figure 3.12: Autocorrelation function of the lightcurve of Kepler-78. It reveals the presence of long-lived active regions, which remain on the stellar disc for several rotations.

4. Smoothing coefficient $\eta_4 = 0.47 \pm 0.05$.

The activity-driven RVs are modelled with a Gaussian process that has the same quasi-periodic covariance function with a set of hyperparameters θ. I set θ_2, θ_3 and θ_4 equal to η_2, η_3 and η_4, respectively. The amplitude θ_1 of the Gaussian process is kept as a free parameter in the MCMC.

3.2.4 Results and discussion

Table 3.4 lists the best-fit parameters I obtain, together with those of Grunblatt et al. (2015). I measure a planet semi-amplitude $K_\mathrm{b} = 1.87 \pm 0.19$ m.s^{-1}. The phase-folded orbital signal of Kepler-78b is shown in Figure 3.13.

My mass determination is consistent with the results found by Grunblatt et al. (2015), Howard et al. (2013) and Pepe et al. (2013). The error bar of my result is slightly smaller than that determined by Grunblatt et al. (2015), but the residuals have an RMS scatter of 2.3 m.s^{-1}, which is slightly higher than the average level of the error bars of 1.92 m.s^{-1} (and the periodogram of the residuals, in panel (d) of Figure 3.15, shows no significant signals). Grunblatt et al. (2015) use additional white noise terms, which act to increase the error bars of their model in order to bring the RMS of the residuals to the level of the error bars. This additional white noise is likely to come from p-mode oscillations and granulation motions that not have been completely averaged out in each individual RV observation.

All the components of the RV model are shown in Figure 3.14. Consider the 2 anomalous HARPS-N observations just before day 70; were it not for the presence of similar outliers around days 40 and 50 in the HIRES observations, these points may have been dismissed as outliers affected by instrumental effects or bad weather (this is in fact what Pepe et al. (2013) did). The Gaussian process, however, has no trouble at all accounting for these measurements. This implies that they are compatible with a process that has the same covariance properties, or frequency structure as the lightcurve, and by extension as the magnetic activity behaviour of Kepler-78. The Gaussian process reconciles the two datasets elegantly and effortlessly. Panels (b) and (c) highlight the amplitude difference between the activity-induced variations and the planet orbit. The difference in frequency structure, which is what this

	My model	Grunblatt et al.
Planet b		
P [days]	$0.35500744 \pm 0.00000006$	
t_0 [BJD - 2450000]	$2454953.95995 \pm 0.00015$	
K [m.s^{-1}]	1.87 ± 0.19	1.86 ± 0.25
e	0 (fixed)	0 (fixed)
m [M$_\oplus$]	1.76 ± 0.18	$1.87^{+0.27}_{-0.26}$
ρ [g.cm^{-3}]	$6.2^{+1.8}_{-1.4}$	$6.0^{+1.9}_{-1.4}$
a [AU]	0.009 ± 0.001	-
Gaussian process for stellar activity		
θ_1 [m.s^{-1}]	8.78 ± 1.11	0
$\theta_{1,\mathrm{HARPN}}$ [m.s^{-1}]	0	$5.6^{+2.0}_{-1.3}$
$\theta_{1,\mathrm{Keck}}$ [m.s^{-1}]	0	$11.6^{+3.7}_{-2.5}$
θ_2 [days]	17 ± 1	$26.1^{+19.8}_{-11}$
θ_3 [days]	12.74 ± 0.06	$13.12^{+0.14}_{-0.12}$
θ_4	0.47 ± 0.05	$0.28^{+0.05}_{-0.04}$
Additional white noise		
σ_{HARPN} [m.s^{-1}]	0	$1.1^{+0.4}_{-0.5}$
σ_{Keck} [m.s^{-1}]	0	$2.1^{+0.3}_{-0.3}$
Constant RV offsets		
$RV_{0,\mathrm{HARPN}}$ [m.s^{-1}]	2.5 ± 3.3	-
$RV_{0,\mathrm{Keck}}$ [m.s^{-1}]	-1.0 ± 3.4	-

Table 3.4: Outcome of my model, which consists of a Gaussian process with a quasi-periodic covariance function, one Keplerian circular orbit and one zero offset for each RV dataset, compared with the model applied by Grunblatt et al. (2015), consisting of two separate Gaussian processes, one Keplerian circular orbit, two RV offsets and two additional white noise terms (σ). The quantities marked as '-' in the second column are part of their model, but their values were not listed in the paper.

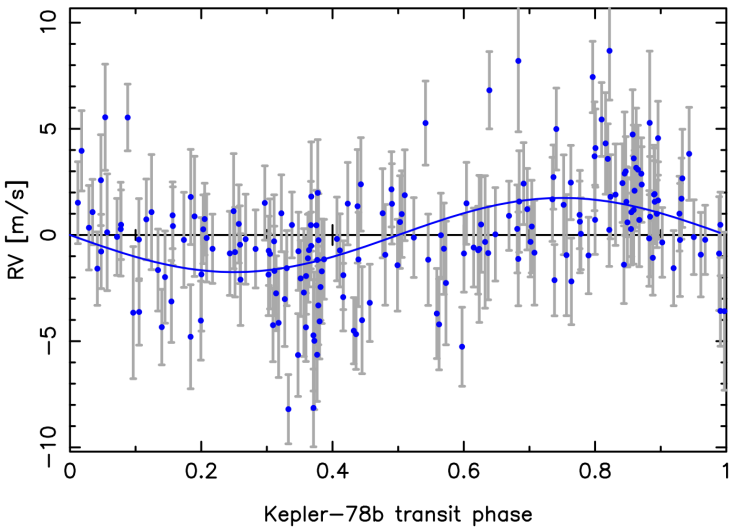

Figure 3.13: Phase plot of the orbit of Kepler-78b (circular model).

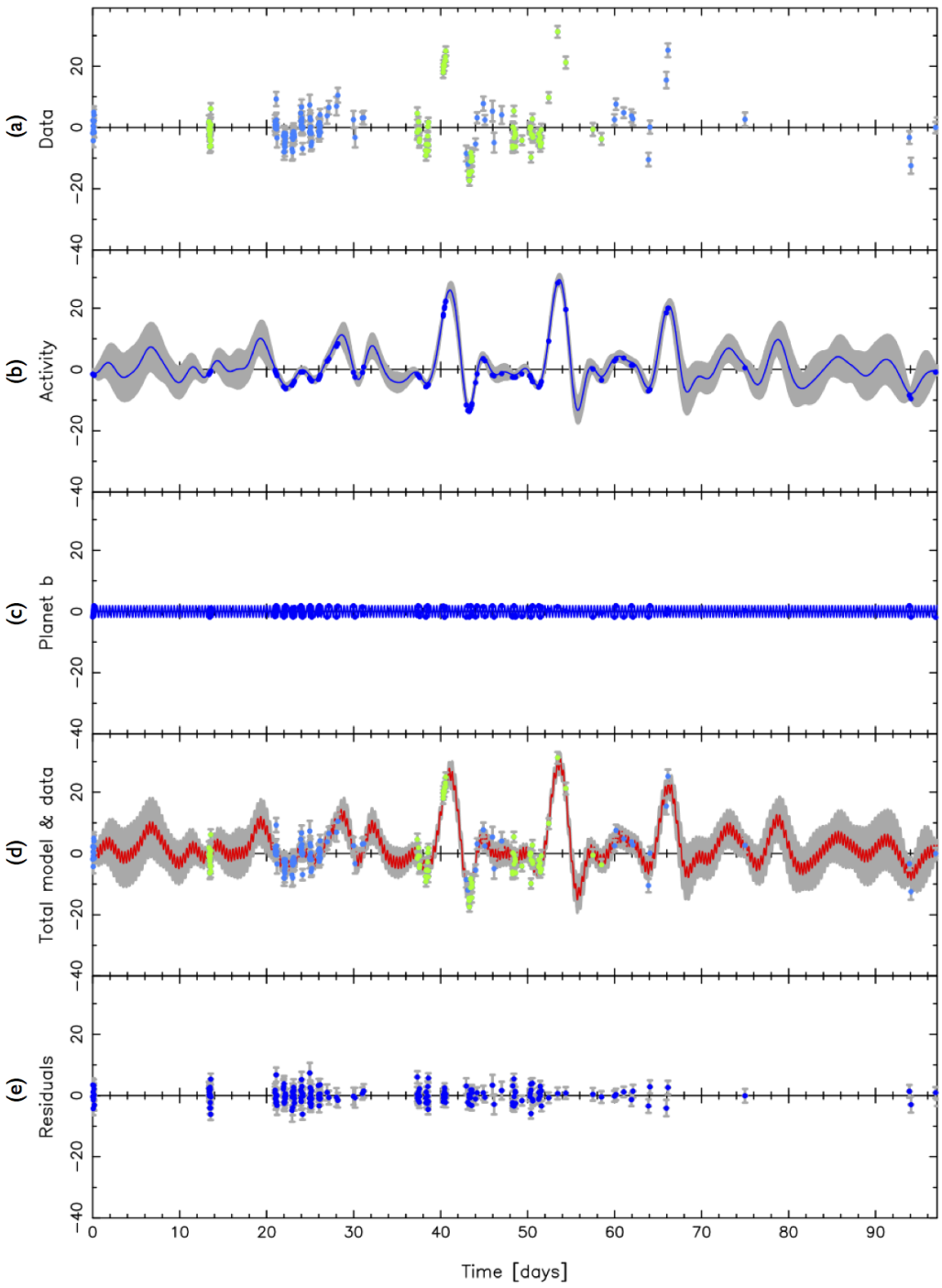

Figure 3.14: *Panel (a):* the HARPS and HIRES observations, after subtracting the RV offsets for each dataset; *Panel (b):* Gaussian process; *Panel (c):* orbit of Kepler-78b; *Panel (d):* total model (red), overlaid on top of the data (blue points). *Panel (e):* residuals obtained after subtracting the model from the observations. All RVs are in $m.s^{-1}$.

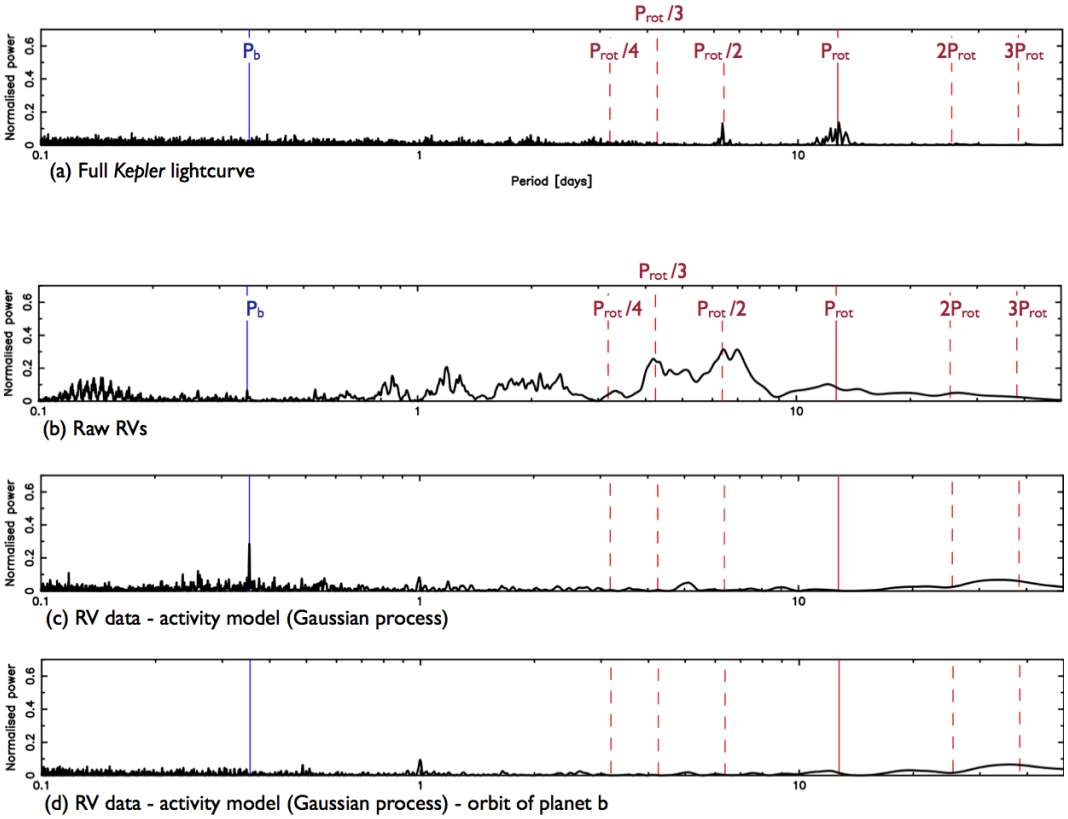

Figure 3.15: Lomb-Scargle periodograms of: (a) the full *Kepler* lightcurve; (b) the raw RV observations (both datasets); (c) the RV data, from which the activity model has been subtracted, revealing a strong peak at the orbital period of Kepler-78b; (d) same as (c), with the orbit of planet b removed.

analysis relies on, is also highlighted by these plots.

3.2.4.1 The magnetic activity of Kepler-78

Figure 3.15 shows Lomb-Scargle periodograms of the *Kepler* lightcurve (panel (a)) and the combined HARPS and HIRES RV data (panel(b)). I computed periodograms on the two RV datasets merged together, assuming a zero RV offset between the two datasets. This is a reasonable assumption, given the estimates of $RV_{0,\mathrm{HARPN}}$ and $RV_{0,\mathrm{Keck}}$ listed in Table 3.4. Although these periodograms are therefore not fully rigorous, they still provide a valuable insight on the frequency structure of the various contributions of my RV model.

The periodogram of the lightcurve, in panel (a) displays strong peaks at P_{rot} and at $P_{\mathrm{rot}}/2$. The periodogram of the raw RVs, in panel (b), is dominated by peaks at $P_{\mathrm{rot}}/2$ and $P_{\mathrm{rot}}/3$; we also see some power at P_{rot} and $P_{\mathrm{rot}}/4$. There is a hint of a peak at the planet's orbital period P_{b}, but we wouldn't be able to tell the presence of a planet. Once I subtract the Gaussian process, however, the orbit of Kepler-78b becomes clear: the Gaussian process has absorbed the activity signal so successfully that the RV signal due to the planet is detected unambiguously, even without the prior knowledge provided by the *Kepler* transits.

3.2.5 Summary

Following the discovery of the transiting Earth-size planet Kepler-78b, the system was observed with both the HARPS and HIRES spectrographs. I combined these two RV datasets together and used a Gaussian process trained on the lightcurve to model the activity-induced RV variations, which dominate the total RV variations and reach amplitudes of up to 20 $m.s^{-1}$. I find that the Gaussian process is reliable and effective at accounting for activity-induced signals and allows me to determine a mass for Kepler-78b which is consistent with previous estimates made by Howard et al. (2013), Pepe et al. (2013) and Grunblatt et al. (2015). The precision of my mass determination is slightly better than that of Grunblatt et al. (2015), who analysed the same combined dataset with a model consisting of two separate Gaussian processes and two white noise terms.

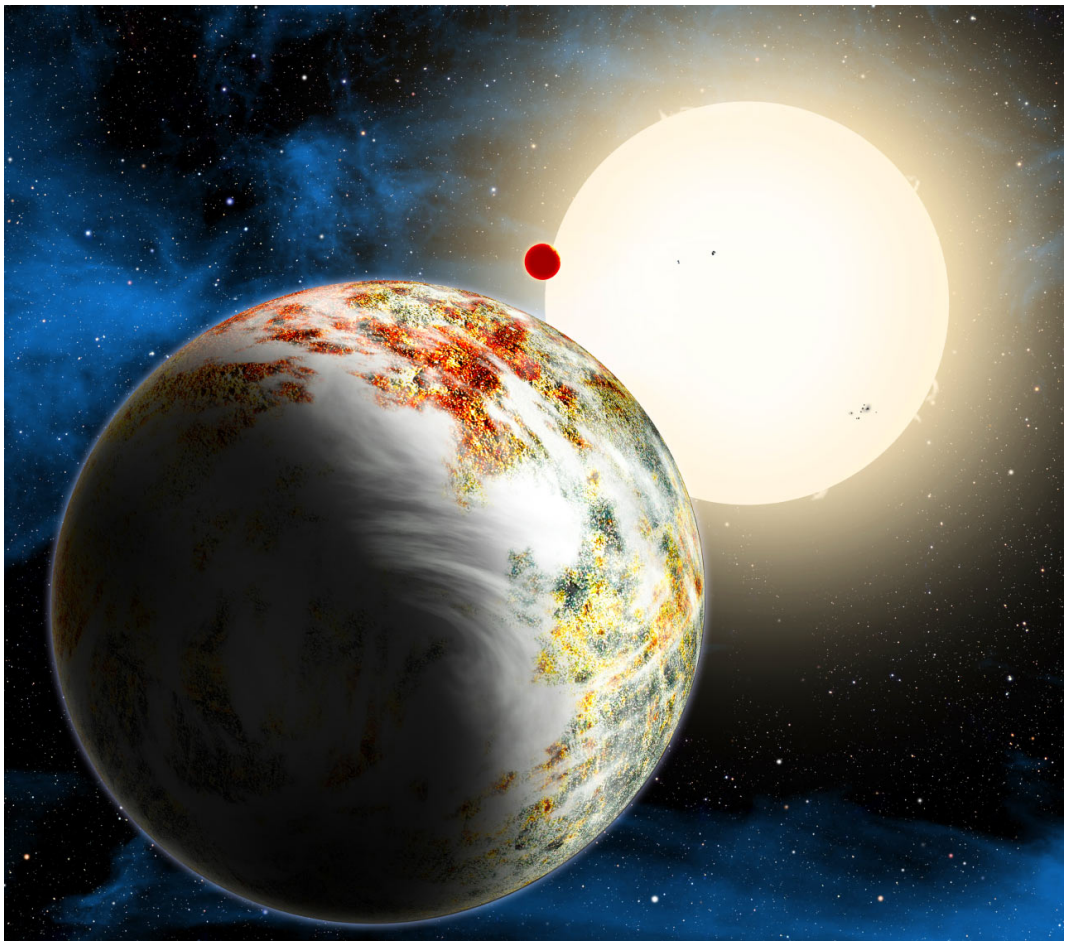

"Kepler-10c, the Godzilla of Earths!" *Term coined by Prof. Dimitar Sasselov*
Artist impression of the Kepler-10 planetary system. *Credit: David Aguilar, Harvard-Smithsonian Center for Astrophysics.*

3.3 Kepler-10

Kepler-10 couldn't be more different to Kepler-78. Due to its old age, it is a very quiet star, making it an ideal target for RV follow-up. It is so well-behaved that Dumusque et al. (2014) determined the masses of Kepler-10b and c to excellent precision without the use of any sophisticated activity model – my Bayesian model comparison ruled out the use of a Gaussian process over a simple white noise term by a factor of 10^{16}!

I can still learn valuable lessons from such a system. In this Section, I show that my Gaussian process model leaves the planet orbits untouched, allowing me to make an honest determination of their masses.

3.3.1 History of the system

A few months after the discovery of CoRoT-7b, the *Kepler* team announced the detection of several more transiting super-Earths (Borucki et al., 2011). Amongst them, Kepler-10b was the smallest transiting planet yet discovered (Batalha et al., 2011b), with a radius of just 1.4 $R_\oplus$. A second planet candidate with an orbital

Kepler-10	
Mass	$0.913 \pm 0.022\, M_\odot$
Radius	$1.065 \pm 0.008\, R_\odot$
Age	10.50 ± 1.33 Gyr
Projected rotation, $v \sin i$	0.5 ± 0.5 km.s^{-1}
Kepler-10b	
Orbital period	$0.837495^{+0.000004}_{-0.000005}$ day
Mid-transit time	$2454964.57375^{+0.00060}_{-0.00082}$ HJD
Orbital inclination	$84.4^{+1.1}_{-1.6}$ deg
Radius	$1.416^{+0.033}_{-0.036}$ R$_\oplus$
Mass	$4.56^{+1.17}_{-1.29}$ M$_\oplus$
Kepler-10c	
Orbital period	$45.29485^{+0.00065}_{-0.00076}$ days
Mid-transit time	$2454971.6761^{+0.0020}_{-0.0023}$ HJD
Orbital inclination	$89.65^{+0.09}_{-0.12}$ deg
Radius	$2.227^{+0.052}_{-0.057}$ R$_\oplus$

Table 3.5: Stellar parameters (from Fogtmann-Schulz et al. (2014)) and transit parameters of Kepler-10b and c (from Batalha et al. (2011b) and Fressin et al. (2011), respectively), adopted in my analysis.

period of about 45 days was also identified, but was not validated by BLENDER (Torres et al., 2011) as scenarios of false positive detections remained too likely with the data available at the time. Follow-up RV observations of Kepler-10 with Keck/HIRES were carried out in order to determine the mass of Kepler-10b (Batalha et al., 2011b). Only 40 measurements were obtained, spread over just under a year. These observations yielded a mass with a precision of less than 3-sigma (see Table 3.5) for Kepler-10b. The orbit of Kepler-10c was not detected in the RV measurements, which meant it was only possible to place an upper limit to the mass of this potential additional planetary companion. Further transit observations were later acquired with the *Spitzer* Space Telescope, allowing Fressin et al. (2011) to perform a new BLENDER analysis and validate this second candidate as a small Neptune with a 2.2 $R_\oplus$ radius.

The discovery of such an exciting planetary system prompted Fogtmann-Schulz et al. (2014) to carry out an asteroseismic analysis of the star's physical parameters, using 29 months of *Kepler* photometry instead of only the first 5 months of the mission, as had been done for the discovery paper. The radius, mass and age of Kepler-10 determined by Fogtmann-Schulz et al. (2014) are listed in Table 3.5. Kepler-10 was found to be over 10 Gyr old, which made it the oldest known star to host rocky planets! This also meant that it should be slowly rotating and magnetically quiet, and indeed, its *Kepler* lightcurve, shown in Figure 3.17, displays almost no variability.

3.3.2 Observations

3.3.2.1 HARPS-N spectroscopy

Kepler-10 seemed like a target of choice for RV follow-up, so the HARPS-N team decided to observe Kepler-10 twice per night over several months. The results of this campaign were reported by Dumusque et al. (2014). A few measurements were discarded from the analysis of Dumusque et al. for the following reasons:

- Measurements that had a signal-to-noise ratio (at 550 nm) lower than 10 (this was the case for 4 observations);

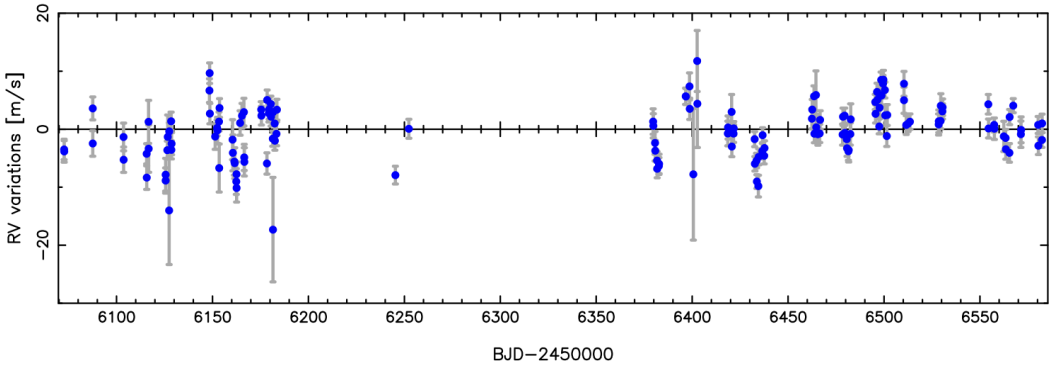

Figure 3.16: RV variations of Kepler-10 measured with HARPS-N.

- All stars observed on the night of 18 October 2013 show an RV offset of 10 m.s^{-1} or more, so we removed the 2 observations taken on this night;
- The original HARPS-N CCD suffered a partial failure in September 2012, and was operated using only the red half of the CCD until a replacement chip was procured and installed in November 2012. We took measurements with only half of the chip for a few nights until the CCD was replaced. This means that the RVs were derived with fewer (and different) spectral lines, so we decided to discard the 5 observations concerned.

This left us with 148 observations, shown in Figure 3.16. The data are avaliable in Table A8 of the Appendix.

3.3.2.2 *Kepler* photometry

The *Kepler* spacecraft observed Kepler-10 with a 1-minute cadence up to Quarter 14 of the mission (Fogtmann-Schulz et al., 2014). Figure 3.18 a shows all the *Kepler* quarters, which I concatenated together by fitting a constant for each – this is a rough procedure but works well (see Chapter 1, Section 1.3).

Determination of the stellar rotation period I computed the autocorrelation of the full lightcurve, shown in Figure 3.18 b (see Section 1.3.2.2). It yields a rotation period of 45 days. It is apparent, however, that the beginning and end of several quarters display unexpected wiggles that look more like instrument systematics than stellar activity; they are likely to affect our estimate of the rotation period. We (Dumusque et al.) computed the autocorrelation of single quarters, with the wiggles cut out, and consistently arrived at periods between 15 and 16 days. This is significantly different to the 45-day period determined from the concatenated lightcurve. It is also incompatible with the old age of Kepler-10, which points towards a rotation period of at least 22 days (Dumusque et al., 2014). The star's projected rotational velocity (see Table 3.5) is very low and consistent with a period of at least 26 days. Kepler-10 seems to be a case where the PDC-MAP data reduction pipeline erased long-term periodic signals; as I explained in Section 1.3 back in Chapter 1, this can unfortunately happen.

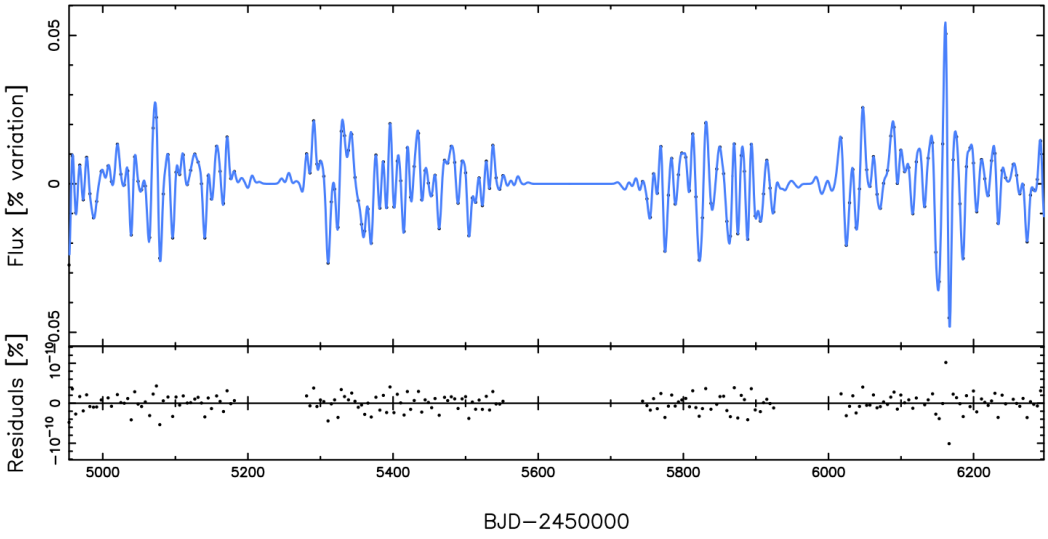

Figure 3.17: *Upper panel:* Selected parts of the (binned) Kepler-10 *Kepler* lightcurve that I used to compute the autocorrelation period (45 days), with my photometric fit overplotted as the blue curve. *Lower panel:* Residuals of the fit.

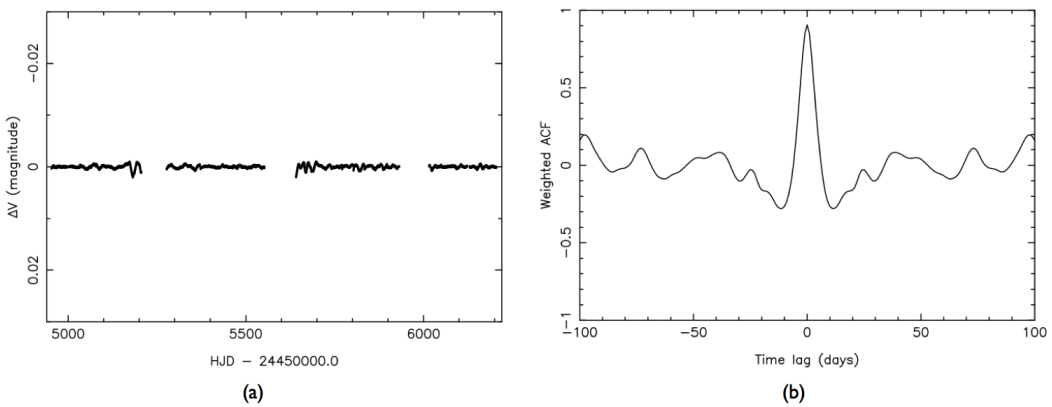

Figure 3.18: *Panel a:* the full concatenated PDC-MAP *Kepler* lightcurve, in which instrumental "wiggles" are clearly present; *panel b:* its autocorrelation function, which indicates a rotation period at 45 days, but shows little structure otherwise. Compare this plot with other similar ones in Figure 1.13 of Chapter 1 to see just how quiet Kepler-10 is!

3.3.3 MCMC analysis

3.3.3.1 RV model

Since we (Dumusque et al.) were not able to obtain a precise and reliable estimate of the rotation period of Kepler-10, we could not justify using a Gaussian process with a quasi-periodic covariance function to account for noise modulated by the rotation of Kepler-10 in the final paper. Besides, the star is very quiet and the RV observations we see in Figure 3.16 display an RMS scatter of just over 4 $m.s^{-1}$, which indicates that any activity-induced variations will be very small and unlikely to significantly affect our planetary mass measurements, and that using a Gaussian process would be excessive (this was confirmed by a Bayesian model comparison which yielded a Bayes' factor of 10^{16} in favour of a white noise term over a Gaussian process). The MCMC analysis presented in Dumusque et al. (2014) accounts for any such variations with a constant white noise term, added in quadrature to the error bars, commonly referred to as a "jitter" term. I did run my code with this model, and the results are included in Section 4.5 of Dumusque et al. (2014). Here, I prefer to show the results I obtained with a model comprising a Gaussian process. We shall see that the final mass determinations are compatible with the ones obtained with the model of Dumusque et al. (2014), which attests that the Gaussian process does not absorb the original signals of the two planets.

I ran my MCMC code for a model consisting of two Keplerian orbits, two zero RV offsets in order to account for any changes incurred by the replacement of the CCD, and a Gaussian process to model activity-induced signals, governed by a quasi-periodic covariance function.

As starting points to my MCMC simulation, I adopted the K amplitudes found by the preliminary analyses done in Sections 4.3 and 4.4 of Dumusque et al. (2014). The orbits of the two planets were constrained by applying Gaussian priors on the orbital period and epochs of transit found by previous photometric analyses, presented in Table 3.5. The usual priors discussed in Section 2.2.4 were applied for all other parameters.

3.3.3.2 Gaussian process

Based on my previous experience of modelling activity-induced RV variations with a Gaussian process, I assumed a quasi-periodic covariance function. Instead of training the Gaussian process on the lightcurve to determine the hyperparameters of the covariance function, I assumed the following hyperparameter values:

- Amplitude: determined via the MCMC procedure that I carried out;
- Recurrence timescale (stellar rotation period): according to the investigations carried out by Dumusque et al. (2014), it is likely to be at least 22 days, and accoring to the autocorrelation function of the lightcurve in Figure 3.18, it is likely to be around 45 days. Looking at the periodogram of the RVs in panel (a) of Figure 3.19, there is a peak at 52 days with clear harmonics at $P/2$, $P/3$ and $P/4$ (see red full and dashed lines). It therefore seems reasonable to assume that this is the stellar rotation period;
- Evolution timescale: I assumed this to be half the rotation period, i.e. 26 days;

	My model	Dumusque et al. (2014)
Kepler-10b		
P [days]	0.8374907(2)	0.8374907(2)
t_0 [BJD - 2450000]	5034.0868(2)	5034.0868(2)
K [m.s^{-1}]	2.37 ± 0.23	2.38 ± 0.34
e	0 (fixed)	0 (fixed)
m [M$_\oplus$]	3.31 ± 0.32	3.33 ± 0.49
ρ [g.cm^{-3}]	$6.4^{+1.1}_{-0.7}$	5.8 ± 0.8
a [AU]	0.016(1)	-
Kepler-10c		
P [days]	45.29429(4)	45.29430(4)
t_0 [BJD - 2450000]	5062.2664(4)	5062.26648(8)
K [m.s^{-1}]	3.09 ± 0.69	3.25 ± 0.36
e	0 (fixed)	0 (fixed)
m [M$_\oplus$]	16.2 ± 3.6	17.2 ± 1.9
ρ [g.cm^{-3}]	8.1 ± 1.8	7.1 ± 1.0
a [AU]	0.24(1)	-
Additional noise		
θ_1 [m.s^{-1}]	2.37 ± 0.34	0
σ_s [m.s^{-1}]	0	$2.45^{+0.23}_{-0.21}$

Table 3.6: Outcome of my model, which consists of a Gaussian process with a quasi-periodic covariance function, 2 planet orbits with eccentricities fixed to 0 and two zero offsets (to account for the CCD replacement), compared with the results of the model applied by Dumusque et al. (2014), in which the Gaussian process is replaced by a white noise term. The numbers in brackets represent the uncertainty in the last digit of the value.

- Smoothing parameter : 0.5.

3.3.4 Results and discussion

3.3.4.1 Selection of the best model

I found that a 2-planet model with fixed circular orbits is preferred over a model with free eccentricities by a factor of 2047 (according to Jeffreys (1961), a Bayes' factor over 150 indicates strong evidence). When the eccentricities are let free, I obtain $e_\mathrm{b} = 0.002 \pm 0.002$ and $e_\mathrm{c} = 0.002 \pm 0.05$, which suggests that both orbits are compatible with circular orbits. Furthermore, I see no significant difference in the planet masses or the RV residuals.

3.3.4.2 Best model

The results for a 2-planet model with forced circular orbits are listed in Table 3.6. The K amplitudes found for both planets in agreement, within 1-sigma, with the main MCMC analysis presented in Dumusque et al. (2014). The uncertainty on my mass determination of Kepler-10b is smaller than that of Dumusque et al. (2014), but in the case of Kepler-10c this goes the other way around.

The Gaussian process framework is more flexible than a white noise term. My intuition tells me that the Gaussian process will allow me to determine the masses of planets at different orbital periods with varying levels of uncertainty, depending on

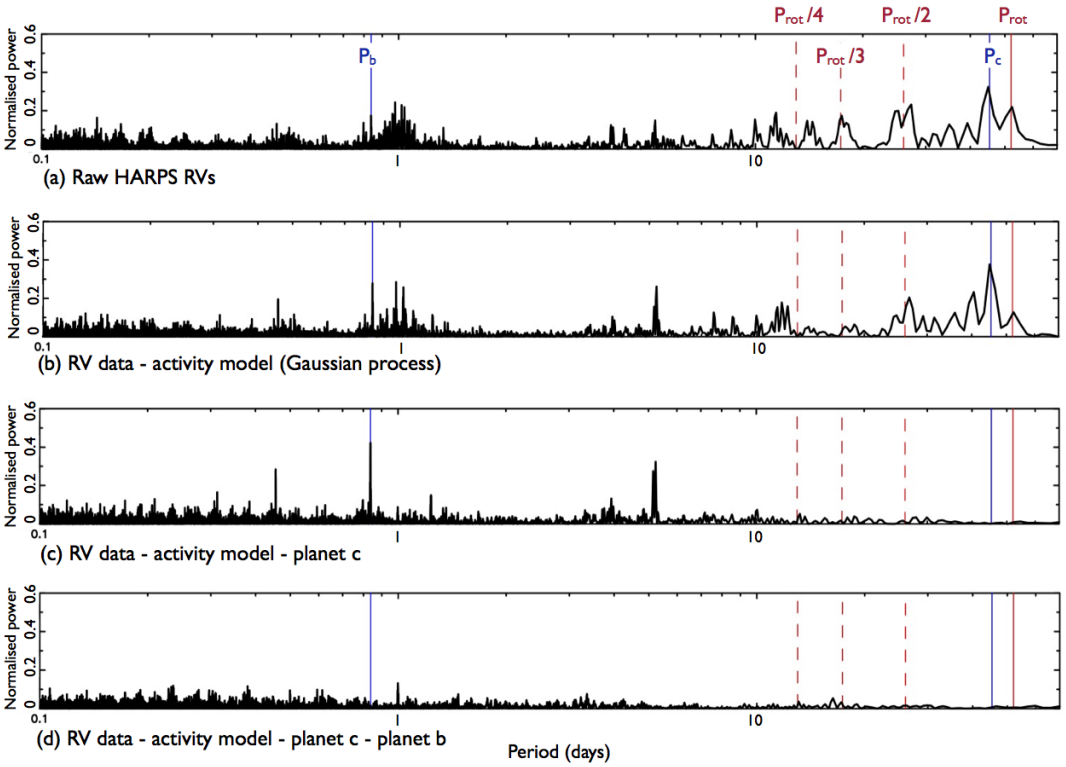

Figure 3.19: Lomb-Scargle periodograms of: (a) the raw RV observations; (b) the RV data, from which the activity RV model has been subtracted; (c) same as (b), with the RV signal of planet c also removed; (d) finally, the RV contribution of planet b is also removed.

their "temporal proximity", i.e. their degree of overlap with the frequency structure of the Gaussian process. If this were the case, the results could be interpreted as follows:

- The orbital period of Kepler-10b (0.85 day) is very distinct from the frequency structure of the Gaussian process (52 days and harmonics thereof). The Gaussian process is unlikely to interfere with the orbit of Kepler-10b. The model is therefore able to unambiguously identify this signal, yielding a precise mass determination.
- The orbital period of Kepler-10c, on the other hand, is much closer to the recurrence timescale governing the structure of the Gaussian process (35 days – see the first two periodograms of Figure 3.19). In this region of parameter space, it is therefore more tricky to isolate the orbital signature of the planet. The uncertainty on the mass determination increases in order to reflect this.
- In comparison, a white noise term would provide a constant level of uncertainty regardless of the stellar activity and orbital timescales.

It would be of utmost interest to see whether this is indeed the case, and further investigation is required. I discuss a possible future project to tackle this at the end of this Chapter.

Figure 4.6 shows each component of the total RV model. We cannot see the variations of Kepler-10b very clearly because its orbital period is very short, but from

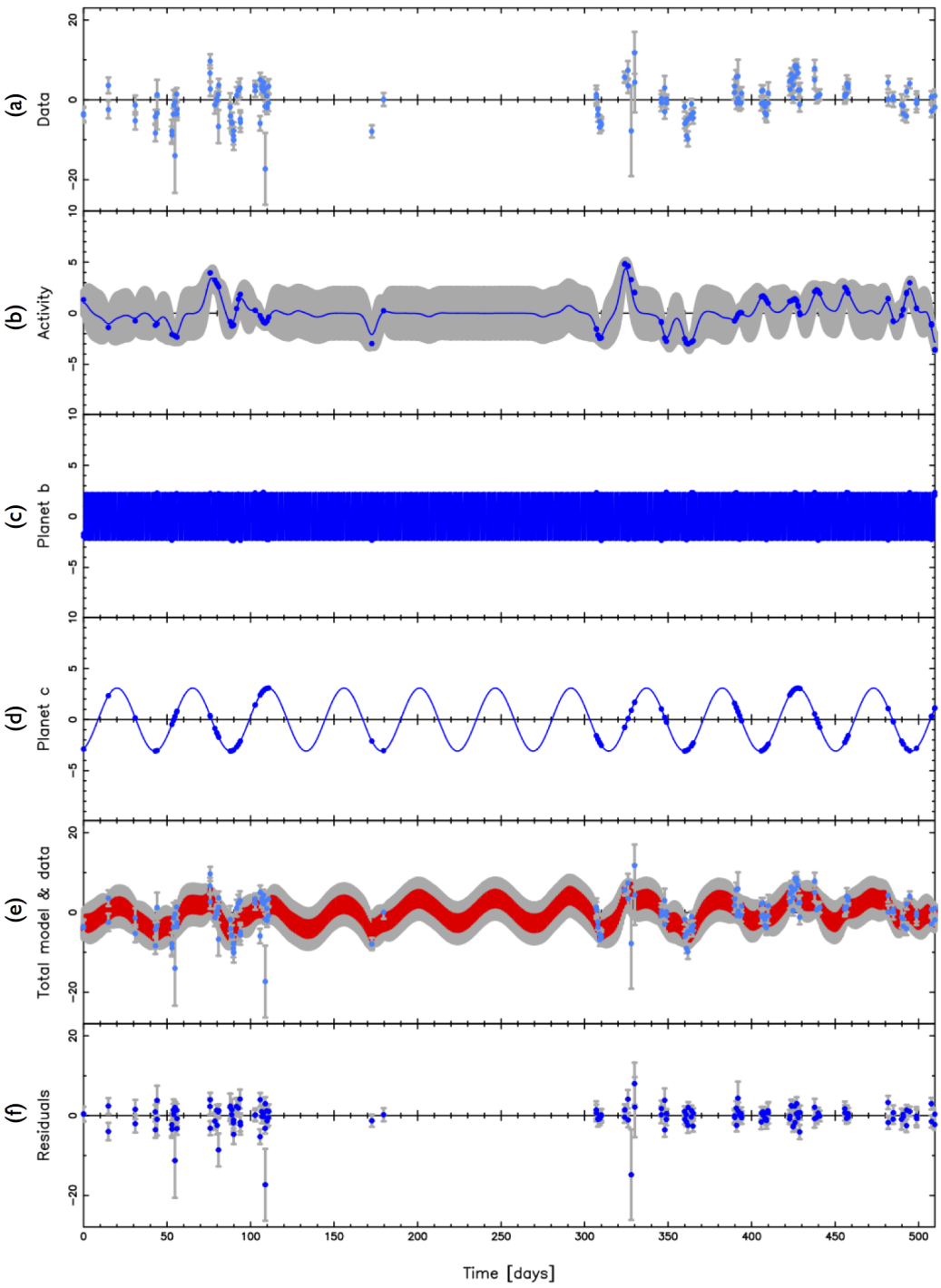

Figure 3.20: *Panel (a):* HARPS observations, after subtracting the star's systemic velocity RV_0; *Panel (b):* Gaussian process activity model; *Panel (c):* orbit of Kepler-10b; *Panel (d):* orbit of Kepler-10c; *Panel (e):* total model (red), overlaid on top of the data (blue points). *Panel (f):* residuals obtained after subtracting the model from the observations. Note that the scale on the y-axis in panels (b), (c) and (d) differ from the other panels. All RVs are in m.s^{-1}.

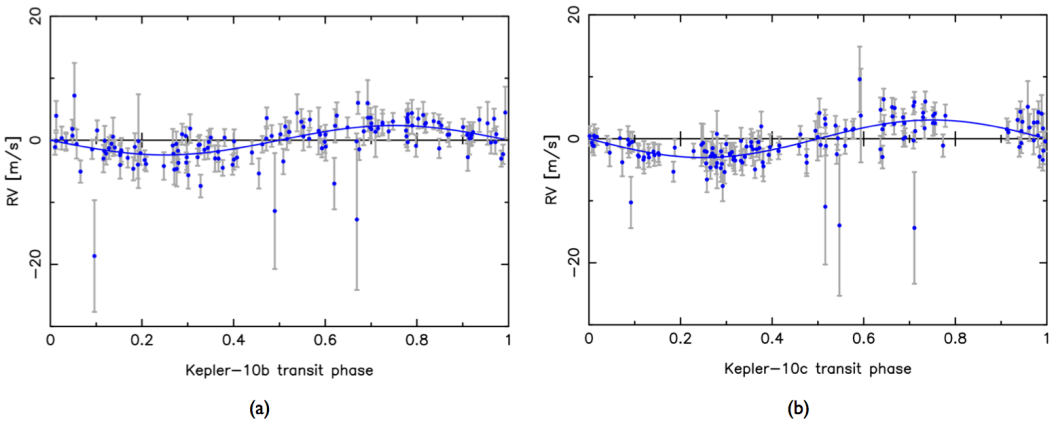

Figure 3.21: *Panel a:* Phase plot of the orbit of planet b (circular model). *Panel b:* Phase plot of the orbit of planet c (circular model).

this plot we can get a sense of the relative amplitudes of the Gaussian process and the two planets, and see over which timescales each one of them is important.

Figure 3.19 shows the periodogram of the HARPS-N RV data in panel (a), and the effect of removing each planet orbit one at a time. Removing the activity RV model in panel (b) reveals the two planets. When the orbit of Kepler-10b is removed in panel (d), we see that the peak at 0.8 days and its 1-day alias at 4.8 days both disappear. The RV residuals remaining after subtracting my model from the observations have an RMS scatter of 3 $\mathrm{m.s^{-1}}$, which is about 1 $\mathrm{m.s^{-1}}$ greater than the average size of the error bars. On the last panel of Figure 3.14, however, we can see that the majority of the residuals are close to zero, while a few isolated points are very far off (they also have larger error bars). This additional 1 $\mathrm{m.s^{-1}}$ is therefore likely to be caused by these few outliers. As shown in panel (d) of Figure 3.19, there are no obvious peaks in the generalised Lomb-Scargle periodogram of the residuals.

I show the phase-folded plots of the two planets in Figure 3.21.

3.3.5 Summary

Following the discovery of two transiting planets, one of them an Earth-size planet, the Kepler-10 system was observed intensively with the HARPS-N spectrograph in order to determine the masses of the planets. Kepler-10 is very old and quiet so a complex activity model was not required; nevertheless, I wished to test whether a Gaussian process still works when it is not needed. This system proved to be a double challenge when it was established that its *Kepler* lightcurve cannot be trusted to reveal the magnetic activity frequency structure of the star; this is the case for a number of lightcurves as cautioned by the *Kepler* Data Release 21 Notes (refer to Section 1.3). Based on my previous experience and on existing analyses of this system, I made guesses for the rotation period and lifetime of active regions and went on to run my MCMC simulation to determine the best-fitting parameters of my RV model.

My planet mass determinations are in agreement, within 1-sigma, with those of Dumusque et al. (2014). The uncertainties found via both methods are different, and I plan to investigate this further. In any case, this analysis shows that the

Gaussian process model does not absorb the planetary signals and provides robust mass determinations.

3.4 Summary & future plans

3.4.1 Determining the bulk densities of transiting exoplanets

Determining the mass of a transiting planet allows us to infer its bulk density, since we can measure its radius from the transits in the photometry. This gives us an insight into what the planet is made of, and what its structure might be like. A precision of at least 10% in mass (and 5% in radius) is required to distinguish rocky planets with iron cores from planets made mostly of water (Zeng & Sasselov, 2013). This is very challenging, but thanks to *Kepler*, soon TESS, CHEOPS and PLATO, and spectrographs such as TNG/HARPS-North and eventually VLT/ESPRESSO, it is becoming a reality!

If we can obtain this information for a large number of exoplanets it can provide essential clues on the processes that led to the formation of these planetary systems.

Using the radius found by Bruntt et al. (2010), I find that CoRoT-7b is slightly denser than the Earth ($\rho_\oplus = 5.52$ g.cm^{-3}), with $\rho_\mathrm{b} = 6.61 \pm 1.72$ g.cm^{-3} (see Table 3.2). Refer to Barros et al. (2014) for a more detailed discussion of the density of CoRoT-7b.

Kepler-10 c has a density of 7.1 ± 1.0 g.cm^{-3} (value of Dumusque et al. (2014)), which indicates that the planet is of rocky composition. Based on current theories of planet formation, this was an unexpected discovery, and earned Kepler-10c the name "Godzilla Earth".

I placed CoRoT-7b, Kepler-10b, Kepler-10c and Kepler-78b on a mass-radius diagram alongside other exoplanets for which mass and radius have been measured in Figure 3.22. According to composition models by Zeng & Sasselov (2013), CoRoT-7b, Kepler-10c and Kepler-78b along with Kepler-20b all have the density expected of a rocky planet; we see that they lie along the black "rocky" line of the diagram, despite displaying a range of radii. Kepler-10b is slightly less dense and its bulk density is more consistent with a composition of half-rock, half-ice.

3.4.2 Assessing the reliability of the Gaussian process framework for exoplanet mass determinations

As unveiled in Chapter 2, I have developed a new data analysis tool that can reproduce the effects of stellar activity in RV observations by using a Gaussian process trained on the variations in the stars lightcurve.

In the present Chapter, I reported on applications of my code to three low-mass planetary systems: CoRoT-7, Kepler-78 and Kepler-10. My Gaussian process framework works well for a variety of magnetic activity levels, and it has the potential to become a state of the art tool for exoplanet characterisation in future years. In order to achieve this, my code requires further testing and systematic benchmarking before it is applied in a more automated way to a large number of planetary systems. I propose the following project:

1. Create sets of synthetic RV data and synthetic lightcurves. The synthetic RV datasets would be a combination of one or more planetary orbits (for

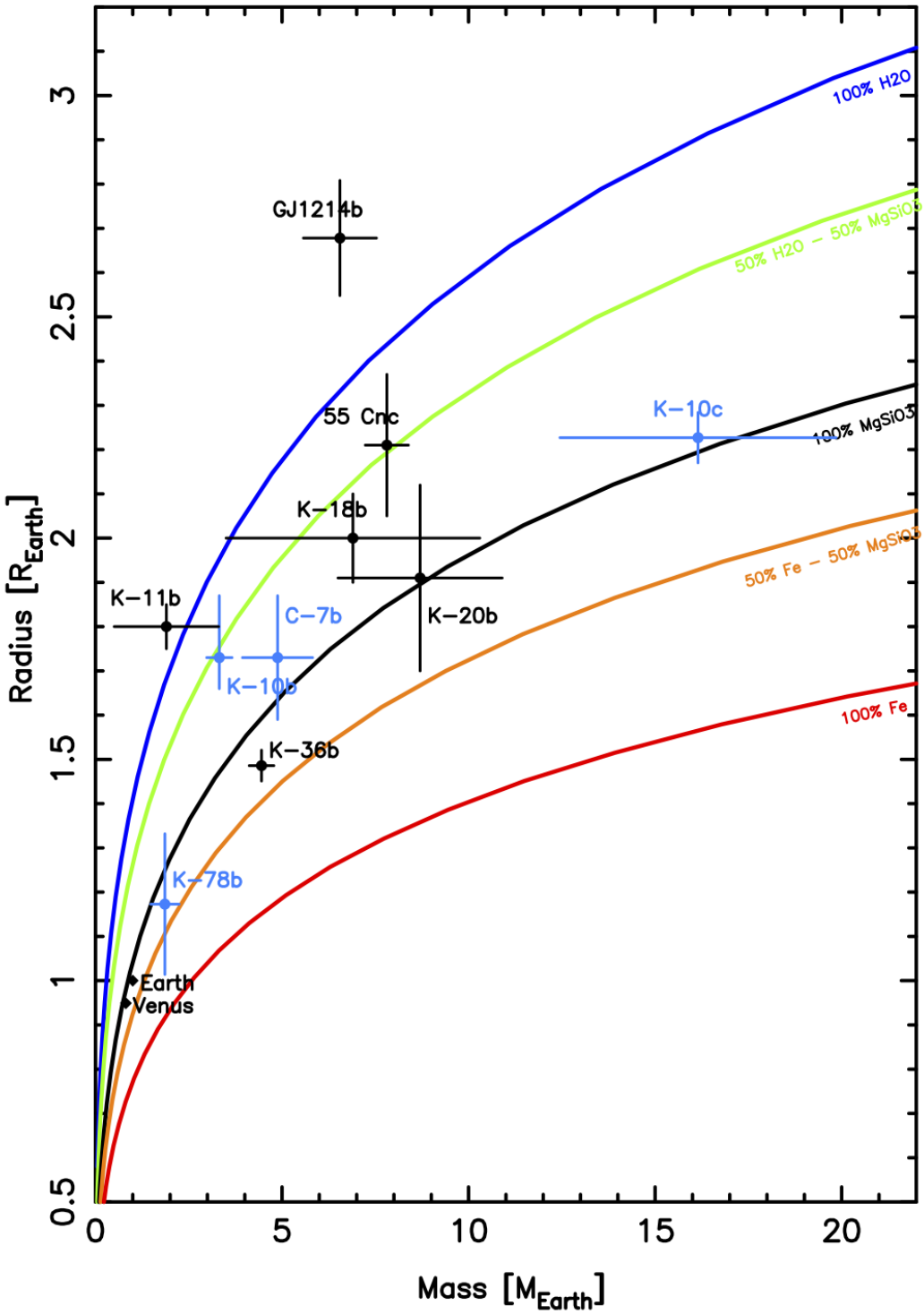

Figure 3.22: CoRoT-7b, Kepler-10b, Kepler-10c and Kepler-78b on a mass-radius diagram. Earth and Venus are shown as diamond shaped symbols for comparison. Other exoplanets for which the radius and mass are known are also represented. The solid lines show mass and radius for planets consisting of (from top to bottom): pure water, 50% water and 50% silicates, pure silicates, 50% silicates and 50% iron core, and pure iron, according to the theoretical models of Zeng & Sasselov (2013).

planets of various masses, orbital periods and orbital eccentricities) and white and red noise, to reproduce instrumental and astrophysical noise. I would design red noise with a quasi-periodic behaviour intended to mimic the effects of stellar activity on RV observations, which are strongly modulated by the stellar rotation period, and depend on the growth and decay of active regions on the stellar surface. The synthetic lightcurves would consist of a simple Fourier series with decaying amplitudes, with white noise.

2. Apply my code to the synthetic datasets. I would check the results to see if the code can detect the fake injected planet signals. As an extension of the investigations I undertook to assess the existence of CoRoT-7d, I would determine how well the code performs for each synthetic model and identify configurations for which the planetary signals are not fully recovered. In particular, I would test whether my code is capable of detecting planets with orbital periods close to the stellar rotation period or its harmonics. I could produce a plot showing the detectability of planets as a function of "temporal proximity".

3. I could further automatise my code so that I can then easily run it on a large number of stars, for example the HARPS-N database, in order to help us determine the number of observations we need for individual planet systems in order to determine planet masses with a 3- (or 6-) sigma precision, for a given radius and assumed composition.

It would also be interesting to carry out rigorous Bayesian model comparison on the Kepler-78 combined dataset, and possibly for other systems with observations from different spectrographs to find out whether two separate Gaussian processes perform better at modelling activity-induced signals as opposed to only one. This would tell us whether the RV amplitude of variations induced by active regions does change significantly as a function of wavelength, to the extent that we can detect these differences with HARPS and HIRES (or other spectrographs).

3.4.3 Concluding note

The intrinsic variability of the stars themselves remains the main obstacle to determining the masses of small planets. It is essential that we develop effective and comprehensive data analysis techniques, and that we establish reliable proxies for activity-induced RV signals to be able to extract the planetary signals from stellar variability. In the next Chapter, I present the work I have done on the activity-driven RV variations of the Sun, in the aim to break this barrier.

4

An exploration into the radial-velocity variability of the Sun*

The presence of starspots, faculae and granulation on the photosphere of a star induces quasi-periodic signals that can conceal and even mimic the Doppler signature of orbiting planets. This has resulted in several false detections (see Queloz et al. (2001a); Bonfils et al. (2007); Huélamo et al. (2008); Boisse et al. (2009, 2011); Gregory (2011); Haywood et al. (2014); Santos et al. (2014); Robertson et al. (2014) and many others). Understanding the RV signatures of stellar activity, in particular those modulated by the stellar rotation, is essential to develop the next generation of more sophisticated activity models and further improve our ability to detect and characterise low-mass planets.

The Sun is the only star whose surface can be directly resolved at high resolution, and therefore constitutes an excellent test case to explore the physical origin of stellar radial-velocity variability. In this Chapter, I present HARPS observations of sunlight scattered off the bright asteroid 4/Vesta, from which I deduced the Sun's activity-driven RV variations. In parallel, the HMI instrument onboard the Solar Dynamics Observatory provided me with simultaneous high spatial resolution magnetograms, dopplergrams, and continuum images of the Sun. I determined the RV modulation arising from the suppression of granular blueshift by magnetically active regions (sunspots and faculae) and the flux imbalance induced by dark spots. I confirm that the inhibition of convection is the dominant source of activity-induced RV variations at play. Finally, I find that the activity-driven RV variations of the Sun are strongly correlated with its full-disc magnetic flux, which could become a useful proxy for activity-related RV noise in future exoplanet searches.

*This Chapter uses material from, and is based on, Haywood et al., submitted for publication to MNRAS.

4.1 Previous studies on the intrinsic RV variability of the Sun

The Sun is a unique test case as it is the only star whose surface can be resolved at high resolution, therefore allowing me to directly investigate the impact of magnetic features on RV observations. Early attempts to measure the RV of the integrated solar disc did not provide quantitative results about the individual activity features responsible for RV variability. Jiménez et al. (1986) measured integrated sunlight using a resonant scattering spectrometer and found that the presence of magnetically active regions on the solar disc led to variations of up to 15 m.s^{-1}. They also measured the disc-integrated magnetic flux but didn't find any significant correlation with RV at the time due to insufficient precision. At about the same time, Deming et al. (1987) obtained spectra of integrated sunlight with an uncertainty level below 5 m.s^{-1}, enabling them to see the RV signature of supergranulation. The trend they observed over the 2-year period of their observations was consistent with suppression of convective blueshift from active regions on the solar surface. A few years later, Deming & Plymate (1994) confirmed the findings of both Jiménez et al. (1986) and Deming et al. (1987), only with a greater statistical significance. Not all studies were in agreement with each other, however; McMillan et al. (1993) recorded spectra of sunlight scattered off the Moon over a 5-year period and found that any variations due to solar activity were smaller than 4 m.s^{-1}.

More recently, Molaro & Centurión (2010) obtained HARPS spectra of the large and bright asteroid Ceres to construct a wavelength atlas for the Sun. They found that these spectra of scattered sunlight provide precise disc-integrated solar RVs, and proposed using asteroid spectra to calibrate high precision spectrographs used for planet hunting, such as HIRES and HARPS. In parallel, significant discoveries were made towards a precise quantitative understanding of the RV impact of solar surface features. Lagrange et al. (2010) and Meunier et al. (2010) used a catalogue of sunspot numbers and sizes and magnetograms from MDI/SOHO to simulate integrated-Sun spectra over a full solar cycle and deduce the impact of sunspots and networks of faculae on RV variations. Flux blocked by sunspots was found to cause variations of the order of the m.s^{-1} (Lagrange et al., 2010; Makarov et al., 2009), while facular suppression of granular blueshift can lead to variations in RV of up to 8-10 m.s^{-1} (Meunier et al., 2010). In particular, it seems that the suppression of granular blueshift by active regions plays a dominant role (Meunier et al., 2010; Haywood et al., 2014).

Following the launch of the Solar Dynamics Observatory (SDO, Pesnell et al. (2012)) in 2010, continuous observations of the solar surface brightness, velocity and magnetic fields have become available with image resolution finer than the photospheric granulation pattern. This allows me to probe the RV variations of the Sun in unprecedented detail. In this Chapter, I deduce the activity-driven RV variations of the Sun based on HARPS observations of the bright asteroid Vesta (Section 4.2). In parallel, I use high spatial resolution continuum, dopplergram and magnetogram images from the Helioseismic and Magnetic Imager (HMI/SDO, Schou et al. (2012)) to model the individual RV contributions from sunspots, faculae and granulation (Section 4.3). This allows me to create a model which I test against the HARPS observations (Section 4.4). Finally, I compute the disc-averaged magnetic flux and

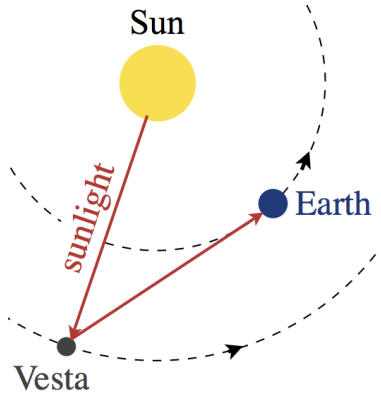

Figure 4.1: Schematic representation of the Sun, Vesta and Earth configuration during the period of observations (not to scale).

show that it is an excellent proxy for activity-driven RV variations (Section 4.5).

4.2 HARPS observations of sunlight scattered off Vesta

4.2.1 HARPS spectra

The HARPS spectrograph, mounted on the ESO 3.6 m telescope at La Silla was used to observe sunlight scattered from the bright asteroid 4/Vesta (its average magnitude during the run was 7.6). Two to three measurements per night were made with simultaneous Thorium exposures for a total of 98 observations, spread over 37 nights between 2011 September 29 and December 7. The geometric configuration of the Sun and Vesta relative to the observer is illustrated in Figure 4.1. At the time of the observations, the Sun was just over three years into its 11-year magnetic cycle; the SDO data confirm that the Sun showed high levels of activity.

The spectra were reprocessed using the HARPS DRS pipeline (Baranne et al., 1996; Lovis & Pepe, 2007). Instead of applying a conventional barycentric correction, the wavelength scale of the calibrated spectra was adjusted to correct for the doppler shifts due to the relative motion of the Sun and Vesta, and the relative motion of Vesta and the observer (see Section 4.2.3). The FWHM and BIS of the cross-correlation function and $\log R'_{\rm HK}$ index were also derived by the pipeline. The median, minimum and maximum signal to noise ratio of the reprocessed HARPS spectra at central wavelength 556.50 nm are 161.3, 56.3 and 257.0, respectively. Overall, HARPS achieved a precision of 75 $\pm$ 25 cm s^{-1} (see Table A11).

I account for the RV modulation induced by Vesta's rotation in Section 4.2.4.1, and investigate sources of intra-night RV variations in Section 4.2.4.2. I selected the SDO images in such a way as to compensate for the different viewing points of Vesta and the SDO spacecraft: Vesta was trailing SDO, as shown in Figure 4.1. This is taken into account in Section 4.2.5.

4.2.2 Solar rest frame

The data reduction pipeline for HARPS assumes that the target observed is a distant point-like star, and returns its RV relative to the solar system barycenter ($RV_{\rm bary}$). In order to place the observed RVs of Vesta in the solar rest frame, I perform the following operation:

$$RV = RV_{\rm bary,Earth} + v_{\rm sv} + v_{\rm ve}, \tag{4.1}$$

where $\rm RV_{bary,Earth}$ is the barycentric RV of the Earth, i.e. the component of the observer's velocity relative to the solar system barycentre, toward the apparent position of Vesta. It can be found in the fits header for each observation. The two components $v_{\rm sv}$ and $v_{\rm ve}$, retrieved from the JPL HORIZONS database[2] correspond to:

- $v_{\rm sv}$: the velocity of Vesta relative to the Sun at the instant that light received at Vesta was emitted by the Sun;
- $v_{\rm ve}$: the velocity of Vesta relative to Earth at the instant that light received by HARPS was emitted at Vesta.

This correction accounts for the RV contribution of all bodies in the solar system and places the Sun in its rest frame.

4.2.3 Relativistic Doppler effects

The only relativistic corrections made by JPL HORIZONS are for gravitational bending of the light and relativistic aberration due to the motion of the observer (Giorgini, priv. comm.). We therefore must correct for the relativistic doppler shifts incurred by space-time path curvature between the target and the observer. The wavelength correction factor to be applied is given by Lindegren & Dravins (2003) as:

$$\frac{\lambda_{\rm e}}{\lambda_{\rm o}} = \frac{\sqrt{1-\frac{v^2}{c^2}}}{1+\frac{v\cos\theta_{\rm o}}{\rm c}}, \tag{4.2}$$

where $\lambda_{\rm e}$ is the wavelength of the light at emission, $\lambda_{\rm o}$ is the wavelength that is seen when it reaches the observer, and c is the speed of light. v is the total magnitude of the velocity vector of the observer relative to the emitter. I apply this correction twice:

- The light is emitted by the Sun and received at Vesta. In this case, v is the magnitude of the velocity of Vesta with respect to the Sun, and the radial component $v\cos\theta_{\rm o}$ is equal to $v_{\rm sv}$ (defined in Section 4.2.2).
- Scattered sunlight is emitted from Vesta and received at La Silla. v is the magnitude of the velocity of Vesta with respect to an observer at La Silla, and $v\cos\theta_{\rm o}$ is $v_{\rm ve}$.

For both cases, v and can be obtained from the JPL HORIZONS database. All velocities are measured at the flux-weighted mid-exposure times of observation ($\rm MJD_{mid}$-UTC).

[2]Solar System Dynamics Group, Horizons On-Line Ephemeris System, 4800 Oak Grove Drive, Jet Propulsion Laboratory, Pasadena, CA 91109 USA – Information: http://ssd.jpl.nasa.gov/, Jon.Giorgini@jpl.nasa.gov

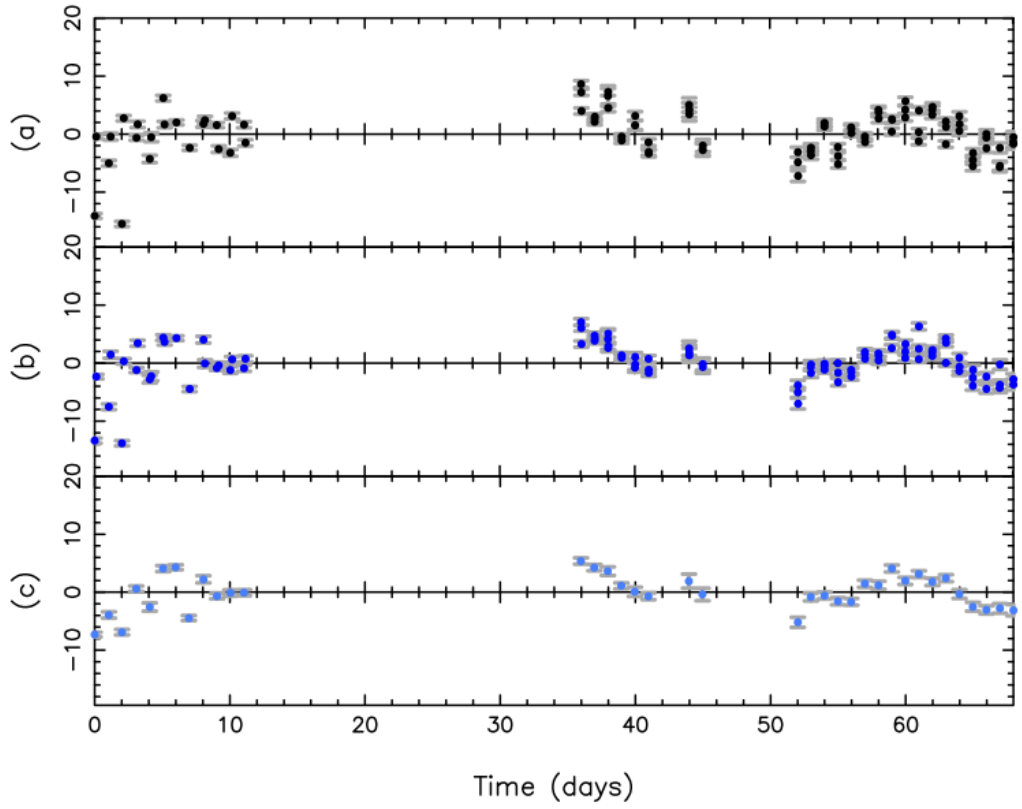

Figure 4.2: Panel (a): HARPS RV variations in the solar rest-frame, corrected for relativistic doppler effects (but not yet corrected for Vesta's axial rotation). Panel (b): HARPS RV variations of the Sun as-a-star (after removing the RV contribution of Vesta's axial rotation). Panel (c): Nightly binned HARPS RV variations of the Sun as-a-star. All RVs are in ms^{-1}.

The two wavelength correction factors are then multiplied together in order to compute the total relativistic correction factor to be applied to the pixel wavelengths in the HARPS spectra, from which I derive the correct RVs, shown in Figure 4.2 (a) (see also column 2 of Table A11).

4.2.4 Sources of intra-night RV variations

4.2.4.1 Vesta's axial rotation

Vesta rotates every 5.34 hours (Stephenson, 1951), so any significant inhomogeneities in its shape or surface albedo will induce an RV modulation. Vesta's shape is close to a spheroid (Thomas et al., 1997), and Lanza & Molaro (2015) found that the RV modulation expected from shape inhomogeneities should not exceed 0.060 m s^{-1}.

Stephenson (1951) presented a photometric study of the asteroid, and suggested that its surface brightness is uneven. He reported brightness variations $\delta m = 0.12$ mag. To make a rough estimate of the amplitude of the RV modulation, I can assume that the brightness variations are due to a single dark equatorial spot on the surface of Vesta, blocking a fraction δf of the flux f. δm and δf are related as follows:

$$\delta m = \frac{2.5\, d(\ln f)}{\log(e)} \sim 1.08\, \frac{\delta f}{f}, \tag{4.3}$$

The fractional flux deficit caused by a dark spot can thus be approximated as:

$$\frac{\delta f}{f} \sim \delta m/1.08 \sim 0.11. \tag{4.4}$$

When the dayside of Vesta is viewed fully illuminated, this spot will give an RV modulation equal to:

$$\Delta RV_{\rm vesta} = -\frac{\delta f}{f}\, v_{\rm eq}\, \cos\theta\, \sin\theta, \tag{4.5}$$

where θ is the angle between the spot on the asteroid and our line of sight, and increases from $-\pi/2$ to $+\pi/2$ as it traverses the visible daylight hemisphere. Due to foreshortening, the RV contribution is decreased by a factor $\cos\theta$. The line-of-sight velocity varies with $\sin\theta$. The asteroid's equatorial velocity $v_{\rm eq}$ is given by:

$$v_{\rm eq} = 2\pi\, \frac{R_{\rm vesta}}{P_{\rm rot}}. \tag{4.6}$$

Using a mean radius $R_{\rm vesta} = 262.7$ km (Russell et al., 2012) and the rotational period $P_{\rm rot} = 5.34$ hours, I obtain $v_{\rm eq} = 85.8$ m s^{-1}. The maximum RV amplitude of Vesta's rotational modulation, expected at $\theta = \pi/4$ is thus approximately 4.7 m s^{-1}. The RV modulation due to surface brightness inhomogeneity should therefore dominate strongly over shape effects.

I find that this RV contribution is well modelled as a sum of Fourier components modulated by Vesta's rotation period:

$$\Delta RV_{\rm vesta}(t) = C\cos(2\pi - \lambda(t)) + S\sin(2\pi - \lambda(t)), \tag{4.7}$$

where $\lambda(t)$ is the apparent planetographic longitude of Vesta at the flux-weighted mid-times of the HARPS observations and can be retrieved via the JPL HORIZONS database (the values of λ are listed in Table A11). C and S are scaling parameters, which I determine via an optimal scaling procedure described in Section 4.4. Since the phase-folded lightcurve of Vesta shows a double-humped structure (Stephenson, 1951), I also tested adding further Fourier terms modulated by the first harmonic of the asteroid's rotation. The improvement to the fit was negligible, so I preferred the simpler model of Equation 4.7.

Figure 4.2 (b) shows the RV observations obtained after subtracting Vesta's rotational signature. The night-to-night scatter has been reduced, even though much of it remains in the first block of observations; I discuss this in the following Section.

4.2.4.2 Solar p-modes and granulation

The RV variations in the first part of the HARPS run (nights 0 to 11 in Figure 4.2) contain some significant scatter, even after accounting for Vesta's rotation. This intra-night scatter does not show in the solar FWHM, BIS or $\log(R'_{\rm HK})$ variations. I investigated the cause of this phenomenon and excluded changes in colour of the asteroid or instrumental effects as a potential source of additional noise. Vesta was very bright (7.6 mag), so I deem the phase and proximity of the Moon unlikely to be responsible for the additional scatter observed.

Solar p-mode oscillations dominate the Sun's power spectrum at a timescale of about 5 minutes. Most of the RV oscillations induced by p-mode acoustic waves are therefore averaged out within the 15-minute HARPS exposures. Granulation motions result in RV signals of several m s^{-1}, over timescales ranging from about 15 minutes to several hours. Taking multiple exposures each night and averaging them together (as plotted in panel (c) of Figure 4.2) can help to significantly reduce granulation-induced RV variations. In addition to this, super-granulation motions commonly take place over timescales of 8 hours or longer, and could potentially result in residual white noise from one night to the next. Two different observing strategies were implemented during the HARPS run:

- ***First part (nights 0-11):*** 2 to 3 observations were made on each night at $\sim$ 2-hour intervals. Within each night, I see scatter with an amplitude of several m s^{-1} (see panel (b) of Figure 4.2). I attribute this to granulation motions with a turnover timescale of 2-3 hours, that are not averaged well with this observational strategy. When I consider the nightly averages (panel (c)), the scatter is considerably reduced, although some residual noise with an amplitude of $\sim$ 3 m s^{-1} remains.

- ***Second part (nights 36-68):*** 3 consecutive exposures were made on each night. This strategy appears to average out granulation motions very effectively, as little intra-night scatter remains.

The remaining variations, of order 7-10 m s^{-1}, are modulated by the Sun's rotation and are caused by the presence of magnetic surface markers, such as sunspots and faculae. These variations are the primary focus of this Chapter, and I model them using SDO/HMI data in Section 4.3.

4.2.5 Time lag between Vesta and SDO observations

At the time of the observations, the asteroid Vesta was trailing the SDO spacecraft, which orbits the Earth (see Figure 4.1). In order to model the solar hemisphere facing Vesta at time t, I used SDO images recorded at $t + \Delta t$, where Δt is proportional to the difference in the Carrington longitudes of the Earth/SDO and Vesta at the time of the HARPS observation. These longitudes can be retrieved from the JPL HORIZONS database. The shortest delay, at the start of the observations was $\sim$ 2.8 days, while at the end of the observations it reached just over 6.5 days (see Table A11). I cannot account for the evolution of the Sun's surface features during this time, and must assume that they remain frozen in this interval. The emergence of sunspots can take place over a few days, but in general large magnetic features (sunspots and networks of faculae) evolve over timescales of weeks rather than days.

4.3 Pixel statistics from SDO/HMI images

In the second part of this analysis I aim to determine the RV contribution from granulation, sunspots and facular regions. I used high-resolution full-disc continuum intensity (6000Å), line-of-sight doppler images and line-of-sight magnetograms from the HMI instrument (Helioseismic and Magnetic Imager) onboard SDO[3]. These were retrieved for the period spanning the HARPS observations of Vesta at times determined by the time lags detailed in Section 4.2.5. SDO/HMI images the solar disc at a cadence of 45 seconds, with a spatial resolution of 1" using a CCD of 4096×4096 square pixels. I first converted the SDO/HMI images from pixel coordinates to heliographic coordinates, i.e. to a coordinate system centered on the Sun. This coordinate system is fixed with respect to the Sun's surface and rotates in the sidereal frame once every 25.38 days, which corresponds to a Carrington rotation period (Carrington, 1859). A surface element on the Sun, whose image falls on pixel ij of the instrument detector, is at position (w_{ij}, n_{ij}, r_{ij}) relative to the centre of the Sun, where w is westward, n is northward and r is in the radial direction (see Thompson (2006) for more details on the coordinate system used). The spacecraft is at position (0, 0, $r_{\rm sc}$). The w, n, r components of the spacecraft's position relative to each element ij can thus be written as:

$$\begin{aligned} \delta w_{ij} &= w_{ij} - 0 \\ \delta n_{ij} &= n_{ij} - 0 \\ \delta r_{ij} &= r_{ij} - r_{\rm sc} \end{aligned} \tag{4.8}$$

The spacecraft's motion and the rotation of the Sun introduce velocity perturbations, which I determine in Sections 4.3.1 and 4.3.2, respectively. These two contributions are then subtracted from each doppler image, thus revealing the Sun's magnetic activity velocity signatures. I compute the RV variations due to the suppression of convective blueshift and the flux blocked by sunspots on the rotating Sun in Sections 4.3.5.3 and 4.3.5.4. I show that the Sun's activity-driven RV variations are well reproduced by a scaled sum of these two contributions in Section 4.4. Finally, I compute the disc-averaged magnetic flux and compare it as an RV proxy against the traditional spectroscopic activity indicators in Section 4.5.

4.3.1 Spacecraft motion

The w, n, r components of the velocity incurred by the motion of the spacecraft relative to the Sun, $\mathbf{v}_{\rm sc}$, are given in the fits header of each SDO/HMI observation. I normalise $\mathbf{v}_{\rm sc}$ to account for variations in the spacecraft's position relative to the Sun. The magnitude of the spacecraft's velocity away from pixel ij can therefore be expressed as:

$$v_{{\rm sc},ij} = -\frac{\delta w_{ij}\, v_{{\rm sc},w_{ij}} + \delta n_{ij}\, v_{{\rm sc},n_{ij}} + \delta r_{ij}\, v_{{\rm sc},r_{ij}}}{d_{ij}}, \tag{4.9}$$

where:

$$d_{ij} = \sqrt{\delta w_{ij}^2 + \delta n_{ij}^2 + \delta r_{ij}^2} \tag{4.10}$$

[3]HMI data products can be downloaded online via the Joint Science Operations Center website: http://jsoc.stanford.edu.

Parameter	Value (deg day^{-1})
A	14.713
B	-2.396
C	-1.787

Table 4.1: Solar differential rotation profile parameters from Snodgrass & Ulrich (1990).

is the distance between pixel ij and the spacecraft. I note that all relative velocities in this Chapter follow the natural sign convention that velocity is rate of change of distance.

4.3.2 Solar rotation

The solar rotation as a function of latitude was measured by Snodgrass & Ulrich (1990) in low resolution full-disc dopplergrams and magnetograms obtained at the Mount Wilson 150 foot tower telescope between 1967 and 1987. By cross-correlating time series of dopplergrams and magnetograms, they were able to determine the rate of motion of surface features (primarily supergranulation cells and sunspots) and deduce the rate of rotation of the Sun's surface as a function of latitude. The solar differential rotation profile $\omega(\phi)$ at each latitude ϕ is commonly described by a least squares polynomial of the form:

$$\omega(\phi) = A + B\sin^2\phi + C\sin^4\phi. \tag{4.11}$$

The best fit parameters found by Snodgrass & Ulrich (1990), used in this analysis, are given in Table 4.1. I apply this rotation profile in the heliographic frame to determine the w, n, r components induced by the solar rotation velocity along the line of sight to a given image pixel, $v_{\mathrm{rot},w}$, $v_{\mathrm{rot},n}$ and $v_{\mathrm{rot},r}$. Normalising again by d, I can write:

$$v_{\mathrm{rot}} = -\frac{\delta w\, v_{\mathrm{rot},w} + \delta n\, v_{\mathrm{rot},n} + \delta r\, v_{\mathrm{rot},r}}{d}. \tag{4.12}$$

4.3.3 Flattened continuum intensity

I flatten the continuum intensity images using a fifth order polynomial function L_{ij} with the limb darkening constants given in Astrophysical Quantities (Allen, 1973), through the IDL subroutine *darklimb_correct.pro*[4]. The flattened and non-flattened continuuum intensities are related via the limb-darkening function L as follows:

$$I_{\mathrm{flat},ij} = \frac{I_{ij}}{L_{ij}}. \tag{4.13}$$

4.3.4 Unsigned longitudinal magnetic field strength

The SDO/HMI instrument measures the line-of-sight (longitudinal) magnetic field strength B_{obs}. The magnetic field of the Sun stands radially out of the photosphere

[4]Source code available at:
http://hesperia.gsfc.nasa.gov/ssw/gen/idl/solar/

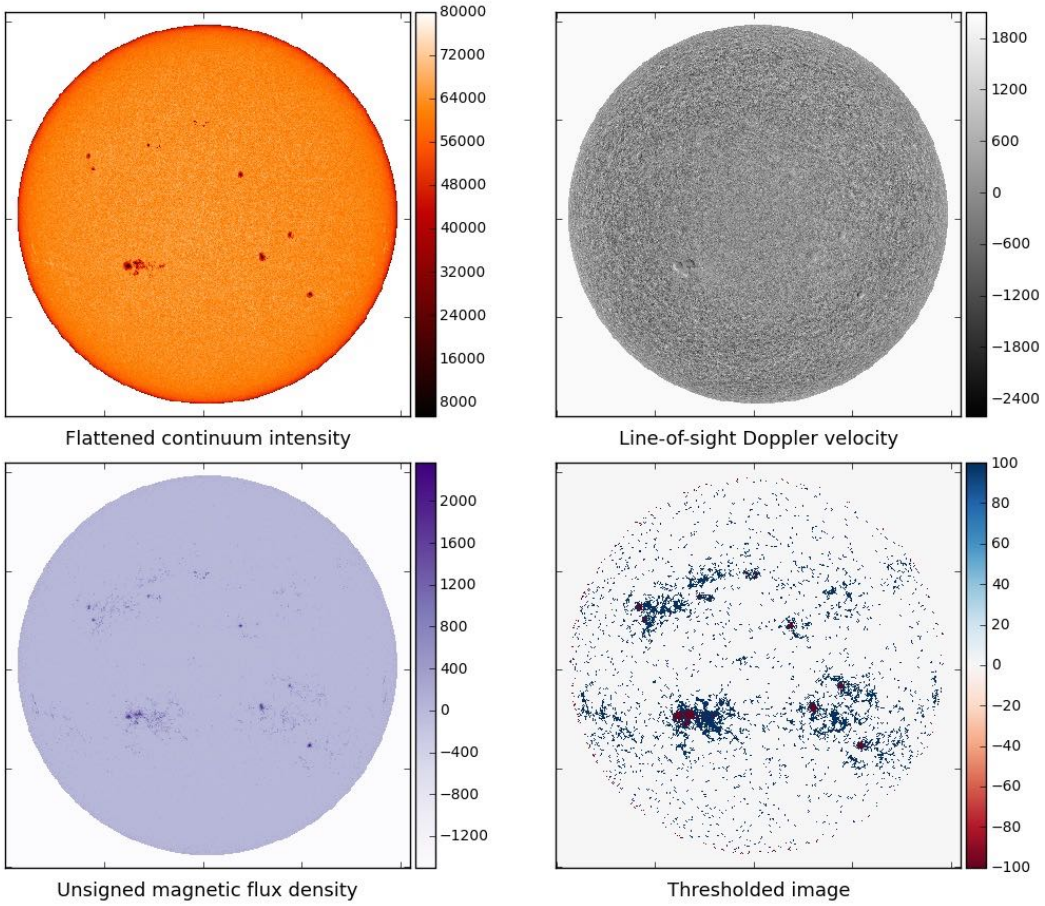

Figure 4.3: *First three panels:* SDO/HMI flattened intensity, line-of sight velocity (km s^{-1}) for the non-rotating Sun and unsigned longitudinal magnetic flux $|B_l|/\mu$ (G) of the Sun, observed on 2011, November 10 at 00:01:30 UTC. *Last panel:* my thresholded image, highlighting faculae (blue pixels) and sunspots (red pixels).

with a strength B_r. Due to foreshortening, the observed (longitudinal) field B_{obs} is less than the true (radial) field by a factor:

$$\mu_{ij} = \cos\theta_{ij}, \tag{4.14}$$

where θ_{ij} is the angle between the outward normal to the feature on the solar surface and the direction of the line-of-sight of the SDO spacecraft.

I can thus recover the full magnetic field strength by dividing by μ_{ij}:

$$B_{r,ij} = B_{obs,ij}/\mu_{ij}. \tag{4.15}$$

As is routinetly done in solar work, I do not apply this operation for pixels that are very close to the limb ($\mu_{ij} < 0.1$) as it would lead me to overestimate the magnetic field strength.

The noise level in HMI magnetograms is a function of μ (Yeo et al., 2013). It is lowest for pixels in the centre of the CCD, where it is close to 5 G, and increases towards the edges and reaches 8 G at the solar limb. For this analysis I assume that the noise level is constant throughout the image with a conservative value $\sigma_{B_{obs,ij}} = 8$ G, in agreement with the results of Yeo et al. (2013). I therefore set $B_{obs,ij}$ and $B_{r,ij}$ to 0 for all pixels with a longitudinal field measurement ($B_{obs,ij}$) below this value.

4.3.5 Surface markers of magnetic activity

4.3.5.1 Identifying quiet-Sun regions, faculae & sunspots

The first three panels of Figure 4.3 show an SDO/HMI flattened intensitygram, line-of-sight Dopplergram and unsigned radial magnetogram for a set of images taken on 2011, November 10, after removing the contributions from spacecraft motion and solar rotation. I identify quiet-Sun regions, faculae and sunspots by applying magnetic and intensity thresholds.

- ***Magnetic threshold:*** The distribution of pixel unsigned observed magnetic field strength as a function of pixel flattened intensity is shown in Figure 4.4. In the top histogram and main panel, we see that the distribution of magnetic field strength falls off sharply with increasing field strength. The vast majority of pixels are clustered close to 0G: these pixels are part of the quiet-Sun surface. I separate active regions from quiet-Sun regions by applying a threshold in unsigned radial magnetic field strength for each pixel. Yeo et al. (2013) investigated the intensity contrast between the active and quiet photosphere using SDO/HMI data, and found an appropriate cutoff at:

$$|B_{\mathrm{r},ij}| > 3\,\sigma_{B_{\mathrm{obs},ij}}/\mu_{ij}, \tag{4.16}$$

  where $\sigma_{B_{\mathrm{obs},ij}}$ represents the magnetic noise level in each pixel (see last paragraph of Section 4.3.4). As in Yeo et al. (2013), I exclude *isolated* pixels that are above this threshold as they are likley to be false positives. I can thus write:

$$|B_{\mathrm{r,thresh},ij}| = 24\,\mathrm{G}\,/\mu_{ij}. \tag{4.17}$$

- ***Intensity threshold:*** The distribution of line-of-sight velocity as a function of pixel flattened intensity is shown in Figure 4.5. The main panel allows us to further categorise active-region pixels into faculae and sunspots (umbra and penumbra). I apply the intensity threshold of Yeo et al. (2013):

$$I_{\mathrm{thresh}} \;=\; 0.89\,\hat{I}_{\mathrm{quiet}}, \tag{4.18}$$

  where $\hat{I}_{\mathrm{quiet}}$ is the mean pixel flattened intensity over quiet-Sun regions. It can be calculated by summing the flattened intensity of each pixel that has $|B_{\mathrm{r},ij}| < |B_{\mathrm{r,thresh},ij}|$:

$$\hat{I}_{\mathrm{quiet}} = \frac{\sum_{ij} I_{\mathrm{flat},ij}\, W_{ij}}{\sum_{ij} W_{ij}}, \tag{4.19}$$

  where the weighting factors are defined as:

$$\begin{aligned} W_{ij} &= 1 \text{ if } |B_{\mathrm{r},ij}| > |B_{\mathrm{r,thresh},ij}|, \\ W_{ij} &= 0 \text{ if } |B_{\mathrm{r},ij}| < |B_{\mathrm{r,thresh},ij}|. \end{aligned} \tag{4.20}$$

  In the main panel of Figure 4.5, quiet-Sun pixels are plotted in black, while active-region pixels are overplotted in yellow.

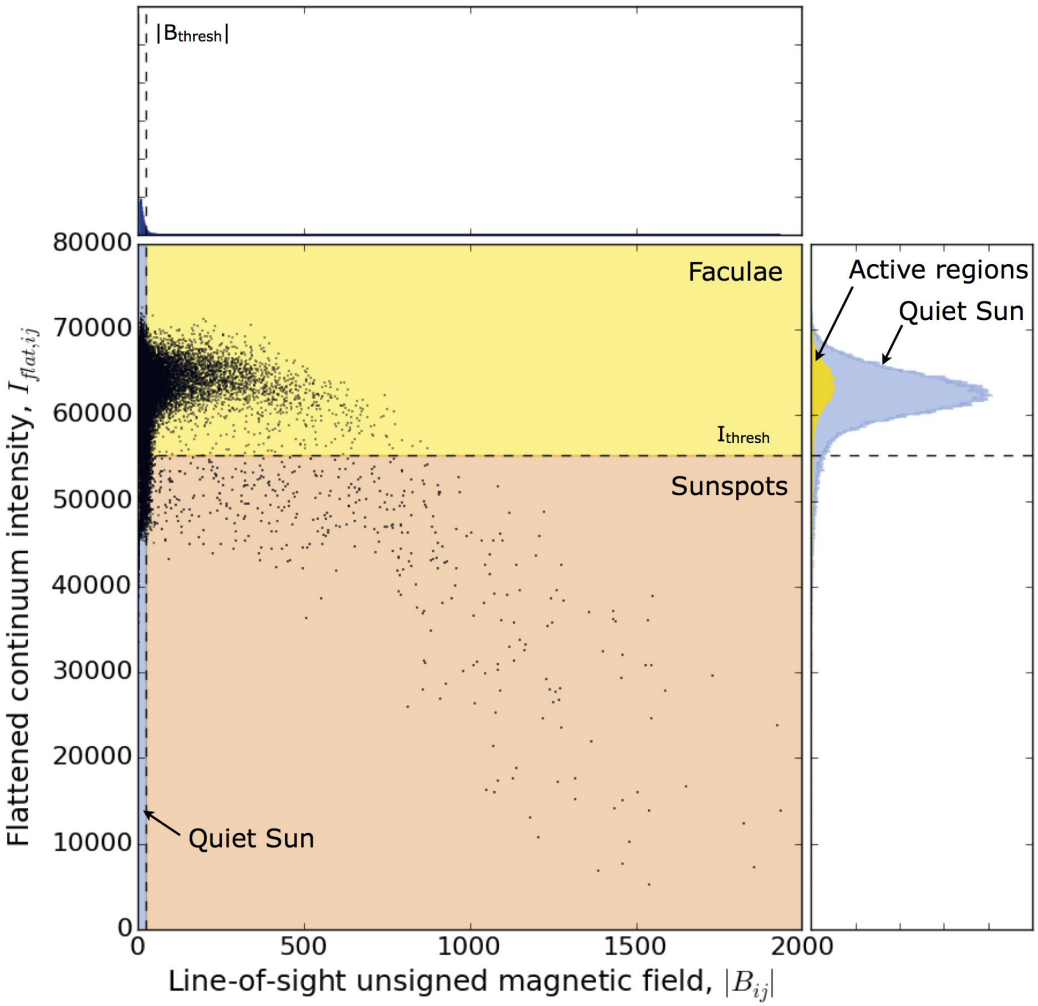

Figure 4.4: Pixel line-of-sight (longitudinal) magnetic field strength, $|B_{\mathrm{obs},ij}|$, as a function of flattened intensity $I_{\mathrm{flat},ij}$, for the Sun on 2011, November 10 at 00:01:30 UTC. The top and right histograms show the distributions of $|B_{\mathrm{obs},ij}|$ and $I_{\mathrm{flat},ij}$, respectively. The dashed lines represent the cutoff criteria selected to define the quiet photosphere, faculae and sunspots. Over 95% of the solar disc is magnetically quiet.

The last panel of Figure 4.3, which shows the thresholded image according to these $I_{\mathrm{flat},ij}$ and $|B_{\mathrm{r},ij}|$ criteria, confirms that they are effective at identifying sunspot and faculae pixels correctly.

4.3.5.2 Velocity contribution of convective motions in quiet Sun regions

I estimate the average RV of the quiet Sun by summing the intensity-weighted velocity of non-magnetised pixels, after removing the spacecraft motion and the Sun's rotation:

$$\hat{v}_{\mathrm{quiet}} = \frac{\sum_{ij}(v_{ij} - \delta v_{\mathrm{sc},ij} - \delta v_{\mathrm{rot},ij})\, I_{ij}\, W_{ij}}{\sum_{ij} I_{ij}\, W_{ij}}. \tag{4.21}$$

For this calculation, I define the weights as follows:

$$\begin{aligned} W_{ij} &= 1 \text{ if } |B_{\mathrm{r},ij}| < |B_{\mathrm{r,thresh},ij}|, \\ W_{ij} &= 0 \text{ if } |B_{\mathrm{r},ij}| > |B_{\mathrm{r,thresh},ij}|. \end{aligned} \tag{4.22}$$

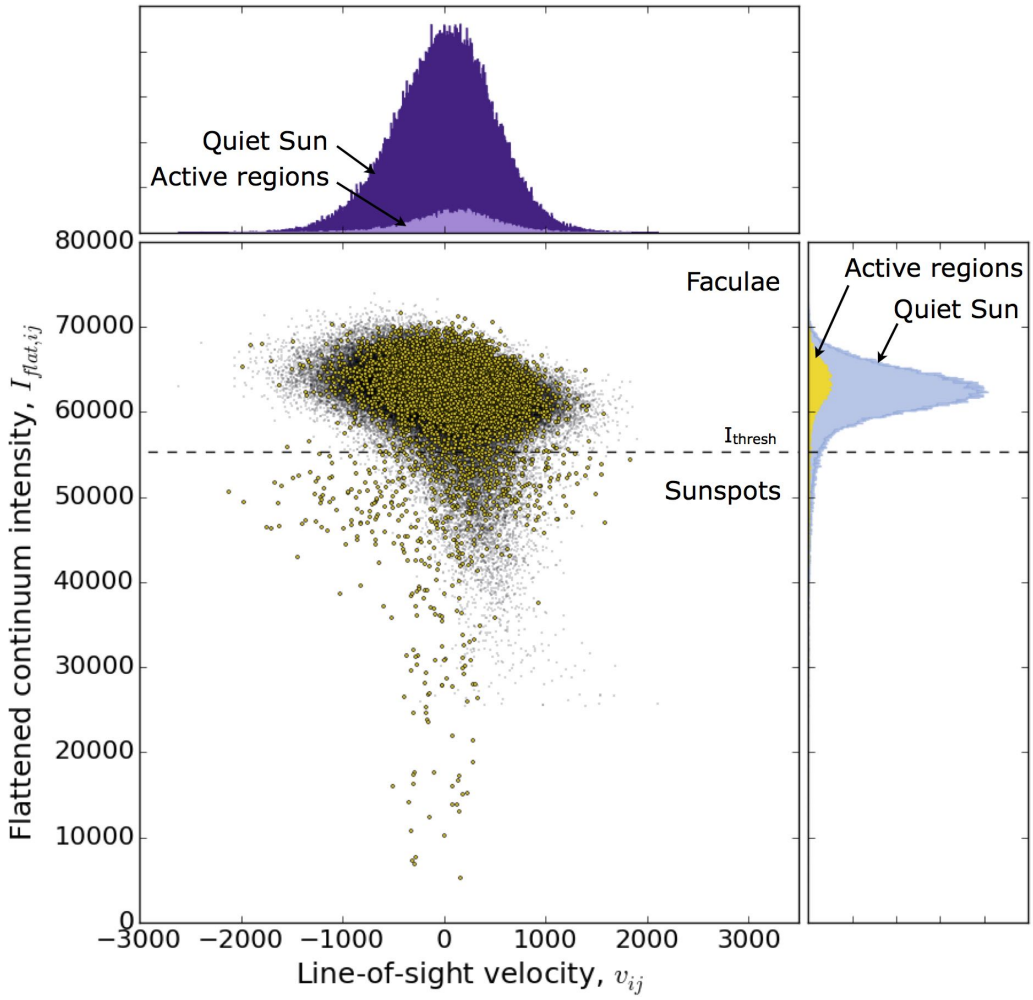

Figure 4.5: Pixel line-of-sight velocity, v_{ij}, as a function of flattened intensity $I_{\mathrm{flat},ij}$, for the Sun on 2011, November 10 at 00:01:30 UTC. The top and right histograms show the distributions of v_{ij} and $I_{\mathrm{flat},ij}$, respectively. In the case of active pixels (yellow dots), the line of sight velocity is invariant with pixel brightness. For quiet-Sun pixels (black dots), however, brighter pixels are blueshifted while fainter pixels are redshifted: this effect arises from granular motions.

This velocity field is thus averaged over the vertical motions of convection granules on the solar surface. Hot and bright granules rise up to the surface, while cooler and darker fluid sinks back towards the Sun's interior. This process is visible in the main panel of Figure 4.5: quiet-Sun pixels (black dots) are clustered in a tilted ellipse. The area of the upflowing granules is larger than that enclosed in the intergranular lanes, and the granules are carrying hotter and thus brighter fluid. This results in a net blueshift, as seen in Figure 4.5.

4.3.5.3 Suppression of convective blueshift from active regions

The presence of magnetically active regions inhibits convection and therefore acts to suppress this blueshift. I measure the total disc-averaged velocity of the Sun $\hat{v}$ by summing the velocity contribution of each pixel ij, weighted by their intensity

I_{ij}, after subtracting the spacecraft motion and solar rotation:

$$\hat{v} = \frac{\sum_{ij}(v_{ij} - \delta v_{\mathrm{sc},ij} - \delta v_{\mathrm{rot},ij})\, I_{ij}}{\sum_{ij} I_{ij}} \tag{4.23}$$

The suppression of granular blueshift induced by magnetically active regions ($|B_{\mathrm{r},ij}| > |B_{\mathrm{r,thresh},ij}|$) is therefore:

$$\Delta\hat{v}_{\mathrm{conv}} = \hat{v} - \hat{v}_{\mathrm{quiet}}. \tag{4.24}$$

The value of $\Delta\hat{v}_{\mathrm{conv}}$ at each time of the HARPS observations is listed in Table A11.

4.3.5.4 Rotational perturbation due to sunspot flux deficit

As the Sun rotates, the presence of dark spots on the solar surface breaks the Doppler balance between the approaching (blueshifted) and receding (redshifted) hemispheres. The resultant velocity perturbation can be obtained by summing the line-of-sight velocity of sunspot pixels corrected for the spacecraft's motion, and weighted by the deficit in flux produced by the presence of a sunspot:

$$\Delta\hat{v}_{\mathrm{spots}} = \frac{\sum_{ij}(v_{ij} - \delta v_{\mathrm{sc},ij})\,(I_{ij} - L_{ij})\, W_{ij}}{\sum_{ij} I_{ij}} \tag{4.25}$$

In this case, the weights are set to 1 only for pixels that fulfill both the magnetic strength and brightness criteria:

$$\begin{aligned} W_{ij} = 1 \text{ if } |B_{\mathrm{r},ij}| > |B_{\mathrm{r,thresh},ij}| \\ \text{and} \\ I_{\mathrm{flat},ij} < 0.89\, \hat{I}_{\mathrm{quiet}}. \end{aligned} \tag{4.26}$$

The value of $\Delta\hat{v}_{\mathrm{spots}}$ at each time of the HARPS observations is listed in Table A11.

4.4 Reproducing the RV variations of the Sun

In this Section, I combine our model of Vesta's rotational RV signal (presented in Section 4.2.4.1) with the two magnetic activity basis functions determined in Sections 4.3.5.3 and 4.3.5.4, in order to reproduce the RV variations seen in the HARPS observations.

4.4.1 Total RV model

The final model has the form:

$$\Delta RV_{\rm model}(t) = A\,\Delta\hat{v}_{\rm conv}(t) + B\,\Delta\hat{v}_{\rm spots}(t) + \Delta RV_{\rm vesta}(t) + RV_0. \quad (4.27)$$

I carry out an optimal scaling procedure in order to determine the scaling factors (A, B, C and S) of each of the contributions, as well as the constant offset RV_0. Each basis function is orthogonalised by subtracting its inverse-variance weighted average prior to performing the scaling. I determine the maximum likelihood via a procedure similar to the one described in Collier Cameron et al. (2006). This procedure is applied to the unbinned (not nightly-averaged) HARPS dataset, in order to determine the appropriate scaling coefficients (C and S) for Vesta's axial rotation. The total amplitude of the modulation induced by Vesta's rotation is equal to 2.39 m s^{-1}, which is of the same order as the amplitude I estimated in Section 4.2.4.1. After all the scaling coefficients were determined, I grouped the observations in each night by computing the inverse variance-weighted average for each night. The final model is shown in Figure 4.6, and the best-fit values of the parameters are listed in Table 4.2.

Panel (e) shows the residuals remaining after subtracting the total model $\Delta RV_{\rm model}$ from the HARPS observations of the Sun as-a-star $\Delta RV_{\rm Sun}$. The first part of the run (nights 0-11) displays a residual rms of 3.72 m s^{-1}, while the second part (nights 36-68) has an rms of 1.38 m s^{-1}. As I mentioned in Section 4.2.4.2, I attribute the excess scatter in the first nights to 2-3 hour granulation signals that were not well-averaged with our observing strategy. The observing strategy deployed in the second part of the run appears to be much more effective at mitigating granulation signals, even though a few outliers do remain (eg, at night 52). They may be affected by super-granulation motions which commonly take place over timescales of 8 hours or longer, and which could result in residual white noise from one night to the next.

4.4.2 Relative importance of suppression of convective blueshift and sunspot flux deficit

We see that the activity-induced RV variations of the Sun are well reproduced by a scaled sum of the two basis functions, $\hat{v}_{\rm conv}$ and $\hat{v}_{\rm spots}$ (shown in panels (b) and (c), respectively). As previously predicted by (Meunier et al., 2010), I find that the suppression of convective blueshift plays a dominant role (rms of 2.22 m s^{-1}). I also found this to be the case for CoRoT-7, a main sequence G9 star with a rotation period comparable to that of the Sun (see Chapter 3, Section 3.1 and Haywood et al. (2014)). The relatively low amplitude of the modulation induced by sunspot flux-blocking (rms of 0.14 m s^{-1}) is expected in slowly-rotating stars with a low $v \sin i$

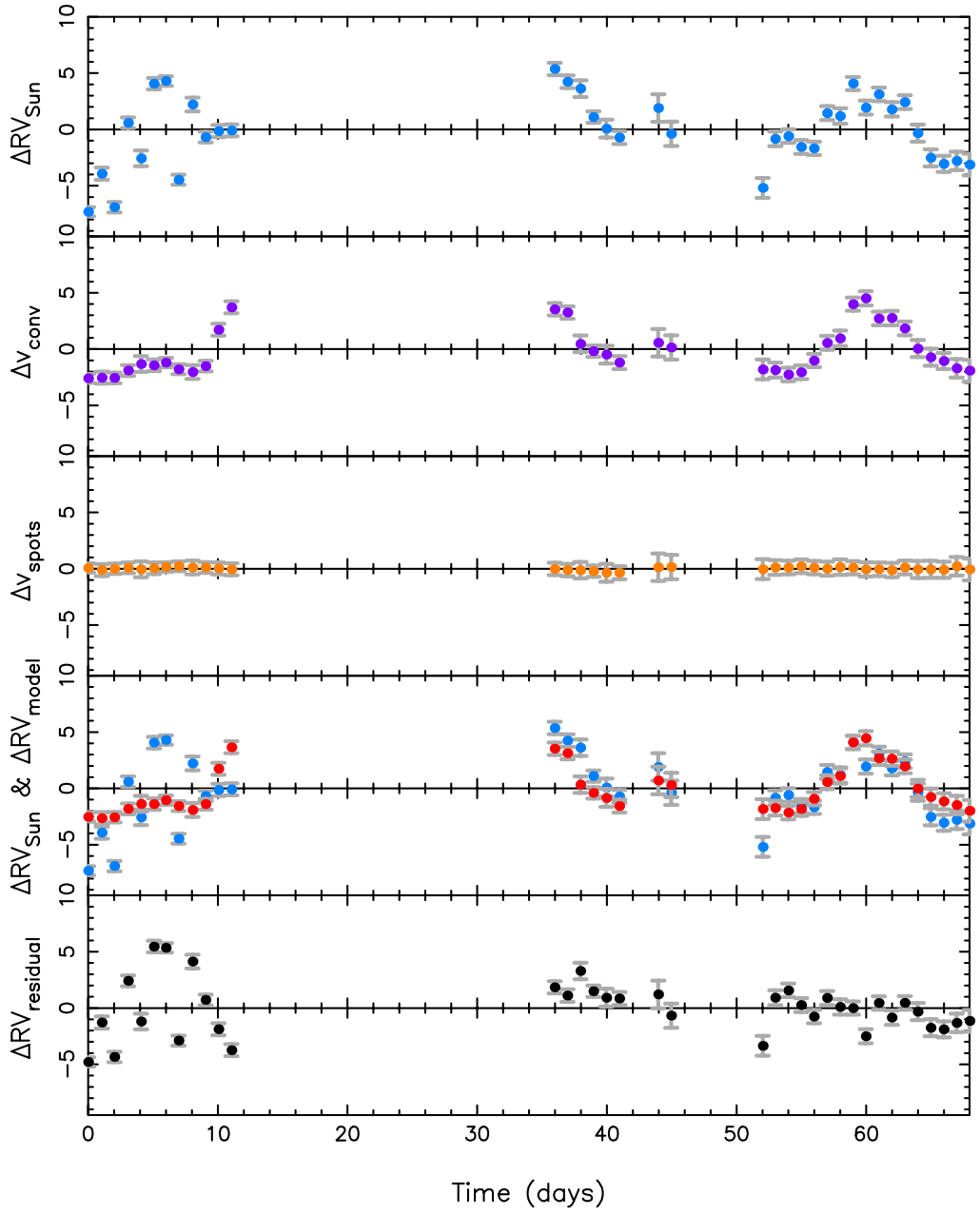

Figure 4.6: Panel (a): HARPS RV variations of the Sun as-a-star, $\Delta RV_{\rm Sun}$; Panel (b): Scaled basis function for the suppression of convective blueshift, $\Delta\hat{v}_{\rm conv}$, derived from SDO/HMI images; Panel (c): Scaled basis function for the rotational perturbation due to sunspot flux deficit, $\Delta\hat{v}_{\rm rot}$; Panel (d): total RV model, $\Delta RV_{\rm model}$ (red), overlaid on top of the HARPS RV variations (blue points); Panel (e): residuals obtained after subtracting the model from the observations. All RVs are in m s^{-1}. Note that the scale of the y-axis is different to that used in Figure 4.2.

(Desort et al., 2007). As the suppression of convective blueshift by active regions clearly dominates the total activity-induced RV variations of the Sun, I did not compute the RV modulation induced by facular flux-brightening; this contribution would only be a second-order effect.

Parameter	Value
A	0.64 ± 0.29
B	2.09 ± 0.06
C	1.99 ± 0.08
S	1.33 ± 0.09
RV_0 (m s^{-1})	99.80 ± 2.90

Table 4.2: Best-fit parameters resulting from the optimal scaling procedure.

4.4.3 Zero point of HARPS

The wavelength adjustments that were applied to the HARPS RVs were based on precise prior dynamical knowledge of the rate of change of distance between the Earth and Vesta, and between Vesta and the Sun. The offset $RV_0 = 99.80 \pm 2.90$ m s^{-1} thus represents the zero point of the HARPS instrument, including the mean granulation blueshift for the Sun.

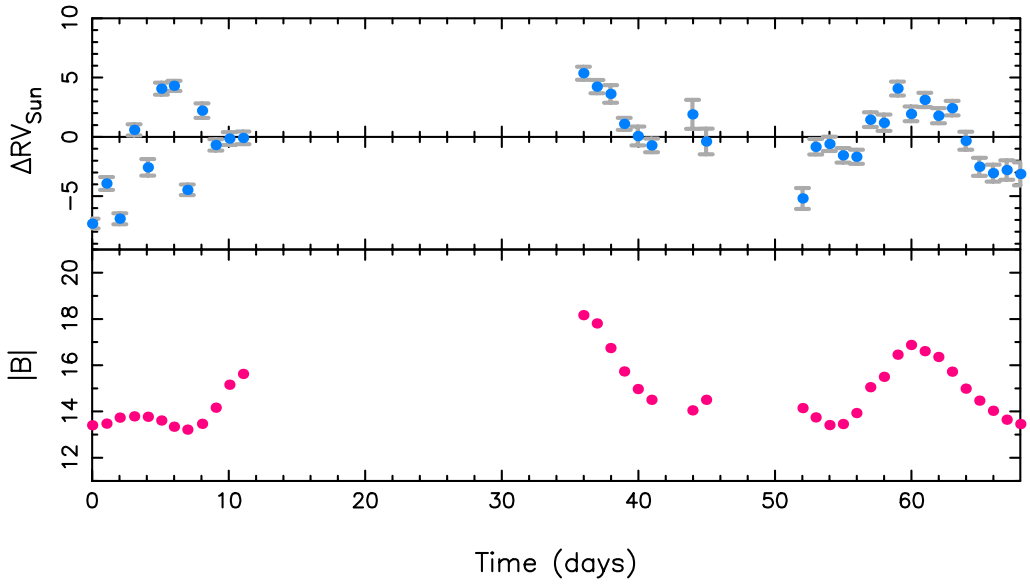

Figure 4.7: Top: HARPS RV variations of the Sun as-a-star (m s^{-1}); bottom: variations of the disc-averaged line-of-sight magnetic flux $|\hat{B}_{\rm obs}|$ (G). The two follow each other closely.

4.5 Towards better proxies for RV observations

4.5.1 Disc-averaged observed magnetic flux $|\hat{B}_{\rm obs}|$

The averaged magnetic flux may be a useful proxy for activity-driven RV variations as it should map onto areas of strong magnetic fields, which suppress the Sun's convective blueshift. The line-of-sight magnetic flux density and filling factor on the visible hemisphere of a star can be measured from the Zeeman broadening of magnetically-sensitive lines (Robinson, 1980; Reiners et al., 2013). Their product gives the disc-averaged flux density that we are deriving from the solar images.

I compute the full-disc line-of-sight magnetic flux of the Sun, by summing the intensity-weighted line-of-sight unsigned magnetic flux in each pixel:

$$|\hat{B}_{\rm obs}| = \frac{\sum_{ij} |B_{{\rm obs},ij}|\, I_{ij}}{\sum_{ij} I_{ij}} \tag{4.28}$$

The variations in $|\hat{B}_{\rm obs}|$ are shown in Figure 4.7, together with the nightly-averaged HARPS RV variations of the Sun as-a-star. We see that the variations in the disc-averaged magnetic flux are in phase with the RV variations, despite the scatter in RV in the first part of the run (discussed in Section 4.2.4.2).

4.5.2 Correlations between RV and activity indicators

Figure 4.8 presents the correlations between the nightly-averaged HARPS RV variations of the Sun as-a-star, the activity basis functions $\hat{v}_{\rm conv}$ and $\hat{v}_{\rm spots}$ and the full-disc magnetic flux computed from the SDO/HMI images, the observed FWHM, BIS, and $\log(R'_{\rm HK})$ derived from the HARPS DRS reduction pipeline. I computed the Spearman correlation coefficent to get a measure of the degree of monotone

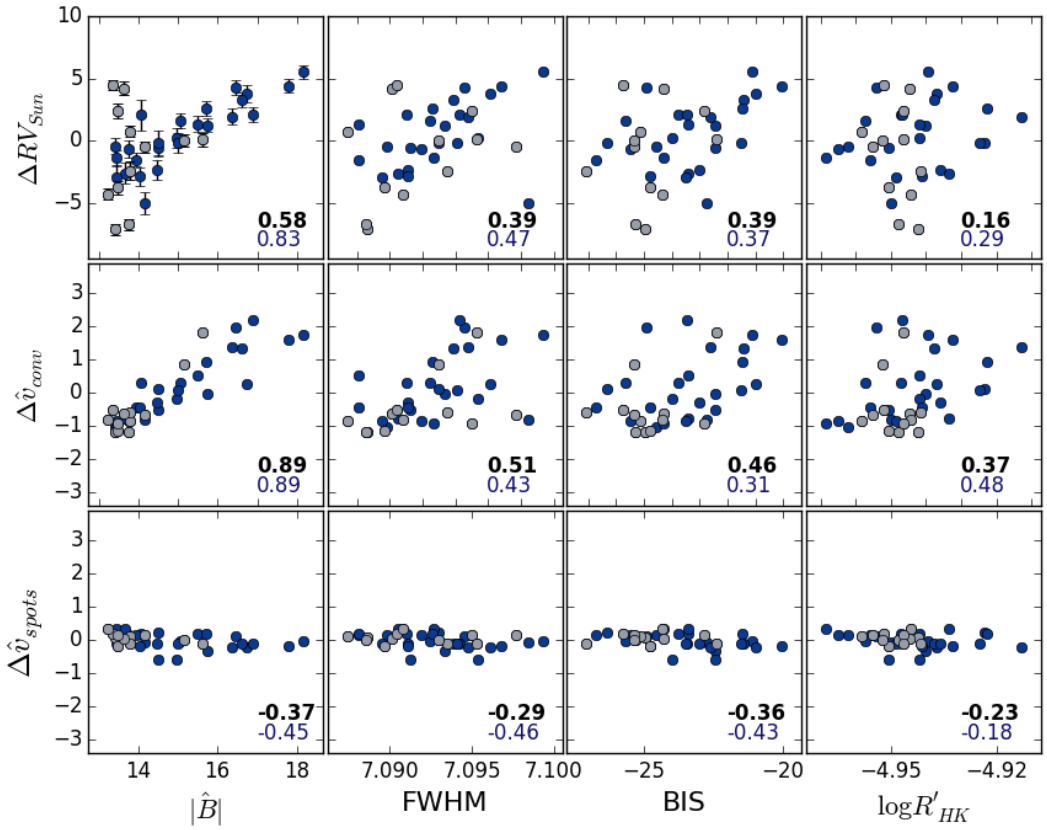

Figure 4.8: Correlation plots of the nightly-averaged HARPS RV variations of the Sun as-a-star, suppression of convective blueshift $\Delta\hat{v}_{\rm conv}$, and modulation due to sunspot flux deficit $\Delta\hat{v}_{\rm spots}$ against (from left to right): the disc-averaged observed magnetic flux $|\hat{B}_{\rm obs}|$ (G), FWHM (km s^{-1}), BIS (m s^{-1}) and $\log(R'_{\rm HK})$. Observations from the first part of the run are highlighted in a lighter shade. Spearman correlation coefficients are displayed in the bottom-right corner of each panel: for the full observing run (in bold and black), and for the second part of the run only (in blue).

correlation between each variable (the correlation between two variables is not necessarily linear, for example between RV and BIS). The coefficients are displayed in each panel of Figure 4.8, both including and excluding the observations made in the first part of the run, which show a lot of intra-night scatter. Although the extra scatter seen in the first block of observations does affect the trend slightly, it is clear that the activity-induced RV variations of the Sun are significantly correlated with the disc-averaged magnetic flux. If I only consider the observations in the second part of the run, the Spearman correlation coefficient between the RV variations of the Sun as-a-star and the disc-averaged magnetic flux is equal to 0.83. The correlation is stronger between $|\hat{B}_{\rm obs}|$ and $\hat{v}_{\rm conv}$, with a correlation coefficient of 0.89, which is in agreement with the fact that magnetised areas suppress convective blueshift. The RV variations due to sunspot flux deficit are not significantly correlated with the disc-averaged magnetic flux (or with any of the other activity indicators), but this is not so critical since these variations only play a minor role in the total activity-induced RV variations of the Sun. When compared against correlations with the traditional spectroscopic activity indicators (the FWHM, BIS and $\log(R'_{\rm HK})$), I see that the disc-averaged magnetic flux $|\hat{B}_{\rm obs}|$ is a much more effective proxy for activity-induced RV variations.

4.6 Summary

In this Chapter, I decomposed activity-induced RV variations into identifiable contributions from sunspots, faculae and granulation, based on Sun as-a-star RV variations deduced from HARPS spectra of the bright asteroid Vesta and high spatial resolution images taken with the Helioseismic and Magnetic Imager (HMI) instrument aboard the Solar Dynamics Observatory (SDO). I find that the RV variations induced by solar activity are mainly caused by the suppression of convective blueshift from magnetically active regions, while the flux deficit incurred by the presence of sunspots on the rotating solar disc only plays a minor role. I further compute the disc-averaged line-of-sight magnetic flux and show that it is an excellent proxy for activity-driven RV variations, much more so than the full width at half-maximum and bisector span of the cross-correlation profile, and the Ca II H&K activity index.

In addition to the existing 2011 HARPS observations of sunlight scattered off Vesta, there will soon be a wealth of direct solar RV measurements taken with HARPS-N, which will be regularly fed sunlight through a small 2-inch telescope developed specifically for this purpose. A prototype for this is currently being commissioned at HARPS-N (Glenday et al., in prep.). Gaining a deeper understanding of the physics at the heart of activity-driven RV variability will ultimately enable us to better model and remove this contribution from RV observations, thus revealing the planetary signals.

In the future, I wish to take this investigation one step further by synthesizing Sun-as-a-star CCFs, using SDO/HMI continuum and Dopplergram images, which contain information on the intensity scale and velocity shift of each pixel of the Sun. This will reveal spectral line profile distortions produced by activity. Comparing these synthetic line profiles with the observed HARPS CCFs (plotted in Figure 1.5 of Chapter 1) will provide a unique insight on the physical processes at play in magnetic RV variability.

Conclusion: Next steps and aims for the future

Thousands of exoplanets have now been found, the majority of which were discovered or confirmed after follow-up with RV observations. Spectrographs such as the 3.6m/HARPS and TNG/HARPS-N are capable of measuring RVs of bright stars with sub-metre per second precision. The intrinsic variability of the stars themselves, however, currently remains the main obstacle to determining the masses of small planets. The presence of magnetic features on the stellar surface, such as starspots, faculae/plage and granulation, can induce quasi-periodic RV variations of over several metres per second, which can easily conceal the orbits of super-Earths and Earth-mass planets.

I developed a Monte Carlo Markov Chain code that detects exoplanet orbits in the presence of stellar activity, which I presented in Chapter 2. Activity-induced RV signals are intimately tied to the star's rotation period, and their frequency structure is governed by the constantly-evolving magnetic features on the stellar surface. I modelled the correlated noise arising from the star's magnetic activity using a Gaussian process that has the same covariance function, or frequency structure, as the off-transit variations in the star's lightcurve. This new activity decorrelation technique allows me to identify the orbital signatures of planets present in a system and to determine their masses, with realistic allowance for the uncertainty introduced by the stellar activity. I implemented state of the art Bayesian model comparison tools to avoid over-fitting and determine the number of planets present in a system.

I applied my code to sereval high-precision RV datasets, as reported in Chapter 3. I analysed the simultaneous 3.6m/HARPS RVs and CoRoT photometric time series of the active star CoRoT-7, host to a transiting super-Earth and a small Neptune, which has been the subject of much debate in recent years due to its high activity levels. I also determined the masses of Kepler-10b and c using HARPS-N RV observations, and of Kepler-78b by combining the HARPS-N and HIRES RV datasets together.

In parallel, I studied the Sun in order to gain a deeper understanding of the processes at the heart of activity-driven RV signals, as described in Chapter 4. The Sun is the only star for which we can resolve individual surface structures that are the source of stellar RV variability. I used high spatial resolution SDO/HMI continuum, Dopplergram and magnetogram images to determine the RV signatures of sunspots, faculae/plage and granulation. I also determined the Sun's total RV variations over two solar rotations using 3.6m/HARPS observations of sunlight scattered by the surface of the bright asteroid Vesta. I tested these variations against the RV contribution determined from the SDO/HMI images and found that the activity-driven RV variations of the Sun are strongly correlated with its full-disc magnetic flux. This result may become key to disentangling planetary orbits from stellar

activity in future years.

Next steps

The detection and characterisation of exoplanets is a very dynamic and fast-moving field. The stellar activity barrier is one of the main challenges faced by the exoplanet community today, and we must overcome this barrier in order to become able to routinely detect Earth-mass planets at larger distances from their stars.

I now intend to tackle this issue via a two-fold approach:

- Incorporate activity proxies into my existing framework based on Gaussian processes and Bayesian model selection;
- Explore the temporal behaviour and physical origin of the magnetic processes at the heart of stellar RV variability, through the study of *Kepler* stars and the Sun.

An intuitive and rigorous approach to modelling RV stellar variability Long term, high precision photometry such as was obtained during the *Kepler* and CoRoT missions, is not available for the majority of candidates selected for RV follow-up. TESS will only provide us with around 30 days of photometry, which will be too short to capture fully the activity patterns of stars on their rotation and magnetic activity timescales. I wish to use Gaussian processes to develop robust activity RV models based on spectroscopic indicators (the bisector and full width at half maximum of the cross-correlation function, the R'_{HK} index) as well as new diagnostics derived from large-scale MHD simulations of photospheric convection (eg., Cegla et al. 2013). Their frequency structure is similar to that of the intrinsic magnetic activity of the host star, and can be encoded within the covariance function of a Gaussian process. Furthermore, stellar activity signals are quasi-periodic in nature, whereas planet orbits are fully periodic. The Gaussian process framework provides a means to identify a truly coherent and periodic signal, when implemented in parallel with a robust model comparison tool. I wish to test my models in a systematic way using synthetic datasets to assess the detectability of planets in the presence of stellar activity. This will help to identify the most promising targets for RV follow-up of *Kepler* and K2 candidates, and to devise observing strategies that will further minimise the impact of stellar activity, in readiness for the TESS, CHEOPS and JWST missions.

Deciphering magnetic activity patterns on the stellar rotation timescale As well as exploring individual systems, I wish to undertake a large-scale study of the activity patterns of Sun-like stars to look for relations between their photometric and RV variability, over stellar rotation timescales (as a continuation of the work I presented in Chatper 1, Section 1.3). The Fourier components of the lightcurve provide important clues about the complexity of the activity-induced RV variations (Bastien et al., 2014). In this perspective, decoding the temporal structure of a star's lightcurve is a natural step towards understanding stellar RV variability. I wish to

find out whether certain groups of stars (eg., for a given spectral type, or age) display a distinct kind of magnetic activity behaviour. It is already known that young stars tend to show spot-dominated photometric variability, whereas old stars are faculae-dominated (Radick et al. 1983, 1987, 1995; Lockwood et al. 1984, 2007). I wish to explore the dependancy of spectral type on the links between the photometric RMS, rotation period and shape of the autocorrelation function of the lightcurve in main-sequence stars (spanning the late F to early M spectral classes). These parameters can be easily obtained from *Kepler* light curves by applying autocorrelation and Lomb-Scargle periodogram techniques, which I have already implemented (see Chapter 1, Sections 1.3.2.1 and 1.3.2.2). Studying the lifetimes and sizes of starspot regions may also allow me to identify different types of magnetic activity behaviour. Classifying stars depending on their activity behaviour will allow the exoplanet community to develop better tailored models to account for RV variability, and may also help to pick more "manageable" stars in future RV surveys. This work will also enhance our understanding of stellar surface details, magnetic fields, and how they vary with mass and age/rotation.

Probing the physics at the heart of the Sun's RV variability I plan to pursue my current study of the Sun to develop the next generation of more sophisticated activity models. In addition to the existing 2012 HARPS observations of sunlight reflected off Vesta, there will soon be a wealth of direct solar RV measurements taken with HARPS-N, which will be regularly fed sunlight through a small 2-inch telescope developed specifically for this purpose by Dr. David Phillips at the CfA. A prototype for this is currently being commissioned at HARPS-N. In particular, I wish to explore the effect of faculae on the suppression of convective blueshift, since this process has been found to be the dominant contribution to the activity-induced RV signal (Meunier et al. 2010; Haywood et al. 2014). Other types of photospheric velocity field may play an important but previously unrecognised role in stellar RV variability; in particular, Gizon et al. (2001, 2010) report the presence of ~ 50 m.s^{-1} inflows towards active regions on the Sun's surface. Planetary signals are the same at all wavelengths, whereas stellar activity signals will change according to the photospheric depth sampled by different line masks of different wavelength ranges (Anglada-Escudé & Butler, 2012; Tuomi et al. 2013). I wish to explore the physical sources of this phenomenon, and investigate the possibility of incorporating the information gained from this wavelength dependance into my code. Gaining a deeper understanding of the physics at the heart of activity-driven RV variability will ultimately enable us to better model and remove this contribution from RV observations, thus revealing the planetary signals.

Appendix

Julian Date [Day] BJD_UTC	RV [km.s^{-1}]	σ_{RV} [km.s^{-1}]	$FWHM$ [km.s^{-1}]	BIS [km.s^{-1}]	$\log(R'_{HK})$	$\sigma_{log(R'_{HK})}$
2'455'939.69948	31.18031	0.00233	6.45633	0.01199	-4.6990	0.0180
2'455'939.76024	31.17814	0.00212	6.46445	0.01966	-4.7188	0.0173
2'455'940.57499	31.18283	0.00251	6.46592	0.01956	-4.6982	0.0210
2'455'940.68929	31.17833	0.00271	6.45650	0.03679	-4.7789	0.0283
2'455'940.79456	31.18415	0.00215	6.46568	0.01359	-4.7204	0.0180
2'455'941.56490	31.18294	0.00241	6.45065	0.01822	-4.7635	0.0245
2'455'941.66870	31.18832	0.00184	6.45273	0.02814	-4.7365	0.0137
2'455'941.77024	31.18890	0.00199	6.45558	0.02559	-4.7510	0.0169
2'455'942.56139	31.17631	0.00263	6.45472	0.01846	-4.6730	0.0191
2'455'942.67696	31.17626	0.00167	6.45427	0.02055	-4.7071	0.0095
2'455'942.78412	31.17705	0.00247	6.45564	0.03818	-4.7222	0.0221
2'455'943.56090	31.17020	0.00239	6.44767	0.02167	-4.7187	0.0215
2'455'943.66570	31.16834	0.00199	6.44649	0.02202	-4.7482	0.0163
2'455'943.76867	31.17497	0.00177	6.45494	0.02110	-4.7508	0.0152
2'455'944.56671	31.17690	0.00213	6.44517	0.02596	-4.7237	0.0180
2'455'944.66911	31.17499	0.00216	6.44351	0.02340	-4.7166	0.0167
2'455'944.77370	31.17966	0.00185	6.44134	0.02035	-4.7206	0.0150
2'455'945.56098	31.18232	0.00238	6.45457	0.01149	-4.7319	0.0221
2'455'945.66736	31.18053	0.00213	6.45674	0.01439	-4.7275	0.0178
2'455'945.77208	31.17698	0.00221	6.44160	0.02874	-4.7497	0.0213
2'455'946.55742	31.17466	0.00222	6.44724	0.00971	-4.7694	0.0214
2'455'946.66311	31.17309	0.00176	6.45013	0.01661	-4.7358	0.0131
2'455'946.76840	31.17567	0.00209	6.45653	0.01566	-4.7467	0.0181
2'455'947.54531	31.17707	0.00223	6.45981	0.02810	-4.7581	0.0210
2'455'947.66174	31.18084	0.00179	6.45909	0.01563	-4.7334	0.0133
2'455'947.76281	31.18561	0.00191	6.46437	0.02390	-4.7700	0.0185
2'455'948.55706	31.18901	0.00217	6.46402	0.01550	-4.7355	0.0188
2'455'948.66364	31.19692	0.00163	6.46248	0.02318	-4.7389	0.0114
2'455'948.76718	31.19676	0.00175	6.46623	0.02778	-4.7548	0.0157
2'455'949.55411	31.18631	0.00247	6.46951	0.02427	-4.8253	0.0283
2'455'949.65555	31.19076	0.00187	6.46200	0.02620	-4.7545	0.0149
2'455'949.75824	31.19305	0.00245	6.46655	0.03246	-4.7434	0.0243
2'455'950.56227	31.17601	0.00168	6.46236	0.03281	-4.7404	0.0130
2'455'950.66816	31.17590	0.00175	6.45419	0.01683	-4.7400	0.0131
2'455'950.76859	31.17096	0.00177	6.45464	0.02764	-4.7633	0.0163
2'455'951.54884	31.17391	0.00182	6.43438	0.03045	-4.7528	0.0158
2'455'951.65576	31.17223	0.00207	6.43799	0.02989	-4.7971	0.0188
2'455'951.75704	31.17219	0.00246	6.44706	0.02311	-4.7875	0.0271
2'455'952.56523	31.17963	0.00204	6.44030	0.01523	-4.7580	0.0187
2'455'952.77021	31.18059	0.00225	6.44565	0.02541	-4.7385	0.0225

Table A1: HARPS 2012 data for CoRoT-7, processed in the same way as the 2008-2009 data (Queloz et al., 2009). From left to right are given: Julian date, radial-velocity RV, the estimated error σ_{RV} on the RV, the full width at half-maximum ($FWHM$) and the line bisector of (BIS) of the cross-correlation function (as defined in Queloz et al. (2001a)), the Ca II activity indicator $\log(R'_{HK})$ and its error $\sigma_{log(R'_{HK})}$.

Julian Date [Day] BJD_UTC	RV [km.s^{-1}]	σ_{RV} [km.s^{-1}]	$FWHM$ [km.s^{-1}]	BIS [km.s^{-1}]	$\log(R'_{HK})$	$\sigma_{log(R'_{HK})}$
2'455'953.55597	31.17395	0.00182	6.43480	0.01000	-4.7119	0.0146
2'455'953.68468	31.17475	0.00195	6.45180	0.00298	-4.7323	0.0152
2'455'953.76300	31.18222	0.00268	6.44616	0.02591	-4.7364	0.0272
2'455'954.55404	31.17790	0.00181	6.44536	0.00875	-4.7410	0.0154
2'455'954.63792	31.18295	0.00168	6.46153	0.01177	-4.7168	0.0118
2'455'955.55847	31.18862	0.00189	6.46166	0.02000	-4.7413	0.0161
2'455'955.63894	31.19331	0.00165	6.46554	0.01452	-4.7438	0.0120
2'455'955.73279	31.19476	0.00179	6.44739	0.00867	-4.7347	0.0148
2'455'956.62463	31.19811	0.00156	6.46579	0.02657	-4.7147	0.0106
2'455'956.72897	31.19191	0.00192	6.47400	0.02364	-4.7015	0.0149
2'455'957.64372	31.18164	0.00206	6.47184	0.02857	-4.7539	0.0179
2'455'958.56684	31.18091	0.00192	6.47635	0.02301	-4.7447	0.0163
2'455'958.65850	31.18392	0.00201	6.47078	0.02216	-4.7459	0.0171
2'455'958.71729	31.18374	0.00201	6.47376	0.02909	-4.6738	0.0158
2'455'959.55361	31.18266	0.00205	6.48019	0.01837	-4.7103	0.0164
2'455'959.64103	31.18817	0.00201	6.46959	0.02289	-4.7087	0.0149
2'455'959.72214	31.18793	0.00210	6.46640	0.02085	-4.7060	0.0177
2'455'960.54986	31.18993	0.00180	6.48016	0.02823	-4.6961	0.0133
2'455'960.64222	31.18652	0.00182	6.48139	0.01905	-4.6868	0.0124
2'455'960.71808	31.18327	0.00202	6.47342	0.03245	-4.6930	0.0161
2'455'961.57133	31.17531	0.00190	6.46406	0.01978	-4.7245	0.0148
2'455'961.71143	31.17428	0.00177	6.47095	0.01987	-4.7172	0.0140
2'455'962.54203	31.18283	0.00239	6.48479	0.01274	-4.7236	0.0204
2'455'962.63340	31.18606	0.00209	6.47948	0.02189	-4.7266	0.0166
2'455'962.72313	31.17570	0.00249	6.47445	0.01550	-4.7286	0.0235
2'455'963.55846	31.18712	0.00187	6.48049	0.01961	-4.7051	0.0135
2'455'963.64853	31.18517	0.00163	6.47868	0.02397	-4.6832	0.0101
2'455'963.70438	31.18517	0.00184	6.47691	0.02248	-4.6987	0.0143
2'455'964.55809	31.18475	0.00195	6.48780	0.03089	-4.7172	0.0148
2'455'964.62532	31.18077	0.00224	6.48025	0.02273	-4.7404	0.0182
2'455'964.70360	31.17426	0.00272	6.47958	0.03171	-4.7357	0.0249

Table A2: (Continued) HARPS 2012 data for CoRoT-7, processed in the same way as the 2008-2009 data (Queloz et al., 2009). From left to right are given: Julian date, radial-velocity RV, the estimated error σ_{RV} on the RV, the full width at half-maximum ($FWHM$) and the line bisector of (BIS) of the cross-correlation function (as defined in Queloz et al. (2001a)), the Ca II activity indicator $\log(R'_{HK})$ and its error $\sigma_{log(R'_{HK})}$.

Julian Date [BJD_UTC]	RV [km.s^{-1}]	$\sigma_{\rm RV}$ [km.s^{-1}]
2456448.88278	0.00175	0.00214
2456448.90334	-0.00103	0.00193
2456448.92171	-0.00038	0.00185
2456448.93995	-0.00093	0.00207
2456448.95738	-0.00026	0.00184
2456448.97341	-0.00264	0.00193
2456448.98941	-0.00642	0.00195
2456449.00348	-0.00191	0.00188
2456449.01627	0.00071	0.00194
2456449.02821	-0.00396	0.00182
2456449.04018	0.00070	0.00189
2456449.05200	-0.00089	0.00188
2456449.06446	-0.00447	0.00212
2456449.07811	-0.00604	0.00186
2456449.09286	0.00603	0.00182
2456449.10900	0.00078	0.00239
2456472.82037	-0.00169	0.00237
2456472.84218	0.00447	0.00198
2456472.86294	-0.00172	0.00182
2456472.92619	-0.00098	0.00169
2456472.94153	-0.00085	0.00172
2456472.95886	0.00173	0.00169
2456473.05970	-0.00473	0.00193
2456473.07770	-0.00094	0.00169
2456473.09709	-0.00389	0.00216
2456473.82630	-0.00765	0.00176
2456473.84243	-0.00924	0.00161
2456473.86077	-0.00560	0.00172
2456473.99527	-0.00550	0.00180
2456474.01574	-0.00289	0.00165
2456474.03286	0.00018	0.00174
2456474.06661	-0.00779	0.00166
2456474.08462	-0.00570	0.00173
2456474.10100	0.00151	0.00157
2456475.80495	0.01791	0.00176
2456475.81937	0.02018	0.00176
2456475.83325	0.01913	0.00163
2456475.95222	0.02003	0.00163
2456475.96478	0.02138	0.00155
2456475.97800	0.02150	0.00165
2456476.08215	0.02288	0.00163
2456476.09379	0.02174	0.00165
2456476.10619	0.02488	0.00151
2456478.80182	-0.01468	0.00177
2456478.82010	-0.01551	0.00157
2456478.83807	-0.01750	0.00156
2456478.96021	-0.01122	0.00159
2456478.97544	-0.00844	0.00165
2456478.98947	-0.00828	0.00157

Table A3: HIRES RV data for Kepler-78. From left to right are given: Julian date, radial-velocity RV and the estimated error σ_{RV} on the RV.

Julian Date [BJD_UTC]	RV [km.s^{-1}]	$\sigma_{\rm RV}$ [km.s^{-1}]
2456479.07694	-0.01450	0.00156
2456479.09508	-0.00971	0.00157
2456479.11666	-0.01099	0.00163
2456483.78932	-0.00614	0.00177
2456483.80904	-0.00675	0.00166
2456483.82822	0.00006	0.00177
2456483.93703	0.00531	0.00168
2456483.95393	-0.00353	0.00183
2456483.97240	-0.00051	0.00182
2456484.08139	-0.00189	0.00162
2456484.10126	-0.00262	0.00183
2456484.11910	-0.00641	0.00172
2456484.86704	-0.00426	0.00159
2456485.78098	-0.00048	0.00154
2456485.79643	0.00004	0.00154
2456485.81186	-0.00064	0.00164
2456485.88961	-0.00007	0.00175
2456485.90234	-0.00986	0.00163
2456485.91463	-0.00225	0.00159
2456486.07175	0.00262	0.00174
2456486.08761	-0.00265	0.00169
2456486.10455	-0.00340	0.00164
2456486.77816	-0.00451	0.00163
2456486.79474	-0.00218	0.00164
2456486.81158	-0.00412	0.00159
2456486.94956	-0.00507	0.00184
2456486.96350	-0.00330	0.00181
2456486.97688	-0.00616	0.00180
2456487.09450	-0.00084	0.00193
2456487.11122	-0.00523	0.00168
2456487.93100	0.00970	0.00175
2456488.95482	0.03116	0.00191
2456489.90345	0.02113	0.00193
2456493.01254	-0.00070	0.00207
2456493.99643	-0.00382	0.00193

Table A4: (Continued) HIRES RV data for Kepler-78. From left to right are given: Julian date, radial-velocity RV and the estimated error σ_{RV} on the RV.

Julian Date [BJD_UTC]	RV [km.s^{-1}]	$\sigma_{\rm RV}$ [km.s^{-1}]
2456435.51292	-3.51192	0.00246
2456435.53406	-3.50781	0.00220
2456435.55521	-3.50957	0.00218
2456435.57634	-3.51437	0.00214
2456435.59748	-3.51086	0.00207
2456435.61863	-3.50984	0.00207
2456435.63976	-3.50512	0.00193
2456435.66092	-3.50600	0.00184
2456435.68207	-3.50799	0.00190
2456435.70320	-3.51162	0.00177
2456456.46507	-3.50922	0.00197
2456456.48977	-3.50808	0.00210
2456456.51440	-3.51034	0.00215
2456456.53902	-3.50984	0.00186
2456456.56315	-3.51045	0.00221
2456456.58768	-3.50798	0.00235
2456456.61247	-3.50081	0.00232
2456456.63656	-3.50766	0.00232
2456456.66187	-3.51058	0.00199
2456456.68591	-3.50940	0.00199
2456456.70988	-3.51349	0.00311
2456457.45301	-3.51280	0.00283
2456457.47415	-3.51266	0.00271
2456457.49848	-3.51804	0.00257
2456457.51963	-3.51202	0.00251
2456457.54360	-3.51812	0.00252
2456457.56473	-3.51555	0.00267
2456457.58899	-3.51656	0.00291
2456457.61014	-3.51471	0.00312
2456457.63537	-3.51408	0.00218
2456457.65652	-3.51208	0.00175
2456457.68068	-3.51273	0.00239
2456457.70181	-3.51276	0.00216
2456458.44957	-3.51717	0.00372
2456458.47071	-3.51335	0.00275
2456458.49468	-3.51228	0.00271
2456458.51583	-3.51804	0.00245
2456458.53986	-3.51393	0.00211
2456458.56099	-3.51331	0.00219
2456458.58499	-3.51313	0.00219
2456458.60612	-3.51142	0.00267
2456458.63003	-3.51166	0.00204
2456458.65118	-3.51254	0.00198
2456458.68064	-3.51234	0.00220
2456458.70178	-3.51309	0.00247
2456459.44426	-3.50546	0.00256
2456459.46540	-3.50794	0.00255
2456459.49047	-3.50930	0.00266
2456459.51161	-3.50990	0.00268
2456459.53564	-3.50344	0.00250
2456459.55680	-3.50821	0.00190
2456459.58083	-3.50712	0.00224

Table A5: HARPS-N RV data for Kepler-78. From left to right are given: Julian date, radial-velocity RV and the estimated error σ_{RV} on the RV.

Julian Date [BJD_UTC]	RV [km.s^{-1}]	$\sigma_{\rm RV}$ [km.s^{-1}]
2456459.60197	-3.50975	0.00198
2456459.62610	-3.51055	0.00211
2456459.64723	-3.51698	0.00183
2456459.67153	-3.50997	0.00222
2456459.69267	-3.51023	0.00216
2456460.44685	-3.51150	0.00346
2456460.46800	-3.50275	0.00334
2456460.49402	-3.51202	0.00285
2456460.51515	-3.50686	0.00239
2456460.53921	-3.51042	0.00283
2456460.56036	-3.50756	0.00219
2456460.58477	-3.50997	0.00193
2456460.60592	-3.51167	0.00181
2456460.63011	-3.51602	0.00178
2456460.65127	-3.51580	0.00186
2456460.67548	-3.51206	0.00212
2456460.69663	-3.51496	0.00223
2456461.47151	-3.50908	0.00214
2456461.49265	-3.51148	0.00215
2456461.51660	-3.51155	0.00220
2456461.53775	-3.50936	0.00192
2456461.56161	-3.51262	0.00204
2456461.58275	-3.50851	0.00198
2456461.60669	-3.50860	0.00193
2456461.62782	-3.51014	0.00176
2456461.65172	-3.50593	0.00189
2456461.67287	-3.50949	0.00221
2456461.69683	-3.51160	0.00217
2456462.46355	-3.50626	0.00259
2456462.66329	-3.50358	0.00220
2456463.54683	-3.50312	0.00301
2456463.69612	-3.49958	0.00241
2456465.50148	-3.50753	0.00281
2456465.68396	-3.51335	0.00324
2456466.52111	-3.50700	0.00198
2456466.67679	-3.50691	0.00224
2456478.46010	-3.51859	0.00257
2456478.64282	-3.52204	0.00225
2456479.52887	-3.51551	0.00185
2456479.70375	-3.50692	0.00178
2456480.43572	-3.50233	0.00231
2456480.60732	-3.50764	0.00162
2456481.48297	-3.50475	0.00338
2456481.65660	-3.51505	0.00324
2456482.53436	-3.50600	0.00290
2456495.49348	-3.50754	0.00179

Table A6: (Continued) HARPS-N RV data for Kepler-78. From left to right are given: Julian date, radial-velocity RV and the estimated error σ_{RV} on the RV.

Julian Date [BJD_UTC]	RV [km.s^{-1}]	$\sigma_{\rm RV}$ [km.s^{-1}]
2456495.66755	-3.50252	0.00185
2456496.56297	-3.50528	0.00173
2456497.44726	-3.50629	0.00209
2456497.62894	-3.50729	0.00206
2456499.40721	-3.52056	0.00220
2456499.57787	-3.50998	0.00211
2456501.46394	-3.49462	0.00268
2456501.63647	-3.48489	0.00222
2456510.50035	-3.50743	0.00225
2456529.39927	-3.51338	0.00209
2456529.57873	-3.52256	0.00262
2456532.41047	-3.51012	0.00184
2456532.58840	-3.50892	0.00210

Table A7: (Continued again) HARPS-N RV data for Kepler-78. From left to right are given: Julian date, radial-velocity RV and the estimated error σ_{RV} on the RV.

Julian Date [BJD_UTC]	RV [km.s^{-1}]	$\sigma_{\rm RV}$ [km.s^{-1}]
2456072.68238	-98.74255	0.00176
2456072.70477	-98.74289	0.00186
2456087.57572	-98.74152	0.00219
2456087.59690	-98.73548	0.00198
2456103.66164	-98.74040	0.00239
2456103.68979	-98.74432	0.00219
2456115.69195	-98.74330	0.00174
2456115.71315	-98.74740	0.00204
2456116.70476	-98.73779	0.00371
2456116.71900	-98.74241	0.00407
2456125.56825	-98.74691	0.00282
2456125.58945	-98.74791	0.00217
2456126.44790	-98.74268	0.00156
2456126.66495	-98.74039	0.00378
2456127.42243	-98.75306	0.00933
2456127.44164	-98.73944	0.00150
2456128.43499	-98.73769	0.00157
2456128.56048	-98.74262	0.00155
2456128.66292	-98.74155	0.00191
2456148.40812	-98.73240	0.00204
2456148.51178	-98.72940	0.00177
2456148.61782	-98.73637	0.00176
2456151.39639	-98.74033	0.00220
2456152.40789	-98.73884	0.00136
2456152.64028	-98.73926	0.00225
2456153.39511	-98.73774	0.00164
2456153.49340	-98.74576	0.00414
2456153.64701	-98.73540	0.00161
2456160.47349	-98.74086	0.00344
2456160.62636	-98.74313	0.00310
2456161.39719	-98.74463	0.00234
2456161.57318	-98.74491	0.00266
2456162.39440	-98.74808	0.00221
2456162.48796	-98.74682	0.00213
2456162.56797	-98.74920	0.00242
2456164.38526	-98.73798	0.00211
2456165.38084	-98.73674	0.00212
2456166.38481	-98.73611	0.00238
2456166.53442	-98.74392	0.00225
2456166.60100	-98.74469	0.00243
2456175.41062	-98.73567	0.00135
2456175.52189	-98.73672	0.00162
2456178.37389	-98.74496	0.00183
2456178.49464	-98.73402	0.00172
2456179.37346	-98.73632	0.00150
2456179.52105	-98.73564	0.00170
2456180.40035	-98.73472	0.00136
2456180.54383	-98.73691	0.00161
2456181.43571	-98.74069	0.00130
2456181.52957	-98.75637	0.00900
2456181.53452	-98.73614	0.00163

Table A8: HARPS-N RV data for Kepler-10. From left to right are given: Julian date, radial-velocity RV and the estimated error σ_{RV} on the RV.

Julian Date [BJD_UTC]	RV [km.s^{-1}]	$\sigma_{\rm RV}$ [km.s^{-1}]
2456182.39829	-98.73807	0.00140
2456182.53510	-98.74104	0.00164
2456183.37354	-98.73985	0.00205
2456183.56015	-98.73569	0.00180
2456245.33252	-98.74697	0.00153
2456252.34146	-98.73899	0.00164
2456379.67743	-98.73774	0.00219
2456379.75048	-98.73848	0.00209
2456380.66345	-98.74142	0.00197
2456380.73986	-98.74277	0.00178
2456381.68562	-98.74447	0.00155
2456381.75076	-98.74588	0.00155
2456382.67190	-98.74540	0.00145
2456382.75352	-98.74504	0.00167
2456396.60874	-98.73338	0.00140
2456396.72449	-98.73343	0.00136
2456398.61485	-98.73168	0.00232
2456398.72770	-98.73555	0.00183
2456400.59433	-98.74684	0.01134
2456402.59048	-98.72731	0.00526
2456402.70771	-98.73467	0.00755
2456418.58871	-98.73980	0.00212
2456418.68919	-98.73876	0.00199
2456420.58504	-98.73607	0.00299
2456420.69846	-98.74206	0.00173
2456421.58973	-98.73982	0.00152
2456421.68630	-98.73891	0.00116
2456432.55950	-98.74077	0.00130
2456432.70481	-98.74502	0.00124
2456433.56250	-98.74446	0.00125
2456433.70881	-98.74808	0.00118
2456434.52317	-98.74886	0.00187
2456434.68979	-98.74383	0.00137
2456436.53921	-98.74284	0.00134
2456436.69836	-98.74009	0.00128
2456437.53706	-98.74365	0.00139
2456437.69887	-98.74230	0.00123
2456462.44091	-98.73725	0.00175
2456462.59533	-98.73568	0.00174
2456463.49967	-98.73338	0.00179
2456463.67340	-98.73983	0.00156
2456464.51508	-98.73316	0.00416
2456464.67568	-98.73873	0.00220
2456465.52353	-98.73992	0.00190
2456466.47765	-98.73979	0.00156
2456466.69868	-98.73746	0.00159
2456478.42237	-98.73998	0.00181
2456478.60722	-98.73691	0.00150
2456479.46830	-98.73672	0.00130

Table A9: (Continued) HARPS-N RV data for Kepler-10. From left to right are given: Julian date, radial-velocity RV and the estimated error σ_{RV} on the RV.

Julian Date [BJD_UTC]	RV [km.s^{-1}]	$\sigma_{\rm RV}$ [km.s^{-1}]
2456479.60626	-98.73968	0.00130
2456480.55093	-98.74078	0.00124
2456480.70258	-98.74235	0.00138
2456481.44340	-98.74286	0.00156
2456481.57823	-98.74265	0.00206
2456482.44415	-98.73988	0.00192
2456482.62878	-98.73737	0.00269
2456495.43934	-98.73437	0.00131
2456495.60647	-98.73641	0.00158
2456496.38568	-98.73264	0.00151
2456496.63902	-98.73396	0.00143
2456497.49820	-98.73858	0.00127
2456497.67948	-98.73537	0.00146
2456498.49493	-98.73056	0.00135
2456498.67162	-98.73325	0.00177
2456499.44478	-98.73121	0.00144
2456499.66910	-98.73053	0.00162
2456500.45004	-98.73231	0.00137
2456500.63489	-98.73667	0.00180
2456501.42551	-98.74023	0.00180
2456501.65852	-98.73661	0.00180
2456510.39567	-98.73406	0.00225
2456510.40634	-98.73123	0.00214
2456511.54777	-98.73834	0.00162
2456512.49135	-98.73811	0.00135
2456513.48302	-98.73776	0.00133
2456528.45989	-98.73824	0.00181
2456528.56496	-98.73769	0.00194
2456529.48076	-98.73763	0.00134
2456529.61478	-98.73502	0.00207
2456530.44419	-98.73598	0.00132
2456530.53025	-98.73528	0.00143
2456554.37335	-98.73476	0.00169
2456554.46788	-98.73894	0.00163
2456557.37108	-98.73832	0.00120
2456557.50307	-98.73898	0.00185
2456562.43589	-98.74030	0.00261
2456563.37324	-98.74056	0.00147
2456563.47280	-98.74250	0.00174
2456565.35294	-98.74314	0.00161
2456565.48258	-98.73696	0.00131
2456567.34757	-98.73499	0.00121
2456571.34474	-98.73993	0.00227
2456571.45502	-98.73917	0.00223
2456580.34233	-98.73832	0.00146
2456580.43589	-98.74190	0.00153
2456582.32927	-98.74092	0.00128
2456582.37676	-98.73806	0.00159

Table A10: (Continued again) HARPS-N RV data for Kepler-10. From left to right are given: Julian date, radial-velocity RV and the estimated error σ_{RV} on the RV.

Julian Date [MJD_{mid}-UTC]	RV [km s^{-1}]	σ_{RV} [km s^{-1}]	FWHM [km s^{-1}]	BIS [km s^{-1}]	$\log(R'_{HK})$	$\sigma_{\log(R'_{HK})}$
2455834.48296192	0.08570	0.00043	0.00709	-0.00002	-4.94110	0.00240
2455834.61321887	0.09936	0.00039	0.00709	-0.00003	-4.94350	0.00190
2455835.53355275	0.09477	0.00049	0.00709	-0.00002	-4.95130	0.00280
2455835.66225392	0.09936	0.00060	0.00709	-0.00002	-4.94980	0.00440
2455836.50488464	0.08431	0.00046	0.00709	-0.00002	-4.94500	0.00270
2455836.63463460	0.10254	0.00047	0.00709	-0.00003	-4.95060	0.00290
2455837.58225198	0.09916	0.00043	0.00709	-0.00002	-4.95750	0.00260
2455837.66801992	0.10148	0.00054	0.00709	-0.00003	-4.95970	0.00410
2455838.56557661	0.09552	0.00065	0.00709	-0.00003	-4.93730	0.00430
2455838.67384272	0.09925	0.00077	0.00709	-0.00003	-4.94750	0.00610
2455839.56369186	0.10600	0.00049	0.00709	-0.00002	-4.94800	0.00310
2455839.66500316	0.10144	0.00054	0.00709	-0.00003	-4.94040	0.00380
2455840.54096382	0.10181	0.00042	0.00709	-0.00003	-4.95190	0.00240
2455841.51821591	0.09743	0.00044	0.00709	-0.00002	-4.94430	0.00230
2455842.54067654	0.10156	0.00058	0.00709	-0.00002	-4.94190	0.00410
2455842.64940682	0.10221	0.00065	0.00710	-0.00002	-4.95210	0.00510
2455843.53446953	0.10135	0.00042	0.00710	-0.00002	-4.95290	0.00230
2455843.66473254	0.09722	0.00057	0.00710	-0.00003	-4.95980	0.00430
2455844.53056656	0.09656	0.00058	0.00709	-0.00002	-4.95380	0.00390
2455844.66179197	0.10292	0.00050	0.00710	-0.00003	-4.95130	0.00330
2455845.54569082	0.10143	0.00053	0.00709	-0.00002	-4.94720	0.00320
2455845.65206487	0.09830	0.00054	0.00710	-0.00002	-4.94560	0.00360
2455870.51420322	0.10843	0.00059	0.00710	-0.00002	-4.93550	0.00320
2455870.52215421	0.10701	0.00053	0.00710	-0.00002	-4.93990	0.00350
2455870.53060607	0.10379	0.00053	0.00710	-0.00002	-4.94190	0.00360
2455871.50280525	0.10250	0.00061	0.00709	-0.00002	-4.93410	0.00330
2455871.51026399	0.10190	0.00053	0.00710	-0.00002	-4.93340	0.00330
2455871.51752074	0.10279	0.00053	0.00710	-0.00002	-4.93070	0.00330
2455872.49503353	0.10638	0.00177	0.00710	-0.00002	-4.88560	0.01930
2455872.50361680	0.10706	0.00063	0.00710	-0.00002	-4.94590	0.00440
2455872.51065080	0.10433	0.00066	0.00709	-0.00002	-4.94170	0.00460
2455872.51832551	0.10431	0.00066	0.00709	-0.00002	-4.92970	0.00440
2455873.50406872	0.09870	0.00050	0.00709	-0.00002	-4.94000	0.00300
2455873.51131777	0.09937	0.00050	0.00709	-0.00002	-4.94250	0.00310
2455873.51863681	0.09933	0.00051	0.00710	-0.00002	-4.93800	0.00300
2455874.50355099	0.10133	0.00077	0.00710	-0.00002	-4.94670	0.00510
2455874.51074342	0.10294	0.00074	0.00709	-0.00002	-4.94020	0.00570
2455874.51805876	0.10132	0.00089	0.00710	-0.00003	-4.93790	0.00690
2455875.50408302	0.09839	0.00058	0.00709	-0.00002	-4.95440	0.00400
2455875.51155021	0.09671	0.00057	0.00709	-0.00002	-4.94720	0.00390
2455875.51886866	0.09645	0.00058	0.00709	-0.00002	-4.95000	0.00400
2455878.50606288	0.10481	0.00123	0.00709	-0.00002	-4.93680	0.01290
2455878.51386630	0.10396	0.00125	0.00709	-0.00002	-4.95210	0.01370
2455878.52076438	0.10324	0.00120	0.00709	-0.00003	-4.95290	0.01280
2455879.50702795	0.09725	0.00112	0.00709	-0.00003	-4.91970	0.01030

Table A11: HARPS 2011-2012 data for the asteroid Vesta, processed by the HARPS pipeline with the correct barycentric RV and accounting for the relativistic correction. From left to right are given: Julian date (flux-weighted mid-exposure times of observation), RV, the estimated error σ_{RV} on the RV, the full width at half-maximum (FWHM) and the line bisector of (BIS) of the cross-correlation function (as defined in Queloz et al. (2001a)), the Ca II activity indicator $\log(R'_{HK})$ and its error $\sigma_{\log(R'_{HK})}$.

Julian Date [MJD_{mid}_UTC]	RV [km s^{-1}]	σ_{RV} [km s^{-1}]	FWHM [km s^{-1}]	BIS [km s^{-1}]	$\log(R'_{HK})$	$\sigma_{\log(R'_{HK})}$
2455879.51427708	0.09705	0.00107	0.00709	-0.00003	-4.93600	0.01000
2455879.52152229	0.09781	0.00105	0.00709	-0.00003	-4.91460	0.00930
2455886.55971131	0.09668	0.00085	0.00710	-0.00002	-4.95370	0.00730
2455886.56696080	0.09496	0.00086	0.00709	-0.00002	-4.94810	0.00750
2455886.57392844	0.09257	0.00093	0.00710	-0.00002	-4.94770	0.00860
2455887.52342644	0.09687	0.00060	0.00709	-0.00002	-4.96360	0.00420
2455887.53095415	0.09745	0.00067	0.00709	-0.00003	-4.97260	0.00520
2455887.53806579	0.09616	0.00072	0.00709	-0.00003	-4.95780	0.00560
2455888.52593242	0.10110	0.00060	0.00709	-0.00003	-4.96610	0.00430
2455888.53317611	0.10158	0.00059	0.00709	-0.00002	-4.96230	0.00430
2455888.54049630	0.10175	0.00062	0.00709	-0.00003	-4.95770	0.00470
2455889.52578074	0.09755	0.00060	0.00709	-0.00003	-4.96420	0.00450
2455889.53310116	0.09601	0.00060	0.00709	-0.00002	-4.96330	0.00460
2455889.54034195	0.09461	0.00065	0.00709	-0.00002	-4.97960	0.00540
2455890.50917526	0.10097	0.00059	0.00709	-0.00003	-4.95050	0.00400
2455890.51649149	0.10074	0.00058	0.00709	-0.00003	-4.95640	0.00400
2455890.52382222	0.09996	0.00059	0.00709	-0.00002	-4.96110	0.00420
2455891.52246765	0.09941	0.00060	0.00709	-0.00003	-4.95910	0.00440
2455891.52978471	0.09921	0.00063	0.00709	-0.00003	-4.96490	0.00490
2455891.53703495	0.09840	0.00063	0.00709	-0.00003	-4.94820	0.00490
2455892.52735539	0.10398	0.00061	0.00709	-0.00002	-4.94420	0.00450
2455892.53453612	0.10358	0.00079	0.00709	-0.00002	-4.93700	0.00680
2455892.54214391	0.10247	0.00069	0.00709	-0.00002	-4.94220	0.00540
2455893.51437423	0.10022	0.00059	0.00710	-0.00002	-4.94400	0.00400
2455893.52626540	0.10239	0.00057	0.00709	-0.00003	-4.95780	0.00400
2455893.53359078	0.10228	0.00060	0.00710	-0.00002	-4.96070	0.00440
2455894.50541095	0.10265	0.00059	0.00709	-0.00002	-4.94990	0.00410
2455894.51266019	0.10400	0.00062	0.00709	-0.00002	-4.94160	0.00440
2455894.52011844	0.10548	0.00068	0.00709	-0.00002	-4.94860	0.00520
2455895.51190055	0.09855	0.00058	0.00709	-0.00002	-4.93410	0.00380
2455895.51928533	0.10014	0.00061	0.00709	-0.00002	-4.93390	0.00410
2455895.52668202	0.10385	0.00060	0.00709	-0.00002	-4.94560	0.00410
2455896.51221054	0.10311	0.00062	0.00710	-0.00002	-4.90820	0.00420
2455896.51945075	0.10402	0.00064	0.00709	-0.00002	-4.92190	0.00440
2455896.52676887	0.10450	0.00065	0.00709	-0.00002	-4.90860	0.00450
2455897.51313557	0.09805	0.00057	0.00709	-0.00002	-4.92790	0.00410
2455897.52017185	0.10199	0.00061	0.00709	-0.00002	-4.92070	0.00450
2455897.52797234	0.10103	0.00066	0.00709	-0.00002	-4.91780	0.00490
2455898.51251923	0.10034	0.00076	0.00709	-0.00003	-4.91390	0.00590
2455898.51955262	0.10292	0.00074	0.00710	-0.00002	-4.92900	0.00600
2455898.52692661	0.10153	0.00078	0.00709	-0.00002	-4.93120	0.00670
2455899.51280365	0.09428	0.00077	0.00709	-0.00002	-4.92950	0.00650
2455899.51984723	0.09535	0.00075	0.00709	-0.00003	-4.94780	0.00660
2455899.52750987	0.09653	0.00076	0.00709	-0.00002	-4.92960	0.00630

Table A12: (Continued) HARPS 2011-2012 data for the asteroid Vesta, processed by the HARPS pipeline with the correct barycentric RV and accounting for the relativistic correction. From left to right are given: Julian date (flux-weighted mid-exposure times of observation), RV, the estimated error σ_{RV} on the RV, the full width at half-maximum (FWHM) and the line bisector of (BIS) of the cross-correlation function (as defined in Queloz et al. (2001a)), the Ca II activity indicator $\log(R'_{HK})$ and its error $\sigma_{\log(R'_{HK})}$.

Julian Date [MJD_{mid}-UTC]	RV [km s^{-1}]	σ_{RV} [km s^{-1}]	FWHM [km s^{-1}]	BIS [km s^{-1}]	$\log(R'_{HK})$	$\sigma_{\log(R'_{HK})}$
2455900.51316244	0.09920	0.00071	0.00709	-0.00002	-4.94570	0.00600
2455900.52048381	0.09737	0.00071	0.00709	-0.00003	-4.93890	0.00590
2455900.52779857	0.09982	0.00073	0.00709	-0.00002	-4.93880	0.00620
2455901.51376528	0.09412	0.00084	0.00709	-0.00003	-4.92440	0.00740
2455901.52080259	0.09432	0.00079	0.00709	-0.00002	-4.93700	0.00680
2455901.52818692	0.09743	0.00084	0.00709	-0.00002	-4.93870	0.00780
2455902.51342158	0.09849	0.00100	0.00710	-0.00002	-4.94530	0.00990
2455902.52087765	0.09811	0.00094	0.00709	-0.00002	-4.96080	0.00970
2455902.52825791	0.09928	0.00096	0.00709	-0.00002	-4.93910	0.00960

Table A13: (Continued again) HARPS 2011-2012 data for the asteroid Vesta, processed by the HARPS pipeline with the correct barycentric RV and accounting for the relativistic correction. From left to right are given: Julian date (flux-weighted mid-exposure times of observation), RV, the estimated error σ_{RV} on the RV, the full width at half-maximum (FWHM) and the line bisector of (BIS) of the cross-correlation function (as defined in Queloz et al. (2001a)), the Ca II activity indicator $\log(R'_{HK})$ and its error $\sigma_{\log(R'_{HK})}$.

Julian Date [MJD_{mid}_UTC]	Δt [days]	λ [deg]	$\hat{v}_{spots}$ [km s^{-1}]	$\hat{v}_{conv}$ [km s^{-1}]
2455834.48296192	2.8365	143.99	0.00007	0.00286
2455834.61321887	2.8451	351.75	0.00007	0.00286
2455835.53355275	2.8901	39.73	-0.00023	0.00296
2455835.66225392	2.9002	247.49	-0.00020	0.00278
2455836.50488464	2.9396	171.93	-0.00006	0.00302
2455836.63463460	2.9487	19.69	-0.00001	0.00273
2455837.58225198	2.9941	112.57	0.00009	0.00319
2455837.66801992	3.0056	252.95	0.00009	0.00319
2455838.56557661	3.0525	261.60	-0.00012	0.00347
2455838.67384272	3.0623	81.28	-0.00012	0.00347
2455839.56369186	3.1099	78.70	0.00002	0.00342
2455839.66500316	3.1058	241.53	0.00002	0.00342
2455840.54096382	3.1535	216.48	0.00018	0.00353
2455841.51821591	3.2110	359.87	0.00030	0.00325
2455842.54067654	3.2579	210.63	0.00014	0.00313
2455842.64940682	3.2673	30.31	0.00014	0.00313
2455843.53446953	3.3128	16.47	0.00013	0.00338
2455843.66473254	3.3214	229.83	0.00013	0.00338
2455844.53056656	3.3722	187.91	0.00002	0.00472
2455844.66179197	3.3799	41.27	-0.00002	0.00507
2455845.54569082	3.4265	33.04	-0.00016	0.00578
2455845.65206487	3.4313	201.48	-0.00009	0.00597
2455870.51420322	4.7844	86.70	-0.00007	0.00579
2455870.52215421	4.7834	97.93	-0.00007	0.00579
2455870.53060607	4.7819	109.16	-0.00007	0.00579
2455871.50280525	4.8375	241.14	-0.00022	0.00565
2455871.51026399	4.8370	252.37	-0.00022	0.00565
2455871.51752074	4.8366	269.21	-0.00022	0.00565
2455872.49503353	4.8869	46.81	-0.00026	0.00454
2455872.50361680	4.8853	63.65	-0.00024	0.00411
2455872.51065080	4.8852	74.88	-0.00027	0.00450
2455872.51832551	4.8914	86.10	-0.00024	0.00435
2455873.50406872	4.9404	240.54	-0.00039	0.00408
2455873.51131777	4.9401	251.76	-0.00037	0.00427
2455873.51863681	4.9397	262.99	-0.00036	0.00367
2455874.50355099	4.9964	57.42	-0.00059	0.00403
2455874.51074342	4.9962	68.65	-0.00061	0.00378
2455874.51805876	4.9958	79.87	-0.00061	0.00378
2455875.50408302	5.0515	234.30	-0.00060	0.00352
2455875.51155021	5.0509	245.52	-0.00060	0.00352
2455875.51886866	5.0506	256.75	-0.00060	0.00352
2455878.50606288	5.2162	44.91	0.00019	0.00443
2455878.51386630	5.2153	56.14	0.00017	0.00429
2455878.52076438	5.2153	67.36	0.00014	0.00438
2455879.50702795	5.2777	227.38	0.00017	0.00412

Table A14: HARPS 2011-2012 data for the asteroid Vesta, processed by the HARPS pipeline with the correct barycentric RV and accounting for the relativistic correction. From left to right are given: Julian date (flux-weighted mid-exposure times of observation), the timelag Δt between the HARPS observations and the time at which SDO observed the same hemisphere of the Sun, the apparent planetographic longitude of Vesta λ, the values of the basis functions for the sunspot velocity signal, $\hat{v}_{spots}$ and the suppression of granular blueshift, $\hat{v}_{conv}$.

Julian Date [MJD_{mid}-UTC]	Δt [days]	λ [deg]	$\hat{v}_{spots}$ [km s^{-1}]	$\hat{v}_{conv}$ [km s^{-1}]
2455879.51427708	5.2774	238.61	0.00019	0.00400
2455879.52152229	5.2771	249.84	0.00021	0.00437
2455886.55971131	5.6625	109.52	-0.00009	0.00324
2455886.56696080	5.6622	120.75	-0.00009	0.00324
2455886.57392844	5.6622	131.98	-0.00009	0.00324
2455887.52342644	5.7196	224.60	0.00013	0.00321
2455887.53095415	5.7190	235.83	0.00013	0.00321
2455887.53806579	5.7189	247.06	0.00013	0.00321
2455888.52593242	5.7727	47.04	0.00012	0.00302
2455888.53317611	5.7724	58.27	0.00012	0.00302
2455888.54049630	5.7720	69.50	0.00012	0.00302
2455889.52578074	5.8284	223.87	0.00031	0.00312
2455889.53310116	5.8280	235.10	0.00031	0.00312
2455889.54034195	5.8277	246.32	0.00031	0.00312
2455890.50917526	5.8867	12.62	0.00011	0.00361
2455890.51649149	5.8863	23.85	0.00011	0.00361
2455890.52382222	5.8859	35.08	0.00011	0.00361
2455891.52246765	5.9428	211.90	-0.00004	0.00436
2455891.52978471	5.9424	223.12	-0.00004	0.00436
2455891.53703495	5.9421	234.35	-0.00004	0.00436
2455892.52735539	5.9935	34.33	0.00020	0.00452
2455892.53453612	5.9932	45.55	0.00016	0.00459
2455892.54214391	5.9995	62.40	0.00016	0.00459
2455893.51437423	6.0551	194.30	0.00011	0.00600
2455893.52626540	6.0501	211.14	0.00011	0.00600
2455893.53359078	6.0497	222.37	0.00011	0.00600
2455894.50541095	6.0988	354.27	-0.00014	0.00625
2455894.51266019	6.1054	5.49	-0.00014	0.00625
2455894.52011844	6.1049	16.72	-0.00014	0.00625
2455895.51190055	6.1617	182.30	-0.00012	0.00540
2455895.51928533	6.1613	193.53	-0.00012	0.00540
2455895.52668202	6.1608	204.76	-0.00012	0.00540
2455896.51221054	6.2170	359.11	-0.00023	0.00542
2455896.51945075	6.2167	10.34	-0.00023	0.00542
2455896.52676887	6.2163	21.56	-0.00023	0.00542
2455897.51313557	6.2716	175.91	0.00015	0.00498
2455897.52017185	6.2715	187.14	0.00015	0.00498
2455897.52797234	6.2776	203.98	0.00015	0.00498
2455898.51251923	6.3278	352.71	-0.00013	0.00401
2455898.51955262	6.3277	3.94	-0.00015	0.00410
2455898.52692661	6.3272	15.17	-0.00012	0.00426
2455899.51280365	6.3830	169.51	-0.00012	0.00374
2455899.51984723	6.3829	180.74	-0.00013	0.00381
2455899.52750987	6.3822	191.96	-0.00011	0.00371

Table A15: (Continued) HARPS 2011-2012 data for the asteroid Vesta, processed by the HARPS pipeline with the correct barycentric RV and accounting for the relativistic correction. From left to right are given: Julian date (flux-weighted mid-exposure times of observation), the timelag Δt between the HARPS observations and the time at which SDO observed the same hemisphere of the Sun, the apparent planetographic longitude of Vesta λ, the values of the basis functions for the sunspot velocity signal, $\hat{v}_{spots}$ and the suppression of granular blueshift, $\hat{v}_{conv}$.

Julian Date [MJD_{mid}-UTC]	Δt [days]	λ [deg]	$\hat{v}_{spots}$ [km s^{-1}]	$\hat{v}_{conv}$ [km s^{-1}]
2455900.51316244	6.4382	346.30	-0.00020	0.00374
2455900.52048381	6.4378	357.53	-0.00019	0.00355
2455900.52779857	6.4444	14.37	-0.00018	0.00348
2455901.51376528	6.4932	163.10	0.00032	0.00319
2455901.52080259	6.4931	174.32	0.00031	0.00348
2455901.52818692	6.4996	191.16	0.00029	0.00316
2455902.51342158	6.5491	339.89	-0.00014	0.00310
2455902.52087765	6.5555	356.73	-0.00016	0.00307
2455902.52825791	6.5551	7.96	-0.00013	0.00337

Table A16: (Continued again) HARPS 2011-2012 data for the asteroid Vesta, processed by the HARPS pipeline with the correct barycentric RV and accounting for the relativistic correction. From left to right are given: Julian date (flux-weighted mid-exposure times of observation), the timelag Δt between the HARPS observations and the time at which SDO observed the same hemisphere of the Sun, the apparent planetographic longitude of Vesta λ, the values of the basis functions for the sunspot velocity signal, $\hat{v}_{spots}$ and the suppression of granular blueshift, $\hat{v}_{conv}$.

Bibliography

Aigrain, S., Hodgkin, S. T., Irwin, M. J., Lewis, J. R., & Roberts, S. J. 2015, Monthly Notices of the Royal Astronomical Society, 447, 2880

Aigrain, S., Pont, F., & Zucker, S. 2012, Monthly Notices of the Royal Astronomical Society, 419, 3147

Allen, C. 1973, Allen: Astrophysical Quantities (3rd edn.) The Athlone Press - Google Scholar (University of London)

Ambikasaran, S., Foreman-Mackey, D., Greengard, L., Hogg, D. W., & O'Neil, M. 2014, Numerical Analysis, pre-print (arXiv:1403.6015)

Athay, R. G. 1974, Proceedings of the International Astronomical Union, 56

Aurière, M., Lignières, F., Konstantinova-Antova, R., Charbonnel, C., Petit, P., Tsvetkova, S., & Wade, G. 2014, in Putting A Stars into Context: Evolution, Environment, and Related Stars, ed. G. Mathys, E. R. Griffin, O. Kochukhov, R. Monier, & G. M. Wahlgren, 444–450, 1310.6942

Auvergne, M. et al. 2009, Astronomy and Astrophysics, 506, 411

Babcock, H. W. 1961, ApJ, 133, 572

Baglin, A., & Team, C. 1998, Proceedings of the International Astronomical Union, 185, 301

Bahng, J., & Schwarzschild, M. 1961, Astrophysical Journal, 134, 312

Bakos, G., Noyes, R. W., Kovács, G., Stanek, K. Z., Sasselov, D. D., & Domsa, I. 2004, PASP, 116, 266

Baliunas, S. L., Donahue, R. A., Soon, W., & Henry, G. W. 1998, Cool Stars, Stellar Systems, and the Sun, 154, 153

Baliunas, S. L. et al. 1995, The Astrophysical Journal, 438, 269

Baluev, R. V. 2013, Monthly Notices of the Royal Astronomical Society, 429, 2052

Baranne, A. et al. 1996, Astronomy and Astrophysics Supplement Series, 119, 373

Barclay, T. 2014, American Astronomical Society Meeting Abstracts #224, 224

Barclay, T., Endl, M., Huber, D., Foreman-Mackey, D., Cochran, W. D., MacQueen, P. J., Rowe, J. F., & Quintana, E. V. 2015, Astrophysical Journal, 800, 46

Barros, S. C. C. et al. 2014, Astronomy and Astrophysics, 569, 74

Bastien, F. A., Stassun, K. G., Basri, G., & Pepper, J. 2013, Nature, 500, 427

Bastien, F. A. et al. 2014, The Astronomical Journal, 147, 29

Batalha, N. M. et al. 2011a, The Astrophysical Journal, 729, 27

——. 2011b, The Astrophysical Journal, 729, 27

Bedding, T. R. et al. 2001, Astrophysical Journal, 549, L105

Berdyugina, S. V. 2005, Living Rev. Solar Phys., 2

Berdyugina, S. V., & Usoskin, I. G. 2003, Astronomy and Astrophysics, 405, 1121

Boisse, I., Bouchy, F., Hébrard, G., Bonfils, X., Santos, N., & Vauclair, S. 2011, Astronomy and Astrophysics, 528, A4

Boisse, I. et al. 2009, Astronomy and Astrophysics, 495, 959

Bonfils, X. et al. 2013, Astronomy and Astrophysics, 549, A109

——. 2007, Astronomy and Astrophysics, 474, 293

Borucki, W. J. et al. 2011, The Astrophysical Journal, 728, 117

Bouchy, F., Bazot, M., Santos, N. C., Vauclair, S., & Sosnowska, D. 2005, Astronomy and Astrophysics, 440, 609

Bruntt, H. et al. 2010, Astronomy and Astrophysics, 519, A51

Bumba, V., & Ambroz, P. 1974, Proceedings of the International Astronomical Union, 56, 183

Cameron, A. C., Pollacco, D., Hellier, C., West, R., & the WASP Consortium and the SOPHIE and CORALIE Planet-Search Teams. 2009, Proceedings of the International Astronomical Union, 4, 29

Campante, T. L. 2015, Submitted to IST Press, pre-print (arXiv:1503.06113)

Campbell, B., & Walker, G. A. H. 1985, Stellar Radial Velocities, -1, 5

Carrington, R. C. 1859, Monthly Notices of the Royal Astronomical Society, 19, 81

Carter, J. A. et al. 2012, Science, 337, 556

Catalano, S., Biazzo, K., Frasca, A., Marilli, E., Messina, S., & Rodonò, M. 2002, Astronomische Nachrichten, 323, 260

Cegla, H. M. et al. 2012, Monthly Notices of the Royal Astronomical Society, 421, L54

Chabrier, G., & Baraffe, I. 1997, Astronomy and Astrophysics, 327, 1039

Chabrier, G., & Küker, M. 2006, Astronomy and Astrophysics, 446, 1027

Chaplin, W. J. et al. 2014, The Astrophysical Journal Supplement Series, 210, 1

Charbonneau, P. 2010, Living Reviews in Solar Physics, 7, 3

Chib, & Jeliazkov. 2001, American Statistical Association Portal :: Marginal Likelihood From the Metropolis–Hastings Output - Journal of the American Statistical Association - Volume 96, Issue 453

Choudhuri, A. R. 2007, in American Institute of Physics Conference Series, Vol. 919, Kodai School on Solar Physics, ed. S. S. Hasan & D. Banerjee, 49–73

Cincunegui, C., Díaz, R. F., & Mauas, P. J. D. 2007, Astronomy and Astrophysics, 469, 309

Collier Cameron, A. et al. 2009, Monthly Notices of the Royal Astronomical Society, 400, 451

——. 2006, Monthly Notices of the Royal Astronomical Society, 373, 799

Cosentino, R. et al. 2012, Society of Photo-Optical Instrumentation Engineers (SPIE) Conference Series, 8446, 84461V

Crossfield, I. J. M. et al. 2015, Astrophysical Journal, pre-print (arXiv:1501.03798)

Cumming, A. 2004, Monthly Notices of the Royal Astronomical Society, 354, 1165

Czekala, I., Andrews, S. M., Mandel, K. S., Hogg, D. W., & Green, G. M. 2014, Astrophysical Journal, pre-print (arXiv:1412.5177)

de Bruijne, J. H. J. 2012, Astrophysics and Space Science, 341, 31

Del Moro, D., Berrilli, F., Duvall, T. L. J., & Kosovichev, A. G. 2004, Solar Physics, 221, 23

Delfosse, X. et al. 2013, SF2A-2013: Proceedings of the Annual meeting of the French Society of Astronomy and Astrophysics, 497, 1310.2991

Deming, D., Espenak, F., Jennings, D. E., Brault, J. W., & Wagner, J. 1987, Astrophysical Journal, 316, 771

Deming, D., & Plymate, C. 1994, Astrophysical Journal, 426, 382

Desort, M., Lagrange, A. M., Galland, F., Udry, S., & Mayor, M. 2007, Astronomy and Astrophysics, 473, 983

Donati, J. F., & Collier Cameron, A. 1997, Monthly Notices of the Royal Astronomical Society, 291, 1

Doyle, L. R. et al. 2011, Science, 333, 1602

Dravins, D., Lindegren, L., & Nordlund, A. 1981, Astronomy and Astrophysics, 96, 345

Dressing, C. D. et al. 2015, Astrophysical Journal, 800, 135

Dumusque, X., Boisse, I., & Santos, N. C. 2014, ApJ, 796, 132, 1409.3594

Dumusque, X. et al. 2014, Astrophysical Journal, 789, 154

——. 2012, Nature,

Dumusque, X., Udry, S., Lovis, C., Santos, N. C., & Monteiro, M. J. P. F. G. 2010, Astronomy and Astrophysics, 525, A140

Duncan, D. K. et al. 1991, The Astrophysical Journal Supplement Series, 76, 383

Edelson, R. A., & Krolik, J. H. 1988, Astrophysical Journal, 333, 646

Ferraz-Mello, S., Tadeu dos Santos, M., Beaugé, C., Michtchenko, T. A., & Rodríguez, A. 2011, Astronomy and Astrophysics, 531, A161

Figueira, P., Santos, N. C., Pepe, F., Lovis, C., & Nardetto, N. 2013, Astronomy and Astrophysics, 557, 93

Fogtmann-Schulz, A., Hinrup, B., Van Eylen, V., Christensen-Dalsgaard, J., Kjeldsen, H., Silva Aguirre, V., & Tingley, B. 2014, ApJ, 781, 67, 1311.6336

Ford, E. B. 2006, The Astrophysical Journal, 642, 505

Foreman-Mackey, D., Hogg, D. W., & Morton, T. D. 2014, Astrophysical Journal, 795, 64

Foreman-Mackey, D., Montet, B. T., Hogg, D. W., Morton, T. D., Wang, D., & Schölkopf, B. 2015, Astrophysical Journal, pre-print (arXiv:1502.04715)

Fortier, A., Beck, T., Benz, W., Broeg, C., Cessa, V., Ehrenreich, D., & Thomas, N. 2014, Society of Photo-Optical Instrumentation Engineers (SPIE) Conference Series, 9143, 91432J

Fressin, F. et al. 2013, ApJ, 766, 81, 1301.0842

Fressin, F. et al. 2011, The Astrophysical Journal Supplement Series, 197, 5

Gelman, A., Carlin, J. B., Stern, H. S., & Rubin, D. B. 2004, Bayesian Data Analysis (Chapman & Hall/CRC)

Gibson, N. P., Aigrain, S., Roberts, S., Evans, T. M., Osborne, M., & Pont, F. 2011, Monthly Notices of the Royal Astronomical Society, 419, 2683

Gilliland, R. L. et al. 2011, The Astrophysical Journal Supplement Series, 197, 6

Gizon, L., Birch, A. C., & Spruit, H. C. 2010, Annual Review of Astronomy and Astrophysics, 48, 289

Gizon, L., Duvall, T. L. J., & Larsen, R. M. 2001, Proceedings of the International Astronomical Union, 203, 189

Gray, D. F. 1989, Astronomical Society of the Pacific, 101, 832

——. 1992, Camb. Astrophys. Ser.

Gregory, P. C. 2011, MNRAS, 415, 2523, 1101.0800

Gregory, P. C. 2007, Monthly Notices of the Royal Astronomical Society, 381, 1607

Grunblatt, S. K., Howard, A. W., & Haywood, R. D. 2015, ApJ, 808, 127, 1501.00369

Grunblatt, S. K., Howard, A. W., & Haywood, R. D. 2015, Astrophysical Journal, pre-print (arXiv:1501.00369)

Haas, M. R. et al. 2014, American Astronomical Society Meeting Abstracts #223, 223

Hale, G. E. 1908, The Astrophysical Journal, 28, 315

Hall, J. C. 2008, Living Reviews in Solar Physics, 5, 2

Hall, J. C., Lockwood, G. W., & Skiff, B. A. 2007, The Astronomical Journal, 133, 862

Hansen, C. J., & Kawaler, S. D. 1994, "Stellar Interiors. Physical Principles

Hathaway, D. H. 2010, Living Reviews in Solar Physics, 7, 1

Hatzes, A. P. 1996, Publications of the Astronomical Society of the Pacific, 108, 839

——. 2014, Nature, 513, 353

Hatzes, A. P. et al. 2010, Astronomy and Astrophysics, 520, A93

——. 2011, The Astrophysical Journal, 743, 75

Haywood, R. D. et al. 2014, Monthly Notices of the Royal Astronomical Society, Volume 443, Issue 3, p.2517-2531, 443, 2517

Hébrard, G. et al. 2014, Astronomy and Astrophysics, 572, 93

Henry, T. J., Soderblom, D. R., Donahue, R. A., & Baliunas, S. L. 1996, The Astronomical Journal, 111, 439

Hilditch, R. W. 2001, An Introduction to Close Binary Stars

Hirayama, T. 1978, Publications of the Astronomical Society of Japan, 30, 337

Högbom, J. A. 1974, Astronomy and Astrophysics Supplement Series, 15, 417

Hogstrom, K. et al. 2013, American Astronomical Society Meeting Abstracts #221, 221

Holman, M. J. et al. 2010, Science, 330, 51

Howard, A. W. et al. 2010, Science, 330, 653

——. 2013, Nature, 503, 381

Huélamo, N. et al. 2008, Astronomy and Astrophysics, 489, L9

Hussain, G. 2002, Astronomische Nachrichten, 323, 349

Ivanov, K. G., & Kharshiladze, A. F. 2013, Geomagnetism and Aeronomy, 53, 677

Jeffers, S. V., Keller, C. U., & Stempels, E. 2009, in Cool Stars, Stellar Systems, and the Sun (AIP), 664–667

Jeffreys, S. H. 1961, The Theory of Probability (Oxford University Press)

Jiménez, A., Pallé, P. L., Régulo, C., Roca Cortes, T., & Isaak, G. R. 1986, COSPAR and IAU, 6, 89

Kjeldsen, H., Bedding, T. R., Frandsen, S., & Dall, T. H. 1999, Monthly Notices of the Royal Astronomical Society, 303, 579

Kjeldsen, H., Christensen-Dalsgaard, J., Handberg, R., Brown, T. M., Gilliland, R. L., Borucki, W. J., & Koch, D. 2010, Astronomische Nachrichten, 331, 966

Knutson, H. A., Charbonneau, D., Allen, L. E., Burrows, A., & Megeath, S. T. 2008, The Astrophysical Journal, 673, 526

Koch, D. G. et al. 2010, Astrophysical Journal, 713, L79

Kopp, G., & Lean, J. L. 2011, Geophysical Research Letters, 38, L01706

Kraft, R. P. 1967, Astrophysical Journal, 150, 551

Kuhn, J. R. 1983, Astrophysical Journal, 264, 689

Labonte, B. J., Howard, R., & Gilman, P. A. 1981, Astrophysical Journal, 250, 796

Lagrange, A. M., Desort, M., & Meunier, N. 2010, Astronomy and Astrophysics, 512, A38

Lagrange, A. M., Meunier, N., Desort, M., & Malbet, F. 2011, Astronomy and Astrophysics, 528, L9

Lanza, A. F., Boisse, I., Bouchy, F., Bonomo, A. S., & Moutou, C. 2011, Astronomy and Astrophysics, 533, A44

Lanza, A. F. et al. 2010, Astronomy and Astrophysics, 520, A53

Lanza, A. F., & Molaro, P. 2015, Experimental Astronomy, 39, 461, 1505.00918

Lanza, A. F. et al. 2009, Astronomy and Astrophysics, 493, 193

Latham, D. W., Stefanik, R. P., Mazeh, T., & Torres, G. 1989, Bulletin of the American Astronomical Society, 21, 1224

Léger, A. et al. 2009, Astronomy and Astrophysics, 506, 287

Leighton, R. B. 1959, The Astrophysical Journal, 130, 366

Leighton, R. B., Noyes, R. W., & Simon, G. W. 1962, Astrophysical Journal, 135, 474

Lindegren, L. 2009, American Astronomical Society, IAU Symposium #261. Relativity in Fundamental Astronomy: Dynamics, Reference Frames, and Data Analysis 27 April - 1 May 2009 Virginia Beach, VA, USA, #16.01; Bulletin of the American Astronomical Society, Vol. 41, p.890, 261, 1601

Lindegren, L., & Dravins, D. 2003, Astronomy and Astrophysics, 401, 1185

Lissauer, J. J., Dawson, R. I., & Tremaine, S. 2014a, Advances in exoplanet science from Kepler

Lissauer, J. J. et al. 2011a, Nature, 470, 53

——. 2013, The Astrophysical Journal, 770, 131

——. 2014b, Astrophysical Journal, 784, 44

——. 2011b, The Astrophysical Journal Supplement Series, 197, 8

Llama, J., Jardine, M., Mackay, D. H., & Fares, R. 2012, Monthly Notices of the Royal Astronomical Society, 422, L72

Lockwood, G. W., Skiff, B. A., Henry, G. W., Henry, S., Radick, R. R., Baliunas, S. L., Donahue, R. A., & Soon, W. 2007, The Astrophysical Journal Supplement Series, 171, 260

Lockwood, G. W., Skiff, B. A., & Radick, R. R. 1997, Astrophysical Journal, 485, 789

Lockwood, M. 2005, Solar outputs, their variations and their effects on Earth

Lomb, N. R. 1976, Astrophysics and Space Science, 39, 447

Lovis, C. et al. 2011, Astronomy & Astrophysics, pre-print (arXiv:1107.5325)

Lovis, C., & Pepe, F. 2007, Astronomy and Astrophysics, 468, 1115

Makarov, V. V., Beichman, C. A., Catanzarite, J. H., Fischer, D. A., Lebreton, J., Malbet, F., & Shao, M. 2009, The Astrophysical Journal, 707, L73

Mallik, S. V. 1996, VizieR On-line Data Catalog, 412, 40359

Marcy, G. W., & Butler, R. P. 1994, Cool Stars, Stellar Systems, and the Sun, 64, 587

Marcy, G. W. et al. 2014, The Astrophysical Journal Supplement Series, 210, 20

Martínez-Arnáiz, R., Maldonado, J., Montes, D., Eiroa, C., & Montesinos, B. 2010, Astronomy and Astrophysics, 520, A79

Matthews, J. M. et al. 2000, Cool Stars, Stellar Systems, and the Sun, 203, 74

Maunder, E. W. 1904, Monthly Notices of the Royal Astronomical Society, 64, 747

Mayor, M., Lovis, C., & Santos, N. C. 2014, Nature, 513, 328

Mayor, M. et al. 2011, Astronomy & Astrophysics, pre-print (arXiv:1109.2497)

——. 2003, The Messenger, 114, 20

Mayor, M., & Queloz, D. 1995, Nature, 378, 355

Mayor, M., & Udry, S. 2008, Physica Scripta, T130, 014010

McQuillan, A., Mazeh, T., & Aigrain, S. 2014, The Astrophysical Journal Supplement Series, 211, 24

Metropolis, N., Rosenbluth, A. W., Rosenbluth, M. N., Teller, A. H., & Teller, E. 1953, The Journal of Chemical Physics, 21, 1087

Meunier, N., Desort, M., & Lagrange, A. M. 2010, Astronomy and Astrophysics, 512, A39

Middelkoop, F. 1982, Astronomy and Astrophysics, 107, 31

Miesch, M. S. 2005, Living Reviews in Solar Physics, 2, 1

Molaro, P., & Centurión, M. 2010, Astronomy and Astrophysics, 525, A74

Morin, J. et al. 2008, MNRAS, 384, 77, 0711.1418

Murdin, P. 2002, Encyclopedia of Astronomy and Astrophysics, -1

Novotny, E. 1971, An introduction to stellar atmospheres and interiors., by Novotny, E.. New York, NY (USA): Oxford University Press, 350 p., -1

Olah, K., Panov, K. P., Pettersen, B. R., Valtaoja, E., & Valtaoja, L. 1989, Astronomy and Astrophysics, 218, 192

Orosz, J. A. et al. 2012a, Astrophysical Journal, 758, 87

——. 2012b, Science, 337, 1511

Parker, E. N. 1963, ApJ, 138, 226

Pepe, F. 2010, The HARPS-N Project, Tech. rep.

Pepe, F. et al. 2013, Nature, 503, 377

Pepe, F., Ehrenreich, D., & Meyer, M. R. 2014a, Nature, 513, 358

Pepe, F. et al. 2014b, Astronomische Nachrichten, 335, 8

Perruchot, S. et al. 2008, Society of Photo-Optical Instrumentation Engineers (SPIE) Conference Series, 7014, 70140J

Perryman, M. 2011, The Exoplanet Handbook by Michael Perryman

Pesnell, W. D., Thompson, B. J., & Chamberlin, P. C. 2012, Solar Physics, 275, 3

Petigura, E. A., Marcy, G. W., & Howard, A. W. 2013, Astrophysical Journal, 770, 69

Petrovay, K., & van Driel-Gesztelyi, L. 1997, Solar Physics, 176, 249

Pollacco, D. L. et al. 2006, Publications of the Astronomical Society of the Pacific, 118, 1407

Pont, F., Aigrain, S., & Zucker, S. 2010, Monthly Notices of the Royal Astronomical Society, 411, 1953

Press, W. H., Flannery, B. P., & Teukolsky, S. A. 1986, Cambridge: University Press, 1986, -1

Queloz, D. et al. 2010, Astronomy and Astrophysics, 517, L1

——. 2009, Astronomy and Astrophysics, 506, 303

——. 2001a, Astronomy and Astrophysics, 379, 279

——. 2001b, The Messenger, 105, 1

——. 2000, Astronomy and Astrophysics, 354, 99

Quintana, E. V. et al. 2014, Science, 344, 277

Quirrenbach, A. et al. 2013, EPJ Web of Conferences, 47, 05006

Radick, R. R., Lockwood, G. W., Skiff, B. A., & Baliunas, S. L. 1998, The Astrophysical Journal Supplement Series, 118, 239

Rasmussen, C. E., & Williams, C. K. I. 2006, Gaussian Processes for Machine Learning (MIT Press)

Rauer, H. et al. 2014, Experimental Astronomy, 38, 249

Reiners, A. 2009, Astronomy and Astrophysics, 498, 853

——. 2012, Living Rev. Solar Phys., 9

Reiners, A., Shulyak, D., Anglada-Escudé, G., Jeffers, S. V., Morin, J., Zechmeister, M., Kochukhov, O., & Piskunov, N. 2013, Astronomy and Astrophysics, 552, 103

Reuyl, D., & Holmberg, E. 1943, Astrophysical Journal, 97, 41

Ricker, G. R. et al. 2015, Journal of Astronomical Telescopes, Instruments, and Systems, 1, 4003

Roberts, D. H., Lehar, J., & Dreher, J. W. 1987, The Astronomical Journal, 93, 968

Roberts, S., Osborne, M., Ebden, M., Reece, S., Gibson, N., & Aigrain, S. 2012, Philosophical Transactions of the Royal Society A: Mathematical, Physical and Engineering Sciences, 371, 20110550

Roberts, W. O. 1945, Astrophysical Journal, 101, 136

Robertson, P., Mahadevan, S., Endl, M., & Roy, A. 2014, Science, 345, 440

Robinson, R. D., & Boice, D. C. 1982, Solar Phys., 81, 25

Robinson, Jr., R. D. 1980, ApJ, 239, 961

Roudier, T., Malherbe, J. M., Vigneau, J., & Pfeiffer, B. 1998, Astronomy and Astrophysics, 330, 1136

Rowe, J. F. et al. 2014, The Astrophysical Journal, 784, 45

Russell, C. T. et al. 2012, Science, 336, 684

Rutten, R. J., & Schrijver, C. J. 1994, NATO Advanced Science Institutes (ASI) Series C, 433

Saar, S. 1991, IAU Colloq. 130: The Sun and Cool Stars. Activity, Magnetism, Dynamos, 380, 389

Saar, S. H., & Donahue, R. A. 1997, The Astrophysical Journal, 485, 319

Sanchis-Ojeda, R., Rappaport, S., Winn, J. N., Levine, A., Kotson, M. C., Latham, D. W., & Buchhave, L. A. 2013, The Astrophysical Journal, 774, 54

Sanchis-Ojeda, R., & Winn, J. N. 2011, The Astrophysical Journal, 743, 61

Sanchis-Ojeda, R., Winn, J. N., Holman, M. J., Carter, J. A., Osip, D. J., & Fuentes, C. I. 2011, The Astrophysical Journal, 733, 127

Santos, N. C. et al. 2014, Astronomy and Astrophysics, 566, 35

Scargle, J. D. 1982, Astrophysical Journal, 263, 835

Schlaufman, K. C. 2010, Astrophysical Journal, 719, 602

Schou, J. et al. 2012, Solar Physics, 275, 229

Schrijver, C. J. 2002, Astronomische Nachrichten, 323, 157

Schrijver, C. J., & Zwaan, C. 2000, Solar and stellar magnetic activity / Carolus J. Schrijver, Cornelius Zwaan. New York : Cambridge University Press, 2000. (Cambridge astrophysics series ; 34), -1

Schwabe, M. 1844, Astronomische Nachrichten, 21, 233

Seager, S., & Mallen Ornelas, G. 2003, The Astrophysical Journal, 585, 1038

Sheeley, N. R. J. 1967, The Astrophysical Journal, 147, 1106

Skumanich, A. 1972, Astrophysical Journal, 171, 565

Snodgrass, H. B., & Ulrich, R. K. 1990, Astrophysical Journal, 351, 309

Solanki, S. K. 2002, Astronomische Nachrichten, 323, 165

——. 2003, Astronomy and Astrophysics Review, 11, 153

Soltau, D. 1993, in The magnetic and velocity fields of solar active regions. Astronomical Society of the Pacific Conference Series; Proceedings of the International Astronomical Union (IAU) Colloquium no. 141; held in Beijing; China; 6-12 September 1992; San Francisco: Astronomical Society of the Pacific (ASP), 225

Sozzetti, A. 2011, EAS Publications Series, 45, 273

Spiegel, E. A., & Zahn, J.-P. 1992, Astronomy and Astrophysics, 265, 106

Spruit, H. C. 1976, Solar Physics, 50, 269

Stephenson, C. B. 1951, Astrophysical Journal, 114, 500

Strand, K. A. 1943, Publications of the Astronomical Society of the Pacific, 55, 29

Strassmeier, K. G. 2009, Astronomy and Astrophysics Review, 17, 251

Strassmeier, K. G., Washuettl, A., & Schwope, A. 2002, Astronomische Nachrichten, 323, 155

Struve, O. 1952, The Observatory, 72, 199

Stumpe, M. C. et al. 2012, Publications of the Astronomical Society of the Pacific, 124, 985

Thomas, J. H., & Weiss, N. O. 2008, Sustainability, -1

Thomas, P. C., Binzel, R. P., Gaffey, M. J., Zellner, B. H., Storrs, A. D., & Wells, E. 1997, Icarus, 128, 88

Thompson, W. T. 2006, Astronomy and Astrophysics, 449, 791

Tobias, S. M. 2002, Philosophical Transactions of the Royal Society A: Mathematical, Physical and Engineering Sciences, 360, 2741

Toner, C. G., & Gray, D. F. 1988, The Astrophysical Journal, 334, 1008

Torres, G. et al. 2011, Astrophysical Journal, 727, 24

Tuomi, M., Anglada-Escudé, G., Jenkins, J. S., & Jones, H. R. A. 2014, MNRAS, pre-print (arXiv:1405.2016)

van de Kamp, P. 1969, Astronomical Journal, 74, 757

Vaughan, A. H., Preston, G. W., & Wilson, O. C. 1978, Publications of the Astronomical Society of the Pacific, 90, 267

Vogt, S. S. et al. 1994, Society of Photo-Optical Instrumentation Engineers (SPIE) Conference Series, 2198, 362

Vogt, S. S., & Penrod, G. D. 1983, Publications of the Astronomical Society of the Pacific, 95, 565

Voigt, H.-H. 1956, Zeitschrift fur Astrophysik, 40, 157

Walder, R., Folini, D., & Meynet, G. 2012, Space Sci. Rev., 166, 145

Walkowicz, L. M. et al. 2011, The Astronomical Journal, 141, 50

Weiss, L. M., & Marcy, G. W. 2014, The Astrophysical Journal, 783, L6

Wilson, O. C. 1963, Astrophysical Journal, 138, 832

——. 1968, The Astrophysical Journal, 153, 221

——. 1978, The Astrophysical Journal, 226, 379

Wolszczan, A., & Frail, D. A. 1992, Nature (ISSN 0028-0836), 355, 145

Yeo, K. L., Solanki, S. K., & Krivova, N. A. 2013, A&A., 550, A95, 1302.1442

Zechmeister, M., & Kürster, M. 2009, Astronomy and Astrophysics, 496, 577

Zeng, L., & Sasselov, D. 2013, PASP, 125, 227, 1301.0818

Zirin, H. 1966, A Blaisdell Book in the Pure and Applied Sciences, Waltham, Mass.: Blaisdell, —c1966, -1